DEFENCE S&T TECHNICAL BULLETIN

VOL. 10 NUM. 3 YEAR 2017 ISSN 1985-6571

CONTENTS

Ministry of Defence
Malaysia

SCIENCE & TECHNOLOGY RESEARCH INSTITUTE
FOR DEFENCE (STRIDE)

AIMS AND SCOPE

The Defence S&T Technical Bulletin is the official technical bulletin of the Science & Technology Research Institute for Defence (STRIDE). The bulletin, which is indexed in, among others, Scopus, Index Corpenicus, ProQuest and EBSCO, contains manuscripts on research findings in various fields of defence science & technology. The primary purpose of this bulletin is to act as a channel for the publication of defence-based research work undertaken by researchers both within and outside the country.

WRITING FOR THE DEFENCE S&T TECHNICAL BULLETIN

Contributions to the bulletin should be based on original research in areas related to defence science & technology. All contributions should be in English.

PUBLICATION

The editors' decision with regard to publication of any item is final. A manuscript is accepted on the understanding that it is an original piece of work that has not been accepted for publication elsewhere.

PRESENTATION OF MANUSCRIPTS

The format of the manuscript is as follows:

a) Page size A4
b) MS Word format
c) Single space
d) Justified
e) In Times New Roman ,11-point font
f) Should not exceed 20 pages, including references
g) Texts in charts and tables should be in 10-point font.

Please e-mail the manuscript to:

1) Gs. Dr. Dinesh Sathyamoorthy (dinesh.sathyamoorthy@stride.gov.my)
2) Dr. Mahdi bin Che Isa (mahdi.cheisa@stride.gov.my)

The next edition of the bulletin (Vol. 11, Num. 1) is expected to be published in April 2018. The due date for submissions is 7 February 2018. **It is strongly iterated that authors are solely responsible for taking the necessary steps to ensure that the submitted manuscripts do not contain confidential or sensitive material.**

The template of the manuscript is as follows:

TITLE OF MANUSCRIPT

Name(s) of author(s)

Affiliation(s)

Email:

ABSTRACT

Contents of abstract.

Keywords: *Keyword 1; keyword 2; keyword 3; keyword 4; keyword 5.*

1. TOPIC 1

Paragraph 1.

Paragraph 2.

1.1 Sub Topic 1

Paragraph 1.

Paragraph 2.

2. TOPIC 2

Paragraph 1.

Paragraph 2.

Figure 1: Title of figure.

Table 1: Title of table.

Content	Content	Content
Content	Content	Content
Content	Content	Content
Content	Content	Content

Equation 1 (1)
Equation 2 (2)

REFERENCES

Long lists of notes of bibliographical references are generally not required. The method of citing references in the text is 'name date' style, e.g. 'Hanis (1993) claimed that...', or '…including the lack of interoperability (Bohara *et al.*, 2003)'. End references should be in alphabetical order. The following reference style is to be adhered to:

Books

Serra, J. (1982). *Image Analysis and Mathematical Morphology*. Academic Press, London.

Book Chapters

Goodchild, M.F. & Quattrochi, D.A. (1997). Scale, multiscaling, remote sensing and GIS. *In* Quattrochi, D.A. & Goodchild, M.F. (Eds.), *Scale in Remote Sensing and GIS*. Lewis Publishers, Boca Raton, Florida, pp. 1-11.

Journals / Serials

Jang, B.K. & Chin, R.T. (1990). Analysis of thinning algorithms using mathematical morphology. *IEEE T. Pattern Anal.*, **12**: 541-550.

Online Sources

GTOPO30 (1996). *GTOPO30: Global 30 Arc Second Elevation Data Set*. Available online at: http://edcwww.cr.usgs.gov/landdaac/gtopo30/gtopo30.html (Last access date: 1 June 2009).

Unpublished Materials (e.g. theses, reports and documents)

Wood, J. (1996). *The Geomorphological Characterization of Digital Elevation Models*. PhD Thesis, Department of Geography, University of Leicester, Leicester.

DESIGN OPTIMISATION OF SOLAR POWERED NEAR-SPACE VEHICLE FOR DEFENCE, SECURITY AND DISASTER MANAGEMENT APPLICATIONS

Azam Che Idris, Noor Azman Dollah, Muhamad Faiz Baharun, Mohd Rashdan Saad, Suriyadi Sojipto & Mohd Rosdzimin Abdul Rahman

Faculty of Engineering, National Defence University of Malaysia (UPNM), Malaysia

*Email: azam.che@gmail.com

ABSTRACT

The near-space region, which is the region between 12 to 62 mi above sea level, is the last frontier to be conquered by aviators. Radars, remote sensing devices and telecommunication satellites can perform better than satellites in orbit if they are flown in the near-space region. They are also cheaper to launch since space launch vehicle systems are exorbitantly expensive. This paper examines the necessary engineering factors that must be considered to design and optimise a perpetually flying near-space flight vehicle. The optimised design is then virtually simulated against real world operating conditions and engineering uncertainties using Simulink and the Monte Carlo method.

Keywords: *Solar; aircraft design; high-altitude, high altitude long endurance (HALE); pseudo-satellite.*

1. INTRODUCTION

The near-space region has been the focus of many military research institutions due to its huge potential and strategic importance. The term near-space is defined as the air space between 12 to 62 mi (approximately 19 to 100 km) of altitude. The area above 62 mi is widely considered as a sub-orbital outer space region. The characteristic of the near-space region is that its atmosphere is too rarefied to the extent that conventional winged flight is very difficult (but not impossible) while at the same time gravity is too strong for a satellite to orbit. If, for example, a pseudo-satellite could be placed on a station between these heights, the reduction of total life-cycle cost and an increase in responsiveness can be achieved (Stephens, 2005). Aircrafts that can carry satellite-capable systems in the near space region are called high-altitude platforms (HAP) (Jamison *et al.*, 2005).

The image capturing capabilities of a HAP carrying intelligence-surveillance-reconnaissance (ISR) equipment is much superior to those of a satellite due to closer distance to the earth surface. This is the reason why the United States Air Force (USAF) employed Lockheed's U2 high altitude long endurance (HALE) spy-planes, which flew at 70,000 ft (21 km) altitude for reconnaissance purposes. This aircraft is still in service, surviving the budget cuts that ended the life of another high-altitude ISR platform, the SR71 Blackbird. However, the USAF is also actively looking to design a successor to U2 as the current system requires two pilots to fly for 8 h before landing for refuelling (Navarro, 2007). In comparison, a perpetual HAP without the need to land and refuel would be a much better ISR system.

A HAP can be inserted into its intended altitude ad-hoc in a battlefield to connect all disparate elements and assets being deployed by the field commander. The HAP could simply act as the node to relay between a broadcast to the receivers, or it could become the hub to connect all incoming and outgoing data streams, such as depicted in Figure 1 (Pinkney *et al*., 1996). Current communication standards, such as the BOWMAN and JTIDS/Link16, can be adopted easily by a HAP system. As a replacement for military satellite communications (MILSATCOM), a pseudo-satellite on board of a HAP can operate at extremely high frequency (EHF) (at either 20 or 45 GHz), which is still uncluttered, has large spectral availability and has low probability of intercept (LPI) (Tozer *et al*., 2000). The range of communications is between 120 to 270 mi depending on the elevation angle of the broadcast and receiver beam (Pinkney *et al*., 1996). The platform itself is stealthy with low radar signature that shields it from enemy detection during active battle. Although possible, there is very limited number of surface to air missiles that can reach the near space altitude (Tozer *et al*., 2000).

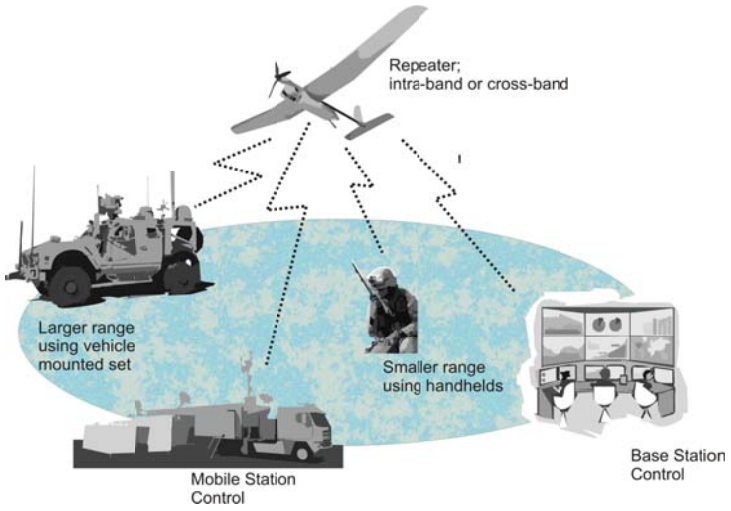

Figure 1: Personnel Communication System for beyond line of sight battlefield communications without the need for terrestrial infrastructure.

Besides communications, a HAP could also carry a portable radar system for over the horizon surveillance. The Missile Defence Agency (MDA) in the USA proposed a high-altitude radar system, weighing not more than 500 lbs, carried by an airship for cruise missile detection (Bolkcom, 2004). The potential is huge since at 20 km altitude, the radar coverage is about 500 km radius and radar would not be affected by any cloud layer in the troposphere (below 18 km altitude) (Colozza & Dolce, 2003).

If a HAP is fitted with a good resolution camera, it can be used effectively as a remote sensing system to observe disaster-prone regions. In the Flemish Institute for Technological Research (VITO), they experimented with a system that can capture an image with sensitivity of 30 cm from 18 km altitude, using a camera weighing no more than 3 kg (Everaerts, 2008). The FiRE project in the USA and COMETS in Europe are developed forest surveillance equipment using high-altitude unmanned aerial vehicle (UAV) to monitor wild forest fire (Ollero & Merino, 2006). This kind of system has better resolution in detecting forest fire since the platform is closer to surface in comparison to a satellite, thus giving a very early warning before the fire could spread further. There are also studies that concentrate on the role that HAPs could play in post-disaster situations. Ad-hoc communication network using a HAP is easy to set-up and can allow for quick connection among dispersed rescue workers and victims. The added benefit of using

HAPs for post-disaster communication networks is that the victims' cell phone location can be triangulated easily by determining the time of arrival (DOA) and time delay of arrival (TDOA) as long as the exact position of a moving HAP is known all the time (Deaton, 2008).

A perpetually flying HAP for defence, security and disaster management must have a rapid deployment mechanism to reach its intended altitude quickly in an emergency (Jamison *et al.*, 2005). A large airship with speed of only 30 kn could take days to reach their operating altitude and is also vulnerable to weather unpredictability. It is clear that current airship technologies are not enough and must include modifications to improve the deployment speed. Thus, in this paper, we devise an optimisation procedure for the design of a HAP flying using conventional wing lift that is augmented by lighter-than-air technology.

Since we endeavour to incorporate conventional lift from the wing for our design, we are at the mercy of the sun to supply power for high cruise speed. Solar powered airplane technology has gone a long way since the first one invented in 1974 by Boucher (1985). NASA's Environmental Research Aircraft Sensor Technology (ERAST) programme produced such successful solar aircrafts, such as Pathfinder, Centurion and Helios (Ehernberger *et al.*, 2004; Noll *et al.*, 2007). Recently, the Solar Impulse project has validated the prospect of perpetual flight by flying 24 h non-stop in 2010 (Courtney, 2015).

Based on our readings, we believe reliable broadband coverage using a pseudo-satellite on HAP can be achieved if the design objectives listed below can be satisfied:

1. Cruise at 21,000 m
2. Carry telecommunication payload of weight 100 kg with maximum power requirement of 400 W (similar to the HeliNet project (Tozer & Grace 2001; Thornton *et al.*, 2001; CAPANINA, 2004))
3. Endurance of more than 24 h (perpetual flight) using only solar power according to Malaysian solar irradiance model.

2. CONCEPTUAL DESIGN AND OPTIMISATION PROCEDURES

Quite a few literatures have been published that discussed the important issues pertaining to designing a solar aircraft (Brandt & Gilliam 1995; Noth, 2008; Ross 2008; Wickenheiser & Garcia 2009; Leutenegger *et al.*, 2011; Vidales, 2013). This paper will follow and modify Noth's (2008) methodology since it has a complete description and its algorithm has been shown as robust enough for many different design scenarios (Noth *et al.*, 2006; Hartney, 2011; Bhatt, 2012; Malaver, 2014). Nevertheless, all the methodologies other than Noth's also rely on similar basic aerodynamics, structural and energy management principles, and thus, they should all converge to similar design solutions.

The first step to satisfy an optimised design solution for a perpetual solar aircraft is to consider the straight level flight or cruise. During the flight cruise, the lift is balanced by the weight, which is constant since there would be no fuel burned. Equally, the thrust power is balanced by the total drag power. Incidentally, weight-lift and thrust-drag pairs are also related to each other. The total weight of the aircraft depends on the solar cells area and battery size, whereby both are designed specifically to satisfy to the power requirement of the aircraft. Thus, to find the design solutions, we could start by assuming thrust and drag power equilibrium, then work out the weight and lift of the aircraft, or in the same token, by first calculating total weight and lift before finding the corresponding power requirements. The aircraft weight optimisation approach seems more reasonable since total weight is constant for both day and night flying, whereas optimising using

the power approach introduces non-linearity early in the iterations since power available from the sun varies with time.

The total weight of solar aircraft (m_{tot}) is represented as Equation 1. It is simply the summation of mass for avionics (m_{avc}), payload (m_{pld}), airframe (m_{af}), solar cells (m_{sc}), maximum power point tracker (MPPT) (m_{mppt}), battery (m_{batt}) and the whole propulsion system (m_{prop}). This equation will be the master equation for optimisation iteration.

$$m_{tot} \cdot g = (m_{avc} + m_{pld} + m_{af} + m_{sc} + m_{mppt} + m_{batt} + m_{prop}) \cdot g \quad (1)$$

The avionic system and payload weight can be considered fixed. For our current design, they are 20 and 100 kg respectively as per the design objectives. The airframe structure weight can then be estimated from the wing span (b) and aspect ratio (Λ) using Equation 2.

$$m_{af} \cdot g = 0.044 b^{3.1} \Lambda^{-0.25} \quad (2)$$

This relation was suggested by Noth (2008) after he meticulously compiled 415 gliders (also called sailplanes) into a database. He chose the lightest 5% out of all gliders and came up with the equation.

The solar cells mass on the other hand is a product of its cell (including encapsulation) density constants ($k_{sc} + k_{enc}$) and their surface area (A_{sc}) such as in Equation 3.

$$m_{sc} = A_{sc} (k_{sc} + k_{enc}) \quad (3)$$

To estimate the solar cells area (A_{sc}), we first assume that the area is specifically chosen to obtain enough energy for day and night flying. Thus, the energy captured must be equal to the energy required by the straight level flight, avionics and payload. The total energy captured from sun rise to sun set is the product of the area under the solar irradiance curve with efficiencies for weather (η_{wt}), solar cells (η_{sc}), airfoil camber (η_{cbr}) and MPPT (η_{mppt}), such as in Equation 4. The energy required (Equation 5) is the time integration of the power for cruise plus the power for avionics and payload (Equation 6). The power for straight level cruise is well known (Filippone, 2006) and given in Equation 7. By inserting Equations 6 and 7 into Equation 5 and equating it to Equation 4, the solar cells area can be calculated:

$$Energy\ captured\ by\ solar\ cells,\ \ E_{total} = \frac{I_{max} T_{day}}{\pi/2} \eta_{wt} \eta_{sc} \eta_{cbr} \eta_{mppt} A_{sc} \quad (4)$$

$$Energy\ required,\ \ E_{tot} = P_{req} \left(T_{day} + \frac{T_{night}}{\eta_{chg} \eta_{dchg}} \right) \quad (5)$$

$$Power\ required,\ \ P_{req} = \frac{P_{lvl}}{\eta_{ctrl} \eta_{mot} \eta_{grbx} \eta_{plr}} + \frac{P_{avc} + P_{pld}}{\eta_{bec}} \quad (6)$$

$$P_{lvl} = \frac{C_D}{C_L^{1.5}} (m_{tot} g)^{1.5} \left(\frac{2}{\rho S} \right)^{0.5} = \frac{C_D}{C_L^{\frac{3}{2}}} (m_{tot} g)^{1.5} \left(\frac{2\Lambda}{\rho b^2} \right)^{0.5} \quad (7)$$

The mass of the MPPT also varies proportionally to the total solar cells area. It is the product of its density constant (k_{mppt}) with maximum irradiance (I_{max}), solar cell efficiency (η_{sc}), camber factor (η_{cbr}), MPPT efficiency (η_{mppt}) and solar cells area (A_{sc}). The relation is:

$$m_{mppt} = k_{mppt} I_{max} \eta_{sc} \eta_{cbr} \eta_{mppt} A_{sc} \tag{8}$$

The mass of the battery varies linearly with the total energy that will be stored for the night time flight, which can be expressed as below:

$$k_{batt} m_{batt} = \frac{T_{night}}{\eta_{dchg}} P_{req} \tag{9}$$

where k_{batt} is the specific energy content or also called as gravimetric energy density of the battery with the unit Wh/kg. This constant is definitely one of the major, if not the only, limiting factor in designing a perpetually flying solar aircraft. The current state-of-the-art of lithium-ion polymer battery contains about 200 Wh/kg or less. This is obviously inadequate to store enough energy for night flying without being an excessive weight burden onto the aircraft. In 2010, the Zephyr7 solar aircraft achieved continuous flight by using lithium-sulfur battery with energy density of 350 Wh/kg even though the manufacturer claimed that it could go up to 600 Wh/kg (Gao *et al*., 2015). Theoretically, Li-S battery could have up to 2,500 Wh/kg (Evers & Nazar, 2012) and this makes it attractive for manufacturers of electric vehicles since sulfur is a cheap and easily available material. However, they are still subjected to more research before it can be commercialised. Currently, a practical Li-S battery has been demonstrated (Liang *et al*., 2015) with capacity of 1,300 mAh/g, which correlates to more than 2,000 Wh/kg of energy density. Thus, for our current project, we believe that a battery with 700 Wh/kg of energy density would be available in the very near future.

For the propulsion system, Noth (2008) suggested that its mass can be modelled simply using the relationship below, where k_{prop} is the power to mass ratio of the propulsion system:

$$m_{prop} = k_{prop} P_{lvl} \tag{10}$$

With all the components known, the original master equation becomes:

$$m_{tot} = m_{avc} + m_{pld} + \frac{0.044}{g} b^{3.1\,\Lambda\,-0.25} + \left\{ (k_{sc} + k_{enc}) \cdot \left[\frac{\frac{C_D}{C_L^{1.5}} (m_{tot} g)^{1.5} \left(\frac{2\,\Lambda}{\rho b^2}\right)^{0.5}}{\eta_{ctrl} \eta_{mot} \eta_{grbx} \eta_{plr}} + \frac{P_{avc} + P_{pld}}{\eta_{bec}} \right] \cdot \left(T_{day} + \frac{T_{nit}}{\eta_{chg} \eta_{dchg}} \right) \cdot \left(\frac{\pi/2}{I_{max} T_{day} \eta_{wt} \eta_{sc} \eta_{cbr} \eta_{mppt}} \right) \right\} + \left\{ (k_{mppt} I_{max} \eta_{sc} \eta_{cbr} \eta_{mppt}) \cdot \left[\frac{\frac{C_D}{C_L^{1.5}} (m_{tot} g)^{1.5} \left(\frac{2\,\Lambda}{\rho b^2}\right)^{0.5}}{\eta_{ctrl} \eta_{mot} \eta_{grbx} \eta_{plr}} + \frac{P_{avc} + P_{pld}}{\eta_{bec}} \right] \cdot \left(T_{day} + \frac{T_{nit}}{\eta_{chg} \eta_{dchg}} \right) \cdot \left(\frac{\pi/2}{I_{max} T_{day} \eta_{wt} \eta_{sc} \eta_{cbr} \eta_{mppt}} \right) \right\} + \left\{ \left(\frac{T_{nit}}{k_{batt} \eta_{dchg}} \right) \cdot \left[\frac{\frac{C_D}{C_L^{1.5}} (m_{tot} g)^{1.5} \left(\frac{2\,\Lambda}{\rho b^2}\right)^{0.5}}{\eta_{ctrl} \eta_{mot} \eta_{grbx} \eta_{plr}} + \frac{P_{avc} + P_{pld}}{\eta_{bec}} \right] \right\} + \left\{ (k_{prop}) \cdot \left[\frac{C_D}{C_L^{1.5}} (m_{tot} g)^{1.5} \left(\frac{2\,\Lambda}{\rho b^2}\right)^{0.5} \right] \right\} \tag{11}$$

Even though the equation is lengthy, it could be reduced to a simple function with a single variable such as below:

$$m_{tot} = \mathbb{A}(b, \Lambda){m_{tot}}^{1.5} + \mathbb{B}(b, \Lambda) \quad (12)$$

By simple substitution of $\mathcal{Z} = {m_{tot}}^{0.5}$

$$\mathbb{A}(b, \Lambda)\mathcal{Z}^3 - \mathcal{Z}^2 + \mathbb{B}(b, \Lambda) = 0 \quad (13)$$

where $\mathbb{A}(b, \Lambda)$ and $\mathbb{B}(b, \Lambda)$ are both functions of wing span and aspect ratio, which will be set by the designer.

Optimisation of design solutions was done using a script written in Matlab environment. The script was set to vary the aspect ratio from 8 to 17 with a unit step increment. At every aspect ratio, the script will vary the wingspan from 10 to 100 m with 0.1 step increment and then find a minimum positive real number solution of Equation 13 at every step. The engineering constants listed in Table 1 were utilised in the script.

Table 1: Engineering constants needed for Equation 11 and their typical values.

Constants	Value	Unit	Notes
C_L	1.1	-	Airfoil lift coefficient
C_{D_afl}	0.013	-	Airfoil drag coefficient. To be added with parasitic & induced drag
C_{D_par}	0.006	-	Parasitic drag coefficient. To be added with airfoil & induced drag
e	0.9	-	Oswald's efficiency factor (assumed value)
ρ_{air}	0.0746	kg/m^3	Density of air at 21km altitude
I_{max}	950	W/m^2	Maximum sun irradiance (typical value for Malaysia (Daut *et al.*, 2011))
k_{bat}	700	Wh/kg	Energy density of LS battery (assumed value)
k_{sc}	0.32	kg/m^2	Mass density of solar cells (based from (Noth, 2008))
k_{enc}	0.26	kg/m^2	Mass density of encapsulation (based from (Noth, 2008))
k_{mppt}	0.00042	kg/W	Mass/power ratio of MPPT (based from (Noth, 2008))
k_{prop}	0.008	kg/W	Mass/power ratio of propulsion system (based from (Noth, 2008))
m_{av}	20	kg	Mass of avionics system (based from (Noth, 2008))
m_{pld}	100	kg	Mass of telecommunication payload (based from (Noth, 2008))
η_{bec}	0.65	-	Efficiency of step-down converter (based from (Noth, 2008))
η_{wt}	1	-	Weather factor which reduces the energy captured. Value of 1 is clear sky(assumed value)
η_{sc}	0.169	-	Efficiency of solar cells (based from (Noth, 2008))
η_{cbr}	0.90	-	Efficiency of curved solar panels (based from (Noth, 2008))
η_{chg}	0.95	-	Efficiency of battery charge (based from (Noth, 2008))
η_{ctrl}	0.95	-	Efficiency of motor controller (based from (Noth, 2008))
η_{dchg}	0.95	-	Efficiency of battery discharge (based from (Noth, 2008))
η_{grb}	0.97	-	Efficiency of gearbox (based from (Noth, 2008))
η_{mot}	0.85	-	Efficiency of motor (based from (Noth, 2008))
η_{mppt}	0.97	-	Efficiency of MPPT (based from (Noth, 2008))

η_{plr}	0.85	-	Efficiency of propeller (based from (Noth 2008))
P_{av}	100	W	Power for avionics (based from the HeliNet project)
P_{pld}	400	W	Power for telecommunication payload (based from the HeliNet project)

It was found that, there could be no close form solution of the equation using the current value of engineering constants and with the current design objectives. Of course, reducing the payload mass to 50 kg and its power to 100 W will yield results by the algorithm but such an exercise would be unrealistic since a practical telecommunication device would be much heavier and require more power. Thus, a modification to the aircraft structure must be made. We propose a hybrid concept combining the aircraft with lighter-than-air technology to assist in carrying the load.

3. MODIFIED NUMERICAL SOLVER FOR HYBRID AIR-VEHICLE CONCEPT

Abundant of literatures can be found on the inflatable wing / aircraft technology. Our design team believes that it is possible to construct an inflatable aircraft using high strength fibre materials such as Kevlar, Vectran or glass fibres. Such an aircraft would then be rigidised in order to give the freedom of varying the internal pressure of the lighter-than-air gas such as Helium. A similar idea has been discussed by Edge *et al*. (2012). The construction of such aircraft will be discussed in the later sections.

By assuming that the total volume for fuselage and wing (V) are linked to the aircraft wingspan and aspect ratio, and that the internal pressure of Helium is set to the atmospheric pressure at 21 km altitude, we could modify the equation to become:

$$g \cdot m_{lift} = g \cdot \mathbb{A}(b, \Lambda) {m_{lift}}^{1.5} + g \cdot \mathbb{B}(b, \Lambda) - \text{buoyancy force}$$

$$g \cdot m_{lift} = g \cdot \mathbb{A}(b, \Lambda) {m_{lift}}^{1.5} + g \cdot \mathbb{B}(b, \Lambda) - g \cdot (\rho_{\text{air}} - \rho_{\text{helium}}) V$$

$$m_{lift} = \mathbb{A}(b, \Lambda) {m_{lift}}^{1.5} + \mathbb{B}(b, \Lambda) - \mathbb{C}(b, \Lambda) \quad (14)$$

The new variable m_{lift} is the weight of the aircraft that is carried by the lift from wing. It is the difference between the total weight minus the buoyancy force. In another word, it simply means the effective weight experienced by the aircraft wing after buoyancy force has been considered.

By simple substitution of $= {m_{lift}}^{0.5}$:

$$\mathbb{A}(b, \Lambda) \mathcal{Z}^3 - \mathcal{Z}^2 + \mathbb{B}(b, \Lambda) - \mathbb{C}(b, \Lambda) = 0 \quad (15)$$

The new optimisation routine was written in Matlab to solve for Equation (15). The engineering constants in Table 1 were kept for this new routine.

4. FINAL DESIGN SOLUTION

Possible solutions for m_{lift} are plotted against wingspan and aspect ratio (range from 8 – 17) (Figire 2). Choosing higher aspect ratio at constant wing span would reduce the burden of the

wing whereby the weight needed to be carried by the wing will be less. However, very high aspect ratio wing would not be very suitable for inflatable wing design such as ours. The wing would be very flexible and can experience excessive aeroelastic problems. Thus, for our current design, we choose wing span of 50 m and aspect ratio of 13. The chosen aspect ratio is comparable than Lockheed's U-2 spy-plane which has similar altitude to ours.

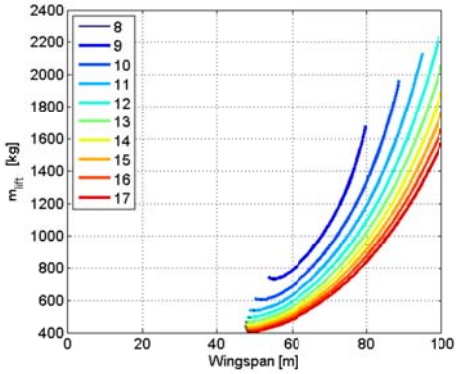

Figure 2: Possible range of wing span and aspect ratio that will give solutions to Equation 15.

The Matlab routine automatically calculates other specifications based on previously listed equations using our chosen aspect ratio and wing span. All specifications are listed in Table 2.

Table 2: Specifications of aircraft that will satisfy our design objectives.

Aspect Ratio (Λ)	13
Wing Span (b)	50 m
Effective Weight (m_{lift})	469 kg
Battery Weight (m_{bat})	144.2 kg
Total weight (m_{tot})	600.44 kg
Volume for Helium (V)	2103.81 m^3
Wing Area (S)	192.31 m^2
Solar Cells Area (A_{sc})	167.94 m^2
Max Battery Capacity ($E_{max-bat}$)	100940 Wh
Cruise Velocity (v)	24.2 m/s

5. DESIGN VALIDATION USING WEIGHT BALANCE ANALYSIS

To check the validity of the design solutions, we first subject it to weight balance analysis. The aircraft must have zero or negligible residue after the total weight minus the sum of lift and buoyancy force. The lift can be calculated from standard lift equations where:

$$Lift = 0.5 C_L \rho_{air} S v^2 = 0.5 * 1.1 * 0.0746 * 192.31 * 24.2^2 = 4620.98 \text{ N}$$

The buoyancy force can be calculated using:

$$Buoyancy = g(\rho_{air} - \rho_{helium})Vol = 9.81 * (0.0746 - 0.0121) * 2103.81 = 1289.90 \text{ N}$$

To balance downward weight force and total upward force:

$$Weight - (lift + buoyancy) = 600.44 * 9.81 - (4620.98 + 1289.9) = -19.58 \text{ N}$$

The residue of -19.58 N is negligible since it is about 0.3% of the total weight of the aircraft. Thus based on the weight balance, we could confirm the validity of the design solutions suggested by our Matlab routine.

6. DESIGN VALIDATION USING POWER BALANCE ANALYSIS

To further validate the design solutions, we perform a power balance check where we model the aircraft flying in 48 h with fluctuating solar irradiance. The objectives are to investigate whether the solar cells can capture, and whether the battery can store, enough energy for night flying mission. The whole aircraft system can be modelled in Simulink and its graphical representation is shown in Figure 3. Firstly, we modelled the solar irradiance using a sine wave. Although it seems simplistic, Noth (2008) demonstrated that sine wave could closely represent hourly irradiance model. We assume that the irradiance is positive from 7 am to 7 pm and zero at other times. The power captured by the solar cells depends on its efficiency and the efficiency of MPPT. The power required to operate the aircraft is the sum of power for cruise, avionics, and payload. For this current model, we assume that the aircraft only cruises at constant altitude and speed.

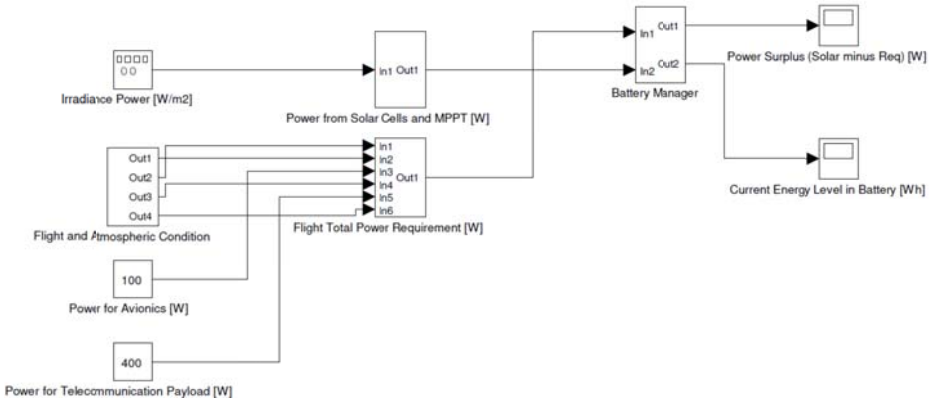

Figure 3: Power system modelled in Simulink.

The aircraft can be modelled with moderate climb during the day before descending to lower altitude at night in order to convert surplus solar energy into potential energy. The battery manager was modelled such as to start discharging the battery whenever the power supplied from solar is less than the power required for aircraft operations. The power manager would also start battery charging only when the battery current energy level is below the maximum and there is surplus in solar power. The time domain is 48 h starting at 7 am. Initially, the battery was given 10,000 Wh of energy level. The plots for power and energy against time are given in Figures 4 and 5.

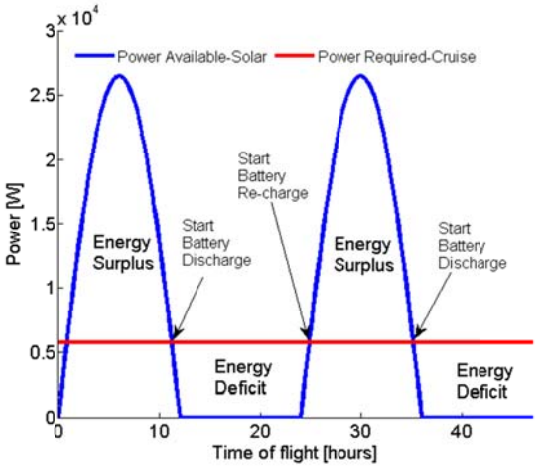

Figure 4: Plot of solar power and power required in 48 h.

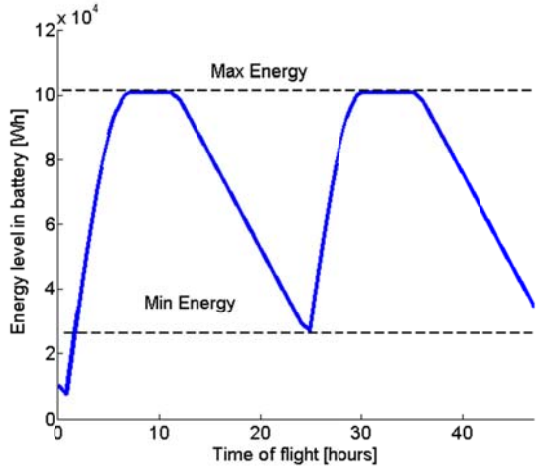

Figure 5: Plot of battery energy level in 48 h.

From Figure 4, we could see that at 7 am, the power from the solar panels is not enough, so some battery power is needed to cover the gap. This lasted for almost an hour before there is a surplus in power, where the initial battery level dropped by 25% (Figure 5). The battery manager allowed for battery recharge whenever there is surplus in power and it would take about 6 h to fully charge it. The battery would stay at the maximum energy level of 101 kWh for about 4 h before THE deficit in power started at about 6 pm. The battery continues its discharge until almost 8 am on the next day, dropping its energy to the minimum level of 27 kWh. The battery would then be fully charged again in less than 6 h before deficit in power requires it to support the aircraft operation once again. This cycle of recharge and discharge between the minimum to maximum energy would continue indefinitely if the simulation was given a bigger time frame. This proves that our design solutions indeed satisfy the mission requirements of perpetual flying.

7. SYSTEM RELIABILITY ANALYSIS

The power and energy analysis done in the previous section has large uncertainty in it since they depend on assumed values listed in the engineering constant in Table 1. Among the parameters with large uncertainty is the maximum irradiance (I_{max}) and solar cells efficiency (η_{sc}). We use 950 W/m^2 as the maximum irradiance of the Malaysian atmosphere at 21km altitude. However, there is no published literature yet that can give clear indications of the maximum irradiance value at that altitude. Few literatures only measured the ground level irradiance on clear sky conditions and the values are around 968 W/m^2 as monthly average (Daut *et al*., 2011). For our design, we conservatively assumed that I_{max} is about 950 W/m^2; a low figure considering that I_{max} for a clear day should increase with altitude.

Nevertheless, I_{max} at an altitude increase and decrease depending on the earth's position on its elliptical orbit around the sun (Hall *et al*., 1983). I_{max} also depends on various solar activities and phenomenon that are said to change periodically every 11 years (Thekaekara, 1976; Beer, 2005). The ozone layer, which is located in the stratosphere (our design altitude), is known to absorb part of the solar spectrum, which would also decrease the overall solar energy received (Hood, 2003); and the ozone concentration itself is highly varied (Yonemura *et al*., 2002). The change of the dominant spectrum in sunlight will affects the performance of solar cells as reported by Boer (Boer, 1977). Various kinds of aerosols polluting the atmosphere have their peak concentration around 20 km altitude. They reduce the energy in sunlight by backscatter and absorption as reported by Marggraf & Griggs (1969).

Solar cells efficiency η_{sc} also varies by a large degrees depending mostly on their operating temperature (Hall *et al*., 1983), and just like the ozone layer concentration, the stratospheric temperature above Malaysia is highly varied (Yonemura *et al*., 2002). The icing problem, which may or may not occur depending mainly on the temperature, could reduce the energy received by the solar panels.

Apart from randomness in the energy collected by the solar panels such as discussed above, we must also anticipate that the energy required by cruise may not be as constant as we initially assumed. This is due mainly to the gust phenomena which should be less in the stratospheric altitude but still significant nevertheless. In one NASA report, it could induce 0.5G of impulse acceleration with occurrence frequency of about 1% of the flight time (Hall *et al*., 1983). Besides gust, the stratosphere typically has wind current that follows the planetary-scale Rossby wave (Baldwin & Dunkerton 2005). However, the magnitude of the velocity at 21 km altitude above Malaysia is highly fluctuated (Yonemura *et al*., 2002). If the wind movement is at a different direction to cruise, then the aircraft would need higher power to maintain its speed relative to the ground. Conversely, if the wind is at a similar direction to cruise then the aircraft would save energy.

To further validate our design, we must demonstrate the reliability of our solar energy harvesting system in fulfilling the total energy needed by cruise and flight mission. One way to convincingly measure reliability of a system plagued by randomness in many of its key parameter, is to use Monte Carlo simulation. Such method has been demonstrated by reference (Popescu *et al*., 2003; Youli & Nagasaka 2010; Honda *et al*., 2011).

Monte Carlo simulation is a statistical tool that incorporates stochastic characters in a deterministic mathematical model (Metropolis & Ulam, 1949). In our case, we can easily calculate total energy collected by the solar panels using the Equation 16. We could also easily

calculate the total energy consumption due to cruise flight, avionics and telecommunication payload using Equation 17.

$$Total\ solar\ energy\ collected\ in\ 48hours = (I_{max}A_{sc}\eta_{sc}\eta_{cbr}\eta_{mppt}) \cdot 12/(\pi/2) \cdot 2 \quad (16)$$

$$Total\ energy\ consumed\ in\ 48hours = (0.5C_D\rho SV^3 + 500) \cdot 48 \quad (17)$$

We must recognise that in both equations, there are ranges of output values that can be attributed to their input parameters. We could for example produce three calculations; the base, worst and best cases. Hitherto, this will produce a misguided prediction since the best and worst cases could have very low probability of actually happening. Using Monte Carlo simulation, we could produce ranges of possible outcomes along with their probability of actually happening. This is done by first identifying the distribution, if any, in the input parameters; which in our case is I_{max}, solar cells efficiency and velocity of flight.

For our simple analysis, we assume that I_{max} will vary by ±20%, solar cells efficiency by ±5% and flight velocity by ±7%. For the best case value, we calculate the balance of energy collected minus the energy required when I_{max} is 1140 W/m^2, solar cells efficiency is 0.24 and flight velocity is 17 m/s. The worst situation for energy balance is when I_{max} is 760W/m2, solar cells efficiency is 0.14 and flight velocity is 31 m/s. Using the balance energy value of best and worst case scenario, we can calculate the overall representative of standard deviation (σ) and average of output. We then produced random number prediction of each variables using Microsoft Excel's **rand()** command. Unique output values are produced for each iterations. The number of iteration (N) required is calculated using (Raychaudhuri, 2008):

$$\sqrt{N} = 3\sigma/\varepsilon \quad (18)$$

Total error (ε) is calculated using our estimated average (i.e., the average of the best and worst cases) divided by the required error. For the current analysis, we conservatively say that we want a correct prediction within 5% of error. Thus, total error is:

$$\varepsilon = (estimated\ average)/0.05 \quad (19)$$

This will result in the minimum iterations required of about 59,606 times. We run our iteration 60,000 times and the frequency results are plotted in Figure 6.

Figure 6 shows the frequency of different outputs of total energy collected by the solar cells minus the energy consumed for cruise, avionics and payload in the duration of 48 h. It can be seen that there is significant probability, about 25% of all cases, of the flight having negative balance. This means that the energy consumed during 48 h is more than the total energy collected. Nevertheless, there are actually less than 10% occurrences of energy deficit cases where the deficit has higher magnitude than the maximum battery capacity. This means that many energy deficit cases can be solved by initially charging the battery to the maximum before the mission begins. We did not incorporate the initial energy charge level in either Equation 16 or 17, whereas we as the designer have the freedom to specify the initial charge level of the battery.

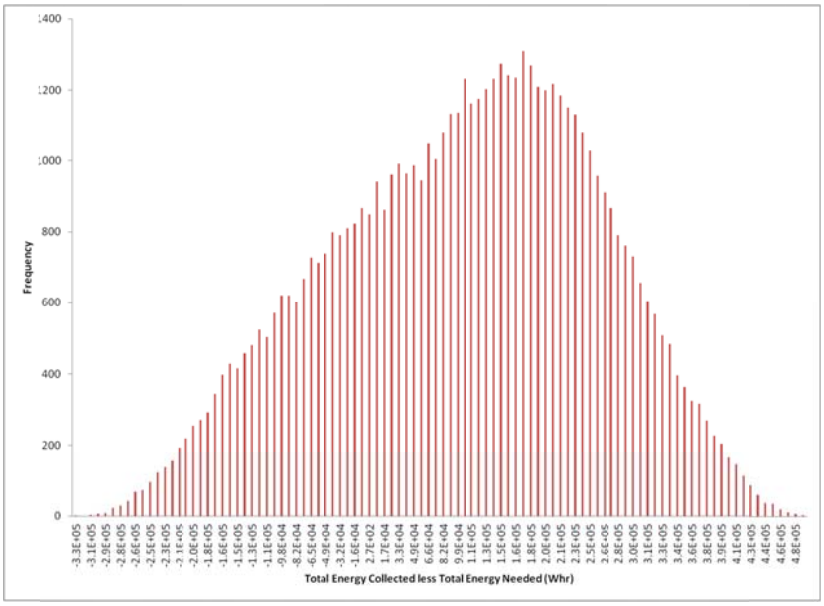

Figure 6: Frequency chart of possible outputs of net energy.

The most likely scenario is the average of all possible outputs, where the total energy collected will be larger than the energy consumed by a margin of about 102 kWh. We can be confident with our design since the energy collected will be in surplus, or at least at similar level to energy consumed, at about 90% of the times. The new standard deviation can be calculated from all samples. The final absolute error can be calculated using the new standard deviation and using Equation 19. This absolute error is aproximately1.8%.

A fascinating question to ponder is what will happen to the HAP if for any reason the solar did not provide enough energy and the battery ran out of power? The payload and propeller will cease to function without power. Since the thrust will be reduced to zero, the lift would also be zero but the buoyancy force would still be there.

Thus, we arrive at an interesting scenario where the aircraft will slowly descend but will never crash to the ground, assuming we maintain the internal pressure of helium gas inside the hybrid aircraft. We can calculate the altitude at which our unpowered hybrid aircraft will hover by relating buoyancy to weight. This is illustrated by calculation below:

$$Buoyancy = 9.81 * (\rho_{air} - 0.0121) * 2103.81 = Weight = 600.44 * 9.81$$

From the calculation, we found that the density of air ρ_{air} is 0.298 kg/m^3 and this translates into an altitude of 12,278 m above sea level. The unpowered aircraft could hover at its minimum altitude before it collects enough energy to climb back to design altitude. On the other hand, by way of manipulating the pressure inside the hybrid aircraft, it could even descend further if required.

8. PRELIMINARY SKETCHES

The early sketches of our current design are given in the Figure 7. To achieve the large volume requirement, we looked up to Airbus A380 as a shape example. We opted for twin fuselage design to reduce the side cross-sectional area thus reducing the probability of side drift. The length of the fuselage is 48 m, which is only slightly shorter than its wing span. The total volume for wing and fuselage is more than 2,700 m^3 providing ample room for Helium and other equipment. The fuselage length could be extended longer if the need arises (for example, to accommodate larger payload) because it is common for passenger aircrafts, for which our design refers, to have fuselage longer than the wingspan.

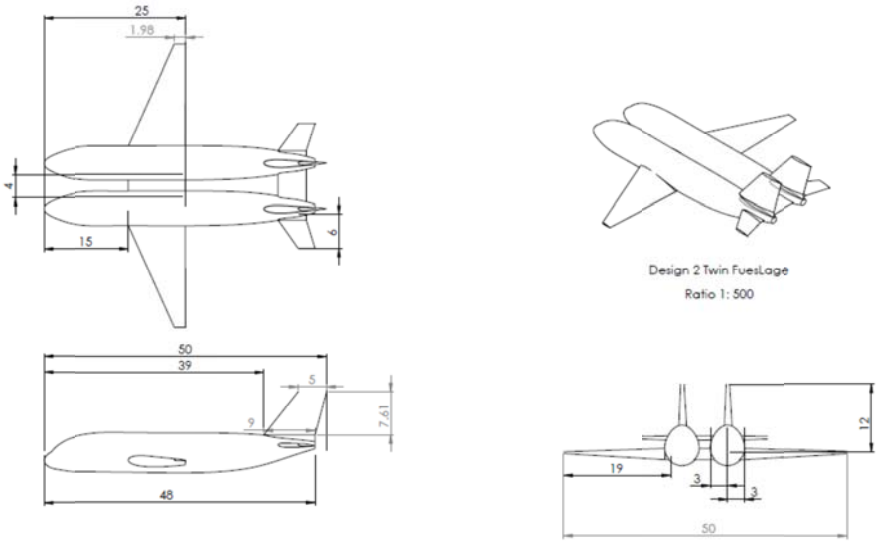

Figure 7: Preliminary sketches for our design. Dimensions in m.

NACA 2421 was chosen for the airfoil because it has a thick profile of 21% of chord and it has airfoil drag coefficient of 0.013 when its lift coefficient is 1.1, just like we assumed during the optimisation process. The airfoil was set at 9^o angle-of-attack (AoA) so as to achieve the required lift coefficient. The airfoil has stall angle of 15^o which leaves sufficient margin from our cruise AoA. The taper ratio was given as such to maximise the wing chord and thickness at root in order to have more structural integrity. The leading edge and trailing edge angle sweep was given arbitrarily and would be decided later after aerodynamic analysis was performed. Similarly, the tail size is given capriciously without proper regards to flight stability analysis which will be done later.

9. MATERIALS AND STRUCTURE CONSIDERATION

After we have tackled the mathematical foundations of our design, we need to address the obvious problem of how to actually build a hybrid air vehicle such as ours. Inflatable wing and fuselage is not actually too-far-fetched an idea because in the 1950s, Goodyear unveiled their Inflatoplane, a fully stowable aircraft made of two rubber-type materials connected with nylon

mesh thread. The idea of an inflatable aircraft structure goes back to 1930s where Taylor MacDaniels experimented and patented the concept of rubber glider (Norris & Pulliam, 2009).

The effort to study and further develop the inflatable wing concept came in the mid-2000s where the group in the University of Kentucky along with their industrial partner ILC Dover pursued the Big Blue project (Cadogan *et al*., 2003; Norris & Pulliam 2009). The project aimed to develop an inflatable wing aircraft that could operate in low density flight applications such as the Mars aerial explorer (Cadogan *et al*., 2003; Usui, 2004). Due to Mars' low-density, an aerial explorer needs to have very large wing span, thus causing a problem to carry the aircraft from earth to the planet. Hence, foldable inflatable wings are needed to fit the aircraft into a suitable spacecraft. Using an inflatable wing aircraft on Mars also has the added advantage of allowing for Helium to be used to aid the lifting of the aircraft, thus reducing the need for an exceptionally long wing span. The Big Blue project has also demonstrated the concept of using the ultraviolet (UV) curing to rigidise their flexible E-glass inflatable wing (Cadogan *et al*., 2003; Usui, 2004; Smith *et al*., 2006). They wanted to rigidise their inflatable wing to reduce the need for maintaining high pressure inside the wing. We propose to use a similar technique for our inflatable aircraft where our aircraft would be made from high strength fabric materials and then cured with UV to allow for freedom in maintaining internal pressure independent from external atmospheric pressure.

10. SUMMARY AND FUTURE STUDIES

Based from our mathematical analysis, the main problem that hindered the development of a perpetual HAP aircraft for pseudo-satellite applications is finding the delicate balance between energy that can be stored for night flying and the total weight of the aircraft. We then proposed for structural modifications of the aircraft concept that we want to design. We suppose that lighter-than-air technology can be used in hybrid with the conventional lift from the wing. Thus, we modify the original total weight equation to include buoyancy force which will be solved numerically.

Our solver indeed found a tractable range of solutions allowing us the flexibility to choose suitable wing span and aspect ratio. We chose a 50 m wing span and aspect ratio of 13 from which the code would then compute the other specifications of the aircraft, such as cruise speed, total weight, volume for helium and solar cells area. We did a power balance check and found that the battery could store enough energy to cover the flight, avionics and payload power every time the solar power was in deficit. The reliability of solar energy to power the whole mission is demonstrated by Monte Carlo simulation.

There is a lot more work that needs to be done since the exercise reported in this paper is just preliminary. Static and dynamic stability of the aircraft are urgently needed since they determine the location of the centre of gravity and tailplane sizing. Aerodynamics and structural analysis will follow afterwards. In every step of the design process, we are humbled by the fact that the whole process is iterative and we may end up back to square one to redo the works done in this paper again.

ACKNOWLEDGMENT

The authors acknowledge the Short Term Grant Scheme from the National Defence University of Malaysia (UPNM) for supporting this research work.

REFERENCES

Baldwin, M.P. & Timothy J.D. (2005). The solar cycle and stratosphere-troposphere dynamical coupling. *J. Atmos. Sol-Terr. Phys,*. **67**: 71–82.

Beer, J. (2005). Solar variability and climate change. *Memorie-Societa Astronomica Italiana* **76**: 751.

Bhatt, M.R. (2012). *Solar Power Unmanned Aerial Vehicle: High Altitude Long Endurance Applications (HALE-SPUAV).* A project presented to The Faculty of the Department of Mechanical and Aerospace Engineering, San Jose State University.

Bolkcom, C. (2004). *Potential Military Use of Airships and Aerostats*. Library of Congress Washington DC Congressional Research Service.

Boucher, R.J. (1985). Sunrise, the world's first solar-powered airplane. *J. Aircraft*, **22**: 840–46.

Brandt, S.A. & Fred, T.G. (1995). Design analysis methodology for solar-powered aircraft. *J. Aircraft*, **32**: 703-709.

Böer, K. W. (1977). The solar spectrum at typical clear weather days. *Sol. Energy* **19**: 525–38.

Cadogan, D., Graham, W. & Smith, T. (2003). Inflatable and rigidizable wings for unmanned aerial vehicles. *2nd AIAA "Unmanned Unlimited" Systems, Technologies, and Operations*, 15–18.

CAPANINA, Deliverable Number. (2004). D12: Report on Delivering Broadband for All from Aerial Platforms Including Commercial and Technical Risk Assessments. *Document Number CAP-D12-WP12-BT-PUB-01, York.*

Colozza, A. & James D. (2003). Initial feasibility assessment of a high altitude long endurance airship *NASA Contractor Report CR-2003-212724*.

Courtney, M. (2015). The future of flight is green. *Eng. Tech.*, **10**: 38-38.

Daut, I., Irwanto, M., Irwan, Y.M., Gomesh, N. & Ahmad. N.S. (2011). Clear sky global solar irradiance on tilt angles of photovoltaic module in Perlis, Northern Malaysia. *2011 International Conference on Electrical, Control and Computer Engineering (INECCE), pp.* 445–450.

Deaton, J.D. (2008). High altitude platforms for disaster recovery: capabilities, strategies, and techniques for emergency telecommunications. *EURASIP J. Wireless Commun. Netw.*, **vol. 2008**: 1–8.

Edge, H.L., Brown, A. & Collins. J. (2012). Pressurized structures-based unmanned aerial vehicle research. *J. Intell.. Robot. Syst.*, **65**: 603–620.

Ehernberger, L.J., Donohue, C., & Teets Jr, E.H. (2004). A review of solar-powered aircraft flight activity at the pacific missile range test facility, Kauai, Hawaii. *11th Confeence on Aviation, Range, and Aerospace Meteorology*.

Everaerts, J. (2008). The use of unmanned aerial vehicles (UAVs) for remote sensing and mapping. *Int. Arch. Photogramm. Remote Sens. Spatial Inform. Sci.*, **37**: 1187–1192.

Evers, S., & Nazar, L. F. (2012). New approaches for high energy density lithium-sulfur battery cathodes. *Accounts Chem. Res.*, **46**: 1135–1143.

Filippone, A. (2006). *Flight Performance of Fixed and Rotary Wing Aircraft*. Elsevier.

Gao, X., Hou, Z., Guo, Z. & Chen., X. (2015). Reviews of methods to extract and store energy for solar-powered aircraft. *Renew. Sust. Energ. Rev.* **44**: 96–108.

Hall, D.W., Fortenbach, C.D., Dimiceli, E.V., & Parks., R.W. (1983). A preliminary study of solar powered aircraft and associated power trains. *NASA Contractor Report CR-3699*

Hartney, C. J. (2011). *Design of a Small Solar-Powered Unmanned Aerial Vehicle*. PhD Thesis. San José State University

Honda, T., Chen, H.Q., Chan, K.Y. & Yang, M.C. (2011). Propagating uncertainty in solar panel performance for life cycle modelling in early stage design. *AAAI Spring Symposium: Artificial Intelligence and Sustainable Design*.

Hood, L. L. (2003). Effects of solar UV variability on the Stratosphere. *Solar Variability and Its Effects on Climate*. Wiley Online Library, pp. 283–303.

Jamison, L., Sommer, G. S., & Porche III, I. R. (2005). *High-Altitude Airships for the Future Force Army.* Rand Arroyo Center Santa Monica CA.

Leutenegger, S., Jabas, M. & Siegwart. R. Y. (2011). Solar airplane conceptual design and performance estimation. *J. Intell. Robot. Syst.* **61**: 545–61.

Liang, X., Hart, C., Pang, Q., Garsuch, A., Weiss, T. & Nazar. L.F. (2015). A highly efficient polysulfide mediator for lithium-sulfur batteries. *Nat. Commun.*, **6**: 5682.

Malaver, R. & Alexander, J. (2014). *Development of Gas Sensing Technology for Ground and Airborne Applications Powered by Solar Energy: Methodology and Experimental Results*. PhD Thesis. Queensland University of Technology.

Marggraf, W.A. & Griggs, M. (1969). Aircraft measurements and calculations of the total downward flux of solar radiation as a function of altitude. *J. Atmos. Scien.,* **26**: 469–77.

Metropolis, N. & Ulam, S. (1949). The Monte Carlo method. *J. Am. Stat. Assoc.*, **44**: 335–41.

Navarro, R. (2007). ER-2: Flying laboratory for earth science studies. *32nd International Symposium on Remote Sensing of Environment,* 25-29 June 2007, San Jose, Costa Rica

Noll, T.E., Ishmael, S.D., Henwood, B., Perez-Davis, M.E., Tiffany, G.C., Madura, J., Gaier, M., Brown, J.M., & Wierzbanowski, T. (2007). Technical findings, lessons learned, and recommendations resulting from the Helios prototype vehicle mishap. *In UAV Design Processes / Design Criteria for Structures* (pp. 3.4-1 – 3.4-18). Meeting Proceedings RTO-MP-AVT-145, Paper 3.4

Norris, R.K. & Pulliam, W. J. (2009). Historical perspective on inflatable wing structures. *50th AIAA/ASME/ASCE/AHS/ASC Structures, Structural Dynamics, and Materials Conference*, pp. 4–7.

Noth, A. (2008). *Design of Solar Powered Airplanes for Continuous Flight*. PhD Thesis, ETH Zurich

Noth, A., Engel, M. W., & Siegwart, R. (2006). Flying solo and solar to Mars. *IEEE Robotics & Automat. Mag.,* **13**: 44–52.

Noth, A., Engel, M. W., & Siegwart, R. (2006). Design of an ultra-lightweight autonomous solar airplane for continuous flight. *Field and Service Robotics*, p. 441–52.

Ollero, A. & Merino, L. (2006). Unmanned aerial vehicles as tools for forest-fire fighting. *For. Ecol. Manag.* **234**: S263.

Pinkney, M. F. J., Hampel, D. & DiPierro, S. (1996). Unmanned aerial vehicle (UAV) communications relay. *Military Communications Conference, 1996*, pp. 47–51.

Popescu, D.E., Popescu, C. & Gabor, G. (2003). Monte Carlo simulation using Excel for predicting reliability of a geothermal plant. *Proc. Int. Geothermal Conf.*, pp. 7–12.

Raychaudhuri, S. (2008). Introduction to Monte Carlo simulation. *Simulation Conference 2008. WSC 2008, pp.* 91–100.

Ross, H. (2008). Fly around the world with a solar powered airplane. *Power*: **1**: 1–9.

Smith, S. W., Jacob, J. D., Jones, R. J., Scarborough, S. E., & Cadogan, D. P. (2006). A high-altitude test of inflatable wings for low-density flight applications. *7th AIAA Gossamer Spacecraft Forum*.

Stephens, H. (2005). Near-space. *Air Force Mag.*, **88**: 31.

Thekaekara, M.P. (1976). Solar irradiance: Total and spectral and its possible variations. *Appl. Optics*, **15**: 915–20.

Thornton, J., Grace, D., Spillard, C., Konefal, T. & Tozer. T.C. (2001). Broadband communications from a high-altitude platform: The European HeliNet Programme. *Electron. Commun. Eng. Journal*, **13**: 138–44.

Tozer, T. C, & Grace, D. (2001). High-altitude platforms for wireless communications. *Electr. Commun. Eng. J.*, **13**: 127–37.

Tozer, T. C., Grace, D., Thompson, J., & Baynham, P. (2000). UAVs and HAPs-Potential convergence for military communications. In *Military Satellite Communications (Ref. No. 2000/024), IEE Colloquium* 10–11.

Usui, M. (2004). *Aeromechanics of Low Reynolds Number Inflatable/Rigidizable Wings.* Masters Thesis. University of Kentucky.

Vidales, H. M. G. (2013). *Design, Construction and Test of the Propulsion System of a Solar Uav*. MSc Thesis Aerospace Engineering, Technical University of Lisbon.

Wickenheiser, A.M. & Garcia. E. (2009). Conceptual design sonsiderations for microwave-and solar-powered fuel-less aircraft. *J. Aircraft* **46**: 510–19.

Yonemura, S., Tsuruta, H., Sudo, S., Peng, L. C., Fook, L. S., & Johar, Z. (2002). Annual and El Niño-Southern oscillation variations in observations of in situ Stratospheric Ozone over peninsular Malaysia. *J. Geophys. Res-Atmos.* **107:** D13.

DEVELOPMENT OF LIGHTWEIGHT AND LOW-COST FULLY AUTONOMOUS HEXACOPTER UAV

Yaakob Mansor[1, 4*], Shattri Mansor[2, 4], Helmi Zulhaidi [2,4] Abdul Rahman Ramli[3] & Ajibola I.Isola[4]

[1]Centre of Foundation Studies for Agricultural Science
[2]Department of Civil, Faculty of Engineering
[3]Department of Computer and Communication System, Faculty of Engineering
[4]Geospatial Information Science Research Centre (GISRC)
Universiti Putra Malaysia (UPM), Malaysia

[*]Email: yaakobms@upm.edu.my

ABSTRACT

This research successfully developed a low-cost and lightweight hexacopter UAVs, with total payload of 1.44 kg and flight time of 15.5 min. The assembly and integration techniques cover the UAV's acquisition system, components and calibration, pre-flight check using waypoints, and diagnosis of problems using telemetry logs with or without a gimbal attached. The components and calibrations include LiPo battery, brushless motors, arm, propeller, electronic speed control (ESC), receiver / transmitter and telemetry, gimbal, generating thrust, payload calculation, and compass setting. These research steps significantly improved the method for aerial typical image overlap, by uniformly distributing the images using high overlap set to 80% to avoid gaps and occlusion in the image data. The overlap generated 234 aerial images with ground image resolution of 4.6 cm and 76,7443 triangle tie-points.

Keywords: *UAV; hexacopter; gimbal; thrust; telemetry*.

1. INTRODUCTION

Manned aircraft systems have disadvantages when compared with unmanned aerial vehicles (UAVs). This is because UAVs can meet the critical needs of spatial, spectral and temporal resolution. This includes high-risk areas, areas that are not accessible to humans, and low altitudes at which the system cannot be flown manned. For areas where access is difficult, such as earthquakes, flood plains, volcanoes, natural disasters, deserts, accident scenes and also areas where the permission is not given for manned aircraft flights, UAVs is the best alternative option. Data acquisition with UAVs also includes during overcast and drizzling weather conditions when the distance to the object permits flying below the clouds. As compared with manned aircraft systems, such weather does not permit data collection using a large format sensor that is integrated into the control plane and the flight altitude is higher above the ground. An additional advantage is the ability of the UAVs' fast data acquisition, real-time capabilities and the ability to send data to the ground control station in real time (Mellinger *et al*., 2012; Ritz *et al*., 2012;Turpin *et al*., 2012; Brescianini *et al*., 2013).

Rotary-wing UAVs, which have the capability for vertical take-off and landing (VTOL) can be based on single, dual, triple, quad and multi-rotors systems (Zischinsky, 2000; Berni, 2011; Pérez, 2011; Joshua, 2012). Nebiker (2008) proposed a multi-spectral micro-sensor (MSMS) based on mini- and micro-UAVs for agricultural monitoring, where a grapevine field was selected for appraisal of plant health using mini-UAV. The mini-UAV was powered by a combustion engine with a rotor diameter of 1.8 m and was capable of carrying sensor payload up to 1 kg. Bendig (2012) used a mini-UAV system with gross weight of less than 2.5 kg. The maximum speed was 30 km/h with total payload of

1 kg and the flight duration was around 15 min. Berni (2011) developed rotary wing UAV with the 7 kg payload. Its endurance was 20 min flying at a maximum speed of 30 km/h. It used 29 cm^3 gas engines with 1.9 m diameter main rotor. Chun (2015) designed a compact hexacopter with flexible gimbal, costing less than $ 1,000, with payload of up to 700 g and hovering for up to 8 min. Meanwhile, commercial products such as Parrot AR Drone (2015) and DJI Phantom (2015) cannot handle payloads of more than 500 g. AcTec Pelican's (2014) maximum payload is 650 g, but the price is € 5,195, which is too expensive.

In Malaysia, the Department of Civil Aviation (DCA) is the responsible federal authority for aircrafts, includes UAVs. According to the issued Aeronautical Information Circular (AIC) policy for UAVs operational standards (AIC, 2008), the certification process is only required for any civil UAV with maximum take-off mass (MTOW) of more than 20 kg. Small aircrafts with a maximum height of 122 m and weight of less than 20 kg are exempted from this requirement because AIC defines a small plane that weighs no more than 20 kg as any unmanned aircraft. However, aircrafts with a capacity of less than 20 kg are prohibited from being in traffic fly zones or controlled airspace, except with the air traffic control unit's permission.

The general objectives of this research are to develop a fully autonomous low-cost hexacopter UAV, perform an accurate calibration of the multispectral sensor and improve aerial overlap typical image block. This study adopts several techniques to investigate, analyse and develop a prototype low-cost rotary wing UAV, which covers components calibrations, pre-flight, diagnosis problem and flight planning using vertical take-off and landing capabilities, and reduce the line-of-sight telemetry.

2. METHODOLOGY

The general hexacopter UAV methodology flow chart is shown in Figure 1. The hexacopter has six motors and propellers that rotate in the opposite direction of the two motors on the side, which control the rotation of the roll and pitch either by speeding up or slowing down the two different motors. The preparation took three days, consisting of two days of hands-on training assembly, and one day of pre-flight test and ground station installation setup. The components for the hexacopter are relatively cheap, easy to build, commonly available spare parts, open source hardware / software, and tough enough able to carry a small sensor payload.

2.1 Propeller Balancing

A propeller is the most common propulsion device used in UAVs, with blades that rotate around an axis to produce thrust by pushing air. The rotations are determined by its geometry, which produces thrust efficiently at given rotational and forward flight speeds. To avoid the hexacopter UAV slight spin or drift when it is flying, it is important that the propellers are balanced with an equal mass on both sides. GWS Style Slowfly 11 x 4.7 red and black propellers were used and Figure 2 shows the propeller balancer technique using sole tape.

2.2 Gimbal

For commercial gimbals, DJI Company (2015) designed a plastic gimbal for the lightweight GoPro camera and Photohigher Company (2014), used carbon fiber used for the larger camera up to 1.8 kg. Since both commercial products are expensive, a creative hobbyist RC Group (2013) used plywood as gimbals. This experiment used sensor gimbal with two axes tilt mount which allows for stability for picture and video recording capability with hexacopter UAV. The gimbal was made using high-quality carbon fibre and for vibration-dampening, rubber grommets were used for high picture and video quality (Figure 3).

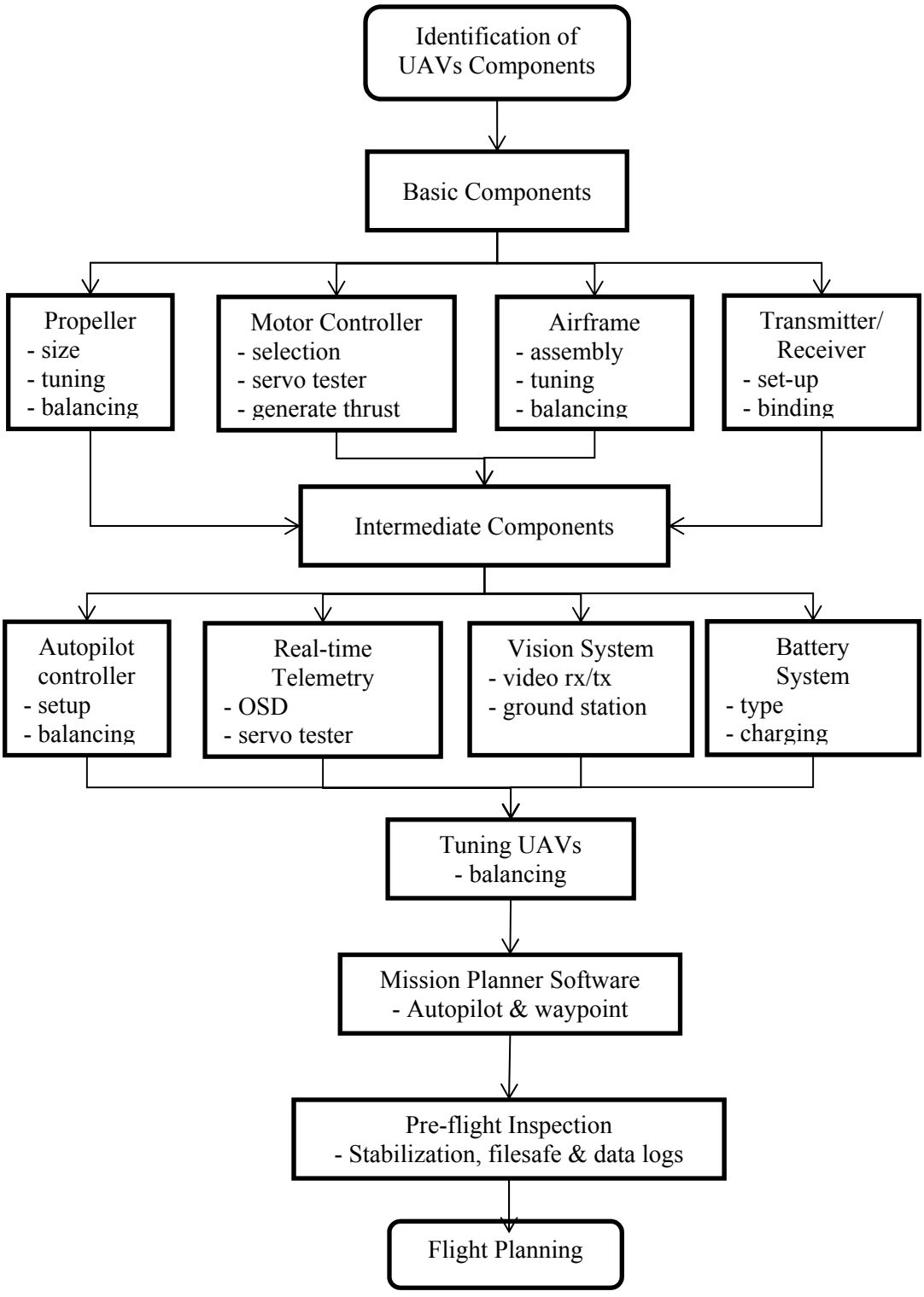

Figure 1: Hexacopter UAV methodology.

Figure 2: Propeller balancing using sole tape.

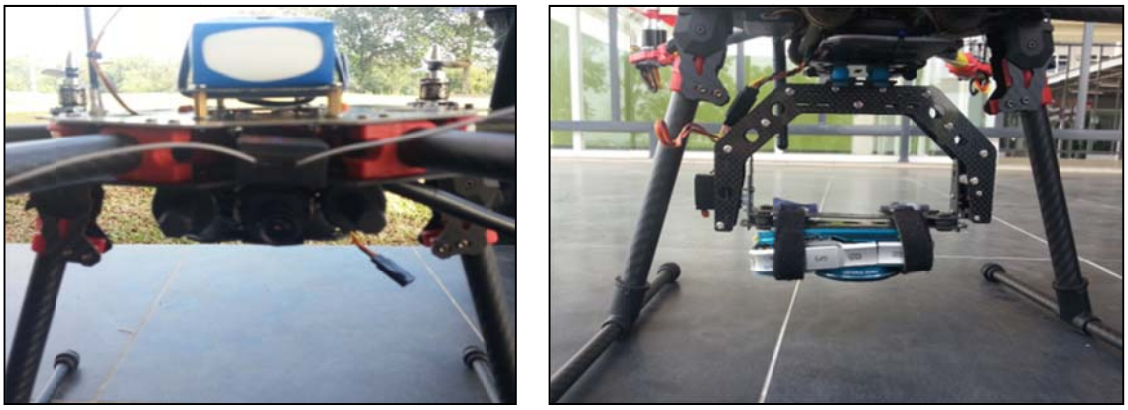

Figure 3: Gimbal installation for RGB / NIR sensor.

2.3 Generating Thrust

Figure 4 shows the weight versus thrust for the hexacopter, where the thrust has twice the amount of the weight of the hexacopter so that it can hover. For 3,000 g of thrust, 20% is added for headroom (hover at 50% throttle) for the maximum current because thrust from the motor is not linear due to the efficiencies of the motor itself and the dynamics of the motor (Asad, 2011). The total thrust of 3,600 g is divided by six (number of motors), where the total thrust per motor is 600 g.

Figure 5 shows the step-by-step calibration for the thrust of 600 g for each motor. All the weight scale results (Figure 6), such as energy, current, and voltage, are compared to the electronic speed control (ESC) specifications for accurate calibration. Based on the thrust calculation, NTM 28-30S 900 kV brushless motors were used, whereby its specifications include weight of 66 g with maximum current of 18 A.

Figure 4: Generating thrust.

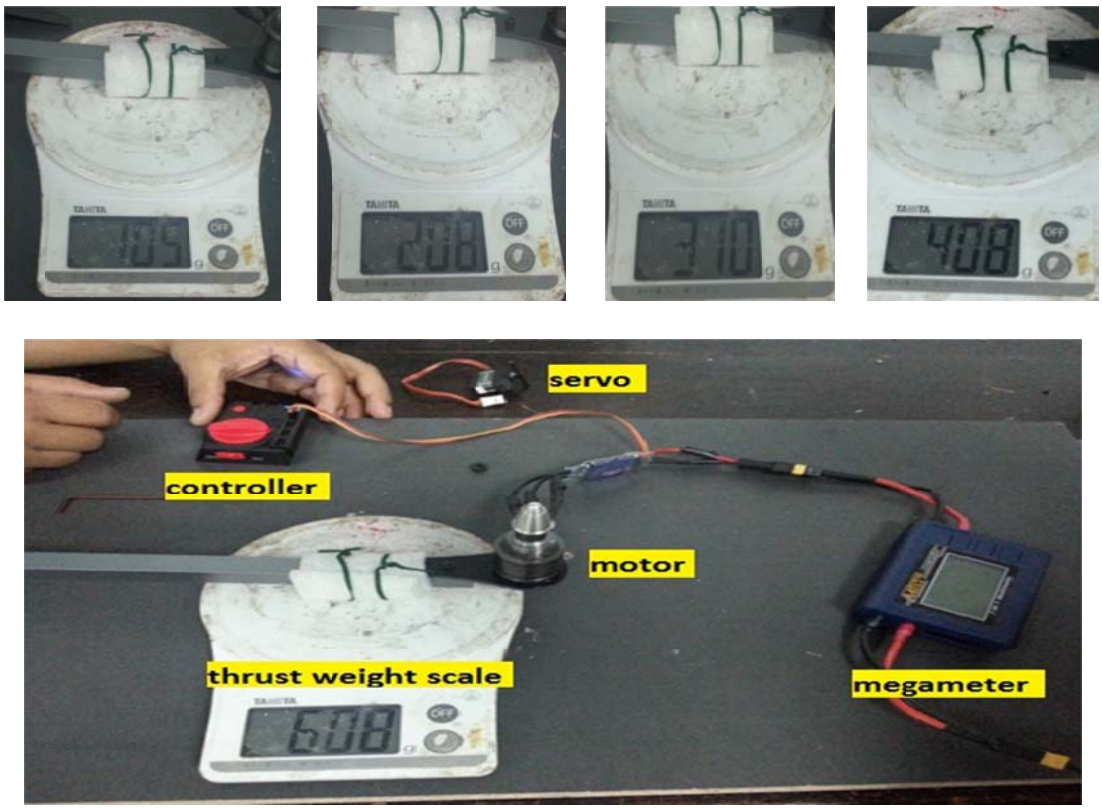

Figure 5: Weight scale output test.

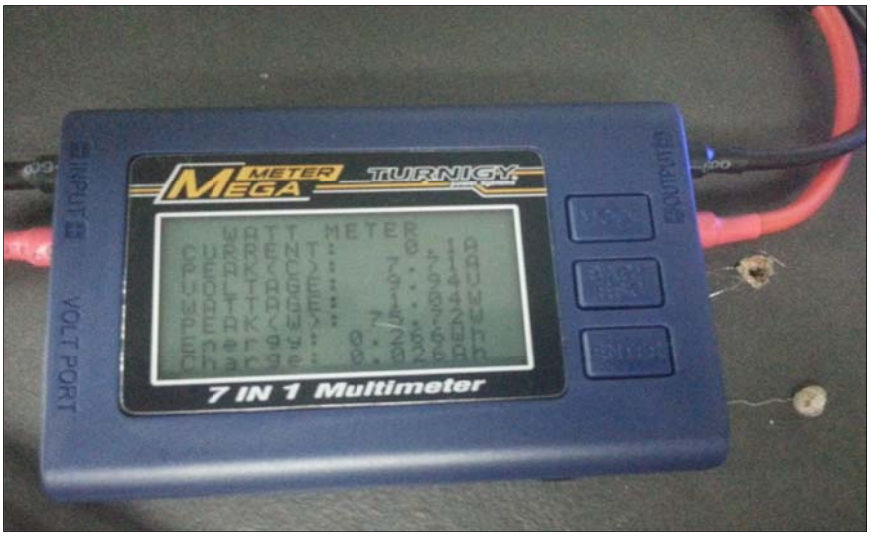

Figure 6: Weight scale results.

2.4 Payload Calculation

After the assembly was completed, the total weight of the hexacopter UAV was measured using a digital scale, as shown in Figure 7. From the measurement, the total thrust was 3.6 g, the UAV's weight was 1.83 kg, while and battery weight was 0.33 kg. Thus, the total payload is calculated as follows:

Total payload = 3.6 kg – 1.83 kg – 0.33 kg = 1.44 kg

2.5 Flight Check

In general, pre-flight check flight modes such as Stabiliser, Altitude Hold, Loiter and Autopilot mode from its current position to hover above the home position were examined. A pre-flight test was conducted in the UPM Golf course. Figure 8 shows the stabiliser mode calibration results and Mission Planner setting waypoints at 30 m altitudes. The maximum flight time is calculated from the flight data results and the LiPo battery was used (Figure 9) with the maximum current during the flight of 19.4 A.

3. RESULTS AND DISCUSSION

All diagnosis is recorded in telemetry logs such as Figure 10, which shows the telemetry logs for battery voltage, relative altitude, and airspeed, tested with or without gimbal for the RGB / NIR sensor. From the pre-flight, good results were achieved except for the battery voltage results (without gimbal) due to telemetry loss. This problem was fixed using the Mission Planner calibration.

Precise flight planning was necessary for the sensor and hexacopter UAV. The Hexacopter UAV was tested at an altitude of 338 m in order to ensure stability the UAV system. A RGB Canon SX230 with focal length 5.2 mm was used and 234 images were captured with the area covering 2.08 km^2.

Figure 7: UAV weight measurements.

Figure 8: Stabiliser mode and waypoint settings.

Figure 9: Flight data results.

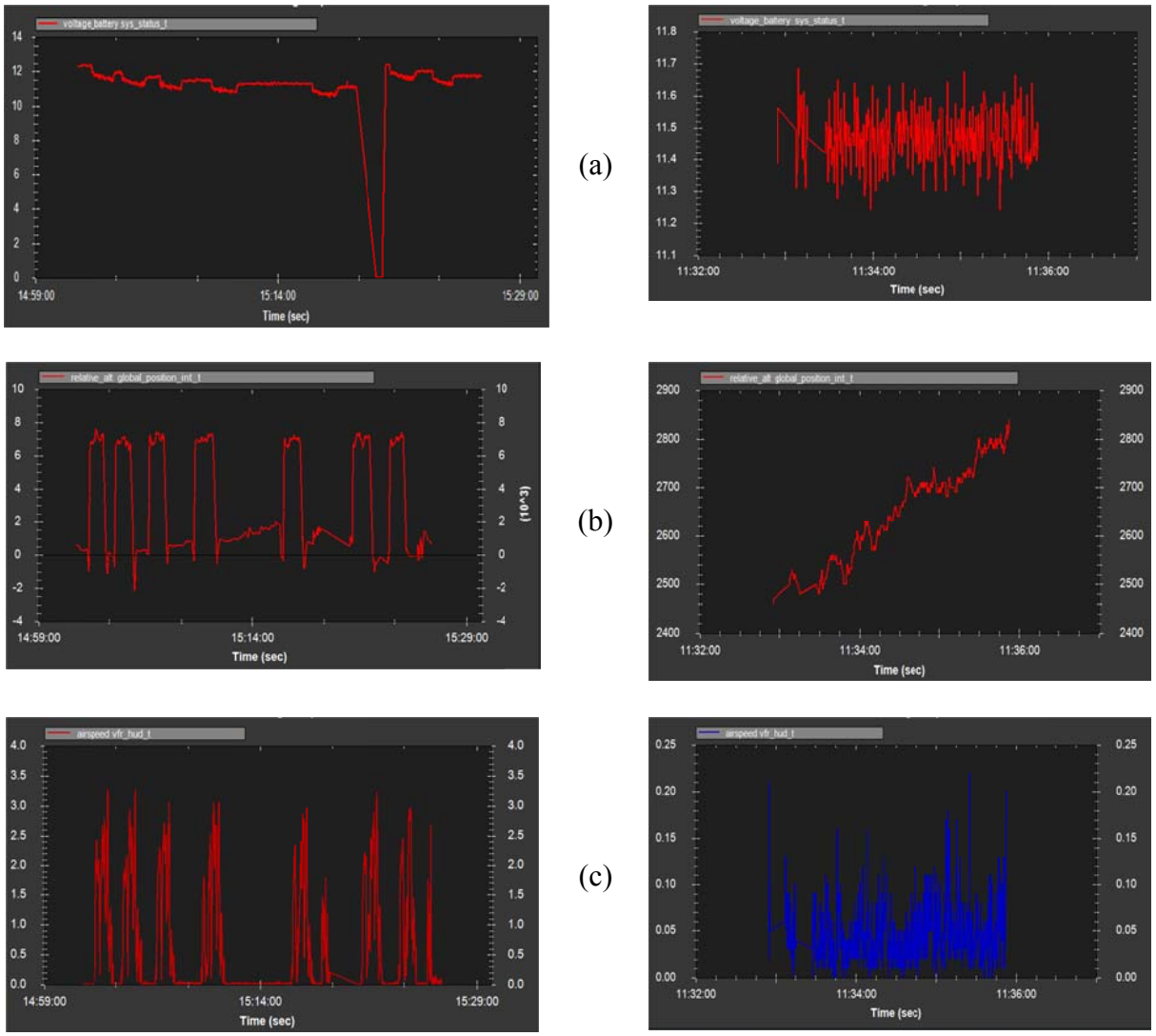

Figure 10: Without and with gimbal telemetry logs for (a) battery voltage, (b) relative altitude, and (c) airspeed.

The projection dimensions coordinate of the sensor locations and error estimate shown in Figure 11. Here, the X and Y projection direction coordinate error is represented by ellipse shape, while Z error direction is represented by different ellipse colours as shown in the figure legend. The estimated sensor location is marked by a black dot.

Table 1 shows the average sensor location error. Figure 12 shows that the aerial typical block images are uniformly distributed over the route plan using the fully autonomous mode, which suitable for image mosaicking. The RGB sensor resolution used is 4,000 x 3,000, 5.2 mm focal length and pixel size is 1.86161 x 1.86161 µm.

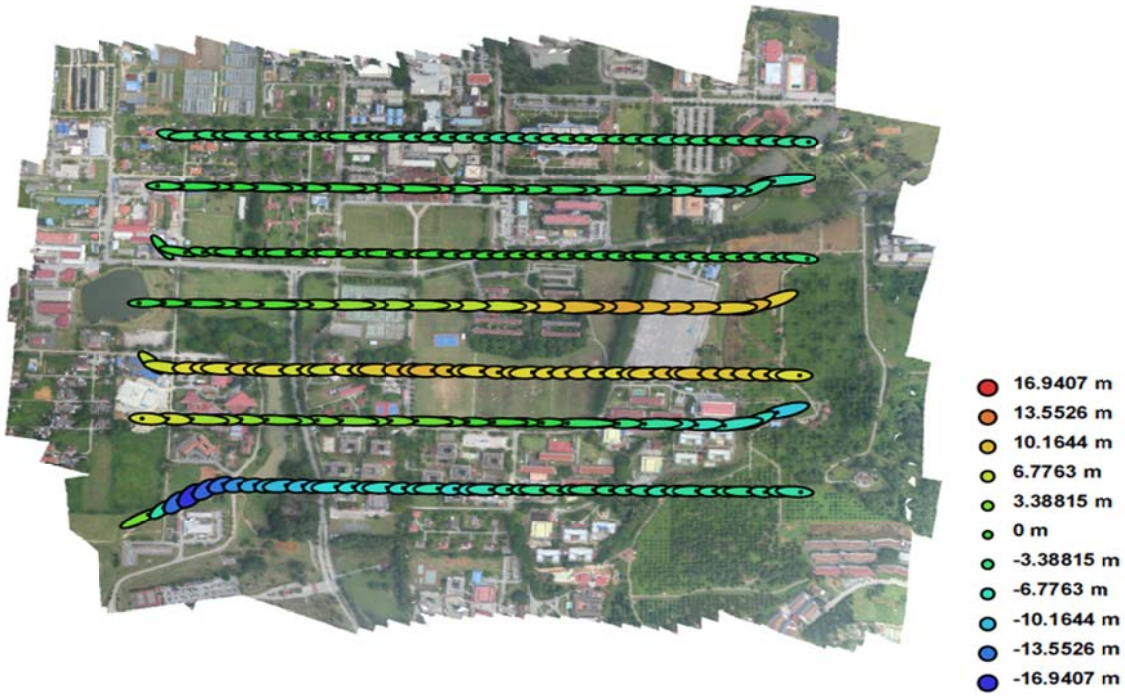

Figure 11: Sensor location and error estimation.

Table 1: An average sensor location error.

X (m)	Y (m)	Z (m)	Total error (m)
20.763939	2.970795	60.39510	21.827562

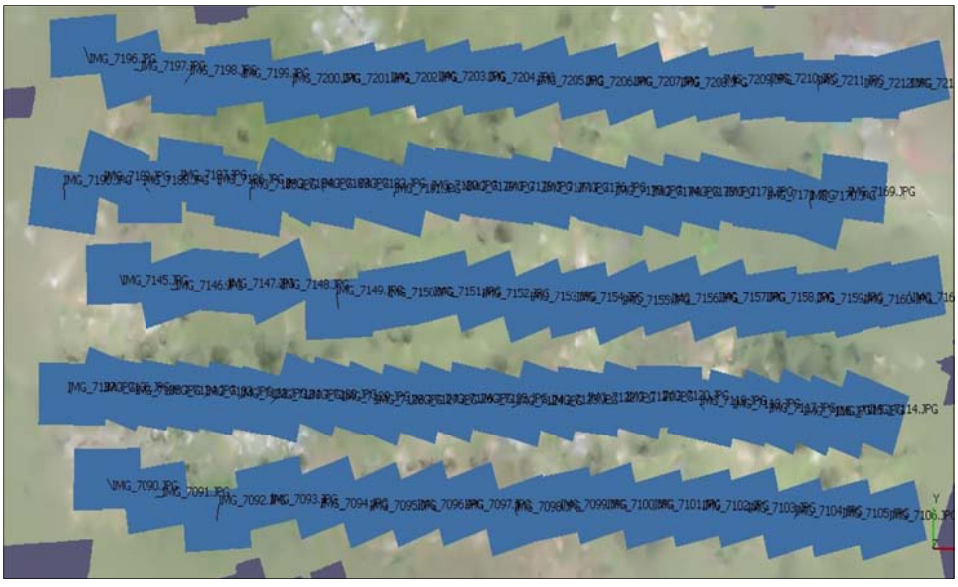

Figure 12: Typical block images uniformly distributed.

4. CONCLUSION

A lightweight hexacopter UAV prototype was successfully developed, which covered the UAV acquisition system, component calibrations, pre-flight test, diagnosis of problems and flight planning. The hardware calibration techniques employed included balancing the propellers with an equal mass on both sides; brushless motors thrust efficiency for a given rotational and forward flight speed; airframe compass calibration; transmitter and receiver binding calibration; servo tester; battery system; autopilot controller; real-time telemetry; tuning-up balancing; and flying technique simulator. The prototype improved the performance significantly for vertical take-off and landing capabilities and reduced the line-of-sight telemetry of the hexacopter UAV as compared to fixed wings. These research steps significantly improved the method for aerial typical image overlap, by uniformly distributing the aerial images using high overlap set to 80% to avoid gaps and occlusion in the image data. This high overlap with 234 aerial images and 767,443 triangle tie-points are suitable for image mosaicking.

REFERENCES

AIC (2008). *Aeronautical Information Circulars (AIC).* Available online at: http://aip.dca.gov.my/aip%20pdf%20new/AIC/AIC%20200804.pdf (Last accessed date: 5 Jan 2015).

Agisoft Software (2014). *Lens Corrections*. Available online at: https://downloads.agisoft.ru/lens/doc/en/lens.pdf (Last accessed date: 4 April 2014).

Arducopter (2015): *Mission Planner.* Available online at: http://ardupilot.org/copter/docs/common-mission-planning.html (Last accessed date: 2 Jan 2015).

Asad, U.A., Jaemann, P. & Hyoun, J. K. (2011). Thrust estimation of quadrotor UAV using adaptive observer. *11th Int. Conf. Control, Automation Syst. (ICCAS),* pp. 26-29.

Bendig, J., Bolten, A. & Bareth, G. (2012). Introducing a low-cost mini UAV for thermal and multispectral imaging. *Int. Arch. Photogramm. Remote Sens. Spat. Inf. Sci.,* **39:** 345–349.

Berni, J.A.J., Zarco-Tejada, P.J., Suárez, L., González-Dugo, V. & Fereres, E. (2011). Remote sensing of vegetation from UAV platforms using lightweight multispectral and thermal imaging sensors. *Int. Arch. Photogramm. Remote Sens. Spatial Inform.*, **38**:6-11.

Brescianini, D., Hehn, M. & D'Andrea, R. (2015). Quadrocopter pole acrobatics. *IEEE/RSJ Int. Conf. Intelligent Robots Syst.*, **13**: 3472–3479.

Chun, F.L. & Takehisa, Y. (2015). Designing a compact hexacopter with gimballed lidar and powerful onboard linux computer. *Proc. 2015 IEEE Int. Conf. Inform. Automation*. **15**: 2523 – 2528.

DJI Zenmuse. *Gimbal*. Available online at: http: //www.dji.com/product/zenmuse-h3-2d/ (Last access date: 14 October 2015).

Joshua, K. & Arko, L. (2012). Sensor correction and radiometric calibration of a 6-band multispectral imaging sensor for UAV remote sensing. *Int. Arch. Photogramm. Remote Sens. Spatial Inform.*, **B1**: 393-398.

Mellinger, D., Michael, N. & Kumar, V. (2012). Trajectory generation and control for precise aggressive maneuvers with quadrotors. *Int. J. Robotics Res.,* **5**: 664 –674.

Nebiker, S., Annen, A., Scherrer, M. & Oesch, D. (2008). A lightweight multispectral sensor for micro UAV - opportunities for very high resolution airborne remote sensing. *Int. Arch. Photogramm. Remote Sens. Spat. Inf. Sci.,* **B1:** 1193-1199.

Pérez, M., Agüera, F. & Carvajal, F. (2011). Digital camera calibration using images taken from an unmanned aerial vehicle. *Int. Arch. Photogramm. Remote Sens. Spat. Inf. Sci.,* **C22**: 14-16.

Photohigher. *Gimbal*. Available online at: http://photohigher.com/collections/halo-gimbal-series/ (last access date: 20 November 2015).

RC Group. *Plywood Gimbal for GoPro Camera*. Available online at: http://blogs.yahoo.co.jp/megumi7000/ archive/2013/04/30/ (Last access date: 6 April 2015).

Ritz, R., Muller, M.W, Hehn, M. & D'Andrea, R. (2012). Cooperative quadrocopter ball throwing and catching. *IEEE/RSJ Int. Conf. Intelligent Robots Syst.*, 4972–4978.

Tetracam ADC (2012): *Tetracam Products*. Available online at: http://www.tetracam.com/Products-ADC_Micro.htm (Last access date: 3 June 2015).

Turpin, M., Michael, N. & Kumar, V. (2014). Trajectory design and control for aggressive formation flight with quadrotors. *Autonomous Robots*, **33**: 143–156.

Zischinsky, T., Dorfner, L. & Rottensteiner, F. (2000). Application of a new model helicopter system in architectural photogrammetry. *Int. Arch. Photogramm. Remote Sens. Spat. Inf. Sci.*, **B5**/**2**: 959 – 965.

PERFORMANCE COMPARISON OF EMITTER LOCATING SYSTEM FOR LOW LEVEL AIRBORNE TARGETS

Ahmad Zuri Sha'ameri*, Abdulmalik Shehu Yaro, Freeha Majeed Amjad & Muhammad Noor Muhammad Hamdi

Faculty of Electrical Engineering, Universiti Teknologi Malaysia (UTM), Malaysia

*Email: zuri@fke.utm.my

ABSTRACT

Emitter locating system – a component of electronic support (ES) - could complement existing radar systems for the detection of low level airborne targets. This is possible since targets emit signals for locating, navigation and communication. Thus, an emitter locating system can locate the target from its emission using spatially located receivers. Two methods will be evaluated: multiangulation (MANG) based on angle of arrival (AOA) estimation, and multilateration (MLAT) based on time difference of arrival (TDOA) estimation. Between the two methods, MLAT has the advantage of detecting targets in 3D. Evaluation is performed using Monte Carlo (MC) simulation, where the parameters used are based on the typical low probability of intercept radar and wireless data link and receiver parameters for range of up to 50 km at a minimum altitude of 400 ft (122 m). On the horizontal position estimation, MANG has lower mean square error over longer ranges between 30 to 50 km, while MLAT is able to estimate altitude for up to 50 km at the lower carrier frequency of 2.4 GHz.

Keywords: *Electronic support (ES); multiangulation; multilateration; Monte Carlo simulation; emitter locating.*

1. INTRODUCTION

Detection of airborne targets is primarily performed by radar. Due to the active nature of radar, its location can be detected by electronic support (ES) and could be subsequently disabled by electronic attack (EA) (Pace, 2009). In order to avoid detection by radar, strike fighters and attack helicopters typically adopt low altitude flight profile, which also reduces line of sight (LOS) distance. Clutter at low altitude introduces interference to the return signal, which reduces the probability of target detection. However, this is not a problem for ES systems, which are expected to give better detection provided the target transmits signals with good received signal quality. The passive nature of ES systems that do not emit any signal minimises the likelihood of detection. Drones are another type of airborne target whose role continues to expand from military towards commercial, scientific and recreational applications (ICAO, 2011). Detection of drones that normally weight less than 25 kg is difficult due to its small radar cross-section and its tendency to be flying slow at low altitude (Ritchie *et al*., 2015).

An ES system, as shown in Figure 1, consists of emitter locating, signal reception, signal analysis and classification, decision making, and signal database (Ahmad & Sha'ameri, 2015). The focus of this paper is on emitter locating, where the possible methods are: receive signal strength (RSS) finger printing, multilateration (MLAT) and multiangulation (MANG). Emitter locating requires the use of multiple

Nomenclatures

$\mathbf{a}$	Steering vector
d_{im}	Path difference measurement of the signal between the i^{th} and m^{th} GRS
e_i	Error due to the i^{th} Grs
$\mathbf{R_x}$	Correlation matrix
$\mathbf{U}_N$	Noise subspace
$\mathbf{U}_S$	Signal subspace
$\mathbf{u}$	Eigenvector
x_i	Signal at the i-th element

Greek Symbols

λ	Eigenvalue
τ_{im}	TDOA measurement between i^{th} and m^{th} GRS
θ	Angle of arrival

Abbreviations

AOA	Angle of arrival
ES	Electronic support
GRS	Ground receiving station
LOB	Line of bearing
LOS	Line of sight
LPI	Low probability of intercept
MANG	Multiangulation
MC	Monte Carlo
MLAT	Multilateration
MUSIC	Multiple signal classification
PE	Position estimation
RMSE	Root mean square error
TDOA	Time difference of arrival
TOA	Time of arrival

receiver stations that are spatially located as shown in Figure 2. It is a two-stage process as shown in Figure 3 (So, 2012). At the first stage, position dependent signal parameters are estimated, such as time of arrival (TOA), time difference of arrival (TDOA), angle of arrival (AOA) and RSS. By using the position dependent signal parameters from the first stage, the second stage involves estimating the position of the emitter using position estimation (PE) algorithms, such as fingerprinting, lateration, and angulation. The term emitter will be used to refer to the target because the target serves as the electromagnetic emission source, which could be either radar or communications.

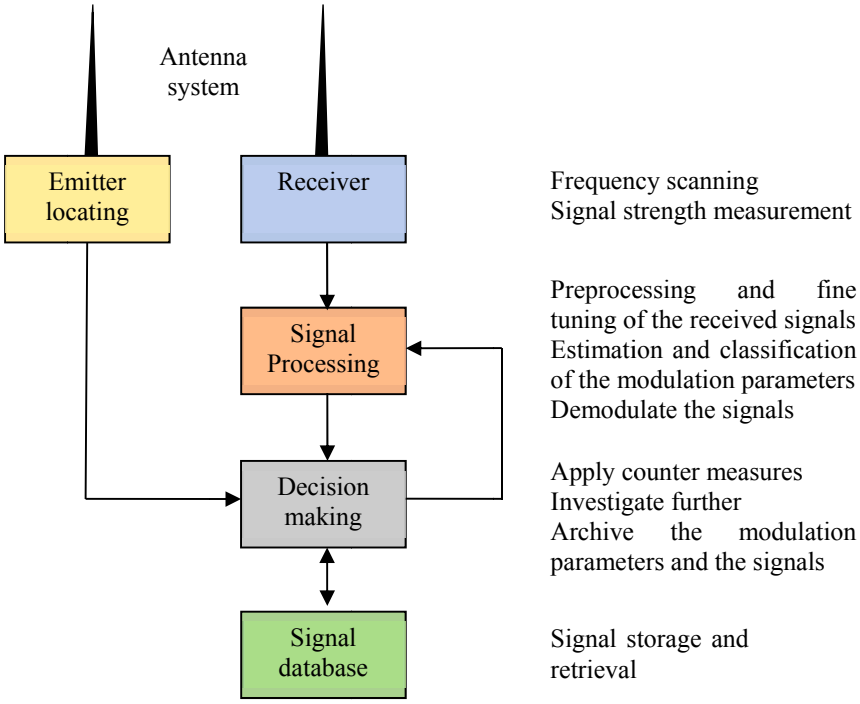

Figure 1: Block diagram of ES system (Ahmad & Sha'ameri, 2015).

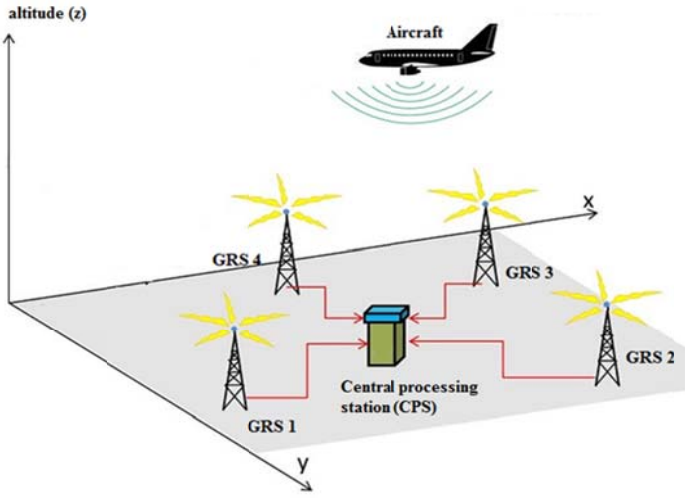

Figure 2: Block diagram for emitter locating system (Sha'meri & Shehu, 2015).

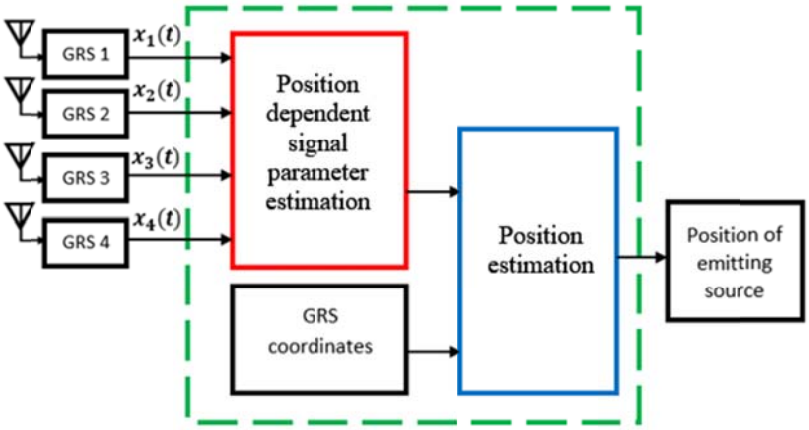

Figure 3: Emitter locating PE process (So, 2012).

MLAT is an example of an emitter locating system that estimates emitter position using its electromagnetic emission. TDOA is used as its position dependent parameters and the lateration algorithm for position estimation. There are several techniques for TDOA estimation but the most commonly used technique is the cross correlation approach (Neven *et al*., 2014; Dou & Xing, 2015). Due to nonlinear relationship between the TDOA measurement and the emitter position, several lateration algorithms have been developed and can be grouped as open-form and closed-form lateration algorithm (So, 2012; Mantilla-Gaviria *et al*, 2015). The open-form lateration algorithm utilises linearisation methods, such as Taylor's series, to obtain the linear relationship, which is followed by an iteration process (So, 2012; Galati *et al*., 2014). This approach is most suitable for an active system but has convergence issues due to the use of the linearisation methods and is also computationally complex (Chaitanya *et al*., 2015). The closed-form approach on other hand performs algebraic manipulations to obtain the linear relationship and is more suitable for an emitter locating system (Bucher & Misra, 2002; So, 2012; Torbati *et al*, 2013; Sha'meri & Shehu, 2015) . It does not suffer from convergence issues as it does not use linearisation methods. For this reason, the closed-form lateration algorithm is adopted for emitter locating with MLAT.

Unlike MLAT, MANG uses AOA measurements as position dependent signal parameters with an angulation algorithm to estimate the emitter position (So, 2012). Several AOA estimation algorithms are present in the literature, which can be classified into subspace and non-subspace methods (Mondal, 2013). Non-subspace estimation techniques, such as beamforming and Capon's minimum variance method, yield poor resolution and can identify only a single emitter source at a time (Chowdary, 2016). Subspace estimation techniques, such as multiple signal classification (MUSIC) and estimation of signal parameter via rotational invariance technique (ESPRIT), have high resolution and perform efficiently where angles are indicated to be closely spaced (Baig & Malik, 2013). These techniques can identify multiple emitters given that the number of sensor elements in the sensor array is more than the number of emitters (GIRD, 2016). A comparison shows that ESPRIT requires less computation and less storage than MUSIC, and has a higher resolution. However, MUSIC on the other hand performs better at low signal-to-noise ratio (SNR) (Dhope, 2015). Due to the advantages of MUSIC, this algorithm is selected for use in AOA estimation and subsequently in the emitter locating process using MANG.

This paper is organised as follows. Section 2 first describes the signal models used in this paper. Section 3 presents the emitter locating methodology using MANG and MLAT. Section 4 discusses the signal parameters used and also the PE results using MANG and MLAT. For both approaches, the PE root means square error (RMSE) is used as the performance measure.

2. SIGNAL MODEL

This paper focuses on low level airborne threats, such as strike fighters, attack helicopters and drones, which are primarily used for tactical applications (Northrop Grumman, 2017). Strike fighters and attack helicopters are usually equipped with on-board radar for target detection and tracking as well as with synthetic aperture radar (SAR) for terrain mapping. Most of the radar technology reported recently is based on low probability of intercept (LPI) radar (Pace, 2009). Unlike conventional radar, LPI radar performs detection with minimum peak power, which makes it difficult to detect using current ES technology. An example of waveform used for LPI radar is continuous wave linear frequency modulated (CW-LFM) or CW nonlinear frequency modulated (CW-NLFM) that operates at the X-band frequency (8 to 12 GHz) (Melvin & Scheer, 2013), with the most recent published work found in Wahab *et al*. (2017). Most information about LPI radar is confidential and could not be found in the open literature. Thus, we will consider an LPI radar similar to the Pilot Mk2 radar that is described in Schleher (2006) for analysis and performance evaluation. The radar has an estimated range of 50 km and the target is expected to fly at an altitude less than 400 ft (122 m). The reason for selecting an estimated range of less than 50 km is the lack of LOS between the targets and ground receiving stations (GRSs). For the LPI radar, the transmit power of 1 W is assumed based on current practice with pulse repetition period and pulse width of 1 ms (Schleher, 2006). It is also assumed that the radar beam is facing in the direction of the emitter locating system to consider the situation if the airborne threat intends to attack targets close by.

Besides airborne radar, low level airborne threats, such as drones, require exchange of telemetry information and video downlink via a wireless datalink. Typically, the signals are continuous in nature with low transmit power. For evaluation purposes, the wireless datalink is selected based the allocation provided by Malaysian Communications and Multimedia Commission (MCMC), as shown in Table 1 (MCMC, 2015). A higher transmit power is assigned to the higher frequency band of 5.8 GHz due to the higher propagation loss and to ensure sufficient receive power over longer distances approaching 50 km.

Table 1: Frequency assignment and maximum equivalent isotopically radiated power (EIRP) (MCMC, 2015).

No.	Radio Frequency (MHz)	Maximum EIRP
1	433 - 435	100 mW
2	2,400 - 2,500	500 mW
3	5,725 – 5,875	1 W

3. EMITTER LOCATING METHODOLOGY

The methodology for emitter locating using MANG and MLAT is described in this section.

3.1 MANG

In this section, the AOA estimation method is first explained followed by the MANG algorithm. A mathematical model is then developed to estimate the PE error from the emitter position and geometry of GRSs.

3.1.1 MUSIC Algorithm for AOA Estimation

Each GRS is equipped with a uniform linear array (ULA) consisting of M elements separated by a distance d. It receives the signal $s(t)$ from the emitter impinging the array at an angle θ. The array element closest to emitter receives the signal earlier than the other elements. As a result, the other array elements receive a delayed version of $s(t)$. The signal at the i-th element is represented as:

$$x_i(t) = e^{-j\omega(i-1)(\frac{d}{c})\sin(\theta)} s(t) \tag{1}$$

where $\omega=2\pi f$ is the angular frequency and c is the speed of electromagnetic waves.

Combining all the signals received at each GRS together with noise forms the input signal matrix $\mathbf{X}(t)$:

$$\mathbf{x}(t) = \begin{bmatrix} x_1(t) \\ x_2(t) \\ x_3(t) \\ \vdots \\ x_M(t) \end{bmatrix} + \mathbf{n}(t) == \begin{bmatrix} 1 \\ e^{-j\omega(\frac{d}{c})\sin(\theta)} \\ e^{-j\omega 2(\frac{d}{c})\sin(\theta)} \\ \vdots \\ e^{-j\omega(M-1)(\frac{d}{c})\sin(\theta)} \end{bmatrix} s(t) + \mathbf{n}(t) \tag{2}$$

$$\mathbf{X}(t) = \mathbf{a}(\theta)s(t) + \mathbf{n}(t) \tag{3}$$

where $\mathbf{a}(\theta)$ is the steering vector that steers the received signal in the direction of the AOA (Waweru *et al*., 2014). Input signal matrix for K emitters is given as:

$$\mathbf{X}(t) = \mathbf{A}(\theta)s(t) + \mathbf{n}(t) \tag{4}$$

where $\mathbf{A}(\theta)= [\mathbf{a}(\theta_1), \mathbf{a}(\theta_2),\mathbf{a}(\theta_3),\ldots\ldots,\mathbf{a}(\theta_K)]$.

The MUSIC algorithm computes the M x M correlation matrix $\mathbf{R}_x$:

$$\mathbf{R}_x = E\left\{\mathbf{x}(t)\mathbf{x}^H(t)\right\} \tag{5}$$

From Equation 5, the eigenvalue decomposition of $\mathbf{R}_x$ results in M eigenvalues ($\lambda_1, \lambda_2, \lambda_3,\ldots, \lambda_K,\ldots, \lambda_M,$) and M associated eigenvectors ($\mathbf{u}_1, \mathbf{u}_2, \mathbf{u}_3,\ldots.., \mathbf{u}_K,\ldots.,\mathbf{u}_M$). The eigenvectors associated to K smallest eigenvalues span the noise subspace $\mathbf{U}_N$ while the rest (M-K) of the eigenvectors span the signal subspace $\mathbf{U}s$:

$$\mathbf{U}_N = \left[\mathbf{u}_1, \mathbf{u}_2, \mathbf{u}_3, \ldots.., \mathbf{u}_K\right] \tag{6}$$

$$\mathbf{U}_S = \left[\mathbf{u}_K, \mathbf{u}_{K+1}, \ldots\ldots, \mathbf{u}_M\right] \tag{7}$$

Due to the orthogonality of the noise subspace and array steering vector at the angles of arrival $\theta_1, \theta_2,\ldots \theta_K$, the matrix product $\mathbf{a}^H(\theta)\boldsymbol{U}_N\boldsymbol{U}_N{}^H\mathbf{a}(\theta)$ is zero for these angles. The reciprocal of this matrix product creates sharp peaks at the angle of arrival. Thus, the MUSIC pseudospectrum is given by:

$$P(\theta) = \frac{1}{\left|\mathbf{a}^H(\theta)\mathbf{U}_N\mathbf{U}_N{}^H\,\mathbf{a}(\theta)\right|} \tag{8}$$

1.
2.
3.
3.1.
3.1.1.

3.1.2 MANG Position Estimation

Estimated AOAs and coordinates of GRSs are used to form the line of bearings (LOB) equations. The point of intersection of the LOB is the estimated position of emitter. Equation of LOB for the i^{th} GRS is:

$$y_i = m_i x_i + c_i \tag{9}$$

where (x_i, y_i) are the coordinates of the i^{th} GRS. The slope and the y-intercept for Equation 9 are given as:

$$m_i = \tan(90 - \theta_i) \tag{10}$$

$$c_i = y_i - x_i \tan(90 - \theta_i) \tag{11}$$

MANG consists of four GRS results with four LOB equations, which can be expressed in matrix form as:

$$\mathbf{Ax} = \mathbf{b} \tag{12}$$

where:

$$\mathbf{A} = \begin{bmatrix} -\tan(90-\theta_1) & 1 \\ -\tan(90-\theta_2) & 1 \\ -\tan(90-\theta_3) & 1 \\ -\tan(90-\theta_4) & 1 \end{bmatrix}, \mathbf{x} = \begin{bmatrix} x \\ y \end{bmatrix}, \mathbf{b} = \begin{bmatrix} y_1 - x_1\tan(90-\theta_1) \\ y_2 - x_2\tan(90-\theta_2) \\ y_3 - x_3\tan(90-\theta_3) \\ y_4 - x_4\tan(90-\theta_4) \end{bmatrix} \tag{13}$$

Since the number of equations is more than the unknowns, the matrix inverse does not exist. Thus, the over-determined least squares approach can be utilised (Anton & Rorres, 2010) and Equation 12 can be represented as:

$$\mathbf{A}^T\mathbf{A}\,\mathbf{x} = \mathbf{A}^T\mathbf{b} \tag{14}$$

The PE solution is found by:

$$\mathbf{x} = (\mathbf{A}^T\mathbf{A})^{-1}\mathbf{A}^T\mathbf{b} \tag{15}$$

3.1.3 Mathematical Model for Position Estimation

Using the geometry of the receiving station configuration, a mathematical function is obtained for PE error based on the emitter position, AOA error and the coordinates of the GRSs, as shown in Figure 4 (Yaro & Sha'meri, 2016).

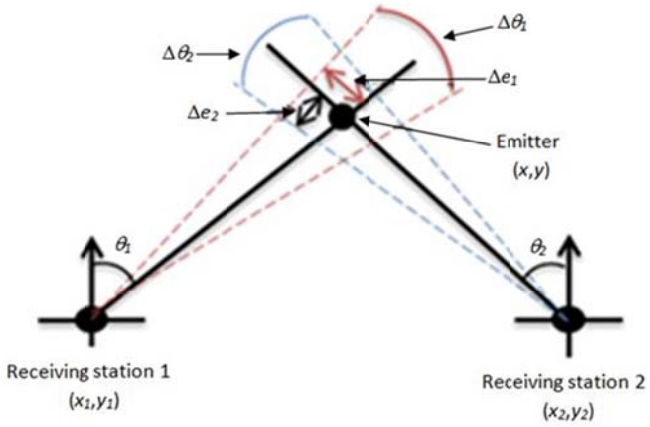

Figure 4: PE error for GRS1 and GRS2 (Yaro & Sha'meri, 2016).

The error due to the i^{th} GRS is given as:

$$\Delta e_i = \tan\left(\frac{\Delta\theta_i}{2}\right)\sqrt{(x-x_i)^2+(y-y_i)^2} \tag{16}$$

where (x, y) are the coordinates of emitter, (x_i, y_i) are the coordinates of i^{th} GRS and $\Delta\theta i$ is twice the AOA RMSE for i^{th} GRS.

The total PE error is the average of PE errors due to the 4 GRSs given as:

$$\begin{aligned}\Delta e_{avg} &= \frac{\sum_{1}^{4}\Delta e_i}{4} \\ &= \frac{\Delta e_1+\Delta e_2+\Delta e_3+\Delta e_4}{4}\end{aligned} \tag{17}$$

3.2 MLAT Position Estimation Methodology

Let the position of a stationary emitter be $\mathbf{x_e} = (x, y, z)$ and the coordinates of the i^{th} and m^{th} GRSs be (x_i, y_i, z_i) and (x_m, y_m, z_m) respectively. The path difference (PD) measurement of the signal between the i^{th} and m^{th} GRS emanating from the emitter is obtained as:

$$d_{im} = \sqrt{(x-x_i)^2+(y-y_i)^2+(z-z_i)^2} - \sqrt{(x-x_m)^2+(y-y_m)^2+(z-z_m)^2} \tag{18}$$

The TDOA measurement obtained between the i^{th} and m^{th} GRS is related to the PD measurement from Equation 18 as follows:

$$d_{im} = c \times \tau_{im} \tag{19}$$

where τ_{im} is the TDOA measurement between the i^{th} and m^{th} GRSs, and c = 3x10^{10} m/s. The subscript "*im*" indicates that the TDOA or PD measurement is obtained using the i^{th} GRS as reference and the m^{th} GRS as non-reference.

The minimum number of GRSs for 3D PE is four. To differentiate between the reference and non-reference GRS for TDOA estimation, let the i^{th} and j^{th} GRSs be chosen as reference, and the m^{th} and k^{th} be the non-reference GRSs. The remainder of the PD equations in the form of Equation 18 are:

$$d_{jm} = \sqrt{\left(x - x_j\right)^2 + \left(y - y_j\right)^2 + \left(z - z_j\right)^2} - \sqrt{\left(x - x_m\right)^2 + \left(y - y_m\right)^2 + \left(z - z_m\right)^2} \tag{20}$$

$$d_{ik} = \sqrt{\left(x - x_i\right)^2 + \left(y - y_i\right)^2 + \left(z - z_i\right)^2} - \sqrt{\left(x - x_k\right)^2 + \left(y - y_k\right)^2 + \left(z - z_k\right)^2} \tag{21}$$

$$d_{jk} = \sqrt{\left(x - x_j\right)^2 + \left(y - y_j\right)^2 + \left(z - z_j\right)^2} - \sqrt{\left(x - x_k\right)^2 + \left(y - y_k\right)^2 + \left(z - z_k\right)^2} \tag{22}$$

From Equations 18-22, a non-linear relationship exists between the input variables (d_{im}, d_{jm}, d_{ik}, d_{jk}) and the output variable (x, y, z). Thus, to solve for the emitter position, a linear relationship between the two variables have to be established first, which can be done through algebraic manipulations (Bucher & Misra, 2002; Sha'meri & Shehu, 2015). The algebraic manipulation of Equations 18 and 20-22 results in two plane equations in forms of (Sha'meri & Shehu, 2015):

$$xB + yC + zD = A \tag{23}$$

where the coefficients A, B, C and D depend on the PD measurements and GRSs coordinates. The pair of equations in the form of Equation 23 are then used to obtain the coordinates of the emitter. A detailed derivation of Equations 18 to 23 and how the coordinates of the emitters can be obtained using the pair of equations in the form of Equation 23 can be found in Bucher & Misra (2002) and Sha'meri & Shehu (2015).

4. SIMULATION PARAMETERS AND RESULTS

In this section, the signal parameters used in this paper are first presented. Next, the result for MANG is presented followed by the results for MLAT. At the final part of this section, a comparison is made between the two methods for PE estimation.

4.1 Simulation Parameters

A square configuration of four GRSs with a separation distance of 2.5 km is used as shown in Figure 5. PE errors are calculated for emitter ranges from 20 to 50 km, emitter bearings from 0 to 90° and altitude of 400 ft. The simulation parameters used are listed in Table 2, which are based on practical values used for LPI radar, wireless datalink for drones and ES systems. The square configuration simplifies the performance analysis because the results obtained for one quadrant from 0 to 90° can be applied over all directions.

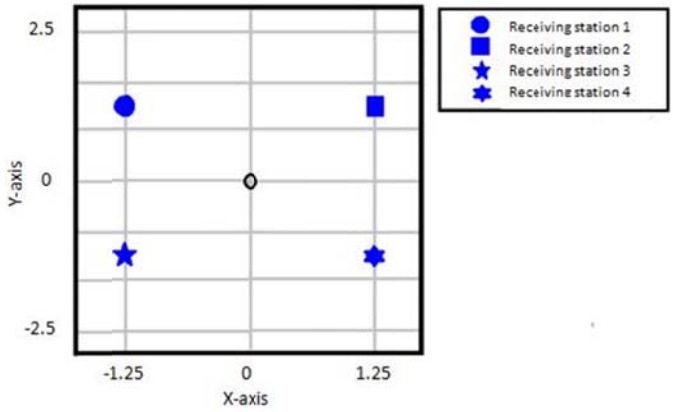

Figure 5: Ground receiving station configuration.

Table 2: Simulation parameters.

No.	Parameter	Value
1	Carrier frequency	2.4, 5.8 and 10 GHz
2	Transmit power	0.5 and 1 W
3	Transmit antenna gain	35 dBi
4	Receive antenna gain	12 dBi
5	GRS receiver sensitivity	-90 dBm

Transmit power of 1 W is used for carrier frequencies of 5.8 and 10 GHz, while 0.5 W is used for 2.4 GHz. The resolution of the MUSIC algorithm is set to 0.15°. The RMSE of position is used for comparison of PE error at various emitter positions. For N-realisation Monte Carlo (MC) simulation, RMSE for position is given by:

$$RMSE = \sqrt{\frac{\sum_{i=1}^{M}\left[(x_i - x)^2 + (y_i - y)^2\right]}{N}} \tag{24}$$

where (x, y) are the actual position coordinates of emitter and (x_i, y_i) are the position coordinates estimated at the i^{th} iteration.

The free space path loss model is assumed for the SNR calculation. Figure 6 shows the effective SNR distribution at different emitter positions within the specified emitter ranges, bearings and altitude of 400 ft for the selected carrier frequencies. There is no significant difference in SNR for emitter altitudes within 400 ft (0.12 km) to 15 km (Sha'meri & Shehu, 2015).

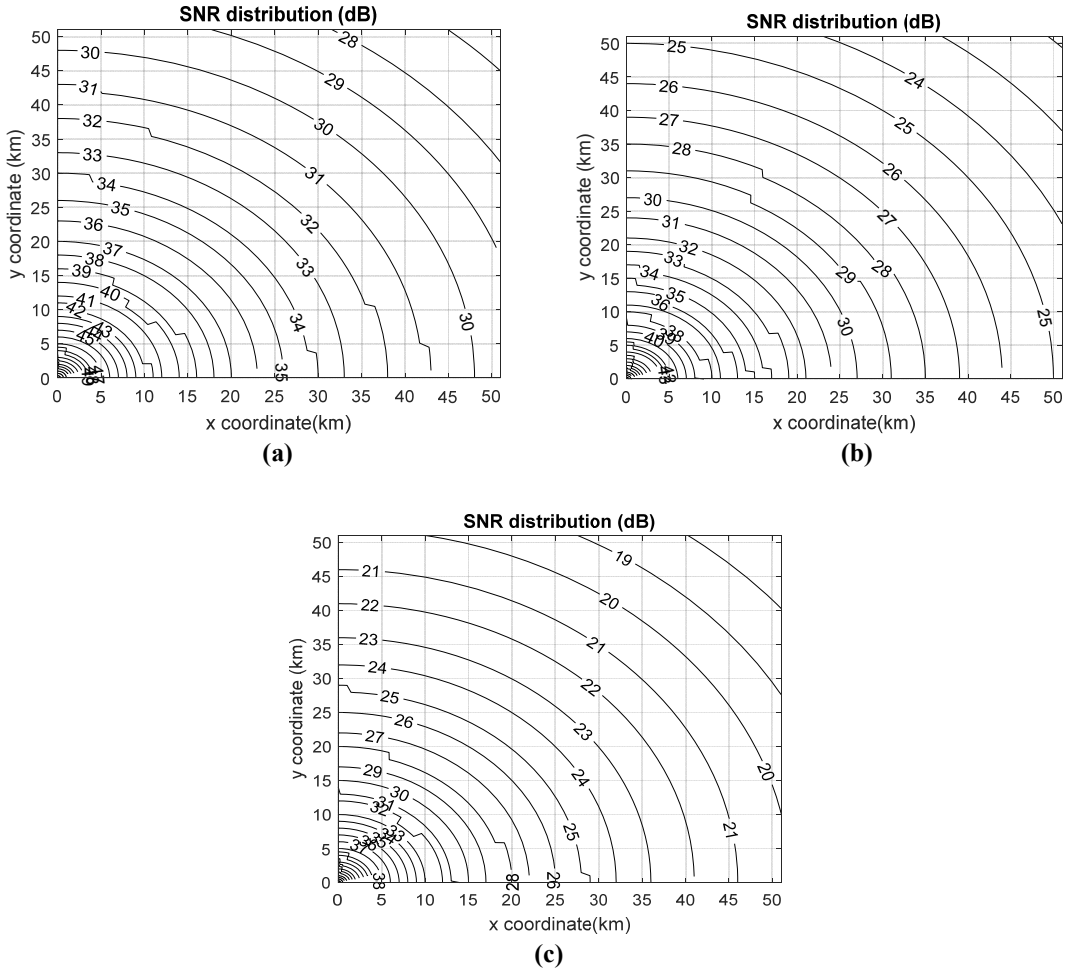

Figure 6: SNR distribution for one quadrant (bearings of 0^o to 90^o) at carrier frequencies of (a) 2.4 GHz (b) 5.8 GHz and (c) 10 GHz.

4.2 MANG Results

The MANG results consist of two parts: AOA estimation error and PE error. This is because the PE error is contributed by the AOA estimation error.

4.2.1 AOA Estimation Error

This section presents the effect of SNR and the number of array elements on the performance of the MUSIC algorithm for AOA estimation. Table 3 shows the errors for certain estimated AOAs using MC simulation for 8- and 16-element arrays. It can be seen that an inverse relationship exists between SNR value and the performance of the MUSIC algorithm, which means that at low SNR, a higher AOA error is expected. The performance is also affected by the number of elements in the array. Increasing the number of array elements improves the performance. For instance, at 85° and 20 dB, the 8-element array gives an error of 0.55°, while the 16-element array gives a much lower error of 0.15°.

It can also be observed from Table 3 that certain AOAs cannot be estimated at low SNR due to high unacceptable errors. The 8-element array is not able to estimate AOA of 87° below 20 dB, 88° below 26 dB and 89° below 40 dB. Comparing this result with the SNR values in Figure 6(c) shows that the 8-element array cannot estimate AOA of 88° for signal with carrier frequency of 10 GHz for ranges beyond 25 km, while AOAs above 88° cannot be estimated within 50 km range. The 16-element array on the other hand is able to estimate AOA of 87° and 88° at an SNR of 20 dB but cannot estimate 89° below 32 dB. Thus, the AOA of 89° for signal with carrier frequency of 10 GHz cannot be estimated using the 16-element array for ranges beyond 12 km. Both arrays fail to estimate AOA of 90° at any SNR value. Figure 6 indicates that at certain emitter ranges, lower carrier frequencies have higher SNR. Thus, the ability of AOA estimation increases at lower carrier frequency.

The comparison of both array results shows that the 16-element array performs better than the 8-element array. Therefore, AOA estimated by the 16 -element array is used for position estimation.

Table 3: AOA error (Yellow shade: Highly unacceptable error).

M=8		SNR (dB)										
		20	**22**	**24**	**26**	**28**	**30**	**32**	**34**	**36**	**38**	**40**
	85	0.55	0.37	0.30	0.22	0.19	0.14	0.12	0.10	0.08	0.07	0.06
	86	0.55	0.49	0.35	0.27	0.23	0.19	0.14	0.12	0.09	0.08	0.07
	87	17.7	0.63	0.50	0.46	0.31	0.24	0.22	0.14	0.12	0.11	0.07
	88	82.9	68.4	53.1	41.6	0.49	0.38	0.32	0.26	0.19	0.14	0.12
	89	121.5	124.3	110.8	97.4	94.1	97.0	78.7	66.7	35.7	37.9	25.2
	90	118.3	135.9	121.1	123.8	120.0	124.2	123.5	116.1	120.3	129.9	125.7

(a) 8-element array.

M=16		SNR (dB)										
		20	**22**	**24**	**26**	**28**	**30**	**32**	**34**	**36**	**38**	**40**
	85	0.15	0.12	0.11	0.10	0.08	0.07	0.06	0.06	0.06	0.06	0.05
	86	0.22	0.19	0.13	0.11	0.09	0.07	0.06	0.07	0.06	0.06	0.05
	87	0.26	0.23	0.16	0.13	0.12	0.08	0.07	0.06	0.03	0.03	0
	88	0.37	0.28	0.22	0.22	0.17	0.16	0.11	0.10	0.08	0.07	0.06
	89	89.0	82.9	69.1	66.8	47.2	18.2	14.4	0.15	0.13	0.12	0.07
	90	136.3	123.6	127.9	134.5	131.8	124.6	119.0	115.5	127.9	134.4	120.2

(b) 16-element array.

4.2.2 PE Error Using MANG and Mathematical Model

In this section, the PE RMSE from the MC simulation is compared with the PE RMSE of the developed mathematical model (MM) in section 3.1.3. The PE errors for MC simulation and MM for various emitter positions are listed in Table 4. The results of MM show that low AOA error results in low PE error. At any emitter range, the lowest PE error is observed at 45° bearing due to lower AOA error at this bearing than other emitter bearings. It can also be seen from the results that the PE error increases with the increase in emitter range.

PE error results from MC simulation listed in Table 4 follows the same trend as the MM results, that is PE error increases with the increase in AOA error and range. MC simulation gives higher PE errors than MM at most of the emitter positions. Absolute difference of MC and MM PE errors is large for shorter ranges and lower bearings. The large difference is due to the AOA error being either negative or positive in MC result while the absolute value of AOA error is considered in MM results. High unacceptable PE error occurs at emitter position of 50 km and 90° bearing. The actual AOAs at each GRS for this location are

above 88°. SNR value at 50 km range is 20 dB as seen in Figure 6(c). AOAs above 88° at SNR below 32 dB give high AOA errors as seen in Table 3. High AOA errors consecutively result in high PE errors and the emitter at this location cannot be detected, creating a blind spot for the system.

Table 4: PE RMSE for MC simulation and mathematical model MM.

No.	Emitter position		Position error (km)		Absolute difference
			$M = 16$		$M = 16$
	Range (km)	Bearing (^{0})	MC	MM	MC/MM
1	20	0	0.37	0.02	16.27
2		30	0.01	0.01	0.98
3		45	0.19	0.01	22.65
4		60	0.02	0.01	1.25
5		90	0.02	0.02	0.85
6	25	0	0.18	0.01	20.8
7		30	0.33	0.03	10.8
8		45	0.03	0.01	29.8
9		60	0.18	0.03	5.60
10		90	0.05	0.06	0.90
11	30	0	0.06	0.03	2.20
12		30	0.31	0.02	13.70
13		45	0.02	0.02	0.90
14		60	0.23	0.02	11.90
15		90	0.11	0.07	1.60
16	40	0	0.12	0.04	3.00
17		30	0.26	0.03	7.90
18		45	0.31	0.01	45.10
19		60	0.20	0.03	6.20
20		90	0.45	0.16	2.90
21	50	0	0.37	0.04	10.60
22		30	0.17	0.03	4.90
23		45	0.13	0.03	4.10
24		60	0.15	0.04	3.80
25		90	x	x	x

4.3 MLAT Results

In this section, the PE accuracy of the TDOA based lateration algorithm in Section 3.2 is presented. Using MC simulation, the relationship between PD estimation error, SNR and emitter position are determined. Figure 7 shows PD estimation error versus SNR.

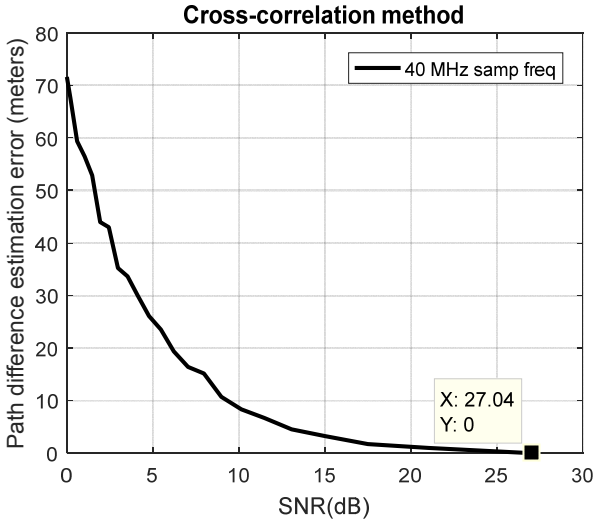

Figure 7: PD estimation error versus SNR.

From Figure 7, the PD estimation error is zero for SNR values greater or equal to 27 dB. This means that if the effective received SNR between signal pairs is 27 dB or more, the TDOA estimation error is zero. With reference to the PD estimation error and SNR relationship in Figure 7, it can be concluded from Figure 6 that the TDOA estimation error for all signal pairs is zero for emitters within the range of 0 to 22 km. This is because the minimum SNR is 27 dB at a range of 22 km and it increases as the range decreases from 22 to 1 km. From the received SNR, the PD estimation error is determined and its effect on the PE error of the lateration algorithm in Section 3.2 is determined. Figure 8 show the PE RMSE for emitters within the ranges of 0 to 50 km, bearings of 0 to 90^0 at altitude of 400 ft. The PE RMSE depends on the emitter position. It increases with increase of range from 0 to 50 km, but is constant with increase of bearing from 1 to 89^0. At emitter bearing of 0^0 and 90^0, the lateration algorithm fails to estimate the emitter position. Along these bearings, a zero PD measurement results in infinite coefficients in the plane equation in Equation 23, making it unsolvable. For altitude estimation, the RMSE within the selected emitter coverage is high at carrier frequency of 10 GHz to allow emitter locating in 3D.

At emitter position with ranges within 0 and 22 km, the PE RMSE is supposed to be zero but it is not the case as shown in Figure 8. This is due to the bias in the PE process introduced by the lateration algorithm, which has been said to be one of its limitations. Another factor that contributes to the PE error is the condition number of the plane equation that is linked with the emitter positions. High condition number means high PE error even at low TDOA error values. The condition number varies with emitter position. Emitter positions with bearings within 1 to 15^0 and 75 to 91^0 have high condition numbers value, which results in high PE RMSE. The PE RMSE of MLAT can be improved by choosing the appropriate reference stations for the TDOA estimation and lateration process. Further improvements can be made by using the generalised cross-correlation approach (Knapp & Carter, 1976) to estimate the TDOA and increase the separation of the GRS.

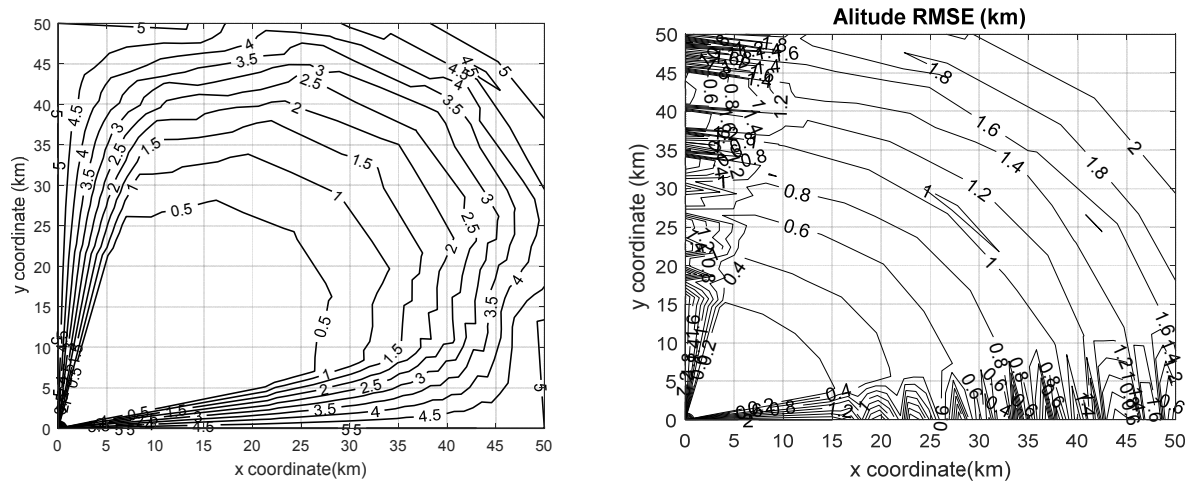

(a) **(b)**

Figure 8: PE RMSE for emitter position within 50 km range and one quadrant (bearing of 0^0 to 90^0): (a) Horizontal RMSE (b) Altitude RMSE.

4.4 Comparison between MLAT and MANG

Once the performance of each of the methods is evaluated, the next step is to compare both MLAT and MANG under the same conditions, as defined in Section 4.1. The PE RMSE for MLAT and MANG is compared at selected emitter positions. Three carrier frequencies are considered: 2.4, 5.8 and 10 GHz.

Table 5 shows the PE RMSE comparison between the MLAT and MANG systems. At bearings of 0, 30 and 45° irrespective of the range, the change in carrier frequency has no significant effect on the PE RMSE for MANG system. However, at bearings of 60 and 90°, the PE RMSE varies with carrier frequency. The emitter at bearing of 90° and 50 km range is detectable at carrier frequencies of 2.4 and 5.8 GHz as no blind spot is shown in Table 5 at this position. This is because the SNR value at this position is higher for carrier frequencies of 2.4 and 5.8 GHz, as shown in Figure 6. For MLAT, at constant emitter range and bearing, the PE RMSE increases with carrier frequency. At emitter range of 40 km and bearing of 45°, the PE RMSE for carrier frequencies of 2.4, 5.8 and 10 GHz are 0, 0.25 and 0.57 km respectively.

For a given carrier frequency and emitter position, MLAT has lower PE RMSE at emitter range lower than 30 km, while MANG performs better at higher emitter range of greater than is 30 km. For instance, at carrier frequency of 10 GHz and emitter position with range of 25 km and bearing of 30°, the PE RMSE for MLAT and MANG are 0.12 and 0.33 km respectively. Increasing the emitter range to 50 km at a given bearing and carrier frequency, the PE RMSE for MLAT and MANG are 1.62 and 0.17 km respectively. On the average, irrespective of the carrier frequency, MLAT performs better at lower range while MANG performs better at higher range.

Table 5 : PE RMSE for MANG and MLAT for carrier frequencies of 2.4, 5.8 and 10 GHz (Columns marked with x means it is not possible to estimate the emitter position).

No.	Emitter position			PE RMSE (km)					
	Range (km)	Bearing (^{o})	Altitude (km)	2.4 GHz		5.8 GHz		10 GHz	
				MANG	MLAT	MANG	MLAT	MANG	MLAT
1	20	0	0.12	0.38	x	0.38	x	0.37	x
2		30		0.01	0	0.01	0	0.01	0
3		45		0.19	0	0.20	0	0.19	0
4		60		0.01	0	0.12	0	0.02	0
5		90		0.12	x	0.06	x	0.02	x
6	25	0		0.18	x	0.18	x	0.18	x
7		30		0.47	0	0.45	0	0.33	0.12
8		45		0.03	0	0.03	0	0.03	0.10
9		60		0.43	0	0.35	0	0.18	0.12
10		90		0.14	x	0.06	x	0.05	x
11	30	0		0.06	x	0.06	x	0.06	x
12		30		0.26	0	0.29	0	0.30	0.22
13		45		0.47	0	0.29	0	0.02	0.20
14		60		0.29	0	0.30	0	0.27	0.24
15		90		0.05	x	0.08	x	0.11	x
16	40	0		0.22	x	0.22	x	0.12	x
17		30		0.41	0	0.30	0.27	0.26	0.70
18		45		0.31	0	0.31	0.25	0.31	0.57
19		60		0.23	0	0.17	0.27	0.20	0.73
20		90		0.11	x	0.18	x	0.45	x
21	50	0		0.39	x	0.39	x	0.37	x
22		30		0.19	0	0.19	0.64	0.17	1.62
23		45		0.13	0	0.09	0.54	0.13	1.38
24		60		0.12	0	0.12	0.65	0.15	1.69
25		90		0.22	x	0.63	x	x	x

One of the advantages of emitter locating using MLAT over MANG is the ability to estimate the altitude of the airborne emitter. Table 6 shows the altitude estimation error of MLAT at selected emitter positions with the selected carrier frequencies. Similar to the horizontal position, the altitude error depends on the emitter carrier frequency and position. The error is the same irrespective of the bearing but changes with range and carrier frequency. For instance, for emitter position with range of 40 km at bearing of 45^0, the altitude errors at carrier frequencies of 5.8 and 10 GHz are 0.70 and 1.11 km respectively. Increasing the emitter range to 50 km at a given bearing, the altitude errors are 1.00 and 1.55 km for carrier frequencies of 5.8 and 10 GHz respectively. Comparing the altitude error with the actual emitter altitude, which is 0.12 km at carrier frequencies of 5.8 and 10 GHz, the altitude error is high, making the estimated altitude of MLAT invalid to locate the emitter. From the results obtained, it is only possible to estimate the altitude of the emitter at 2.4 GHz for up to 50 km.

Table 6: Altitude estimation error for MLAT for carrier frequencies of 2.4, 5.8 and 10 GHz (Columns marked with x means it is not possible to estimate the emitter position).

No.	Emitter position			Altitude RMSE (km)		
	Range (km)	Bearing (^{o})	Altitude (km)	2.4 GHz	5.8 GHz	10 GHz
1	20	0	0.12	x	x	
2		30		0	0	0.34
3		45		0	0	0.34
4		60		0	0	0.34
5		90		x	x	x
6	25	0		x	x	x
7		30		0	0	0.50
8		45		0	0	0.50
9		60		0	0	0.50
10		90		x	x	x
11	30	0		x	x	x
12		30		0	0.45	0.64
13		45		0	0.45	0.64
14		60		0	0.45	0.64
15		90		x	x	x
16	40	0		x	x	x
17		30		0	0.70	1.11
18		45		0	0.70	1.11
19		60		0	0.70	1.11
20		90		x	x	x
21	50	0		x	x	x
22		30		0	1.00	1.55
23		45		0	1.00	1.55
24		60		0	1.00	1.55
25		90		x	x	x

5. CONCLUSION

The emitter locating system detects the target from its emission, which is used for locating, navigation and communications. The signal is obtained by spatially located receivers and the position is estimated either by the MANG or MLAT techniques. Between the two methods, MLAT has the advantage of PE in 3D. MC simulation is used to verify both methods, and the transmitter and receiver parameters are selected based on current practices. For PE in the horizontal position, MLAT provides lower RMSE at ranges less than 30 km while MANG performs better at lower RMSE at ranges greater than 30 km for up to 50 km. In general, the RMSE increases with frequency due to the expected path attenuation. Error free altitude estimation is possible for 2.4 GHz for MLAT for up to 50 km. However, this is not possible for the higher frequencies that were selected at 5.8 and 10 GHz respectively. The findings of this study considered the current generation of LPI radar and the possible communications signal types used by low level airborne targets. Both methods should provide better PE for older generation airborne targets where the peak power used in radar is much higher.

ACKNOWLEDGEMENT

The authors would like to thank Universiti Teknologi Malaysia (UTM) under project Vot No. Q.J130000.7823.4F188 and the Ministry of Higher Education (MOHE), Malaysia for providing the resources for this research.

REFERENCES

Ahmad, A.A., & Sha'ameri, A.Z. (2015). Classification of airborne radar signals based on pulse feature estimation using time-frequency analysis. *Defence S&T Tech. Bull.*, **19**: 103–120.

Northrop Grumman (2017). *AN/APG-81 AESA Radar*. Available online at:
http://www.northropgrumman.com/Capabilities/ANAPG81AESARadar/Pages/default.aspx (Last access date: 24 August 2017).

Anton, H. & Rorres, C. (2010). *Elementary Linear Algebra, 10th Ed.*. Wiley and Sons, New York.

Anwar Baig, N. & Bilal Malik, M. (2013). Comparison of direction of arrival (DOA) estimation techniques for closely spaced targets. *Int. J. Future Comp. Commun.*, **2**: 654–659.

Bucher, R. & Misra, D. (2002). A synthesizable VHDL model of the exact solution for three-dimensional hyperbolic positioning system. *VLSI Des.*, **15**: 507–520.

Chaitanya, D.E., Kumar, M.N.V.S.S., Rao, G.S. & Goswami, R. (2015). Convergence issues of taylor series method in determining unknown target location using hyperbolic multilateration. *2014 Int. Conf. Sci. Eng. Manage. Res. (ICSEMR 2014)*, pp. 1–4.

Chowdary, G.P. (2016). Performance comparison of various DOA estimation techniques based on antenna parameter. *Int. J Rev Electr Commun. Eng.*, **4**: 15–19.

Dhope, T.S. (2015). *Cognitive Radio Networks Optimization with Spectrum Sensing Algorithms*. River Publisher, Aalborg, Denmark.

Dou, H., Lei, Q., Li, W. & Xing, Q. (2015). A new TDOA estimation method in Three-satellite interference localisation. *Int. J. Electr.*, **102**: 839–854.

Galati, G., Leonardi, M., Balbastre-Tejedor, J.V. & Mantilla-Gaviria, I.I.A. (2014). Time-difference-of-arrival regularised location estimator for multilateration systems. *IET Radar, Sonar Navigation*, **8**: 479–489.

ICAO (International Civil Aviation Organization) (2011). *Unmanned Aircraft Systems*. *Cir 328 AN/190*, *Vol. 23*. International Civil Aviation Organization, Montreal.

Knapp, C. & Carter, G. (1976). The generalized correlation method for estimation of time delay. *IEEE T. Acoust., Speech Signal Proc.*, **24**: 320–327.

Mantilla-Gaviria, I.A., Leonardi, M., Galati, G. & Balbastre-Tejedor, J.V. (2015). Localization algorithms for multilateration (MLAT) systems in airport surface surveillance. *Signal, Image Video Proc.*, **9**: 1549–1558.

MCMC (Malaysian Communications & Multimedia Commision) (2015). *Notice: Use Of Frequencies For Unmanned Aircraft Systems*. Available online at:
https://www.mcmc.gov.my/media/announcements/notice-use-of-frequencies-for-unmanned-aircraft-s (Last access date: 24 August 2017).

Mondal, D.K. (2013). Studies of different direction of arrival (DOA) estimation algorithm for smart antenna in wireless communication. *Int. J. Electr. Commun. Tech.*, **4**: 43–47.

Neven, W.H.L., T.J. Quilter, Weedon, R., & Hogendoorn, R.A. (2014). *Wide Area Multilateration*. Report on EATMP TRS 131/04 Version 1.1, Eurocontrol, Brussels.

Pace, P. E. (2009). *Detecting and Classifying Low Probability of Intercept Radar*, *2nd Ed*. Norwood: Artech House. Norwood, Massachusetts.

Ritchie, M., Fioranelli, F., Griffiths, H. & Torvik, B. (2015). Micro-drone RCS analysis. *2015 IEEE Radar Conf. Proc.*, **6**: 452–456.

Yaro, A.S & Sha'meri, A.Z. (2016). Mathematical model of position estimation error for a

multiangulation system. *6th Int. Graduate Conf. Eng., Sci. Humanity: Empowering Innovat. Entrepreneurship Sustain. Dev.*, pp. 134–136.
Schleher, D.C. (2006). LPI radar: Fact or fiction. *IEEE Aero. Electr. Syst. Mag.*, **21**: 3–6.
Sha'meri, A.Z & Shehu, Y. (2015). Performance analysis of a minimum configuration multilateration system for airborne emitter position estimation. *Defence S&T Tech. Bull.*, **8**: 27–41.
So, H.C. (2012). Source localization: algorithms and analysis. In *Handbook of Position Location: Theory, Practice, and Advances*. John Wiley & Sons, Inc. Hoboken, New Jersey, pp. 25–66.
Systems, G. (2016). *Direction of Arrival Estimation (DOA) in Interference & Multipath Propagation*. Available online at: http:// http://www.girdsystems.com/pdf/GIRD_Systems_DOA_Multipath.pdf (Last access date: 24 August 2017)
Torbati, F.H.., Atashbar, M., Norouzi, Y. & Hojjat, K.F. (2013). Multireference TDOA-based source localization. *Turk. J. Electr. Eng. Comp. Sci.*, **21**: 1920–1929.
Melvin, W.L., & Scheer, A.J. (2013). *Principles of Modern Radar Vol. II: Advanced Techniques*. Institution of Engineering and Technology, Stevenage, UK.
Wahab, M., Saputera, Y.P., Adhi, P., & Wahyu, Y. (2017). Development of Indonesian low probability of intercept (LPI) radar system. *Defence S&T Tech. Bull.*, **10**: 150–159.
Waweru, N.P., Konditi, D.B. & Langat, P.K. (2014). Performance analysis of MUSIC, root-MUSIC and ESPRIT DOA estimation algorithm. *Int. J. Electr., Comp., Energetic, Electr. Commun. Eng.,* **8**: 209–216.

PREDICTION OF SCINTILLATION AND SIGNAL QUALITY ON GPS L2 BAND

Ho Yih Hwa* & Emad Fathi Mohamed Aon

Centre for Telecommunication Research & Innovation, Faculty of Electronic & Computer Engineering, Universiti Teknikal Malaysia Melaka (UTeM), Malaysia

*Email: yihhwa@utem.edu.my

ABSTRACT

The propagated wireless signals along the Global Navigation Satellite System (GNSS) channels are affected by ionospheric electron density irregularities. Therefore, GNSS signals may experience amplitude and phase fluctuations. The GNSS ionospheric scintillation and Total Electron Content (TEC) Monitor (GISTM) receiver is installed at Universiti Teknikal Malaysia Melaka (UTeM), Malaysia (2.3139°N, 102.3183°E) for the purpose of monitoring ionospheric scintillation and Total Electron Content (TEC) variations. In this study, Global Positioning System (GPS) ionospheric scintillations are investigated for dual frequency L1 (1.57542 GHz) and L2C (1.2276 GHz). The data of GPS ionospheric scintillation and TEC variations is collected during the 24th solar maximum from 2013 to 2014. This proposed period is very important due to increasing solar activity directly affected the GPS link performance. Mathematical models for scintillation index S4(L2C) and carrier-to-noise ratio C/N_0(L2C) are statistically proposed based on the collected data for different levels of ionospheric scintillation. This enables the prediction of the scintillation and C/N_0 of L2 when only L1 information is available. This is particularly important because of only L1 scintillation historical information is available before 2012.

Keywords: *Global Positioning System (GPS); ionosphere; scintillation; solar maximum; nonlinear regression (NLR).*

1. INTRODUCTION

Satellite communication is one of the most important and useful technologies that have ever been developed. This technology is used in many business applications, because it makes things go quite easier without wasting time. Many commercial communication services can be offered by satellite communication like voice services and data transfer services. The advantages of such communication system are high quality data transfer with reduced cost comparison to other technologies (Kolawole, 2013).

The Global Positioning System (GPS) is the most famous navigation system among the Global Navigation Satellite Systems (GNSSs), since it operates well under any weather condition with high accuracy and does not require a subscription fee. Ionospheric scintillation induces rapid fluctuations in the phase and amplitude of received GPS signals. These rapid fluctuations or scintillation potentially introduce cycle slips, degrade range measurements, and if severe enough, lead to loss of lock in phase and code. This phenomenon is particularly important in the equatorial region, where the scintillations activities are considered maximum. GPS scintillations at low latitudes are primarily associated with equatorial spread F, which is caused by scattering from ionospheric irregularities. Equatorial ionosphere is a region comprising two ionisation belts located approximately $\pm 15°$ on the magnetic equator, where scintillation activities are maximum. Malaysia is located in this region, and thus, GPS ionospheric scintillation and availability are observed and studied during solar maximums in this location (Hassan *et al*., 2002; Aon *et al*., 2017). In the last decade, many work have done on the L band ionospheric effects in Malaysia using GNSS receiver networks in TEC analysis (Ho *et al*.,

2001, 2002; Zain *et al*., 2002, 2005; Mardina *et al*., 2009), ionosphere F3 layer studies (Zain *et al*., 2008) and scintillation studies (Ho *et al*., 2013, 2014).

There is a relationship between GPS ionospheric scintillation variations and total electron content (TEC) variations, where both of them degrade the GPS signals (Jain *et al*., 2011). Solar activity also has direct impact on the two parameters, since increasing of solar activities result in increase of TEC variations, which then lead to increase of GPS ionospheric scintillations (Conker *et al*., 2000). This problem increases during the solar maximum, which directly decreases GPS system performance (Aon *et al.,* 2015). As a result, the solar maximum for any solar cycle must be considered (Devasia & Ravindran, 2006). In this study, the solar maximum of the 24th solar cycle (2009 – 2019) is considered. The Global Ionospheric Scintillation Model (GISM) was used to compute the amplitude scintillation parameter for each GPS satellite visible from Melaka, Malaysia (2^0 14' N, 102^0 16' E) as its location has strong equatorial scintillation behavior. The availability of GPS at the solar maximum at the equatorial region must be studied to estimate the effect of ionospheric scintillation on the availability during this period and at this region (Aon *et al.,* 2014).

This study is aimed at developing the mathematical models for the ionospheric scintillation index *S4* and carrier-to-noise ratio (C/N_0) based on the collected data during the 24th solar maximum. The correlation between the L1 scintillation and L2 scintillation were investigated. A mathematical model is proposed to predict the L2 scintillation based on the L1 scintillation covering different levels of the scintillation from weak to strong scintillation events. This is important because of all the historical scintillation data are only based on L1 band.

2. METHODOLOGY

2.1 Experimental Setup

Figure 1 shows the experimental setup to measure and analyse GPS ionospheric scintillation. The dataset used for this study is collected at Universiti Teknikal Malaysia Melaka (UTeM), Malaysia (2.3139° N, 102.3183° E), which is located at the region of equatorial anomaly. The data is measured using a scintillation monitor that is part of the GPStation-6 GISTM Receiver. The GISTM has a graphical user interface (GUI) that allows for easy access to the receiver's many features without the need to use a terminal emulator or custom software. The multiband GNSS antenna is used to track various GPS satellites signals along the proposed period. The GPStation-6 receiver collects data of ionosphere scintillations, information of GPS signals and TEC variations. The collected data is then analysed and used to derive a mathematical model of the ionospheric scintillation.

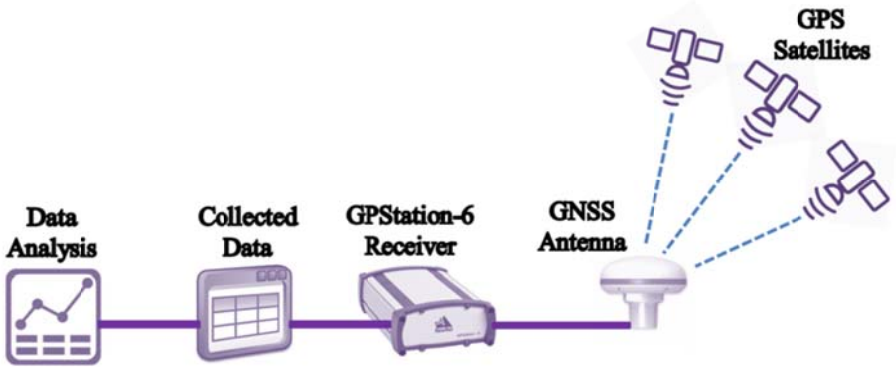

Figure 1: Experimental setup.

The antenna of the GPS receiver is located at the top of the building, as shown in Figure 2, to avoid multipath. Multipath effects appear even at small elevation angles, so the analysis of ionospheric scintillation will be considered at elevation angles that are greater than 30° (Aon *et al*., 2014). This

project considers all the available GPS satellites (with pseudo random numbers (PRNs) PRN01 – PRN32) at dual frequency L1 / L2C. The data is used for the analysis of the ionospheric scintillation effects on the GPS system during period of 2013 –2014, which has been considered as the rising phase of the maximum solar activity that produces increasing ionospheric scintillation.

Figure 2 GPS antenna located on top of the building to avoid the multipath.

2.2 Mathematical Modelling

The amplitude scintillation *S4* index is defined as the standard deviation of the detrended signal intensity by normalisation. The S4 index is calculated as (Tanna & Pathak, 2014):

$$S4 = \sqrt{{S4_t}^2 - {S4_N}^2} \tag{1}$$

where the amplitude scintillation recorded by the GPStation-6 receiver has two parameters: total scintillation $S4_t$ and total scintillation due to the ambient noise $S4_N$. $S4_t$ is recorded over a 60 s interval in real-time but includes the effect of ambient noise, while the corrected *S4* was calculated by removing the ambient noise.

Past related studies (Carrano *et al*., 2012) did not use the measured values of the *S4* at the frequency band of L2C to analyse the ionospheric scintillation at this band *S4*(*L2*). These studies just estimated *S4*(*L2*) from *S4*(*L1*) using different estimated methods such as (Carrano *et al*., 2014):

$$\begin{aligned} S4(L2) &= S4(L1) \cdot \left(\frac{f_1}{f_2}\right)^{n} \quad ; n \approx 1.5 \\ S4(L2) &= S4(L1) \cdot \left(\frac{f_1}{f_2}\right)^{1.5} = 1.454\ S4(L1) \end{aligned} \tag{2}$$

where this relationship is estimated based on the frequencies f_1 and f_2 of the L1 and L2 respectively bands.

This study determines a mathematical model based on the collected data during the proposed period. This model is more realistic and has less error as compared to Carrano's model. This is proven when the proposed model is validated later in this section.

The collected data (with a total number of samples of N_T) is divided to two parts:

1. Most of the data with a number of samples of $N_S \approx N_T$ that is applied to drive the equation of the proposed mathematical model. This part has the most collected data to propose a mathematical model covering different situations along the solar maximum cycle. The nonlinear regression (NLR) method is used in this derivation.
2. Some other data (different from the first part of the data) that has number of samples of $N_O \ll N_S$. This part is used to check the validity of the proposed mathematical model using different data that is different from the first part of the data.

The NLR almost generates a best relationship between a single independent variable x and a single dependent variable y. This relationship can be described by an equation that includes one or more parameters, such as y_o, a, and b constants in a second order polynomial $y = y_o + a\,.\,x + b\,.\,x^2$. The NLR method fits the data and determines values of the parameters that minimise the sum of the squares of the distances of the data points to the fitted curve. In another expression, the NLR fits the data until it get a lowest root mean square error (RMSE), which is calculated as:

$$RMSE = \sqrt{mean\left(\left(S4_{ms}(L2) - S4_{pr}(L2)\right)^2\right)} \tag{3}$$

where $S4_{ms}(L2)$ is the measured *S4* index at the L2 frequency band, and $S4_{pr}(L2)$ is the predicted *S4* index using the nonlinear regression.

The mathematical model of carrier-to-noise ratio (C/N_0) is also estimated by the same algorithm. For the mathematical model of *S4*, the proposed mathematical model is compared with Carrano's model for the *S4* index (Carrano *et al*., 2014).

3. RESULTS & DISCUSSION

If *S4*(*L2*) is considered as a dependent variable and represented by *Y*, and *S4*(*L1*) is considered as an independent variable and represented by *X*, the mathematical model determined by NLR to get the second order polynomial as:

$$Y = 0.0325 + 0.6779 * X - 0.0633 * X^2 \tag{4}$$

where *Y* is *S4*(*L2*) and *X* is *S4*(*L1*).

The RMSE for this model is 0.0523, which indicates a good value according to its scales in the *x*- and *y*- axes as shown in Figure 3.

The proposed model (Equation 4) for *S4*(*L2*) is validated with other different data (second part of the collected data). The measured (collected) data {$S4_{ms}(L1)$, $S4_{ms}(L2)$} of this part is compared with the predicted data {$S4_{ms}(L1)$, $S4_{pr}(L2)$} that is estimated by the proposed mathematical model. The model validation is done for GPS PRNs of 31, 27, 15, and 7, as shown in Figure 4 a-d, with predicted RMSE of 0.0514, 0.0570, 0.0415 and 0.0566 respectively.

The model is further validated with different categories of scintillation as (Seif *et al*., 2012):

$S4 > 0.4$	(strong scintillation)
$0.2 \leq S4 \leq 0.4$	(moderate scintillation)
$S4 < 0.2$	(weak scintillation)

as shown in Figure 5 for low scintillation, Figure 6 for moderate scintillation, and Figure 7 for strong scintillation. Table 1 summarises the predicted RMSE values for the scintillation categories.

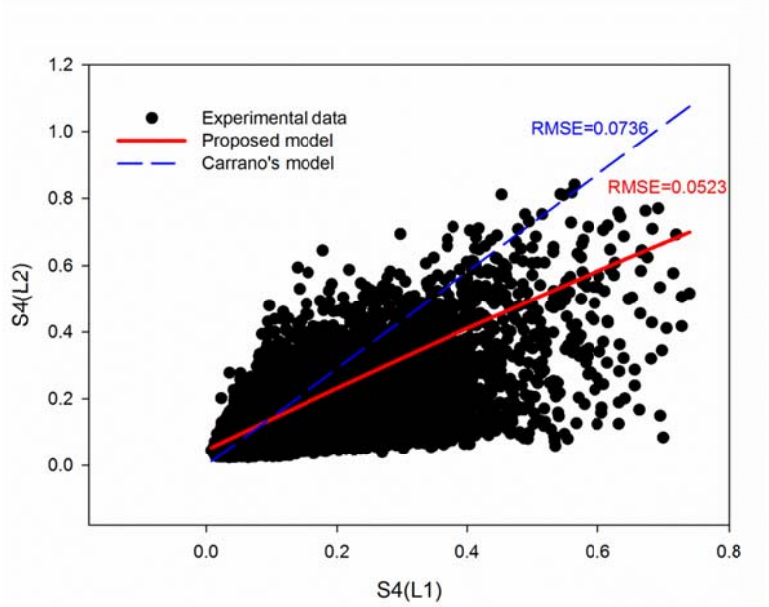

Figure 3: Comparison of the mathematical model with the experimental data.

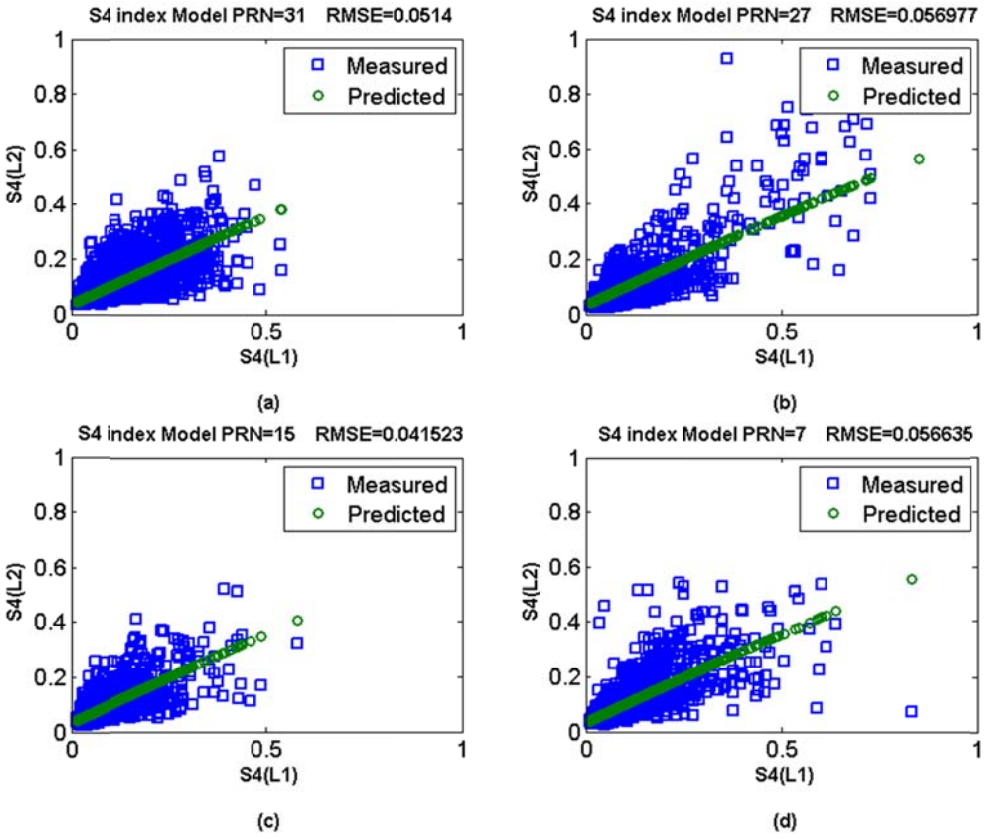

Figure 4: Validation of the proposed model on different GPS PRNs.

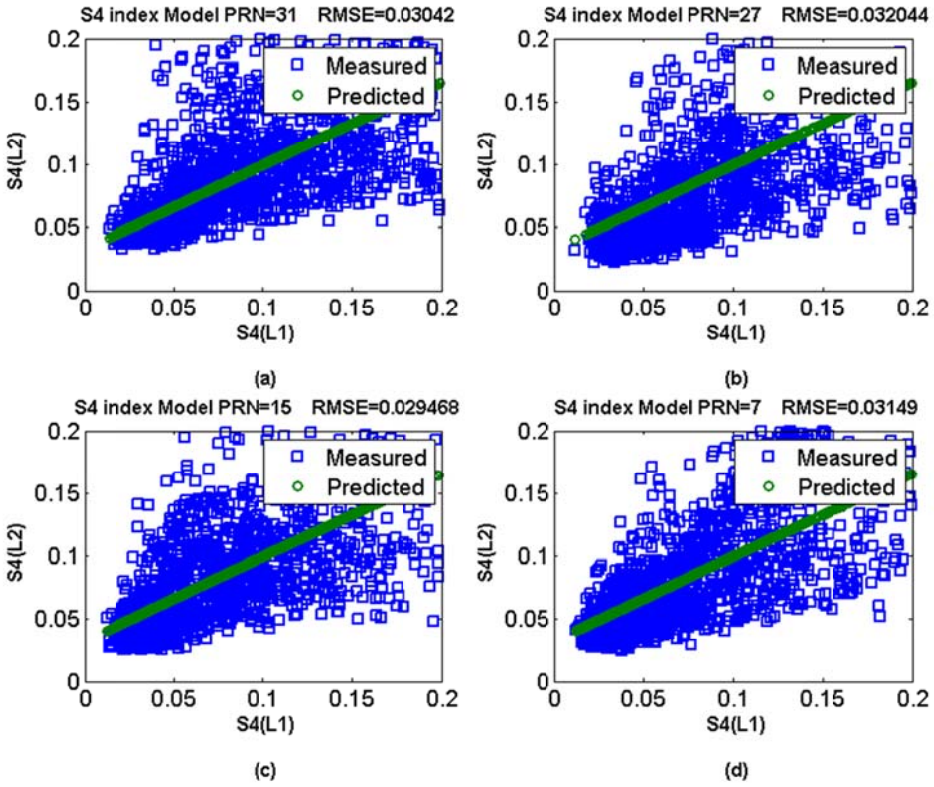

Figure 5: Validation of the proposed model only on the low *S4* levels.

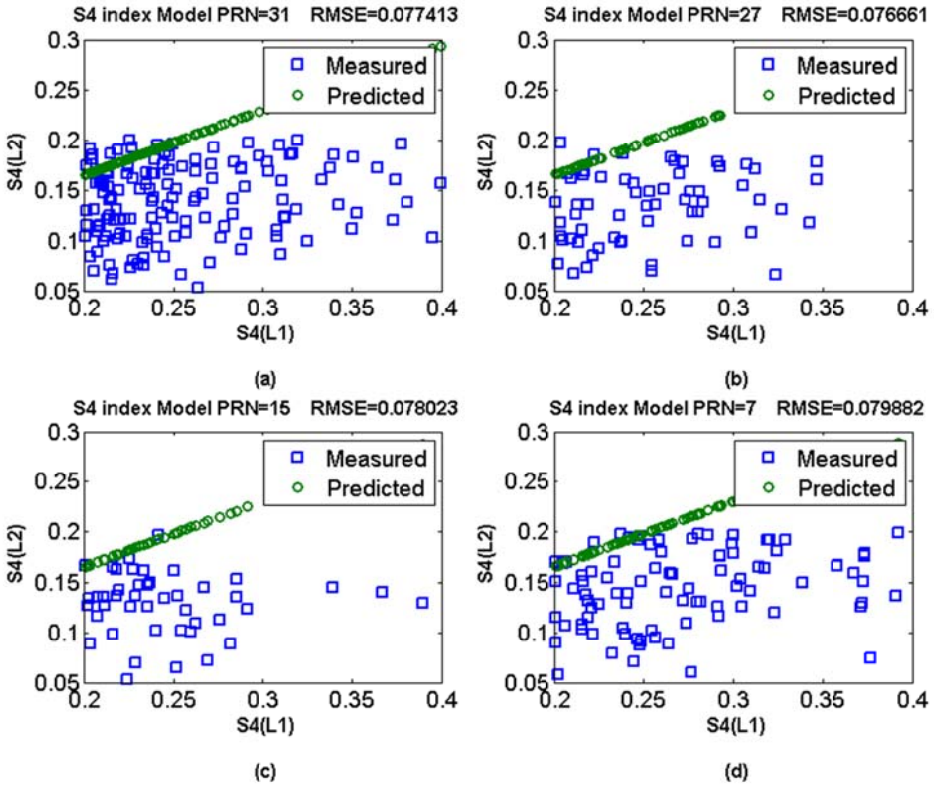

Figure 6: Validation of the proposed model only on the moderate *S4* levels.

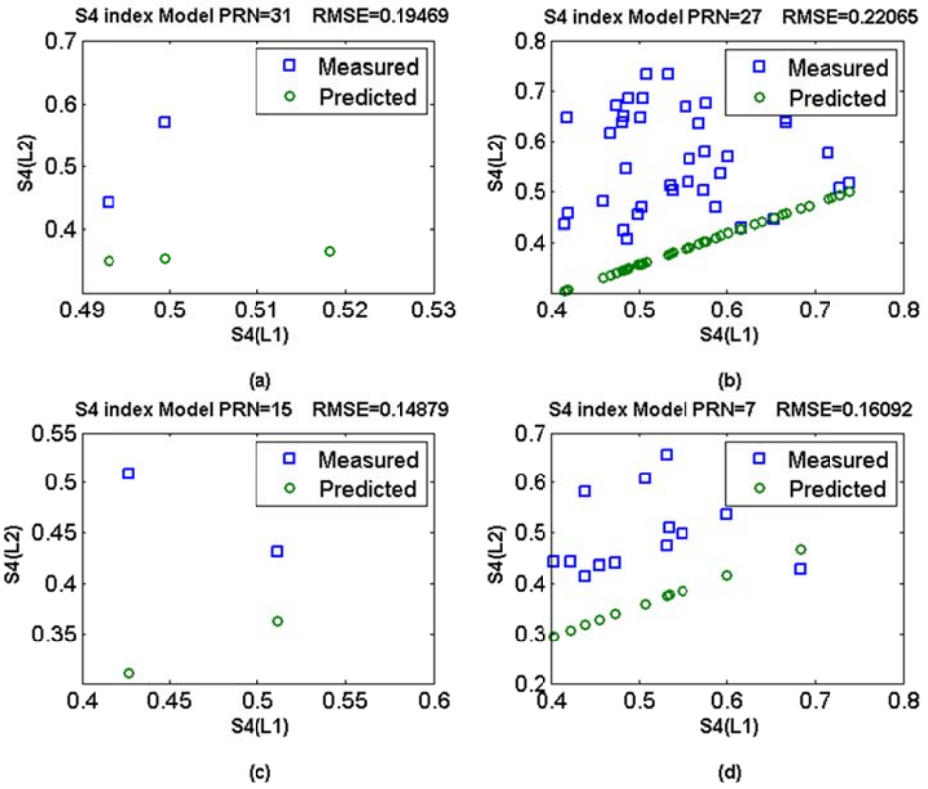

Figure 7: Validation of the proposed model only on the strong *S4* levels.

Table 1: The predicted RMSE values for different GPS PRNs for different levels of S4 index.

GPS PRN#	RMSE		
	Low scintillation	Moderate scintillation	Strong scintillation
31	0.030420	0.077413	0.149469
27	0.032044	0.076661	0.220650
15	0.029468	0.078023	0.148790
07	0.031490	0.079882	0.160920

It is clear that the proposed mathematical model is applicable for all levels of ionospheric scintillation. Since this model is estimated from the collected data that mostly are low and moderate scintillation levels, it is more reliable for these scintillation levels. The collected data are mostly in these two levels because the elevation angle of the GPS receiver is 30º.

As shown in Figure 7, the proposed mathematical model is not so reliable for strong scintillation levels. As the predicted RMSE is almost greater than the proposed RMSE, a special mathematical model can be proposed for strong scintillations. The mathematical model for strong levels of *S4*(*L2*) is defined as a second order polynomial using the following equation:

$$Y = -0.0323 + 1.8922 * X - 1.4311 * X^2 \quad (5)$$

where $Y = S4(L2)$, and $X = S4(L1)$.

The proposed model for strong scintillation is further validated, with the results shown in Figure 8.

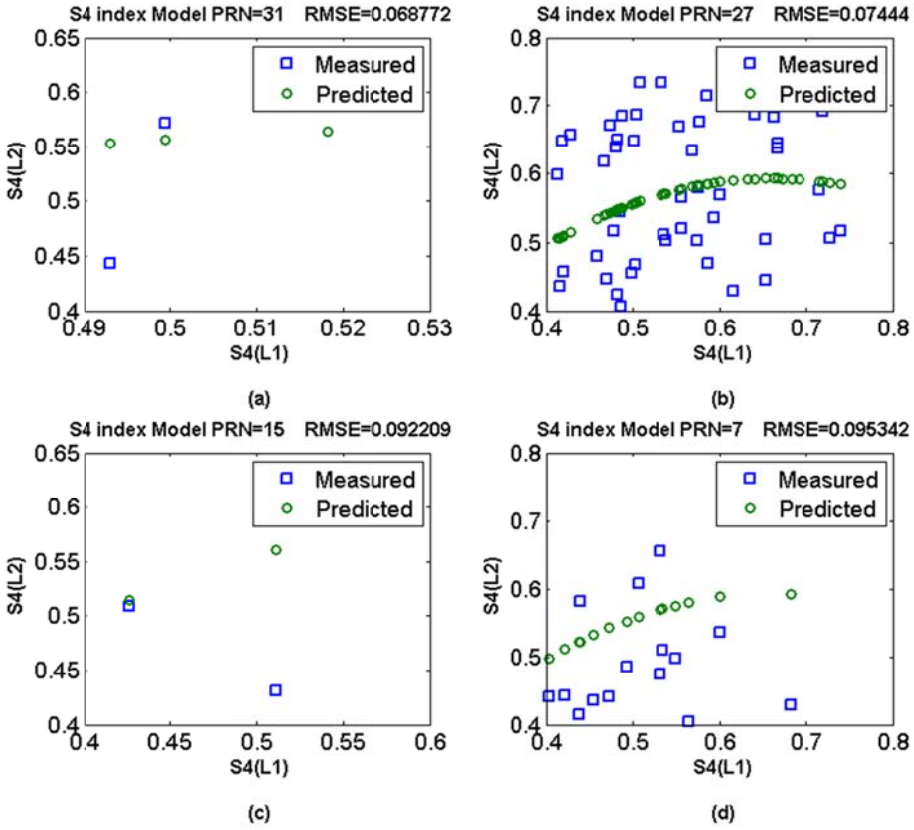

Figure 8: Validation of the proposed strong scintillation model.

In addition, the proposed mathematical model is validated with previous Carrano's model as shown in Figure 9, where the proposed model shows the lowest RMSE.

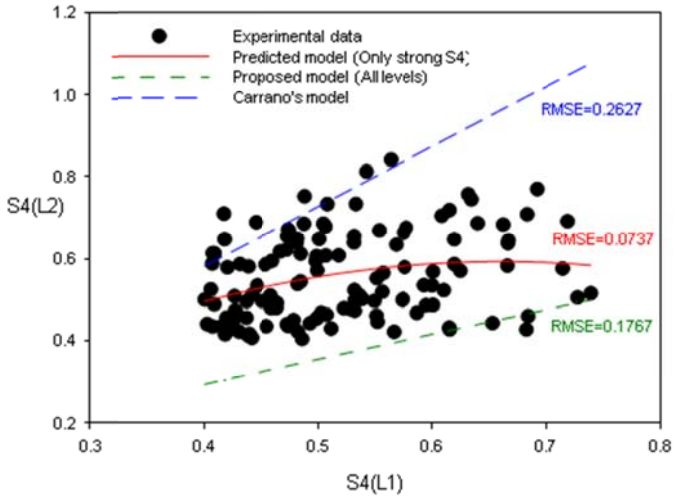

Figure 9: Validation of the proposed model for the strong *S4* levels by comparing to Coronna's model.

The predicted C/N_0 for L2C from the C/N_0 (CNR) for L1 can be modelled using the same algorithm, but the collected data is $\{CNR(L1),\ CNR(L2)\}$. In this case, $Y = CNR_2 = CNR(L2) and\ X = CNR_1 = CNR(L1)$. This model is estimated as:

$$CNR_2 = 127.8395 - 4.3103\,CNR_1 + 0.0537\,CNR_1^2 \quad (6)$$

where CNR_2 is the C/N_0 ratio for L2 and CNR_1 is the C/N_0 ratio for L1; both in dB/Hz. The estimated RMSE for this proposed model is 1.6067, as shown in Figure 10. The validation of the C/N_0 mathematical model is done using GPS PRNs of 31, 27, 15, and 7, as shown in Figure 11.

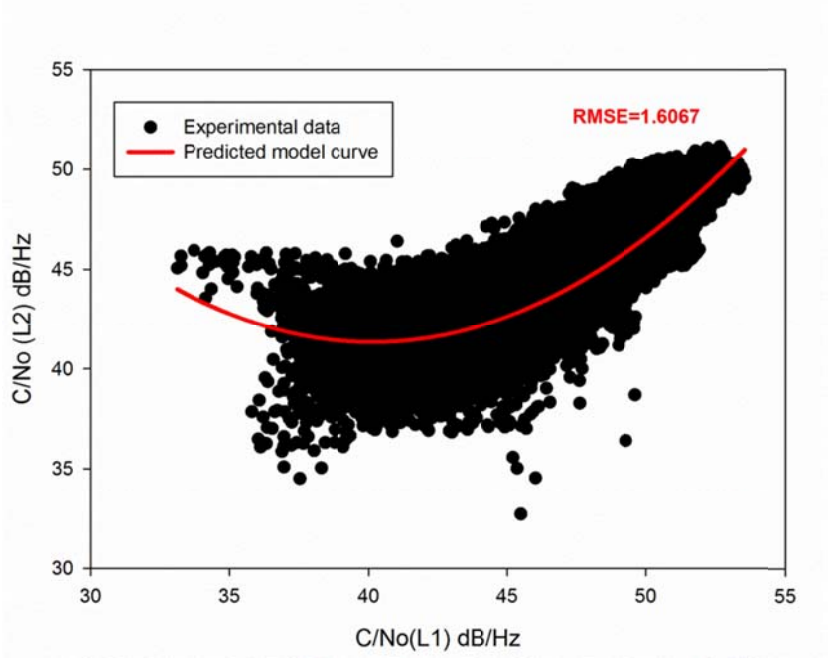

Figure 10: The proposed mathematical model for C/N_0.

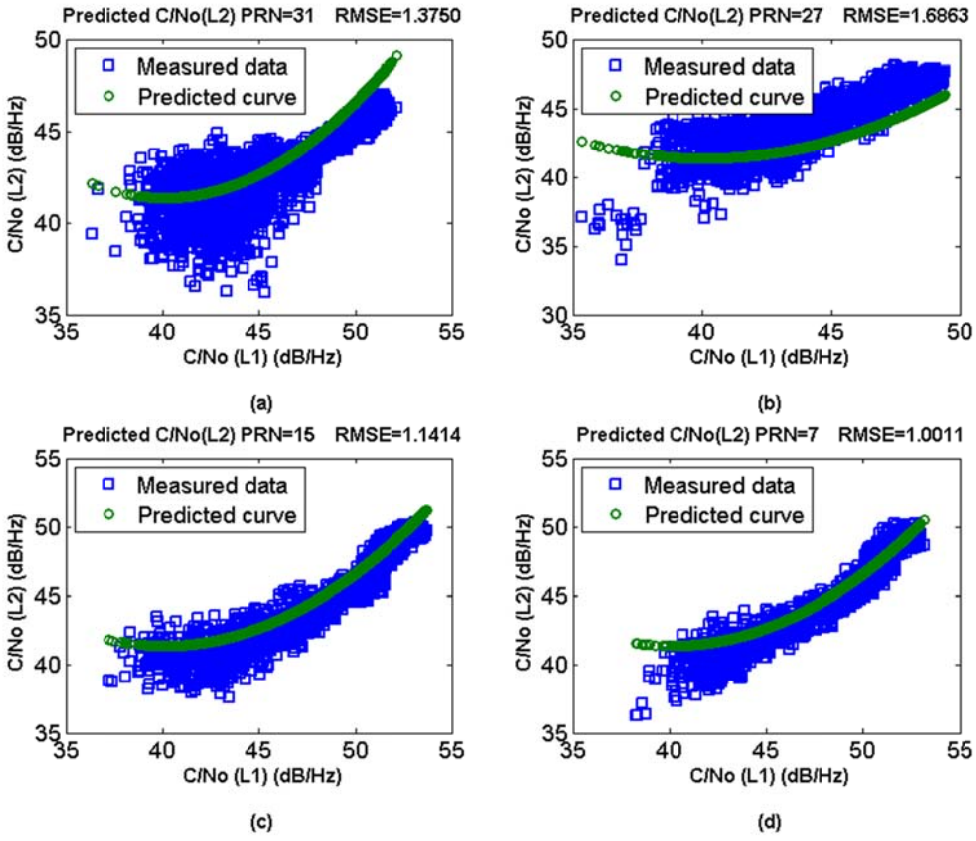

Figure 11: Validity of the C/No proposed model on different GPS PRNs.

4. CONCLUSION

In this paper, a scintillation model was introduced that predicts the *S4* index for the L2 band from *S4* index for the L1 band based on the collected data. Another model was also proposed to predict C/N_0 for the L2 band from the C/N_0 for the L1 band. Both models are particularly important for some researchers where L2 scintillation and C/N_0 can be predicted using L1 scintillation data and C/N_0 even when dual frequency scintillation monitoring is not available. By having this, L2 scintillation can be predicted for modernised GPS L2C signals based on historical L1 scintillation data.

ACKNOWLEDGEMENT

The authors would like to acknowledge the support of this work by Ministry of Higher Education Malaysia and Universiti Teknikal Malaysia Melaka (UTeM) on research grant FRGS/2012/FKEKK/SG02/02/1/F00125 and FRGS (RACE)/2012/FKEKK/SG02?02/01/F00150.

REFERENCES

Abdullah, M., Zain, A.F.M., Ho, Y.H. & Abdullah, S. (2009). TEC and scintillation study of equatorial ionosphere: A month campaign over Sipitang and Parit Raja stations, Malaysia. *Am. J. Eng. Appl. Sci*., **2**: 44-49.

Aon, E.F., Othman, A.R. & Ho, Y.H. (2017). Study of GPS scintillation during solar maximum at Malaysia. *Int. J. Inform. Commun. Tech.*, **10:**299-307.

Aon, E.F., Othman, A.R., Ho, Y.H. & Shaddad, R.Q. (2014). Analysis of GPS link ionospheric scintillation during solar maximum at UTeM, Malaysia. *Proc. 2014 IEEE 2nd Int. Symp. Telecommun. Tech. (ISTT2014),* Langkawi, Malaysia, pp. 84 - 87.

Carrano, C.S., Groves, K.M., McNeil, W.J. & Doherty, P.H. (2012). Scintillation characteristics across the GPS frequency band. *Proc. 2012 Inst. Navigation ION GNSS Meet.*, Nashville, Tennessee.

Carrano, C., Groves, K., Delay, S., & Doherty, P. (2014). An Inverse diffraction technique for scaling measurements of ionospheric scintillations on the GPS L1, L2, and L5 carriers to other frequencies. *Proc. 2014 Inst. Navigation ION ITM Meet*., San Diego, California.

Conker, R., El-Arini, M., Hegarty, C. & Hsiao, T. (2000). Modeling the effects of ionospheric scintillation on GPS/SBAS availability. *Proc. Int. Assoc. Inst. Navigation (IAIN) 25th Anniversary World Cong.*, California.

Devasia, C. & Ravindran, S. (2006). The role of post□sunset vertical drifts at the equator in predicting the onset of VHF scintillations during high and low sunspot activity years., *Ann. Geophys*., **24**: 1609 - 1616.

Hassan, W.S.W., Zain, A.F.M., Ramli A.G., Ho, Y.H., & Abdullah, M. (2002) Studies on equatorial total electron content near solar maximum activity from 1998–2000. *General Assembly Union Radio Sci. Int.*, Maastricht, Netherlands.

Ho, Y.H., Abdullah, S. & Mokhtar, M.H. (2014). Global Positioning System (GPS) positioning errors during ionospheric scintillation Event. *J. Tek.*, **69**: 33 - 38.

Ho, Y.H., Zain A.F.M. & Abdullah, M. (2001) Hourly variations total electron content (TEC) for quiet ionosphere over Malaysia. *Proc. Annual Workshop National Sci. Fellowship (NSF) 2001*, pp. 77-79.

Ho, Y.H., Zain, A.F.M, Abdullah, M., Ramli, A.B. & Hassan, W.S.W. (2002) Equatorial TEC variations during the Geomagnetic Storm of July 15–17, 2000. *General Assembly Union Radio Sci. Int.*, Maastricht, Netherlands.

Jain, A., Tiwari, S., Jain, S. & Gwal, A.K. (2011). Nighttime enhancements in TEC near the crest of northern equatorial ionization anomaly during low solar activity period. *Indian J. Phys.*, , **85**:: 1367 - 1380.

Kolawole, M.O. (2013). *Satellite Communication Engineering*. CRC Press. US.

Shanmugam, S., Jones, J., MacAulay, A. & Dierendonck, A.J. (2012). Evolution to modernized GNSS ionospheric scintillation and TEC monitoring. *Proc. IEEE/ION PLANS 2012*, Myrtle Beach, South Carolina.

Tanna, H.J. & Pathak, K.N. (2014). Multiracial behavior of the ionospheric scintillation index time series over an Indian low latitude station Surat. *J. Atmos. Solar-Terrestrial Physic.*, **109**: 66 - 74.

Zain, A.F.M., Ho, Y.H. & Abdullah, M. (2002). Enabling GPS technology on Equatorial Ionosphere monitoring during geomagnetic storm of July 15- 17, 2000, *15th Int. Tech. Meet. Satellite Division Inst. Navigation*. Portland, Oregon.

Zain, A.F.M., Ho, Y.H., Abdullah, M., Rhazali, Z.A., Abdullah, S. & Marsimin, M.F. (2005). First ionospheric experimental campaign and observation at Fraser's Hill, Malaysia: total electron content (TEC) and scintillation measurements. *2005 Asia-Pacific Conf. Appl. Electromagn.*. Malaysia.

Zain, A.F.M., Abdullah, S., Homam, M.J., Seman, F.C., Abdullah, M. & Ho, Y.H. (2008). Observations of the F3-layer at equatorial region during 2005, *J. Atmos. Sol. Terr. Phys.*, **70**: 918–925.

EVALUATION OF GLOBAL POSITIONING SYSTEM (GPS) ADJACENT BAND COMPATIBILITY VIA GPS SIMULATION

Dinesh Sathyamoorthy*, Zainal Fitry M Amin & Shahrudin Abu Hassan

Science & Technology Research Institute for Defence (STRIDE), Ministry of Defence, Malaysia

*Email: dinesh.sathyamoorthy@stride.gov.my

ABSTRACT

This study is aimed at evaluating adjacent radio frequency band power levels that can be tolerated by the Global Positioning System (GPS) L1 coarse acquisition (C/A) signal and the extent to which such power levels impact GPS performance. The study is conducted using GPS simulation, which allows for the tests to be held with various repeatable conditions, as defined by the authors. It is found that the factors that affect the level of disruption from adjacent band interference include GPS signal power level, and carrier frequency and bandwidth of interference signals. Decreasing power levels of the GPS signal decreases the power levels and increases the range of frequencies of interference signals that affect the GPS signal. As the carrier frequency of the interference signals moves away from the frequency of the GPS signal (1575.42 MHz), the power levels required to affect the GPS signal increase. Furthermore, increasing bandwidths of interference signals increase the power levels but increase the range of frequencies that can affect the GPS signal.

Keywords: Adjacent band compatibility; Global Positioning System (GPS) simulation; GPS L1 coarse acquisition (C/A) signal; estimate probable error (EPE); signal degradation and jamming.

1. INTRODUCTION

Jamming is defined as the broadcasting of a strong signal that overrides or obscures the signal being jammed (NAWCWD, 2013; Poisel, 2013; Adamy, 2015). Since Global Navigation Satellite System (GNSS) satellites, powered by photocells, are approximately 20,000 km above the Earth surface, GNSS signals that reach the Earth have very low power levels (approximately -160 to -130 dBm), rendering them highly susceptible to jamming (Dinesh, 2009; Jones, 2011; Last, 2016; Parkinson, 2016). For example, a simple 1 W battery-powered jammer can block the reception of GNSS signals approximately within a radius of 35 km from the jammer (Papadimitratos & Jovanovic, 2008; Borio *et al*., 2016). Given the various incidents of intentional and unintentional jamming of GNSS signals, including military GNSS signals (Adams, 2001; Jewell, 2007; Seo & Kim, 2013; Buesnel, 2016), the development of various GNSS anti-jamming technologies has received significant attention (Wilde & Willems, 2010; Jones, 2011; Sanou & Landry, 2013; Bar-Sever, 2016). In addition, many current GNSS receiver evaluations concentrate on radio frequency interference (RFI) operability (ION, 1997; Gautier, 2003; Boulton *et al*., 2011; Glomsvoll, 2014).

In previous studies conducted by the Science & Technology Research Institute for Defence (STRIDE), the effect of RFI on Global Positioning System (GPS) performance was studied using fields evaluations (Dinesh *et al*., 2009, 2010a, b; Ahmad Norhisyam *et al*., 2013a, b) and GPS simulation (Dinesh *et al*., 2012, 2014a). These studies focused on in-band interference, whereby the interference signals occur in the bandwidth of the GPS L1 coarse acquisition (C/A) signal, which is an unencrypted civilian GPS signal widely used by various GPS receivers. The signal has a fundamental frequency of 1,575.42 MHz, and a code structure that modulates the signal over a 2 MHz bandwidth (DOD, 2001; Kaplan & Hegarty, 2006; USACE, 2011).

Adjacent band signals at frequencies close to the GPS signal bandwidth can also disrupt the performance of GPS receivers, in particular those that incorporate poor filtering design to achieve a low-cost product. Every signal, even though it operates in a specific portion of the spectrum, introduces interference into adjacent portions of the spectrum. The amount of interference that is permissible to seep over into adjacent spectrums is controlled in many countries by their respective communications commissions, but it is not possible to eliminate it completely. The higher the transmission power used, the higher the interferences will be in adjacent portions of the spectrum. The number of systems that make use of the radio frequency spectrum has significantly increased in recent years and the number of users increases daily. This development has crowded the radio frequency spectrum significantly, resulting in increased occurrences of adjacent band interferences for GPS receivers (de Bakker, 2007; Powell, 2013; Seybold, 2014). To this end, various studies have been conducted to evaluate GPS adjacent band compatibility, with the aim of developing new GPS spectrum interference standards to ensure that future proposals for use of spectrum bands adjacent to GPS signals will not compromise GPS performance, in particular for vital applications such as public safety, navigation and time synchronisation (Boulton *et al*., 2011; Powell, 2013; Van Dyke, 2016; Zdunek, 2016).

This study is aimed at evaluating adjacent radio frequency band power levels that can be tolerated by the GPS L1 C/A signal and the extent to which such power levels impact GPS performance. It will be conducted using GPS simulation, which will allow for the tests to be held with various repeatable conditions, as defined by the authors. As the tests are conducted in controlled laboratory environments, they will not be inhibited by unintended signal interferences and obstructions (Aloi *et al*., 2007; Kou & Zhang, 2011; Pozzobon *et al*., 2013). In our previous studies, in addition to RFI, GPS simulation was used to evaluate the vulnerabilities of GPS to multipath (Dinesh *et al*., 2013, 2014b), GPS satellite clock error (Dinesh *et al*., 2015a), varying speeds (Dinesh *et al*., 2015b), power consumption (Dinesh *et al*., 2016) and GPS antenna orientation (Dinesh *et al*., 2017).

2. METHODOLOGY

The apparatus used in the study are an Aeroflex GPSG-1000 GPS simulator (Aeroflex, 2010), an Advantest U3751 spectrum analyser (Advantest, 2009), an IFR 2023B signal generator (IFR, 1999), a Hyperlog 60180 directional antenna (Aaronia, 2009) and a notebook running GPS Diagnostics v1.05 (CNET, 2004). The study is conducted in STRIDE's semi-anechoic chamber (A. Faridz, 2010) to avoid external interferences signals and multipath errors. The test setup employed is as shown in Figure 1. The tests are conducted on a Garmin GPSmap 60CSx handheld GPS receiver (Garmin, 2007). Simulated GPS signals are generated using the GPS simulator and transmitted via the coupler, while interference signals are generated using the signal generator and transmitted via the directional antenna. The following assumptions are made for the tests:

i) No ionospheric or troposheric delays
ii) No clock and ephemeris error
iii) No multipath fading or unintended obstructions
iv) No unintended interference signals.

The date of simulation is set at 10 October 2016. The almanac data for the period is downloaded from the US Coast Guard's web site (USCG, 2016), and imported into the GPS simulator. This study is conducted for GPS signal power levels of -130, -135, -140 and -145 dBm. The test procedure is conducted for coordinated universal time (UTC) of 0000 at Kajang, Selangor, Malaysia (N 2° 58', E 101° 48').

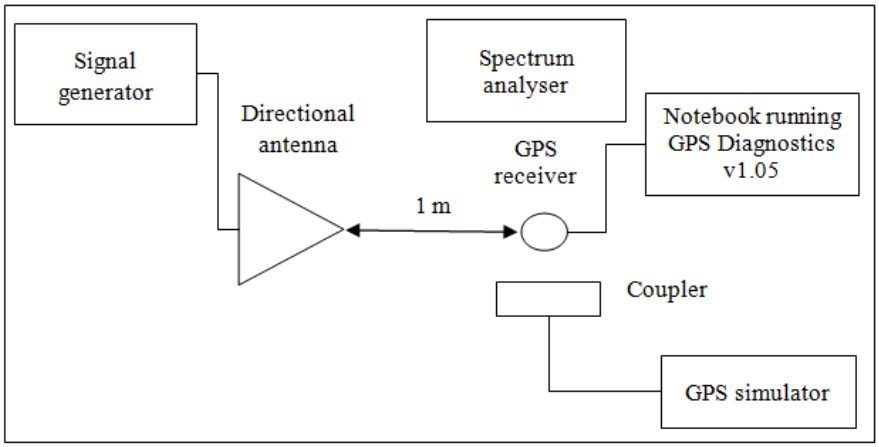

Figure 1: The test setup employed for the study.

Once a location fix is obtained with the GPS receiver, the estimate probable error (EPE) is recorded using GPS Diagnostics. The interference signal used is a frequency modulated (FM) signal with information frequency of 5 kHz, with bandwidths of 2, 5, 10 and 20 MHz used. The carrier frequency is varied from 1,475 to 1,675 MHz at intervals of 5 MHz. Interference signal transmission is started at power level of -140 dBm. The power level is increased by increments of 3 dBm and the corresponding EPE values are recorded.

3. RESULTS & DISCUSSION

For the tests conducted, the power levels at which the first degradation of accuracy is noticed and the location fix is lost are shown in Figures 2 and 3 respectively. It is observed that with decreasing power levels of the GPS signal, the power levels of interference signals required to degrade and jam the GPS signals decrease, and the range of frequencies of interference signals that affect the GPS signal increase. This is as decreasing GPS signal power level results in reduced carrier-to-noise density (C/N_0) levels for GPS satellites tracked by the receivers, which is the ratio of received GPS signal power level to noise density. Lower C/N_0 levels result in increased data bit error rate when extracting navigation data from GPS signals, and hence, increased carrier and code tracking loop jitter. This, in turn, results in more noisy range measurements and thus, the GPS signal is more susceptible to interference (DOD, 2001; Kaplan & Hegarty, 2006; Petovello, 2009; USACE, 2011).

It is found that as the carrier frequency of the interference signal moves away from the frequency of the GPS L1 C/A signal (1575.42 MHz), the power levels required to affect the GPS signal increase. Furthermore, increasing bandwidth of interference signals increases the range of frequencies that can affect GPS signal. However, the power levels that affect GPS signal increase, as the interference signal's strength is dispersed over a wider bandwidth.

It is observed that the interference signal power levels required to affect the GPS signal are significantly high as compared to the corresponding GPS signal power levels. The noise-like C/A code structure, which modulates the L1 signal over a 2 MHz bandwidth, allows for the signal to be received at low levels of interferences. The P(Y) code (restricted to the US military) has a more robust structure, modulating the L1 and L2 signals over 20 MHz bandwidths, and has better resistance to interference. The absence of other error parameters, including ionospheric and tropospheric delays, satellite clock, ephemeris and multipath errors, and unintentional signal interferences and obstructions, resulted in the required minimum jamming power levels in this study to be significantly higher as compared to field evaluations conducted in Dinesh *et al*. (2009a, 2010a,b) and Ahmad Norhisyam *et al*. (2013a, b).

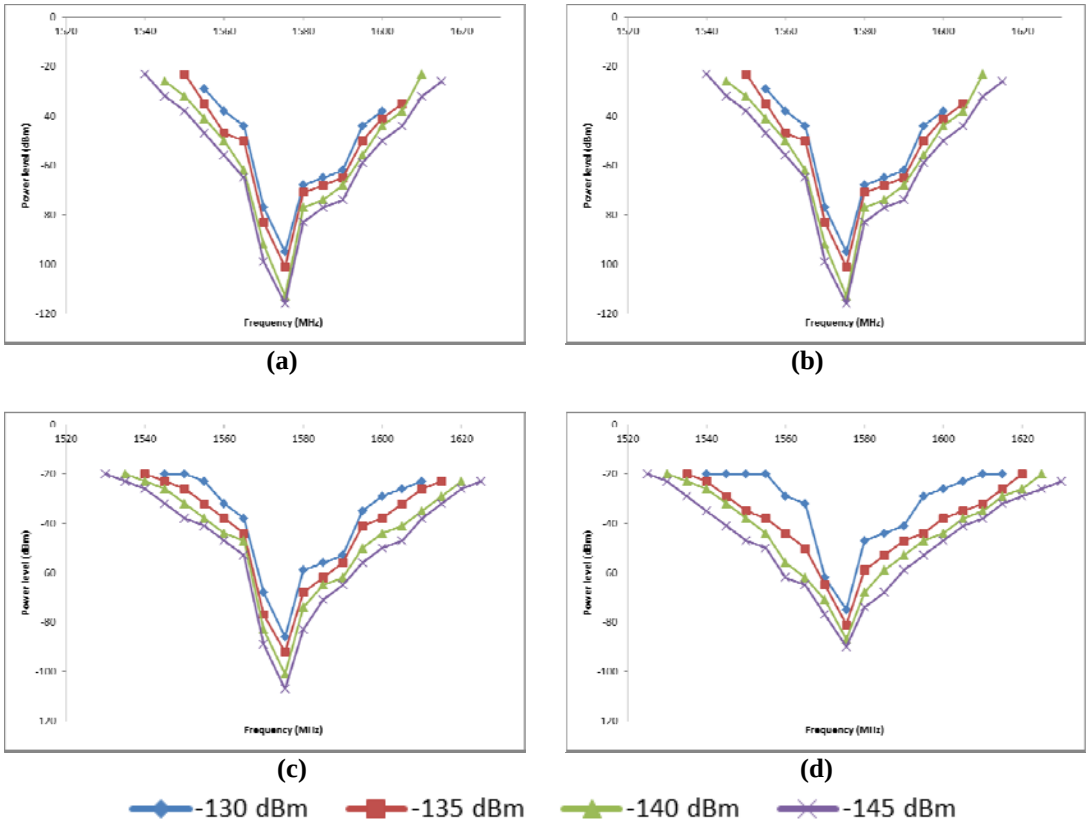

Figure 2: Interference signal power levels at which first degradation of accuracy is noticed for interference signal bandwidths of: (a) 2 MHz (b) 5 MHz (c) 10 MHz (d) 20 MHz.

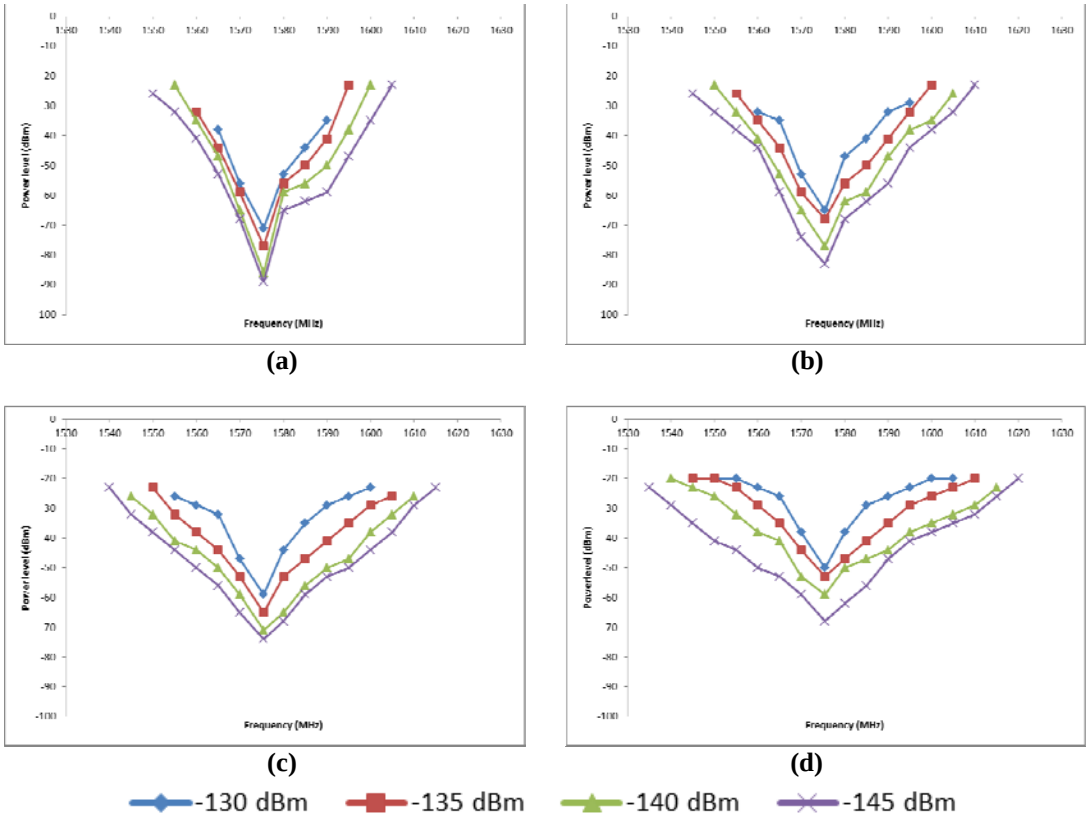

Figure 3: Interference signal power levels at which location fix is lost for interference signal bandwidths of: (a) 2 MHz (b) 5 MHz (c) 10 MHz (d) 20 MHz.

It should be noted that the tests conducted in this study were for only one GPS receiver. Additional tests using a wider range of GPS receivers are needed to further validate the findings of this study. Furthermore, a limitation faced in this study was that the GPS simulator used only allows the transmission of the GPS L1 C/A signal. The proposed future work is for the procurement of a GNSS simulator that will allow transmission of other GPS signals, in particular L2C and L5, along with signals of other GNSS systems (GLONASS, BeiDou and Galileo).

4. CONCLUSION

This study has demonstrated that the GPS L1 C/A signal is susceptible to adjacent band interference. Factors that affect the level of disruption include GPS signal power level, and carrier frequency and bandwidth of interference signals. Decreasing power levels of the GPS signal decreases the power levels and increases the range of frequencies of interference signals that affect the GPS signal. As the carrier frequency of the interference signals moves away from the frequency of the GPS signal (1575.42 MHz), the power levels required to affect the GPS signal increase. Furthermore, increasing bandwidths of interference signals increase the power levels but increase the range of frequencies that can affect the GPS signal. Further studies are required using a wider range of GPS signals, in particular L2C and L5, as well as other GNSS systems, in order to develop appropriate GNSS spectrum interference standards.

REFERENCES

A. Faridz, A.G., M. Razali, M.Y. & W. Salwa, W.H. (2010). STRIDE's 3 meters EMC semi-anechoic chamber: Design considerations and compliance to standards. *2010 IEEE Asia-Pacific Conf. Appl. Electromagnetics (APACE 2010)*, 9-11 November 2010, Port Dickson, Negeri Sembilan, Malaysia.

Adams, T.K. (2001). GPS vulnerabilities. *Mil. Rev.*, **1**: 10-16.

Adamy, D.L. (2015). *Electronic Warfare Against a New Generation of Threats*. Artech House, Boston.

Advantest (2009). *U3741/3751 Spectrum Analyzers*. Advantest Corporation, Chiyoda-ku, Tokyo.

Aeroflex (2010). *Avionics GPSG-1000 GPS / Galileo Portable Positional Simulator*. Aeroflex Inc., Plainview, New York.

Ahmad Norhisyam, I., Dinesh, S. & Azman, M.S., 2013. Effect of radio frequency interference (RFI) on the performance of Global Positioning System (GPS) static observations. *9th IEEE Colloq. Signal Process. Appl. (CSPA 2013)*, 8-10 March 2013, Kuala Lumpur.

Ahmad Norhisyam, I., Dinesh, S. & Azman, M.S., 2013. Effect of radio frequency interference (RFI) on the precision of GPS relative positioning, *8th Int. Symp. Digital Earth 2013 (ISDE 2013)*, 26-29 August 2013, Kuching, Sarawak.

Aloi, D.N., Alsliety, M. & Akos, D.M. (2007). A methodology for the evaluation of a GPS receiver performance in telematics applications. *IEEE T. Instrum. Meas.*, **56**: 11-24.

Bar-Sever, Y. (2016). Networks for robust civil signal performance monitoring & RFI detection. *17th Space-Based PNT Advisory Board Meet.*, 18-19 May 2016, National Harbor, Maryland.

Borio, D., Dovis, F., Kuusniemi, H. & Lo Presti (2016). Impact and detection of GNSS jammers on consumer grade satellite navigation receivers. *Proc. IEEE*, **104**: 1233-1245.

Boulton, P., Borsato, R., Butler, B. & Judge, K. (2011). GPS interference testing: Lab, live, and LightSquared. *Inside GNSS*, **5**: 32-45.

Buesnel, G. (2016). *GPS Jamming Incident at Cairo Airport Highlights Growing Risks to Navigation Systems*. Available online at: https://www.linkedin.com/pulse/gps-jamming-incident-cairo-airport-highlights-growing-guy-buesnel (Last access date: 9 September 2016).

CNET (2004). *GPSDiag 1.0*. Available online at:

http://download.cnet.com/GPSDiag/3000-2130_4-4951103.html (Last access date: 31 January 2010).

de Bakker, P.F. (2007). *Effects of Radio Frequency Interference on GNSS Receiver Output*. Master's thesis, Delft University of Technology, Delft, Netherlands.

Dinesh, S. (2009). Vulnerabilities of civilian Global Navigation Satellite Systems (GNSS) signals: A review. *Defence S&T Tech. Bull.*, **2**: 100-114.

Dinesh, S., Wan Mustafa, W.H., Mohd Faudzi, M., Kamarulzaman, M., Nor Irza Shakhira, B., Siti Robiah, A., Norhayaty, Z., Aliah, I., Lim, B.T., Arumugam, P., Zainal Fitry, M.A., Mohd Rizal, A.K., Azlina, B. & Mohd. Hasrol, H.M.Y. (2009). Evaluation of the effect of radio frequency interference (RFI) on Global Positioning System (GPS) receivers. *Defence S&T Tech. Bull.*, **2**: 115-129.

Dinesh, S., Wan Mustafa, W.H., Mohd Faudzi, M., Kamarulzaman, M., Hasniza, H., Nor Irza Shakhira, B., Siti Robiah, A., Shalini, S., Jamilah, J., Aliah, I., Lim, B.T., Zainal Fitry, M.A., Mohd Rizal, A.K., Azlina, B. & Mohd Hasrol, H.M.Y. (2010a). Evaluation of power levels required by interference signals at various distances to jam the Global Positioning System (GPS) L1 coarse acquisition (C/A) signal. *Defence S&T Tech. Bull.*, **3**: 14-28.

Dinesh , S., Wan Mustafa, W.H., Mohd Faudzi., M., Kamarulzaman, M., Hasniza, H., Nor Irza Shakhira, B., Siti Robiah, A., Shalini, S., Jamilah, J., Aliah, I., Lim, B.T., Zainal Fitry, M.A., Mohd. Rizal, A.K., Azlina, B. & Mohd. Hasrol, H.M.Y. (2010b). Evaluation of the effect of radio frequency interference (RFI) on Global Positioning System (GPS) accuracy. *Defence S&T Tech. Bull.*, **3**: 100-118.

Dinesh, S, Mohd Faudzi, M. & Zainal Fitry, M.A. (2012). Evaluation of the effect of radio frequency interference (RFI) on Global Positioning System (GPS) accuracy via GPS simulation. *Defence. Sci. J.*, **62**: 338-347.

Dinesh, S., Shalini, S., Zainal Fitry, M.A. & Siti Zainun, A. (2013). Evaluation of the repeatability of Global Positioning System (GPS) performance with respect to GPS satellite orbital passes. *Defence S&T Tech. Bull.*, **6**: 130-140.

Dinesh, S., Mohd Faudzi, M., Rafidah, M., Nor Irza Shakhira, B., Siti Robiah, A., Shalini, S., Aliah, I., Lim, B.T., Zainal Fitry, M.A., Mohd Rizal, A.K. & Mohd Hasrol Hisam, M.Y. (2014a). Evaluation of the effect of radio frequency interference (RFI) on Global Positioning System (GPS) receivers via GPS simulation. *ASM Sci. J.*,**8**: 11-20.

Dinesh, S., Shalini, S., Zainal Fitry, M.A., Siti Zainun, A., Siti Robiah, A., Mohd Idris, I. & Mohd Hasrol Hisam, M.Y. (2014b). Evaluation of the effect of commonly used materials on multipath propagation of Global Positioning System (GPS) signals via GPS simulation. *Adv. Mil. Tech.*, **9**: 81-95.

Dinesh, S., Shalini, S., Zainal Fitry, M.A., Asmariah, J. & Siti Zainun, A. (2015a). Evaluation of the effect of Global Positioning System (GPS) satellite clock error via GPS simulation. *Defence S&T Tech. Bull.*, **8**: 51-62.

Dinesh, S., Shalini, S., Zainal Fitry, M.A., Asmariah, J. & Siti Zainun, A. (2015b). Evaluation of the accuracy of Global Positioning System (GPS) speed measurement via GPS simulation. *Defence S&T Tech. Bull.*, **8**: 121-128.

Dinesh, S., Shalini, S., Zainal Fitry, M.A., Asmariah, J. & Siti Zainun, A. (2016). Evaluation of trade-off between Global Positioning System (GPS) accuracy and power saving from reduction of number of GPS receiver channels. Appl. Geomatics, **8**: 67-75.

Dinesh, S., Shalini, S., Zainal Fitry, M.A., Mohamad Firdaus, A., Asmariah, J. & Siti Zainun, A. (2017). Evaluation of the effect of Global Positioning System (GPS) antenna orientation on GPS performance. *Defence S&T Tech. Bull.*, **10**: 33-39.

DOD (Department of Defence) (2001). *Global Positioning System Standard Positioning Service Performance Standard, Command, Control, Communications, and Intelligence*. Department of Defence (DOD), Washington D.C.

Garmin (2007). *GPSmap 60CSx Owner's Manual*. Garmin International Inc., Olathe, Kansas.

Glomsvoll, O. (2014). *Jamming of GPS and GLONASS Signals: A Study of GPS Performance in Maritime Environments Under Jamming Conditions, and Benefits of Applying GLONASS in*

Northern Areas Under Such Conditions. Master's thesis, University of Nottingham, Nottingham.

Seo, J. & Kim, M. (2013). Loran in Korea: Current status and future plans. *Eur. Navig. Conf. (ENC 2013)*, 23–25 April 2013, Vienna, Austria.

Jewell, J. (2007). *GPS Insights: JNC Briefing on Jamming Incident.* Available online at: http://gpsworld.com/defensegps-insights-april-2007-8428 (Last access date: 9 September 2016).

Jones, M. (2011). The civilian battlefield: Protecting GNSS receivers from interference and jamming. Inside GNSS, 6(2), 40-49.

Kaplan, E.D. & Hegarty, C.J. (2006). *Understanding GPS: Principles and Applications*. Artech House, Norwood, Massachusetts.

Kou, Y. & Zhang, H. (2011). Verification testing of a multi-GNSS RF signal simulator. *Inside GNSS*, **6**: 52-61.

Last, D. (2016). GNSS vulnerability to jamming and spoofing. *Nordic Navigation Forum*, 2 February 2016, Bodø, Norway.

NAWCWD (Naval Air Warfare Center Weapons Division) (2013). *Electronic Warfare & Radar Systems Engineering Handbook.* Raleigh, North Carolina.

Papadimitratos, P. & Jovanovic, A. Protection and fundamental vulnerability of GNSS. *Int. Workshop Satell. Space Commun.* 2008 (IWSSC'08), France, 1-3 October 2008, Institut Supérieur de l'Aéronautique et de l'Espace (ISAE), Toulouse, France.

Parkinson, B. (2016). GPS spoofing & jamming: Uncovering vulnerability truths & myths. *17th Space-Based PNT Advisory Board Meet.*, 18-19 May 2016, National Harbor, Maryland.

Petovello, M. (2009). Carrier-to-noise density and AI for INS / GPS integration. *Inside GNSS*, **4**: 20-29.

Poisel, A.R. (2013). *Information Warfare and Electronic Warfare Systems*. Artech House, Boston.

Powell, T. (2013). *Adjacent Band Interference to Consumer Receivers*. The Aerospace Corporation, El Segundo, California.

Pozzobon, O., Sarto, C., Chiara, A.D., Pozzobon, A., Gamba, G., Crisci, M. & Ioannides, R. (2013). Developing a GNSS position and timing authentication testbed: GNSS vulnerability and mitigation techniques. *Inside GNSS*, **8**: 45-53.

Seybold, A.M. (2014). *Why LightSquared's Proposed System Will Interfere with GPS*. Available online at: http://www.fiercewireless.com/wireless/seybold-s-take-why-lightsquared-s-proposed-system-will-interfere-gps (Last access date: 8 September 2016).

Sanou, D.A. & Landry, R.J. (2013). Analysis of GNSS interference impact on society and evaluation of spectrum protection strategies. *Positioning*, **4**: 169-182.

USACE (US Army Corps of Engineers) (2011). *Engineer Manual EM 1110-1-1003: NAVSTAR Global Positioning System Surveying.* US Army Corps of Engineers (USACE), Washington D.C.

USCG (US Coast Guard) (2016). *GPS NANUs, Almanacs, & Ops Advisories*. Available online at: http://www.navcen.uscg.gov/?pageName=gpsAlmanacs (Last access date: 20 June 2016).

Van Dyke, K. (2016). GPS adjacent band compatibility (ABC) assessment. *17th Space-Based PNT Advisory Board Meet.*, 18-19 May 2016, National Harbor, Maryland.

Zdunek, K. (2016). GPS and adjacent band co-existence study: Summary of method and results. *17th Space-Based PNT Advisory Board Meet.*, 18-19 May 2016, National Harbor, Maryland.

ESTIMATION OF UPPER LIMB REAL DYNAMIC FORCE USING SURFACE ELECTROMYOGRAM (sEMG)

Shaiful Bahri Zainal Abidin[1,2,*], Wan Nor Izzati Wan Jusoh[1], Hasyatun Che-Nan[1], Wan Fadilah Wan Abdullah[2] & Gan Kok Beng[1]

[1]Department of Electrical, Electronic and Systems Engineering, Faculty of Engineering and Build Environment, University Kebangsaan Malaysia (UKM), Malaysia
[2]Instrumentation and Electronics Technology Division (BTIE), Science and Technology Research Institute for Defence (STRIDE), Malaysia

[*]Email: shaiful1400@yahoo.com

ABSTRACT

Understanding of the muscle characteristic mechanism involved in force generation is essential for researcher for professionals who work to improve and promote health. Surface electromyogram (sEMG) is one of the sensors that can monitor muscle characteristic. Thus, the objective of this study is to determine the relationship between sEMG signal and real dynamic force of the upper limb. Real dynamic force estimation using sEMG comprises of three main processes, which are sEMG signal data acquisition, sEMG features extraction and dynamic force validation. Muscle contraction activities was recorded using a high-performance and high-accuracy bio signal data acquisition system. Three types of upper limb muscles, which are triceps, biceps and upper brachioradialis, were involved in these measurements. Simultaneous measurements were conducted using the two types of sensors (dynamometer and sEMG) and were placed accordingly at the upper limb muscle to measure the signals at the same time domain. The sEMG signals were preprocessed using Butterworth filter (10–400 Hz), full-wave rectification, low-pass filtering (10-20 Hz) and rectification. The processed sEMG signals were compared with the conventional force sensor signals using statistical correlation test analysis. The results showed a similarity graph pattern between the sEMG signal and real dynamic force recorded using force sensor with a correlation value of 0.685.

Keywords: *Surface electromyogram (sEMG); real dynamic force estimation; feature extraction; dynamometer; biosignal amplifier.*

1. INTRODUCTION

Monitoring functional motor activities using wearable device technologies is one of the interesting fields in medical engineering applications. Motor activities can be monitored using electronic sensors, such as accelerometers, gyrometers, magnetometers and electromyograms, which are used to capture movements and muscle activity patterns and data. Wolf (1983) developed a wearable monitor that measures finger posture in order to record fine motor control tasks of hands and fingers involving manipulation of objects. This technology can be used to monitor the progress of fine motor control skills for post-stroke individuals undergoing rehabilitation. While the initial research in the area of wearable technologies was aimed at combining and integrating the existing miniature sensors with special fabrics or wireless technology, recent advanced research in this field has been focused on the development of sensing elements that can be even more easily embedded into wearable devices (Rodgers *et al*., 2003).

Recently, researchers have been fascinated by the use of the surface electromyogram (sEMG) biofeedback signal method for estimating the real dynamic force of limbs (Lloyd & Bessier, 2003). SEMG sensors allow for the investigation of human muscle-activity without penetrating deep into the muscle area that lies under the skin. In the current practice, it is impractical and inconvenient to

measure the generated limb real dynamic forces using conventional force sensors such as dynamometer because of the large size, heavy equipment and complicated method (Staudenmann *et al*., 2006). One of the main reasons sEMG sensors are able to replace the conventional force sensors is because the mean signals of the sEMG characteristic vary linearly with the muscle generated force.

The objective of this research is to determine the relationship between the actual dynamic force signals of upper limbs using a dynamometer and sEMG sensor for lifting activities. The expected outcome of this research is to predict the real dynamic force of upper limbs using sEMG as an alternative to the dynamometer's function for wearable sensor applications.

2. ELECTROMYOGRAM

Electromyography is used to evaluate and record electrical activities produced by the muscles of the human body. An electromyogram (EMG) signal is an electrical manifestation of contractions of the muscles (Gerdle *et al*., 1999. Currently, there are three types of EMG sensors available and each of them has different principles of operation (Wheeler *et al*., 2011) :

1. **Needle electrodes** are widely used in clinical procedures in neuromuscular evaluations. The tip of the needle electrode is bare and used as a detection surface. It contains an insulated wire in the cannula. The signal quality from needle electrodes is better as compared to the other two types of electrodes. There are two advantages of using needle electrodes: (1) It needs a relatively small pickup area to enable electrodes to detect individual muscles during relatively low force contractions; (2) The electrodes conveniently can be repositioned within the muscle (after insertion) so that new tissue territories can be explored.

2. **Wire electrodes** are made from a small diameter of highly non-oxidising, stiff wire with insulation. Alloys of platinum, silver, nickel and chromium are easy to be implanted and withdrawn from skeletal muscles, are generally less painful as compared to needle electrodes, and the cannula will remain in the muscle throughout the duration of the test.

3. **Surface electrodes** are used in sEMG to provide a non-invasive technique for measurement and detection of EMG signals. The principal of sEMG is the electrode forms a chemical equilibrium between the surface and the skin of the body through electrolytic conduction, so that current can flow into the electrode (Bosco, 2010). These electrodes were simple and easy to be implemented. The sEMG sensors have the capability to measure voltage differences on the surface of the skin, and the electrical signal produced during muscle activation is known as the myoelectric signal. The signal was produced from small electrical currents generated by the exchange of ions across muscle membranes and is detected through the surface electrodes.

Each type of EMG sensor has its advantages and disadvantages for the purpose of implementation in wearable devices which is shown in Table 1. It is concluded that sEMG sensor is the most suitable sensor for detecting the muscle activities, as it is easier to be assembled and causes less pain to the skin.

Table 1: Comparison amongst the EMG electrodes.

EMG Electrodes	Advantages	Disadvantages
Needle electrode	Best signal quality Able to detect fine individual muscle	Painful Discomfort
Wire electrode	Enables the electrode to detect individual muscles	Not able to detect fine individual muscle
Surface electrode	Good signal quality Simple Easy to implement Comfort	Not able to detect fine individual muscle

3. METHODOLOGY

3.1 Preparation and Clean Data Measurement

The data collection protocol of the conducted research was based on the guidelines from the Surface Electromyography for the Non-Invasive Assessment of Muscles (SENIAM) project (Hermens e*t al*., 1996). By following the recommendations for electrode size and design, electrode placement procedures, recording and processing of sEMG signals, and a set of reference signals (Stegeman & Hermens, 2007), it ensures that all the data collection and procedures were valid and can be compared easily with the other existing published data. The standard recommendation for the electrodes and procedures used are as follows:

3.1.1 Type of Electrode

Bipolar silver / silver chloride (Ag / AgCl) electrodes were used to detect the muscle force potential difference. It is a sensitive electrode to measure potential difference and has less resistance between the skin and the electrode. Its maximum resistance is 10kΩ; the electrode base size is 20 mm and has a fixed centre-to- centre spacing of 9 mm. It comes with pre-gelled discs and adhesive sponge-like foam pad, as shown in Figure 1.

Figure 1: Fixed distance surface gel abrasive electrode.

3.1.2 Electrode Placement

Three pairs of electrodes were placed at the biceps, triceps and branchioradialis, as shown in Figure 2. The selection of the area was based on the sensitivity of myoelectric control (Geethanjali, 2015).

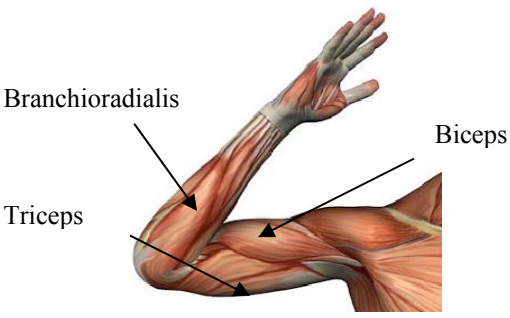

Figure 2: Electrode placements at the peaks of the each muscle.

3.1.3 Skin Preparation

The application of sEMG electrodes requires proper skin preparation beforehand in order to reduce skin resistance uncertainty and obtain a good quality EMG signal. The subjects were advised to shave and clean the skin before placing the electrode to reduce the skin's impedance. The dead cells on the skin and hair should be removed from the sEMG electrode location. An abrasive gel was used to reduce electrode-skin impedance and the skin was cleaned with alcohol to remove any moisture.

3.1.4 Clean Data Measurement

There are several intrinsic and extrinsic sources of low frequency noise (Abser *et al*., 2011) that may contaminate the sEMG signal. Two extrinsic noise sources were identified, which were powered line noise and cable motion artefacts. Two intrinsic noise sources were also identified, which were thermal noise (originating from the electronics of the amplification system) and electrochemical noise (at the skin-electrode interface) (Chan & MacIsaac, 2011). These noises were eliminated using a voltage regulator, shielded cable, appropriate circuit design and a Matlab program that can filter the raw data using Butterworth filter, low-pass filtering and full wave rectification. It is strongly recommended that before any measurement, any possibility of contamination in the sEMG recordings should be avoided to ensure that the signal is clean, in order to obtain more accurate data (Fraser *et al*., 2011).

3.2 Test Protocol and Data Acquisition

Five subjects performed the lifting task for the research experiment; all were healthy subjects and aged between 26 to 36 years old. The subjects were asked to perform a lifting task while seated in a straight-back chair. Their torsos were stabilised to the back of a chair to minimise compensatory trunk movements and the start position is with the tested upper extremity resting on a pillow on the ipsilateral thigh. The shoulder was in approximately 0° flexion and extension with 0° internal rotation. Minor modifications, such as increased or decreased shoulder internal rotation, to the start position were allowed for some subjects to minimise any positional discomfort. The subjects were instructed to lift their arms at 30° on their maximum lifting strength and hold the position for eight second. The sEMG signal was measured using a Shimmer sEMG sensor and real force was measured using a Hogan microFET dynamometer. Three trials of reaching movement were recorded. The data collection was limited to only three trials of reaching because it can contribute to fatigue. Subjects were given maximum two training sessions to familiarise with the task and instructions prior to the recording session.

The events of starting, lifting and ending positions were determined through velocity measurement. Velocity positively increasing from 0 ms^{-1} indicates the beginning of the activity. The lifting was determined when the velocity decreased to 0 ms^{-1}, while the end of the movement was determined when the velocity decreased and reached 0 ms^{-1}. Table 2 shows that definition for each movement and its detection methods.

Table 2: Phase movement definitions.

Phase	Activity	Detected by
Rest Position	Hand position is 0° from the target object	Velocity will be zero
Move Upward	Hand begin to move upward 30° to the target object	Velocity positively increased
Lifting target	Hand will reach the target object and lift for 8 seconds	Velocity will be zero / nearly zero
Move Downward	From the target object hand will move down ward to rest position	Velocity will negatively decreased
Rest Back	Hand position is horizontal 0 degree from the target object	Velocity value will be zero

Two electrodes were placed within the same electric field of the tissue and were connected to a differential amplifier to record neurophysiological signals, as shown in Figure 3. The electrode pair measured the difference of voltage between the two inputs (Arnold *et al*., 2010). The electrode that was connected to the input is known as an active electrode and the other electrode as a reference electrode. Eventually, the electrodes picked up the signal of interest together, along with noises, which is known as a common mode signal. The common mode signal, which contaminated the signal of interest, comes from different sources, including the main interference signal at 50 Hz, thermally generated noise in the electrodes and amplifier, and electrochemical instability on the surface of the electrodes.

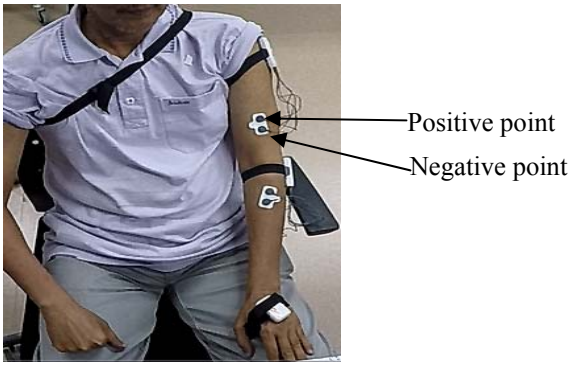

Figure 3: Two electrodes were placed for sEMG data collection.

The data was captured using low power Shimmer sEMG sensors, and a wireless sensor platform using the bluetooth protocol to the computer and has a pre-noise filter function. Each sEMG Shimmer board connects to three points, namely, a positive, a negative (muscle area) and a neutral reference (at the elbow position). The reason for using three electrodes in this way was that the EMG signal amplitude is typically very small relative to the noise signal. The signal picked up by each individual electrode consists of noise from the environment along with the local electrical signal from the muscles of the position of skin contact. The noise from the environment is common to all electrodes, whilst the local electrical signal depends on the electrode's position. Thus, if one signal is subtracted from another, the common component (the undesired noise) will be cancelled by the subtraction, whilst the local signals (the desired EMG component) will remain after subtraction and can be amplified to make it easier to process (Andreas, 2013). This process is known as Common Mode Rejection (CMR) and is used in the Shimmer EMG data acquisition system.

3.3 Signal Processing for sEMG

The sEMG signal processing (Figure 4) includes acquisition of raw sEMG signal, pre-processing using the sEMG Shimmer device, post processing using Matlab, signal rectification, and comparing these values with a dynamometer.

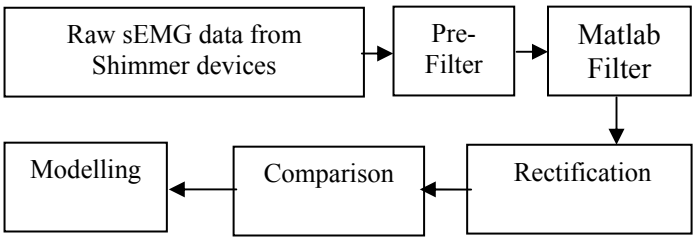

Figure 4: The sEMG signal processing flow.

3.3.1 Raw sEMG Data

The frequency of the sEMG spectrum is between the ranges of 0-400 Hz, but the majority of the signal lies in the 20-250 Hz spectrum domain (Norali & Som, 2009). Data acquisition with sampling rate of 500 Hz (two times the maximum frequency) or higher is required to ensure high quality reproducibility of the actual summation of the muscle activity. Therefore, for this application, a sampling rate of 1,024 Hz (four times higher) was selected to have a better quality signal.

3.3.2 Filtering

The original sEMG signal contained the local electrical signal from the muscle and several noise signals (Jamal, 2012), as shown in Figure 7. These noise signal components contaminate the sEMG signal and may lead to errors when interpreting the signal. This is especially the case when the signal is obtained during dynamic contractions (Gerdle *et al*., 1999). The simplest and most direct means of increasing the fidelity of the sEMG signal is to filter the maximum amount of noise, while retaining as much of the desired sEMG signal frequency spectrum as possible (Giovanni & Roberto, 2007). Commonly, the effective frequency spectrum of the sEMG signal is collected between range from 0-400 Hz, depending on the electrode spacing, amount of fat in the tissue between the skin and muscle tissue, shapes of the action potentials, and muscle type (Piervirgili *et al*., 2014).

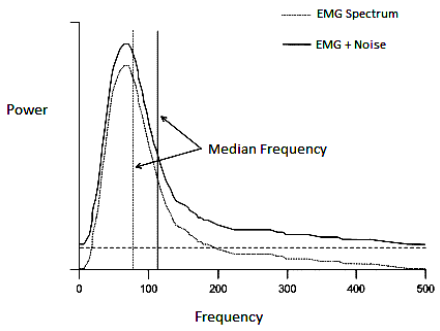

Figure 7: The EMG spectrum contains sEMG signal and noise signal.
(Source: http://www.intechopen.com/http://www.intechopen.com.ololo.sci-hub.cc/books/computational-intelligence-in-electromyography-analysis-a-perspective-on-current-applications-and-future-challenges/signal-acquisition-using-surface-emg-and-circuit-design-considerations-for-robotic-prosthesis)

The frequency bandwidth was generally greater if the sensor was placed over the insertion of the muscle fibres into the tendons or on top of the innervation zone of the muscle. However, such a placement was not advisable because it can cause pain to the subjects. At the high-frequency end of the sEMG signal spectrum, the low-pass filter corner frequency should be set where the amplitude of the noise components surpasses the sEMG signal (Fraser *et al*., 2012). Hermens *et al*. (1996) recommended that for the high end of the sEMG frequency spectrum, the low-pass corner frequency should be in the range of 400–450 Hz. At the low frequency end of the spectrum, the high-pass filter corner frequency was more involved because several noise sources contribute signals whose low frequency spectrum overlap with the sEMG signal. Hermens *et al*. (1996) recommended a range of 10–20 Hz for the lower frequency filter corner.

For this test, the sEMG data were filtered using a Butterworth filter between sEMG spectrum frequency at 10 and 400 Hz, and at a sampling rate of 1,024 Hz. The Butterworth filter was selected due to its filter characteristic that not only can completely reject the unwanted frequencies but also has uniform sensitivity for the intended frequencies. The difference between the sEMG signal before and after the filtering process can be seen in Figure 8. The unfiltered data shows an incremental trend along the time and is not uniformly scattered, so it was difficult to conclude the data pattern for the raw sEMG data with the data pattern for the real force. After it was filtered using the Butterworth

filter, the data trend and signal envelope can be seen on the graph.

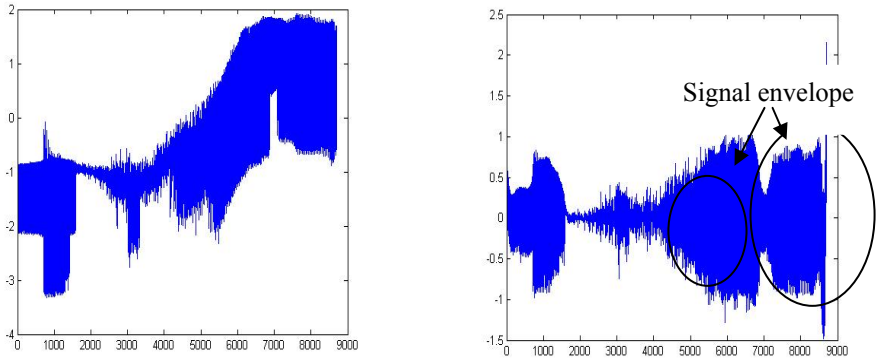

(a) Raw data **(b) Filtered data**

Figure 8: The sEMG signal (a) without and (b) after filtering.

3.3.3 Rectification

Rectification of the sEMG signal as shown in Figure 9 is commonly done using a pre-processing procedure that allows the detection of significant coherence between the signal and measured dynamic force signals. This method takes the spectrum of the original data and assigns a positive phase to each frequency component. Rectification processing was done using the absolute values of the filtered sEMG signal and since the real dynamic force only has a positive value, it can easily be compared. After that, the value was filtered using the three points moving average method for marker trace data smoothing. The moving average method was to minimise the error using a simple and efficient method (Sun *et al*., 2016).

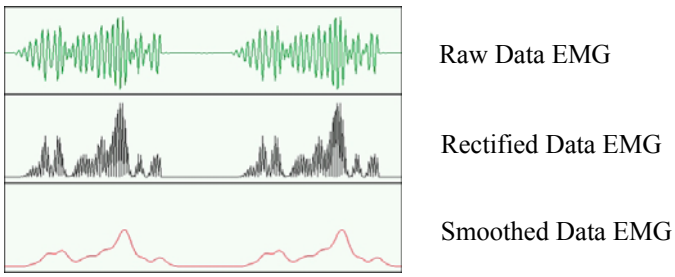

Figure 9: Rectification and smoothing of the sEMG signal.

3.3.4 Data Comparison

The measurement value must be compared to ensure that the measured data was valid. A MicroFET-3 digital manual muscle dynamometer, which is able to measure force for up to 100 kN, was used to measure the force and was compared with muscular force measured using sEMG. The dynamometer was placed on the subject's wrist. The subject was asked to lift their arms from a rest state to the maximum force, with the pattern of the sEMG signal and the real force signal observed during the trial. The correlation between the signals was validated using Statistical Package for the Social Sciences (SPSS).

Since the processed sEMG data and real force data are linear, they can be compared directly after being time synchronised. The sampling frequency for the sEMG sensor was 1,024 Hz (muscular force) and 100 Hz for the dynamometer (real force). The sEMG data was averaged for every 102 data to reduce number of samples to 100 data per second. The graph comparison between both the data after the time synchronisation is shown in Figure 10.

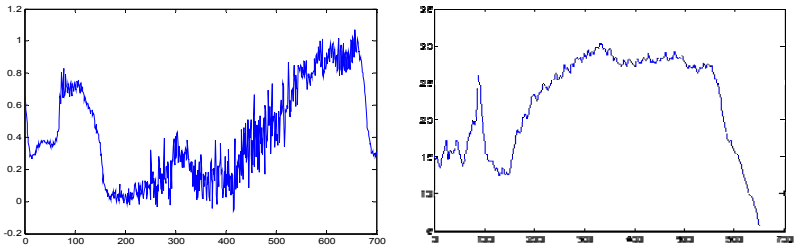

Resample rectified sEMG Real force dynamometer Time

Figure 10: Post-processed sEMG signal vs dynamometer signal.

4. RESULTS & DISCUSSION

The Pearson correlation method (Lin, 1989) was used to determine the correlation between the real force and sEMG data (Table 3). From the statistical Pearson correlation test value, there was a significant relationship between the two data (sigma < 0.01) and there was a positive correlation between the data (Pearson correlation = 0.658). The results show with 99% of confidence level there is 66% of strong linear relationship between the sEMG measurement and real force data from the correlation analysis. According to this value, the sEMG signal has a high possibility to estimate the real force value.

Table 3: Correlations between real Force and sEMG signal.

Correlations		Force	sEMG
Force	Pearson Correlation	1	.658**
	Sig. (2-tailed)		.000
	N	447	447
sEMG	Pearson Correlation	.658**	1
	Sig. (2-tailed)	.000	
	N	447	447

**Correlation is significant at the 0.01 level (2-tailed)

Although there was a similarity pattern between the sEMG graph and real force graph, there were slight differences between the graph patterns. One of the major reasons that has been identified to contribute to the differences between the graphs is muscle fatigue. In order to maintain the linear force, a constant force must be applied to the muscle, but naturally a muscle has its own rest period and within the rest period, the force will decrease before it starts to increase again to maintain the constant strength (Bogey *et al.*, 2005). There is also a possibility that a few more parameters need to be identified in recording the clean sEMG signals, such as impedance of the skin, electrode locations, variation caused by fatigue and sweat, and better time synchronisation, which are noise contributions that affect the measurement of the sEMG. Although the filtering process was applied to the signal, this noise parameter still needs to be considered. It is also important to develop more advanced techniques for sEMG processing, taking into account the natural variability of these signals.

5. CONCLUSION

The purpose of the study was to determine the relationship between sEMG signals and real dynamic force. It was shown that the filtered sEMG signals have a relationship with the dynamic force strength. For the statistics result, from the Pearson correlation value of the test (0.658), it showed that there was a strong and positive linear relationship between sEMG signal and dynamic force of real upper limb for the lifting activity. Based on this, it can be concluded that SEMG models are

promising to predict human moments, where it can estimate the basic dynamics force of the human body.

In military area, the application of force estimation using sEMG can be employed as a soft contact sensor for detection and evaluation of the effect of the personal muscle (Bogey *et al*., 2005). We can study the characteristics of the military personnel muscle and the effect to their body muscles so that the muscle characteristics can be scientifically and precisely evaluated. Using this assessment method, we can determine the most effective training to strengthen muscles; develop new exercise programmes for the military that can enhance the endurance and strength of the physical muscle of military personnel; develop new rehabilitation monitoring methods; and detect phases of human gait. For advanced military applications, exoskeletons, orthotics and wearable devices may be developed based on the sEMG signal. The information from the sEMG signal is related to human gait and can be used as a signal reference for movement of any device. These profiles and measures are developed for researchers and clinical investigators as a baseline reference of motor patterns and for use in the diagnosis of gait pathologies. It is an advantage to use sEMG force estimation method in developing sEMG based military exoskeletons because it is deployable, wearable, light and small sized. Hence, it can be concluded that sEMG research has potential to be explored for military application.

ACKNOWLEDGEMENT

This research was partially supported by the Ministry of Higher Education, Malaysia (MOHE) under Fundamental Research Grant Scheme: FRGS/1/2016/TK04/UKM/02/5 and Universiti Kebangsaan Malaysia (UKM) under the Research University Grant: AP-2014-014.

REFERENCES

Abser, N., MacIsaac, D., Chan, A.D.C., Fraser, G.D. & Green, J.R. (2011). Clean EMG: Quantifying power line interference in surface EMG signals.*Proc. 34th Conf. Can. Medical Biological Eng. Soc. Festival Int. Conf. Caregiving, Disability, Aging Technol*. Toronto, Canada., pp 1–4.

Andreas, A. (2013), Wavelet-based detrending for EMG noise removal, *20th Annu. IEEE Int. Conf. Workshops Eng. Comput. Based Syst.*, pp. 60-65.

Arnold, E.M., Ward. S.R., Lieber, R.L. & Delp, S. L. (2010). A model of the lower limb for analysis of human movement. *Ann. Biomed. Eng.*, **38**: 269-279.

Bosco, G. (2010). Principal Component Analysis of Electromyographic Signals: An Overview. *The Open Rehabilitation Journal.*, **3**: 127-131.

Bogey, R., Perry, J. & Gitter, A. (2005). An emg-to-force processing approach for determining muscle forces during normal human gait. *Neural Syst. Rehabil. Eng.*, **13**: 302–310.

Chan, A.D.C. & MacIsaac, D. (2011). Clean EMG: Assessing the quality of EMG signals. *Proc. 34th Conf. Med. Biol. Eng. Soc. and FICCDAT 69826*, Toronto, Canada., pp. 1–4.

Fraser G.D., Chan A.D.C., Green J.R., Abser N. & MacIsaac. D. (2011). Clean EMG -Power line interference estimation in sEMG using adaptive least squares algorithm. *Proc. IEEE Eng. Med Biol. Soc.*, pp. 7941–7944.

Fraser, G. D., Chan, A.D.C., Green, J.R. & Mac Isaac, D. (2012). Removal of electrocardiogram artifacts in surface electromyography using a moving average method. *Proc. IEEE Int. Symp. Medical Measurements Applicat. (MeMeA).*, pp. 128–131.

Geethanjali, P. (2015). Comparative study of PCA in classification of multichannel EMG signals. *Australas Phys Eng Sci Med.,*

Gerdle, B., Karlsson, S., Day, S. & Djupsjöbacka, M. (1999). Acquisition, processing and analysis of the surface electromyogram. *Modern Tech. Neurosci.*, **26**: 705-755.

Giovanni, B. & Roberto, S. (2007). *Electronic Filter Simulation & Design*. McGraw-Hill Professional, pp.17–20.

Hermens, H.J., Merletti, R. & Freriks, B. (1996). European activities on surface electromyography research and development. *Proc. First General SENIAM Works.*, Torino, Italy.

Jamal, M.Z., (2012). *Signal Acquisition Using Surface EMG and Circuit Design Considerations for Robotic Prosthesis, Computational Intelligence in Electromyography Analysis - A Perspective on Current Applications and Future Challenges*. Available online at: http://www.intechopen.com.ololo.sci-hub.cc/books/computational-intelligence-in-electromyography-analysis-a-perspective-on-current-applications-and-future-challenges/signal-acquisition-using-surface-emg-and-circuit-design-considerations-for-robotic-prosthesis. (Last access date: 28 August 2017).

Lin, L.I. (1989). A concordance correlation coefficient to evaluate reproducibility biometrics. *Biometrics,* **45**: 255-268.

Lloyd, D.G. & Bessier, T.F. (2003). An EMG-driven musculoskeletal model to estimate muscle forces and knee joint moment in vivo. *J. Biomechanics.*, **36**: 765-776.

Norali, A.N., & Som, M. (2009). Surface electromyography signal processing and application: A review. *Int. Conf. Man-Mach. Syst. (ICoMMS).*,pp. 1–9.

Piervirgili, G., Petracca, F. & Merletti, R. (2014). A new method to assess skin treatments for lowering the impedance and noise of individual gelled Ag–AgCl electrodes. *Phys. Eng. Med. Physiol. Meas..*, **35**: 10-11.

Rodgers, H., Mackintosh, J. & Price, C. (2003). Does an early increased-intensity interdisciplinary upper limb therapy programme following acute stroke improve outcome?. *Clin. Rehabil.*, **17**: 579-589.

Staudenmann, D., Kingma, I., Daffertshofer, A., Stegeman, D.F. & Van Dieën, J.H., (2006). Improving EMG-based muscle force estimation by using a high-density EMG grid and principal component analysis. *IEEE T. Biomed. Eng.,* **53**: 712-719.

Stegeman, D. & Hermens, H. (2007). Standards for suface electromyography: The European project Surface EMG for non-invasive assessment of muscles. *Surface ElectroMyoGraphy for the Non-Invasive Assessment of Muscles*., 108-112.

Sun, L., Ahlfors, S.P. & Hinrichs, H. (2016). Removing cardiac artefacts in magnetoencephalography with resampled moving average subtraction *Brain Topogr.*, **29**:783–790.

Wheeler, K.A., Kumar, D.K., Shimada, H., Arjunan, S.P.S. & Kalra, C. (2011). Surface EMG model of the bicep during aging: A preliminary study. *Proc. Annu. Int. Conf. IEEE Eng. Medicine Biology*,. pp. 712–713.

Wolf, S.L. (1983). Stroke patients: A critical review electromyographic biofeedback applications to stroke patient. *Phys. Theraphy J.*, **63**: 1448–1459.

REVIEW ON RAPID PORTABLE BRIDGE SYSTEM: STATE-OF-THE-ART AND TECHNOLOGY DEVELOPMENTS

Azrul Affandhi Musthaffa, Norazman Mohamad Nor* & Muhamad Azani Yahya

Faculty of Engineering, National Defence University Malaysia (UPNM), Malaysia

*Email: azman@upnm.edu.my

ABSTRACT

Rapid portable bridges are crucial for providing routes for troops during the military operations and the restoration of vital lifelines for communities affected by large-scale disasters. This paper reviews on the state-of-the-art technologies of rapid portable bridge, particularly the military bridge in Malaysia. Several types of rapid portable bridge systems are reviewed in the current work, including (1) assault bridge (e.g., LEGUAN AVLB), (2) support bridge (e.g., BR90 General Support Bridge), (3) logistic bridge (e.g., Compact 100 Bailey Bridge), and (4) floating bridges (e.g., Tactical Floating Bridge). In this paper, the function, characteristics and capability of each bridge type is discussed. In addition to providing a review of current technology, this paper also highlights recent research and development of rapid portable bridge. The paper concludes with the application prospect of rapid portable bridge technology.

Keywords: *Portable bridge; military bridge; composite material; finite element analysis; disaster-relief.*

1. INTRODUCTION

In the military field, the bridge serves as an important route for troops during the military operations. During peacetime, military bridging asset is needed by the public to temporarily replace a damaged bridge caused by natural disaster such as flood, landslide, earthquake or tsunami while waiting for the construction of a new bridge. In this situation, a military bridge or also known as the rapid portable bridge can be utilized. For example, military bridges such as Bailey Bridge and Medium Girder Bridge (MGB) had been deployed during the large-scale disasters such as the Indian Ocean Tsunami in 2004, the Hai Tang Typhoon occurred at Taiwan in 2005 and the Pakistan Earthquake in 2005. In Malaysia, military bridging asset such as General Support Bridge (GSB), Compact 100 Bailey Bridge and Portable Floating Platform (PFP) have been regularly used for logistic purpose during disaster. Military bridging has been identified as the fastest and the most effective solution to open up the line of communication for Humanitarian Assistance and Disaster Relief (HADR) operation. However, the review paper detailing on the rapid portable bridge technology is somehow limited. Thus, this paper aims to review the state-of-the-art development of rapid portable bridge in Malaysia, dedicated for those who may be interested in this technology for military or emergency purposes.

Figure 1: BR90 GSB deployed during Bukit Antarabangsa landslide (Jusoh, 2008).

2. MILITARY BRIDGE SYSTEM

Based on The Trilateral Design and Test Code (TDTC) for Military Bridging and Gap-Cross Equipment 2005, the military bridges are divided into three main categories, i.e.–clear-span bridge, floating bridge and raft and equipment causeway. Malaysia inventory contains only the clear-span bridge and the floating bridge; therefore, both of them will be emphasised in this paper. A clear-span bridge can be further divided into assault bridge, support/tactical bridge and line of communication (LOC)/logistic bridge (Robinson & Kosmatka, 2006). The military bridging functions in war or conflict are summarised by the author in the graphic as shown in Figure 2. In this figure, military forces are advancing to area of operation. The lead elements in the advance (usually armour) requires assault bridging to breach the natural or manmade obstacles quickly. The follow-on elements require support bridging to continue supporting the lead elements. Usually, the follow-on support bridging will replace assault bridging to allow the former assault bridge to be used further in advance or during an attack. The sustainment elements require logistic bridging to maintain continuous logistical support for the follow-on and lead elements. The logistic bridging typically replaces the support or assault bridging systems.

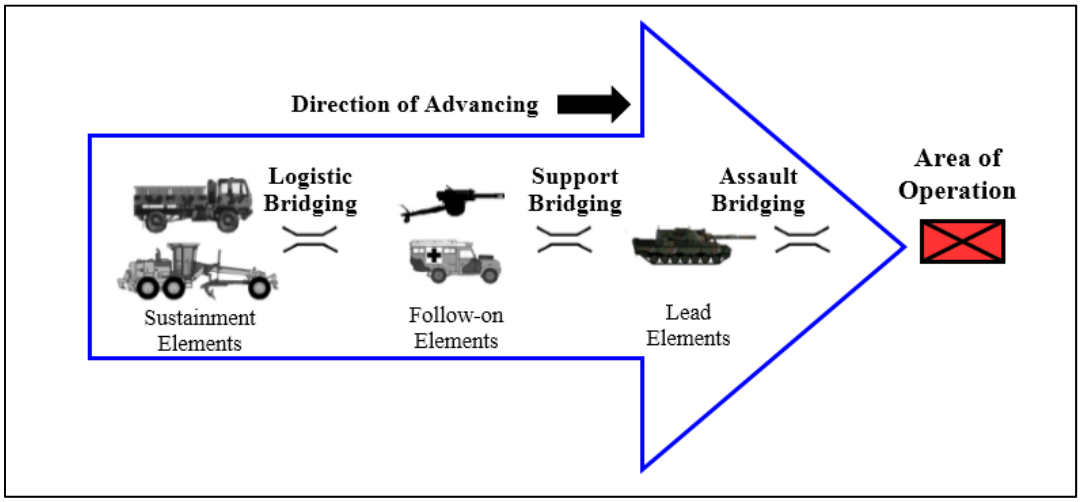

Figure 2: Battlefield graphic of military bridging function.

The capability of military bridge is measured by the Military Load Classsification (MLC). MLC is a NATO standard classification for military vehicles based on weight and dimension of a particular vehicle (Tytler *et al*., 1985). Vehicles are allowed to travel cross a particular military bridge if its MLC is equal to or less than the bridge's MLC. Table 1 shows maximum allowed weight of hypothetical tracked (T) and wheeled (W) vehicles based on various MLC as taken from TDTC.

Table 1: MLC (SI Units) (Hornbeck *et al*., 2005).

MLC	Tracked (T) (Tonnes)	Wheeled (W) (Tonnes)
30	27.22	30.84
40	32.69	42.63
50	45.36	52.62
60	54.43	63.50
70	63.50	73.02
80	72.58	83.45
90	81.65	93.89
100	90.72	104.33

The Trilateral Design and Test Code (TDTC) for Military Bridging and Gap-Cross Equipment 2005 serve as the basis in military bridge design. The TDTC is a collaborative design code assembled and agreed upon by the Federal Republic of Germany (FRG), the United Kingdom (UK), and the United States of America (US). The TDTC provides detailed guidance on all design aspects of military bridge system such as material requirement, design parameters, load combinations, safety consideration, and testing requirements to be used for the development and design of military bridges, floating bridges, rafts and launching structures (Hornbeck *et al*., 2005). In the following sections, the state-of-the-art of military bridge system in Malaysia, i.e., assault bridge, support bridge and logistic bridge will be reviewed. The function and capability of each bridge will be focused and discussed.

2.1 Assault Bridge: LEGUAN 26 m Armoured Vehicle Launch Bridge (AVLB)

The LEGUAN 26 m AVLB is a fixed span bridge mounted on a modified Main Battle Tank (MBT) chassis. This bridge system was developed by Krauss-Maffei Wegmann (KMW) Company, Germany, and its first production was in 1975. This bridge uses a bridge laying system (also known as horizontal launch system). The LEGUAN 26m AVLB is used by armies from US (M1A1 Abrams MBT chassis), Denmark (Centurion Mk V MBT chassis), Germany (Leopard MBT chassis), Italy (Leopard MBT chassis), Spain (M60 MBT chassis), and Malaysia (PT91-M MBT chassis) (KMW, 2006). This bridge system was firstly put in the Malaysian Army inventories in 2011 under the command of Royal Armour Corp (KMW, 2006).

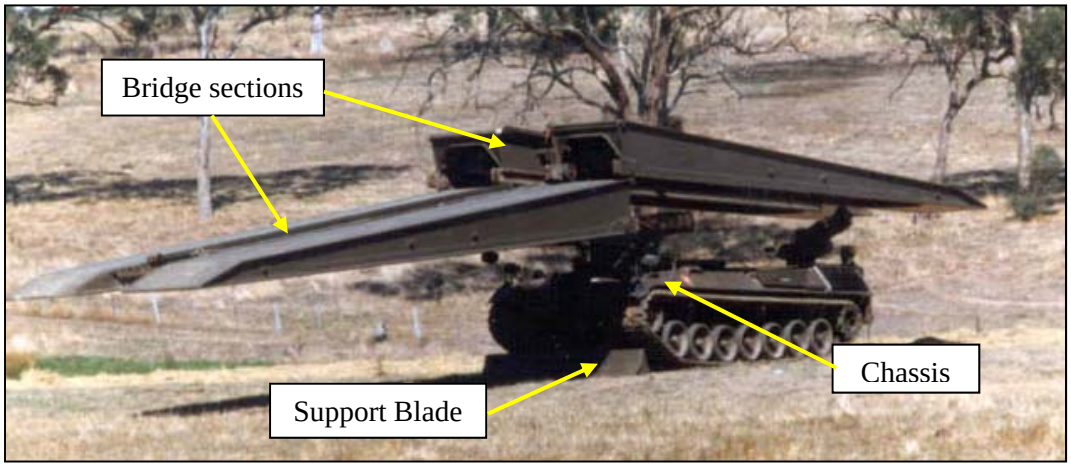

Figure 3: The LEGUAN 26m AVLB action during launching (KMW, 2006).

This bridge has an effective length of 25 m and width of 4.01 m. It can provide a MLC 60 (T) gap crossing capability. It is operated by two crews, with launching and retrieval times of less than 5 minutes each. The total weight of the complete bridge is 10.8 tonnes. This bridge is made from aluminium-zinc-magnesium alloy class AlZnMg1 (Germany designation) as stated in Appendix A TDTC. This type of alloy is also known as the 7020 alloy by international designation (Mazzolani, 1994). The launching and retraction operations of the bridge can be performed from either end.

2.2 Support Bridge - BR90 General Support Bridge (GSB)

The BR90 GSB is one of the variants of British Army Bridge for Nineties (BR90) program. This bridge was first manufactured by ALVIS Bridging Limited, United Kingdom and currently the BAE Systems Land Systems Limited has been granted permission to manufacture the bridge. The bridge system entered into the British Army inventories in 1996. This bridge uses the concept of modularity, whereby the bridge structure consists of panels and the lengths are customisable. This bridge has two types of bridge configurations which are General Support Bridge (GSB) and Axially Tensioned Long Span Bridge (ATLSB). GSB configuration is used to construct bridge of length ranging from 16 m to

32 m while ATLSB configuration is used to construct bridge of length ranging from 38 m to 52 m (ALVIS, 2004). This bridge system has been used in the Malaysian Army since 2006 under the command of Royal Engineer Regiment.

The BR90 GSB consists of four major sections, which are the launcher, the launch rail, the bridge and the bridging vehicle. The launcher is mounted on the 8x8 wheeled vehicle chassis, which is also known as Automotive Bridge Launching Equipment (ABLE). The bridge consists of the ramp of length 8 m, and the bridge panels of lengths of 2 m, 4 m and 8 m translating to a total bridge length of 16 m to 52 m. Also, this bridge consists of other components such as deck, curb, bracing frame, brace strut and edge marker. The Bridging Vehicle (BV) is a flat platform 8x8 wheeled vehicle used to transport bridge components and equipment to the site (ALVIS, 2004).

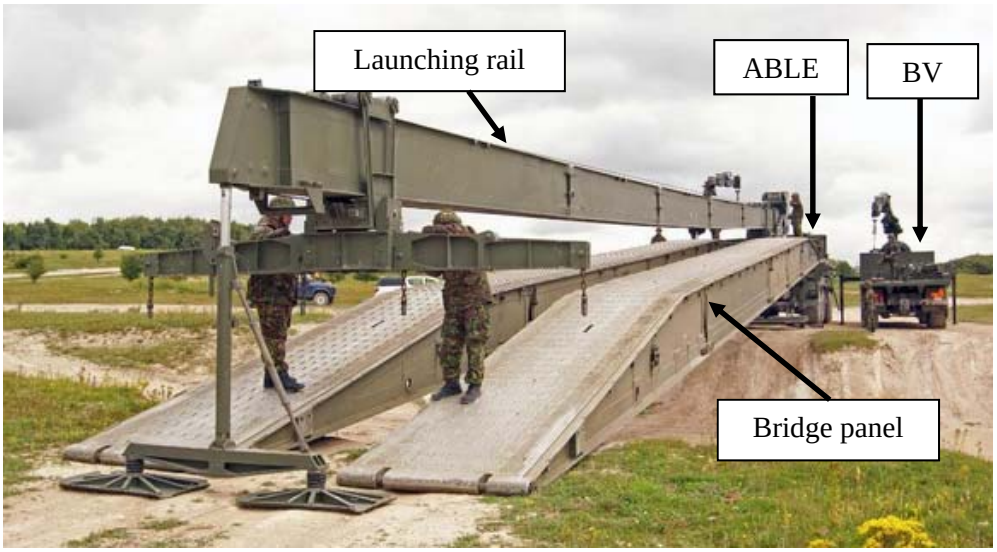

Figure 4: BR90 GSB during launching process (ALVIS, 2004).

The standard dimension of BR90 GSB is 16 m to 32 m in length (with 2 m increment), 4 m in roadway width and 1m in bridge depth. It is designed to support MLC 70 vehicle load. The 32 m bridge can be launched in 40 minutes by ten crews. The total weight of the complete 32 m bridge is 16.95 tonnes. The bridge is designed and tested in accordance with the internationally accepted TDTC (ALVIS, 2004). The main structure of the bridge is made from the specially developed aluminium-zinc-magnesium alloy, coded as DGFVE 232B alloy or also known as 7019 alloy (Ministry of Defence, 2004). This alloy is well-known for its high strength, lightweight and corrosion-resistant properties.

2.3 Logistic Bridge: Compact 100 Bailey Bridge

The Compact 100 Bailey Bridge is a portable pre-fabricated truss bridge, designed to replace the assault bridge, the support bridges and the civilian bridge damaged by enemy action or natural disasters such as flood and landslide. The bridge was designed and developed by Mabey & Johnson Ltd., United Kingdom and its first production was in 1983. The bridge is the improved version of the Bailey Bridge which was firstly used during World War 2 in 1941 (Mabey & Johnson Ltd., 2007). Recently, the Compact 100 Bailey Bridge system has been used by 31 armed forces worldwide including Malaysia. In Malaysian Army, this bridge is currently allocated under the command and control of the Royal Engineer Regiment. Besides that, the Public Work Department of Malaysia has included this bridge system in their inventory.

Figure 5: Compact 100 Bailey Bridge constructed during flood relief operation (Rasyid, 2008).

The Compact 100 Bailey Bridge consists of panel, transom, deck unit, reinforcement chord and bracing units. The main structure is constructed by two panels arranged in a parallel manner. Transom forms the cross girders of the bridge, spanning between the panels. The deck units are laid between the panels to form a 4.2 m width roadway. The bridge is designed to support vehicles of load up to MLC 60 (Mabey & Johnson Ltd., 2007).

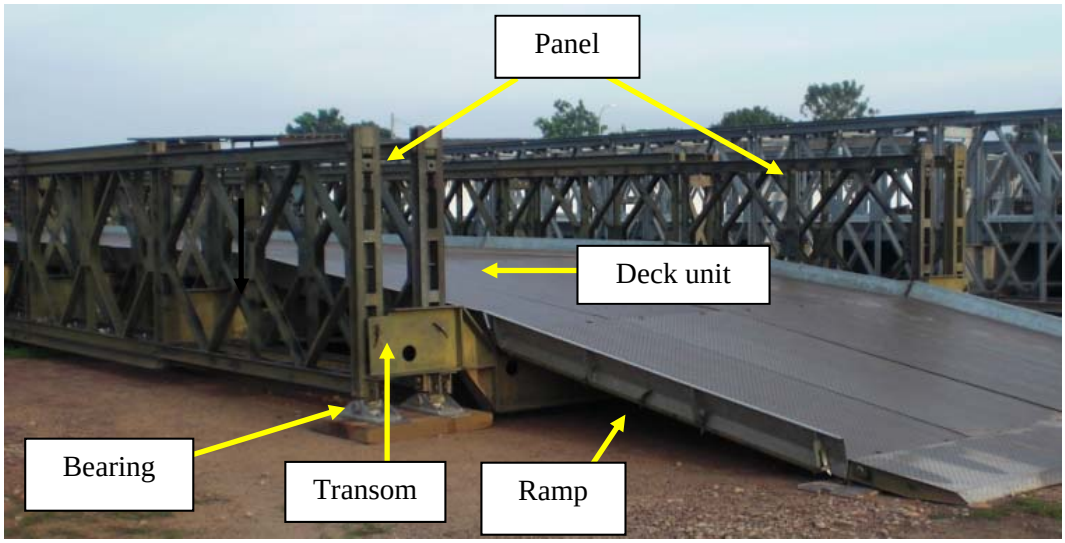

Figure 6: Compact 100 Bailey Bridge parts.

The Compact 100 Bailey Bridge can be constructed by the cantilever launch method, by relying on manpower without the need of any temporary intermediate support. This is achieved by erecting a temporary launching nose at the front of the bridge and pushing the bridge over the gap on rollers. The standard Compact 100 Bailey Bridge can be built from 15.24 m (5 bays) to 60.96 m (20 bays) at 3.05 m (1 bay) increments and provides a 4.2 m width roadway. This bridge is launched by 40 crews. The Compact 100 Bailey Bridge structural parts are fabricated from Grade 55 Steel with ultimate yield strength of 450 MPa. Its construction time varies depending on many factors such as bank condition, number of crews and supporting equipment (Mabey & Johnson Ltd., 2007). In 2008, a MLC 30 bridge of length 18.29 m (6 bays) was constructed in 6 hours during the flood relief operations in Melaka.

2.4 Floating Bridge - Tactical Floating Bridge (TFB) / *Pont Flottant Motorised* (PFM)

The Tactical Floating Bridge (TFB) / *Pont Flottant Motorised* (PFM) bridge is a modular floating bridge developed by CNIM Company, France (CNIM, 2006). It is used to cross over wet obstacles such as rivers and lakes during the military operations. The PFM can be used as a Pontoon Bridge or Tactical Heavy Raft for the purpose of crossing the military assets. Currently, the Royal Engineer Regiment are equipped with 2 sets of PFM, whereby each set consists of three Standard Module, six Standard Module with Short Integrated Ramp and two Long End Ramp. The PFM is transported by using 11 carrier vehicles. A set of PFM can be used to construct a Pontoon Bridge of 100 m length. For Tactical Heavy Raft, each PFM can be configured into 3 variations of varying lengths, i.e. 30 m, 40 m and 50 m (CNIM, 2006).

PFM can be constructed by launching the pontoon modules into the wet obstacle. Then the modules are connected depending on the configuration required, e.g. Floating Bridge or Tactical Heavy Raft. The maximum loading capacity for Tactical Heavy Raft and Pontoon Bridge are MLC 90 and MLC 70, respectively. A floating bridge of 100m length is launched by 42 crews. The PFM structural parts are made from two types of materials. The marine grade aluminium alloy is used in the overall load-bearing parts of the vehicle while the glass fibre material is used on the side of the module to ease floating. The advantages of PFM are its short construction time and ease of control. More importantly, its construction does not require major site preparation and it can also be used as a ferry (CNIM, 2006).

Figure 7: PFM in Tactical Heavy Raft and Pontoon Bridge configuration (Army HQ, 2016)

2.5 Portable Floating Platform (PFP)

The Portable Floating Platform (PFP) can be regarded as multi purposed floating platform. The PFP is suitable to be used in all weather conditions involving high waves and strong winds. It is also suitable to be used as bridges, rafts, jetties and helipads. Each set of PFP consists of 800 standard modules, whereby the allowable load of each module is 100 kg. All PFP modules and accessories are made from High Density Poly-Ethylene (HDPE). The floating capabilities of PFP are 375 kg/m^2 for one layer, 725 kg/m^2 for double layer and 1125 kg/m^2 for triple layer (Jetfloat, 2010). In general, PFP is able to support load up to 30 tonnes and is easy to be fixed and removed by all personnel with minimum training (Malaysian Army, 2009). Recently, Royal Engineer Regiment has constructed a temporary bridge using PFP to replace the bridge across Sg. Lebir in Kuala Krai, Kelantan, which was collapsed due to the flood on 31st December 2015. The temporary bridge is 80 m in length and its construction time is 6 hours (Malaysian Army, 2016).

Figure 8: PFP constructed to temporary replace the collapsed bridge (Army HQ, 2016).

3. RECENT RESEARCH AND DEVELOPMENT ON RAPID PORTABLE BRIDGE

3.1 Medium Trackway Bridge (MTB)

General Dynamics European Land System (GDELS), located in Germany, has developed a commercially available mobile bridge known as the Medium Trackway Bridge (MTB) in 2011. It is an aluminium modular lightweight bridge for military and civilian vehicles up to MLC 40 that can be connected to form bridge lengths of 2, 4, 6 or 8 m respectively. The bridge is composed of two parallel treadways, fabricated using high strength aluminium and weighing 540 kg for complete 4 m MTB. The bridge modules can be transported directly on the light tactical or commercial vehicle, and can easily be launched and retrieved on the same vehicle by the crew with a simple adapter. The launching and retrieving time for a 4 m MTB is approximately 10 minutes with 4 soldiers. The MTB increasing tactical mobility to units with no gap-crossing capability without rely on engineer bridging unit (GDELS, 2011).

Figure 9: MTB during launching from light tactical vehicle (GDELS, 2011).

3.2 Composite Army Bridge (CAB)

The United States Army has been developing new light-weight mobile bridging systems since 1990s. New technology bridging system known as the Composite Army Bridge (CAB) was developed by Kosmatka in 2000 and tested at the University of California, San Diego. The bridge is composed of a carbon/epoxy substructure with a balsa core sandwich deck. The bridge comprises of two parallel treadways, with gap-crossing capability up to 12 m for MLC 100 (90,720 kg). The CAB has been proven to be lighter as compared to the existing bridging systems from the same load class. Currently, there is a complete CAB weighing 4763 kg with total length of 12 m (Robinson, 2008).

Figure 10: Field testing of CAB by MLC 100 vehicle (Robinson, 2008).

3.3 Short Span Fiber Reinforced Composite (FRC) Bridge

Robinson *et al*. (2008) from University of California have developed and tested a short span FRC bridge with length of 5.6 m, width of 0.76 m and weight of 177 kg. The bridge was designed to support load of MLC 30. Apart from serving as the short span bridge, the bridge can be used for others applications such as decking system, roadway matting, and overlaying of damaged bridge deck. It has been proven that the bridge is capable of supporting load of MLC 30 and Palletized Load System (PLS) vehicles.

Figure 11: Proof test of Short Span FRC Bridge using whiffle tree (Robinson *et al*., 2008).

3.4 Portable Foot Bridge

The portable foot bridge has been developed in Birla Institute of Technology, India to provide a mean for emergency crossing. The bridge's structural member consists of a rectangular hollow beam made of aluminium alloy and a plate of length 1.5 m and 0.5 m width. This bridge is designed for emergency purpose, supporting a load up to 1000 kg. The weight and length of the module are 13.437 kg and 1.5 m, respectively. So, for a bridge length of 9 m, the estimated weight is 80.622 kg. This bridge structure is suitable to be carried by a person (single span configuration) or by a rescue team (multiple span configuration) (Rahul & Kumar, 2014).

Figure 12: Portable foot bridge in multi span configuration (Rahul & Kumar, 2014).

3.5 Hybrid Fiber Reinforced Polymer (FRP)-Aluminium Modular Bridge

Zhang *et al*. (2013) have developed a lightweight space truss bridge with a modular structure catered for emergency purposes. A hybrid FRP-aluminium space truss structure was implemented in the design of a single-span simply supported one-lane bridge with a span length of 12 m and width of 3.2 m. Each rut was designed as a triangular cross section with 1.2 m width and 0.85 m depth, and linked up by transverse braces. The bridge comprises of an aluminium deck supported by FRP and aluminium trussed members. The bridge is capable to support a load of 10 tonnes, while the total weight of the bridge is only 1.2 tonnes.

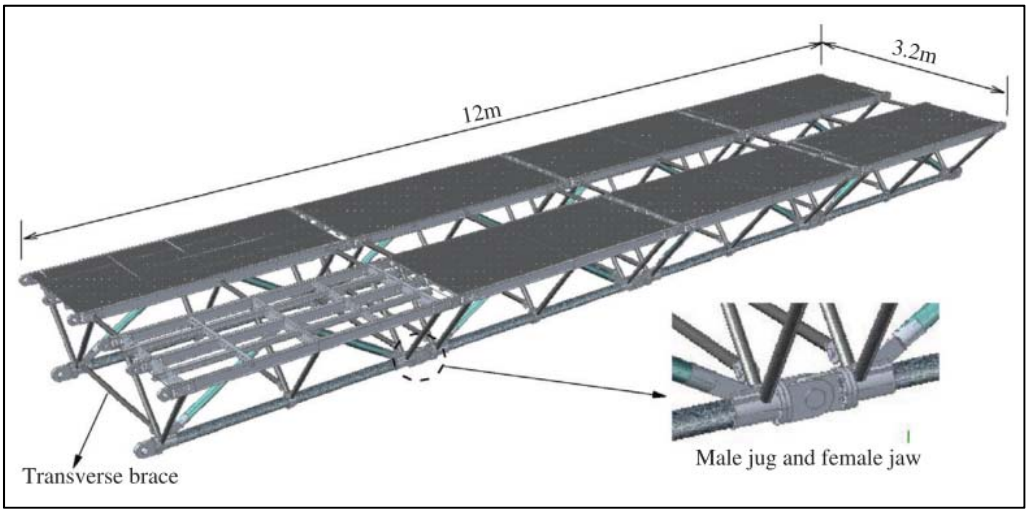

Figure 13: Illustration of Hybrid FRP-Aluminium Modular Bridge (Zhang *et al*., 2013).

3.6 Carbon Fiber Reinforced Polymer (CFRP) Portable Bridge

Agusril & Norazman (2013) have developed a portable bridge, which is consisting of two foldable beams by using Carbon Fiber Reinforced Polymer (CFRP) and aluminium honeycomb. Each beam consists of three sections connected by steel joints that allow the beam to be folded for storage and mobility. The unfold bridge is 30 m in length and the predicted weight is 5852 kg. The fabrication of the beam has been performed by using the wet hand lay-up method. From the analysis, the bridge of two beams is able to support an ultimate load of up to 470 kN (or MLC50).

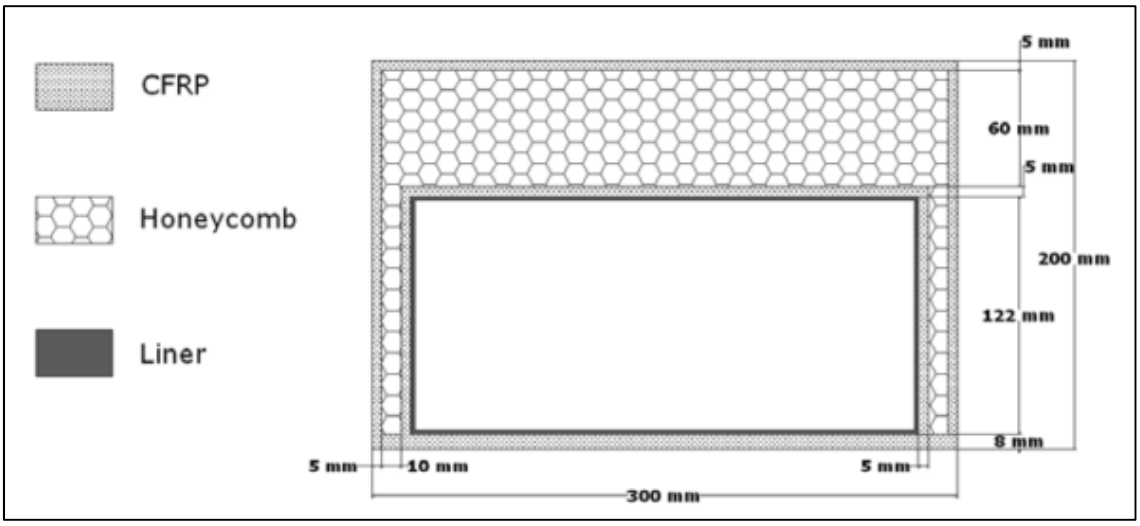

Figure 14: Cross section of CFRP Portable Bridge Beam (Agusril & Norazman, 2013).

3.7 Single Span Military Bridge

Recently, Azrul (2014) has developed a single span military bridge structure by using the 6061-T6 aluminium alloy as the main material. The bridge is a girder type with 41.1 m length and 4 m width, and it is able to carry a *Pendekar* tank vehicle load (MLC 70). The total weight of this bridge is 31 tonnes. The design of the military bridge is based on the operational requirements provided by the Malaysian Army and as outlined in the Trilateral Design and Test Code (TDTC) for Military Bridge and Gap-Crossing Equipment. Structural analysis has been performed by using the Finite Element Method (via MSC PATRAN/NASTRAN simulation software). Structural testing has been performed as well on the scaled-down girder model in accordance with all procedures outlined in the TDTC.

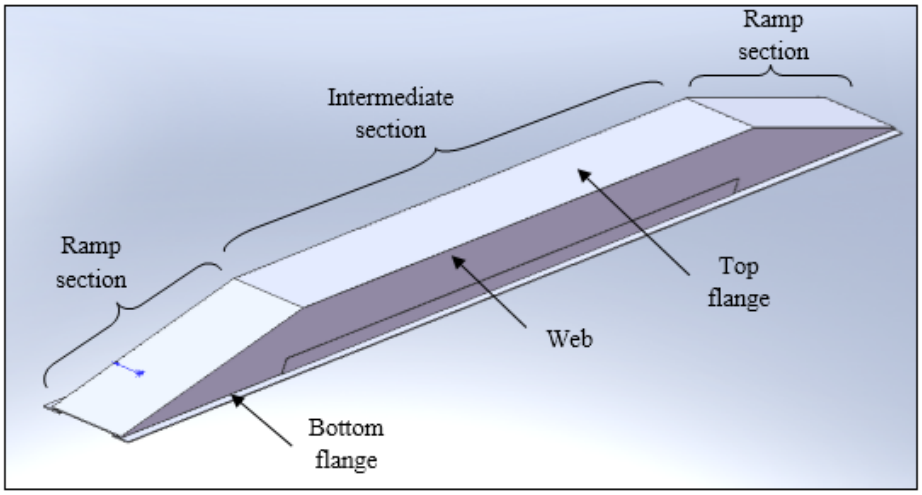

Figure 15: Illustration of the proposed bridge girder (Azrul, 2014).

4. CONCLUSION

This paper has reviewed the state-of-the-art technology of rapid portable bridge, which is dedicated for readers who are working in military and emergency applications. In general, rapid portable bridges vary in terms of function, characteristic, capability, launching method and material used. Recent research and development on rapid portable bridge technology proved that this equipment have a lot of area of improvements, due to the recent advancements in the structural and material engineering. A lighter, stronger and versatile bridge must be designed in order to provide a better prospect in the rapid portable bridge technology. Finally, as a preparation for the increasing trends of disaster occurred around the world, perhaps planner and engineer around the world will start to consider designing a new concept rapid portable bridge system for the next generation.

REFERENCES

Agusril, T. & Norazman, M.N. (2013). Design and testing of carbon fiber reinforced polymer foldable tapered bridge beam. *Aust. J. Basic Appl. Sci.*, **7**: 197-205.

ALVIS. (2004). *Single Span Tactical Bridge* – Illustrated Parts Catalogue. ALVIS Bridging Ltd. United Kingdom.

Azrul Affandhi. (2014). *Analysis and Design of Single Span Military Bridge Using Aluminium Alloy*. Master of Science Thesis. Universiti Pertahanan Nasional Malaysia. Kuala Lumpur.

Tytler, I.F.B., Thompson, N.H., Jones, B.E., Wormell, P.J.H. & Ryley, C.E.S. (1985). *Vehicles and Bridging (Battlefield Weapons Systems & Technology)*. Brassey's Defence Publishers, London.

Constructions Industrielles De La Mediterranee (CNIM). (2006). *Pont Flottant Motorised* – Product Brochure, France.

Zhang, D., Zhao, Q., Huang, Y., Li, F., Chen, H. & Miao, D. (2014). Flexural properties of a lightweight hybrid FRP-aluminium modular space truss bridge system. *Compos. Struct*., **108**: 600–615.

Garcia, R.P. & Lambrecht, S.G. (1999). *Finite Element Analysis of the Armoured Vehicle Launched Bridge (AVLB*). Technical Report No. 13557. US Army Tank Automotive Command. US.

General Dynamics European Land System (2011). *Medium Trackway Bridge*. General Dynamics European Land, Germany.

Hornbeck, B.K., Kluck, J. & Connor, R. (2005). *Trilateral Design and Test Code for Military Bridging and Gap Crossing Equipment*. Defense Technical Information Center (DTIC), Fort Belvoir, Virginia

Hornbeck, B.K. (2009). *Bridging Team Efforts Supporting Current & Future Forces*. US Army Tank Automotive Research Development and Engineering Center.

Jane's. (2010). *Military Vehicles and Equipment*. Available online at: http://www.jane's.com (Last access date: 1 July 2010).

Jetfloat (2010). *Portable Floating Platform*. Jetfloat, Canada.

Jusoh, Z. (2008, December). Tentera bergandingan bahu bantu mangsa tanah runtuh. *Buletin Tentera Darat Malaysia*, Malaysia.

Kosmatka, J.B. (1999). Structural testing of DARPA/BIR composite army bridge treadway. *Compos. Struct*., **4**: 99-115.

KMW (Krauss–Mafeii Wegmann). (2006). *LEGUAN Bridgelayer*. Krauss–Mafeii Wegmann (KMW), Munich.

KMW (Krauss–Mafeii Wegmann). (2009). *The Leguan System*. Available online at: http://www.armedforces-int.com/article/leguan-system.html (Last access date: 6 September 2009).

Lian, Duan and Wai-Fah Chen. (2000). *Bridge Engineering Handbook*. CRC Press, US.

Mabey & Johnson Ltd. (2007). *Technical Notes for Malaysia Compact 100 Logistic Bridge*. Mabey & Johnson Ltd.., Gloucestershire, UK.

Malaysian Army (2016). *Laporan Bantuan Jurutera Dalam Operasi Bencana Alam*. Malaysian Army HQ, Kuala Lumpur.

Malaysian Army (2009). *Format Keperluan Staf Am (KESAM)*. Malaysian Army HQ, Kuala Lumpur.

Mazzolani, F.M. (1994). *Aluminium Alloy Structures, 2nd Ed*. E & FN SPON. Chapman & Hall. London.

Mazzollani, F.M. (2004). Structural use of aluminium alloys in civil engineering. *Proceedings of the 2nd International Conference on Structural Engineering, Mechanics and Computation (SEMC)*, Cape Town, South Africa.

Ministry of Defence (2004). *Aluminium Alloy (7019) for Structural (Non-Armour) Application*. Defence Standard, Ministry of Defence, UK.

MSC Patran (2007). *User's Guide of Basic Dynamic Analysis*. MSC Software Corporation, Newport Beach, California.

Norazman M.N, Agusril, T., Alias, Y., Risby, S. & Ahmad, M.A.Z (2011). Analysis of sandwiched composite long-span foldable beam. *World J. Eng.*, **19**: 877-878.

Rahul & Kumar, K. (2014). Design and optimization of portable foot bridge. *Procedia Eng*., **97**: 1041-1048.

Rasyid, A. (2008, March). *Tentera Bantu Mangsa Banjir di FELDA Selancar*. Utusan Malaysia. Malaysia.

Robinson, M.J. & Kosmatka, J.B. (2008). Development of a short-span fiber-reinforced composite bridge for emergency response and military applications. *J. Bridge Eng.*, **13**: 388-396.

Robinson, M.J. & Kosmatka, J.B. (2008). Lightweight fiber-reinforced polymer deck panels for extreme applications. *J. Compos. Constr.*, **12**: 344-354.

U.S Army (2002). *FM 3-34.343: Nonstandard Fixed Bridging Field Manual*. Headquarters Department of Army. U.S

Wight R.G., Erki M.A., Shyu C.T., Tanovic R. & P.J Heffernan P.J. (2006). Development of FRP short span deployable bridge: Experimental result. *J. Bridge Eng*., **11**: 489-498.

QUASI-STATIC INDENTATION BEHAVIOUR OF KENAF BAST FIBRE REINFORCED METAL LAMINATE SYSTEM

Sivakumar Dhar Malingam[1*], Nisallini Pilvamangalam[1], Omar Bapokutty[1], Sivarao Subramonian[2] & Mohd Zulkefli Selamat[1]

[1]Centre for Advanced Research on Energy, Faculty of Mechanical Engineering
[2]Faculty of Manufacturing Engineering
Universiti Teknikal Malaysia Melaka (UTeM), Malaysia

[*]Email: sivakumard@utem.edu.my

ABSTRACT

Fibre Metal Laminate (FML) is hybrid material that has the combined advantages of metallic materials and fibre reinforced matrix. It has been widely used in the aircraft industry for impact prone applications due to its excellent fatigue and impact resistance. This research focuses on the quasi-static indentation behaviour of fibre metal laminates based on NaOH treated and untreated kenaf bast fibre with fibre loading wt% of 50, 60 and 70 and fibre length in cm of 3, 6 and 9. Aluminium 5052-O has been used as the skin layers of FML in this study. Hot compression moulding method has been used to fabricate the composite and FML panels for this study. The prepared specimens were tested in accordance with ASTM D 6264 using Instron 5585 universal testing machine to assess their quasi-static indentation performance. The results revealed that treated FMLT-60(9) with fibre loading 60wt% and fibre length of 9cm exhibited the highest energy absorption at 30.82 J.

Keyword: *Fibre metal laminate; thermoplastic; indentation; kenaf fibre; quasi-static.*

1. INTRODUCTION

Over the past decade, there has been an increasing interest in developing high-performance and lightweight structures for impact prone applications in numerous engineering sectors especially aerospace and motorised industries. The low fatigue strength of the aluminium alloys and the problems related to the damage tolerance in fibre reinforced composites (FRPs) has called for the development of a hybrid material which is known as fibre metal laminate (FML). These hybrid materials can overcome the limitations of metals and FRPs by combining composites and conventional metallic alloys (Vogelesang & Vlot, 2000). FML is a hybrid structure consisting of thin sheets of metallic alloy sandwiching a FRP layer. The FMLs as shown in Figure 1 have collective benefits of fibres in the composite material which acts as a barrier against crack propagation and of metallic materials which improves the ductility and impact resistance properties of the structure (Cortes & Cantwell, 2006). According to prior studies, it was found that FMLs are nearly 20-30% lighter than monolithic aluminium (Chai & Manikandan, 2014; Dharmalingam *et al*., 2014; Sivakumar *et al*., 2016; Sivakumar *et al*., 2017). Furthermore, the FMLs offer additional advantages such as superior fatigue toughness and impact damage tolerance in contrast to conventional metals (Santiago *et al*., 2017). A series of localised blast loadings conducted by detonating PE4 plastic explosive shows FML has tremendous potential in resisting explosion (Langdon *et al*., 2007; Lemanski *et al*., 2007).

The past decades have seen the rapid development of several types of FMLs such as the Aramid fibre reinforced Aluminium Laminate (ARALL), the Glass Laminate Aluminium Reinforced Epoxy (GLARE)

and the Carbon Reinforced Aluminium Laminates (CARALL) (Sinmazçelik *et al*., 2011). FMLs used in aerospace industry were based on thermoset-based polymer matrices, which is stronger and stiffer with enhanced performance in high temperature applications. However, thermoset-based FMLs require long processing cycle whereas thermoplastic-based FML offers low manufacturing cost since it requires short processing cycle (Cortes & Cantwell, 2006). Composton *et al*. (2001) found that the thermoplastic-based FMLs require nearly 23% more specific energy to perforate than thermoset-based FMLs during impact loading. Thus, the use of thermoplastic-based FMLs has been growing in recent years as it is considered as potential alternatives for thermoset-based FMLs.

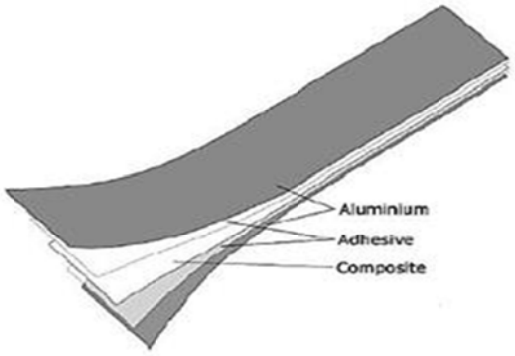

Figure 1: A sample of FML layup (Dharmalingam *et al.* 2009).

New regulations on environment and the growing concerns in reducing the use of petroleum based products in the production of engineering materials have led to the development of composites based on natural fibres such as kenaf, coir, hemp, sisal and jute (Ramesh, 2016; Ng *et al*., 2017). The application of natural fibres in composite materials has been driven by the need of manufacturing eco-friendly materials due to its biodegradable and low cost characteristics (Vieira *et al*., 2017). Kenaf is the common name for *hibiscus cannabinus* which is originated from Africa. Kenaf bast fibres have low density and exhibit high specific mechanical properties which make them suitable for structural applications (Avella *et al*., 2008; Sivakumar *et al*., 2017). It has been shown that kenaf fibres possess excellent potential and economic feasibility for future applications (Cieh *et al*., 2017; Sulaiman *et al*., 2017). Furthermore, flexibility is one of the significant technical characteristics of kenaf fibres, which enhances their energy dissipation capabilities, damage tolerances and impact resistance properties (Salman *et al*., 2017). Previous research on the kenaf fibre reinforced polypropylene composites has provided insights of its tensile and flexural strength as well as its applications in several industries such as automotive and aerospace industry (Zampaloni *et al*., 2007).

Numerous experimental works have been reported on the quasi-static response of the natural fibre reinforced FMLs. Abdullah *et al*. (2014) investigated the indentation fracture behaviour of fibre metal laminates based on kenaf/epoxy with varying thicknesses and the FML lay-ups. It was concluded that thickness and lay-up of the FMLs have a significant effect on their energy absorbing properties where the increasing number of lay-up and thickness led to improved energy absorption as well as better resistance towards deformation. More recently, Pang *et al*. (2015) studied the indentation behaviour of fibre metal laminates based on kenaf/epoxy with different loading rate. It was found that the maximum contact force and energy absorption of FMLs increased with the increment of loading rate. Yahaya *et al*. (2014) conducted an experimental work to determine the quasi-static penetration properties of non-woven kenaf fibre/Kevlar reinforced epoxy hybrid composite for ballistic armour spall-liner application. Significant improvement in term of energy absorption and the resisting load was found when a layer of kenaf mat

was placed in between two layers of high strength Kevlar fabric. Moreover, the outer Kevlar fabrics can resist the shear plug formation and prolong the load-displacement curve. To date, limited research studies were established on the natural fibre reinforced thermoplastic-based FML. This research presents an experimental study on the quasi-static indentation behaviour of kenaf bast fibre reinforced polypropylene metal laminates (KFML). The response of the KFML under quasi-static loading is evaluated, where the effect of fibre loading, length and treatment are studied.

2. METHODOLOGY

2.1 Composite and FML Preparation

In this research, kenaf bast fibres were used as the reinforcement while polypropylene (PP) granules were used as the matrix. The PP granules used in this study has a density of 0.95 g/cm^3 was supplied by Basell Asia Pacific Ltd, Malaysia. The chemical treated fibres were prepared by soaking in 5% Sodium Hydroxide (NaOH) solution at room temperature for 4 hours to produce a clean and rough surface on the fibre. Chemical treatment enhances the interfacial bonding of polymer and kenaf fibre owing to the better interlocking between fibres and matrix (Mahjoub *et al*., 2014). The fibres were then filtered out and washed with tap water until the traces of sodium hydroxide were removed. The treated fibres were then dried at room temperature overnight followed by drying in an oven at 40 °C for 24 h. The fibres were then cut into short pieces with three different lengths; 3, 6 and 9 cm. The PP sheets were prepared by compressing PP granules in a 200 mm × 200 mm × 1 mm (width × length × thick) picture frame mould using the hot press machine at 175 °C. Random kenaf fibre mats were formed by compressing the fibres at 180 °C for 2 min according to the respective fibre length and compositions. The fibre mats and PP sheets are then stacked alternately in a picture frame mould with a size of 200 mm × 200 mm × 3 mm. It was then compressed for 8 min at a temperature of 180 °C and pressure of 5 MPa in the hot press machine to form composite panels with a consistent thickness of 3 mm as shown in Figure 2. The 0.5 mm thick aluminium 5052-O sheets were cut to a dimension of 200 mm x 200 mm. To increase adhesion level between the aluminium and the composite, the surface of aluminium sheets was mechanically coarsen using sandpaper grit size 80. KFMLs with 2/1 configuration was formed by stacking two aluminium layers to the composite in which a 0.05 mm thick modified PP adhesive sheet was placed between the layers of aluminium and the composite panels as shown in Figure 3. The prepared FML assembly was subjected to hot compression moulding process at the temperature of 170 °C and pressure of 0.4 MPa for 10 min. The KFML panel was removed upon reaching room temperature. The composition of KFMLs prepared for this research is presented in Table 1. The KFML panels were cut using a shearing machine according to dimension shown in Figure 4.

2.2 Quasi-Static Indentation Test

The quasi-static indentation test was repeated three times to study the damage mechanism and energy absorption of KFMLs. The indentation tests were conducted with reference to the ASTM D 6264 using Instron 5585 universal testing machine with a 150kN load cell. A series of quasi-static tests were performed using 12.7mm diameter hemispherical tip indenter in an edge supported configuration. The KFML samples were bolted between the top plate and bottom support plate by four screws with sufficient force to prevent slippage of the specimen during the test as shown in Figure 5. The load versus displacement curves were recorded, at a crosshead displacement rate of 1.25 mm/min. The energy dissipation was calculated by integrating the area under the curve. The specimens were then visually examined to analyse the failure mechanisms.

Figure 2: Kenaf reinforced polypropylene composite.

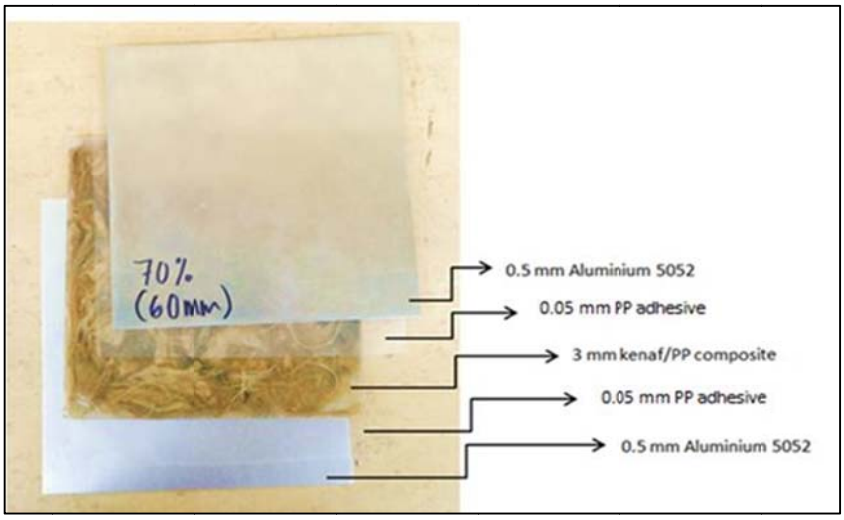

Figure 3: Typical stacking sequence of KFML.

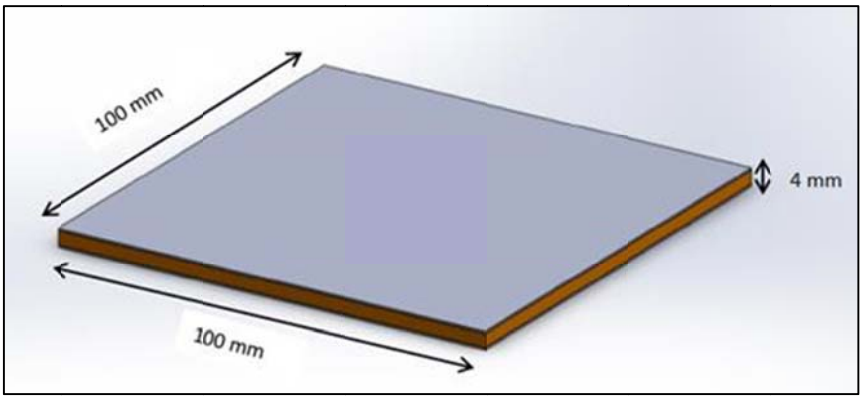

Figure 4: Schematic illustration of the specimen for quasi-static indentation test.

Table 1: Specifications of the KFMLs fabricated.

Specimen code	Fibre weight (%)	Fibre length (cm)	Fibre treatment
UT-50(3)	50	3	Untreated
UT-60(3)	60		
UT-70(3)	70		
UT-50(6)	50	6	
UT-60(6)	60		
UT-70(6)	70		
UT-50(9)	50	9	
UT-60(9)	60		
UT-70(9)	70		
T-50(3)	50	3	Treated
T-60(3)	60		
T-70(3)	70		
T-50(6)	50	6	
T-60(6)	60		
T-70(6)	70		
T-50(9)	50	9	
T-60(9)	60		
T-70(9)	70		

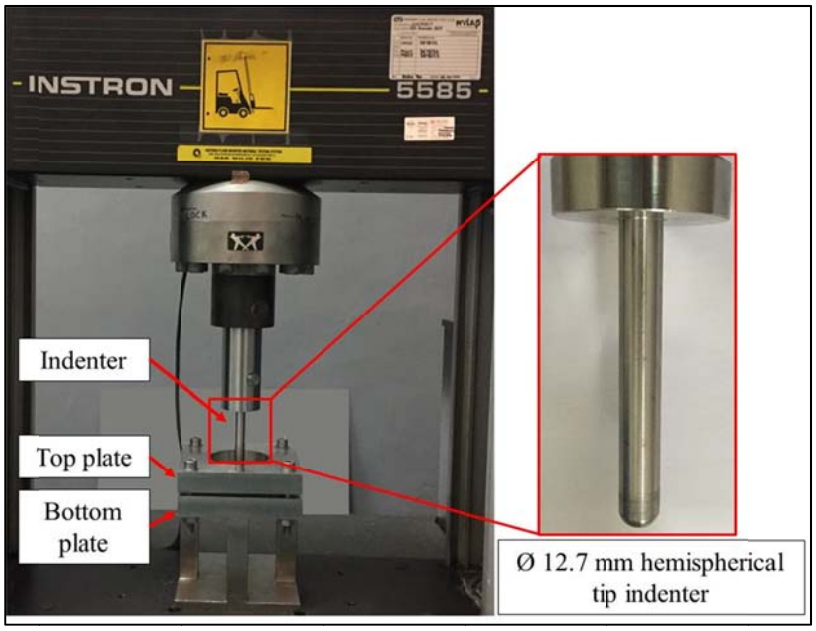

Figure 5: Quasi-static indentation test setup.

3. RESULTS AND DISCUSSION

Quasi-static indentation experiment was performed to study the effect of kenaf bast fibre length, loading and treatment on the energy absorption and damage mechanisms of KFMLs. Figures 6 and 7 show the average load versus displacement curves for each composition of FMLs with untreated and treated kenaf fibres respectively.

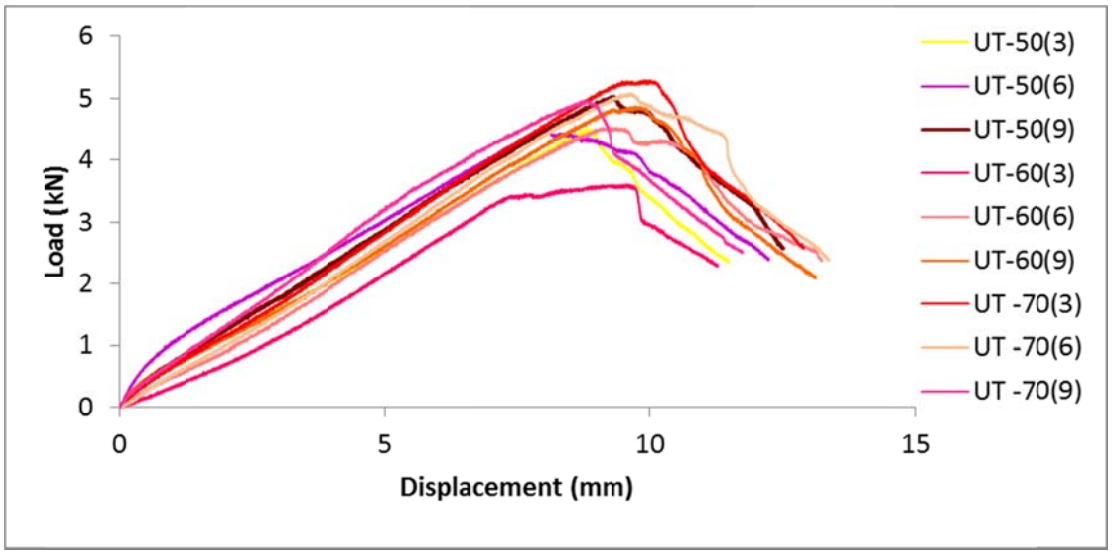

Figure 6: Load versus displacement curves of KFMLs with untreated fibre.

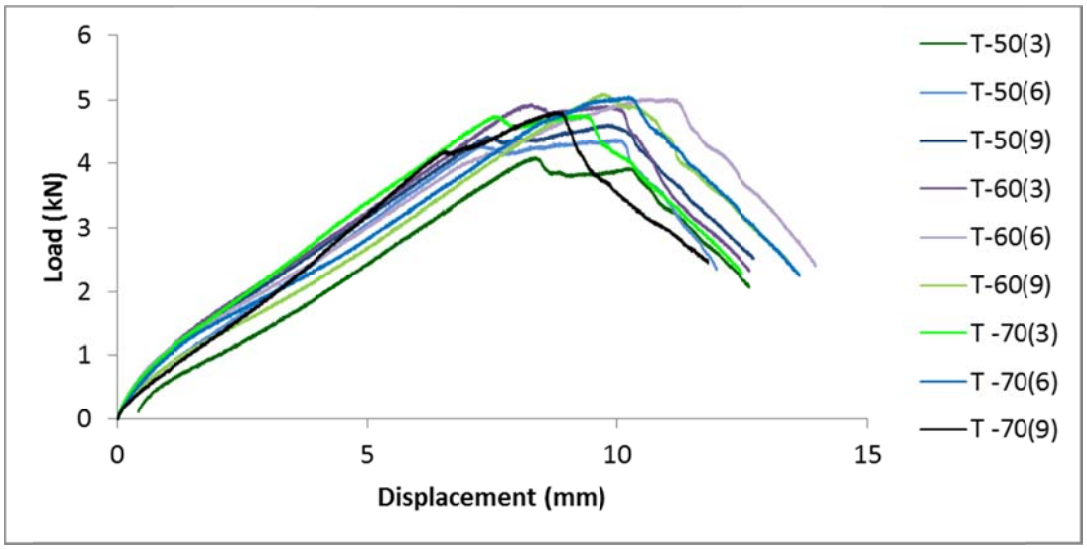

Figure 7: Load versus displacement curves of KFMLs with treated fibre.

These curves exhibit similar trend but with a different maximum load for each specimen tested. The trend of the load versus displacement curve can be divided into three distinct phases as indicated in Figure 8. Initially, the curve increases linearly with displacement up to a knee point. Beyond the knee point, the curve continued to increase in a non-linear behaviour until a maximum peak load is achieved. The initial increase in load is due to the plastic deformation of the indented surface (top surface) of the FMLs. The indenter then moves through the composite thickness of the FMLs by pushing the top aluminium sheet through the matrix and kenaf fibres to the bottom surface. Finally, when the indenter penetrates the bottom aluminium sheet, the curve plummeted drastically. This marks the failure of the specimens. The maximum load-carrying capacities were found to vary with each composition of FML tested, as shown in Figure 9. Figure 10 shows the average maximum energy absorbed during the quasi static indentation measured by integrating the area under the force versus displacement curves up to respective maximum load. The average maximum load and maximum energy for each composition tested are summarised in Table 2.

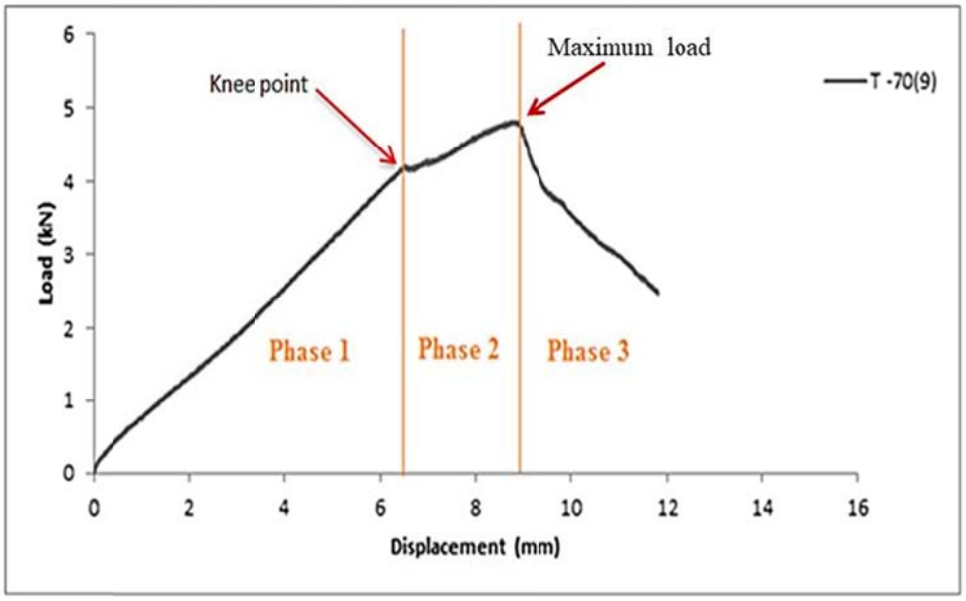

Figure 8: Phases of a load versus displacement graph for FML with 70% weight composition of 9mm untreated kenaf fibre.

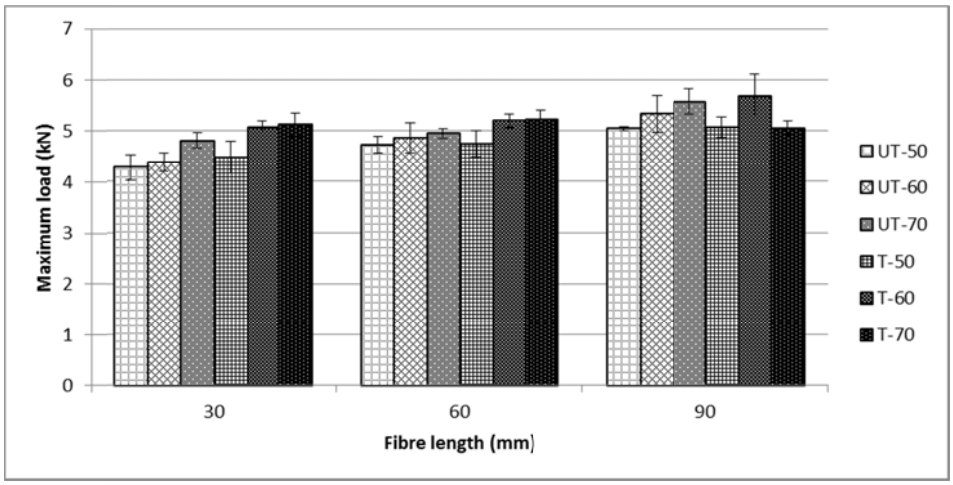

Figure 9: Maximum quasi-static indentation load.

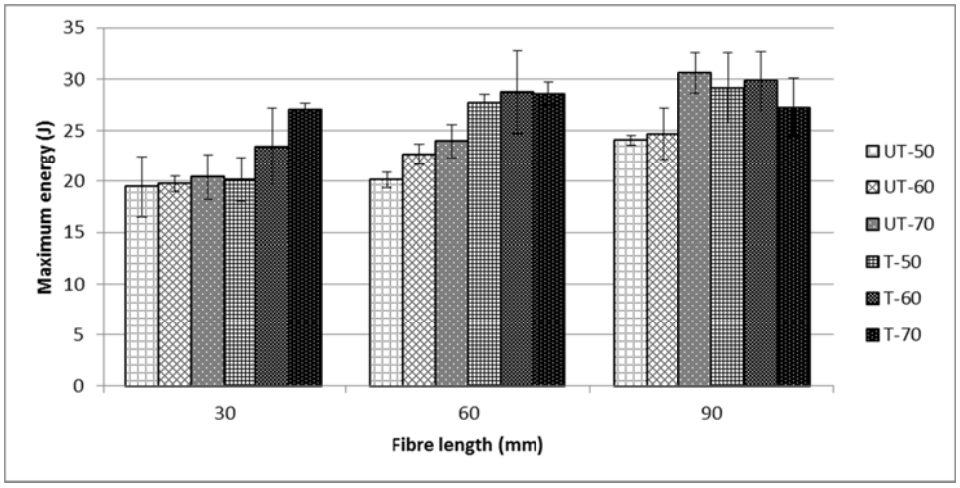

Figure 10: Maximum quasi-static indentation energy.

Table 2: Maximum load and energy absorption of quasi-static indentation**.**

Specimen code	Maximum load (kN)	Maximum energy (J)
UT-50(3)	4.27 ± 0.25	19.48 ± 2.93
UT-60(3)	4.38 ± 0.18	19.79 ± 0.77
UT-70(3)	4.81 ± 0.15	20.43 ± 2.22
UT-50(6)	4.72 ± 0.16	20.14 ± 0.78
UT-60(6)	4.86 ± 0.30	22.67 ± 1.03
UT-70(6)	4.95 ± 0.10	23.98 ± 1.62
UT-50(9)	5.04 ± 0.04	24.05 ± 0.46
UT-60(9)	5.33 ± 0.36	24.66 ± 2.52
UT-70(9)	5.57 ± 0.25	30.58 ± 1.97
T-50(3)	4.48 ± 0.31	20.18 ± 2.17
T-60(3)	5.07 ± 0.11	23.42 ± 3.76
T-70(3)	5.12 ± 0.23	27.06 ± 0.62
T-50(6)	4.74 ± 0.26	27.74 ± 0.77
T-60(6)	5.20 ± 0.13	28.76 ± 3.98
T-70(6)	5.21 ± 0.2	28.61 ± 1.10
T-50(9)	5.07 ± 0.19	29.21 ± 3.41
T-60(9)	5.68 ± 0.42	30.82 ± 1.83
T-70(9)	5.05 ± 0.16	27.28 ± 2.84

It is evident that the maximum penetration load of FMLs increases as the fibre length increases for both treated and untreated fibre. FMLs with 50 wt% untreated fibre loading (UT-50) and 50 wt% treated fibre loading (T-50) showed an average increase of 4.92 and 0.60% respectively in terms of the maximum load when the fibre length was increased from 3cm to 9cm. This may be due to uneven stress distribution along the fibre when shorter fibre was used. Shorter fibre form more fibre ends that act as stress concentration points which will eventually lead to fibre breakage followed by a crack on the matrix and metal layer (Farahani *et al*., 2012). Thus, certain fibre length is required to ensure efficient and uniform distribution of stress between fibre, matrix and metal layer in FMLs.

The maximum energy absorbed is generally higher in FMLs with treated kenaf fibre compared to FMLs with untreated fibre irrespective of fibre loading and length. The maximum energy absorption for FMLs with 70 wt% treated 3 cm kenaf fibre, T-70(3) indicated an improvement of 32.5% compared to FMLs with 70 wt% untreated 3 cm kenaf fibres, UT-70(3). The trend was similar for FMLs with 6cm kenaf

fibres at 50 wt% loading where the maximum energy recorded for FMLs T-50(6) is 37.7% higher than FML UT-50(6). The result is consistent with the study conducted by Bakar et al. (2010) that noted the improvement in mechanical properties of composite reinforced with treated kenaf fibre. The increase in energy absorption properties of FMLs can be explained in terms of fibre-matrix interfacial bonding. Alkaline treatment performed on kenaf fibres removes lignin hemicelluloses and impurities from the fibre surfaces. This increases the surface area of kenaf fibre and provides better interlocking between the polymer and fibre. Thus, FMLs with treated fibres has stronger fibre-matrix interfacial bonding compared to FMLs with untreated fibres. However, for FML with 9cm kenaf fibre at 70 wt% loading, the ones with treated kenaf fibre showed a decline of 10.79% in maximum energy absorbed in comparison to FMLs with untreated fibre.

In terms of fibre loading, it is observed in Figure 10 that the overall energy absorbing properties of FMLs increases as the fibre weight percentage increases for both treated and untreated kenaf fibre. For instance, the maximum energy absorbed by FMLs with treated 3cm kenaf fibre recorded an increment of 16.1% when the fibre loading was increased from 50 to 60 wt%. The energy absorption rose by 15.5% when the fibre loading was further increased to 70 wt%. As the fibre content in FMLs increases, more energy was required to weaken the fibre-matrix interfacial bonding. However, for certain combination, the value of maximum energy absorbed reduces when the fibre content was increased beyond 60 wt%. The maximum energy absorbed by FML T-70(9) was 11.5% lower than FML T-60(9).The increased fibre content results in agglomeration of fibres which disrupts the distribution of stress along the fibres (Tay *et al*., 2012). In general, FML T-60(9) recorded the highest energy absorption at 30.82 J, indicating that this configuration provides a better penetration resistance compared to other configurations tested.

4. DAMAGE MECHANISM

Post-test examination of the selected specimens was performed in the rear and indented surface to analyse the failure mechanisms during the quasi-static indentation tests for various fibre loading. The photographs of specimens are presented in Figure 11. In general, all three specimens showed similar failure mechanism where the initial failure started from a dent on the indented surface. It was then followed by a small crack on the aluminium sheet placed on the rear surface. The size of the indentation increased along with the crack length on the rear surface as the load increases. This causes the formation of a second crack that propagated in a perpendicular direction to the initial crack.

Cracks at the rear surface of the specimens were also observed to be longer in comparison to cracks on the indented surface which indicated that the rear surface exhibited more deformation compared to the indented surface as the indenter moves through the composite thickness of the FMLs. It is also visible in Figure 11, the presence of petaling failure on the rear surface of the all three specimens examined. The petaling failure is caused by of crack propagating away from the centre point which was subjected to the pressure of penetrating indenter during indentation. However, a circular crack that replicates the shape of the indenter which is a result of aluminium sheets and kenaf fibre being pushed through the rear surface as the load increases is visible in Figure 11(c).

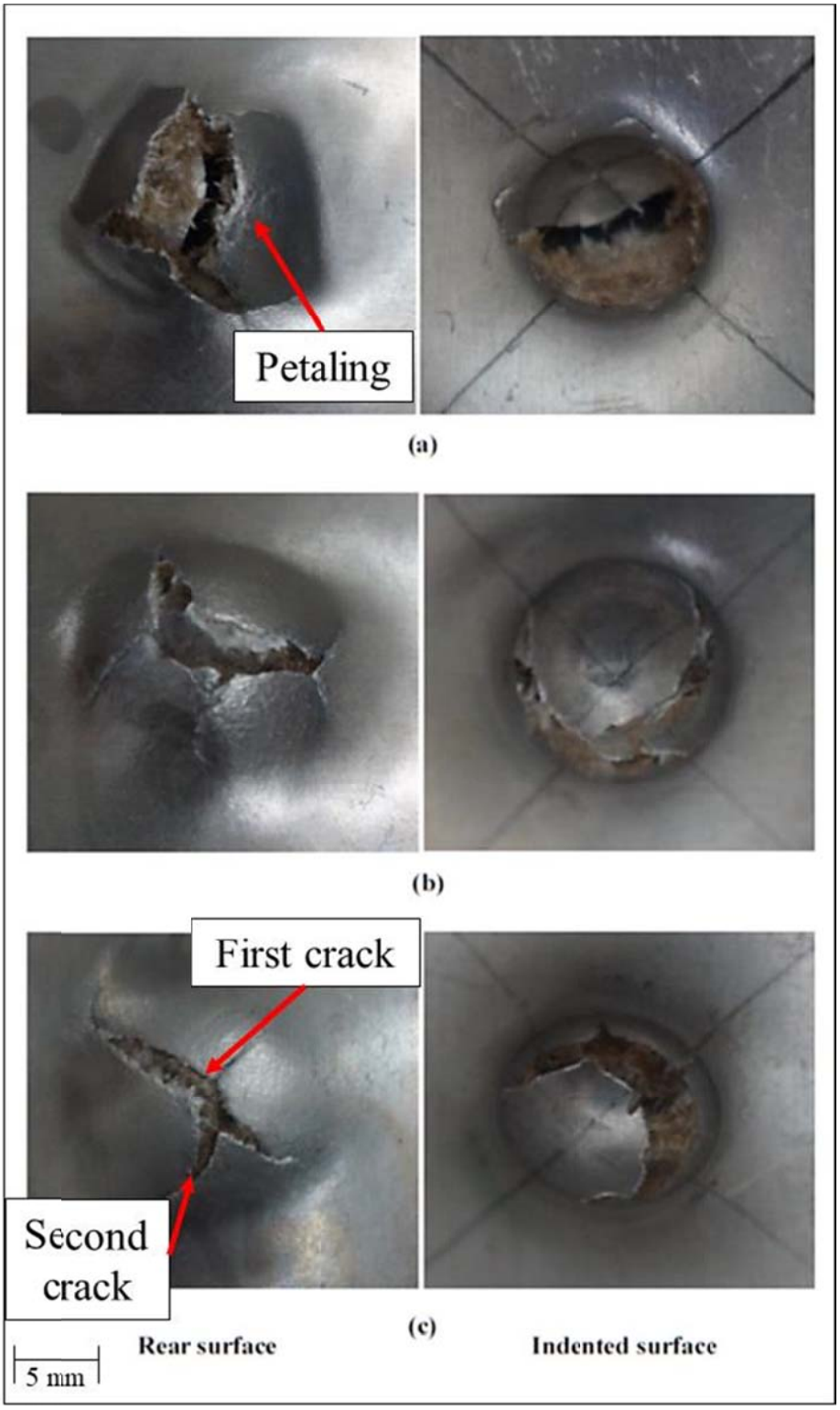

Figure 11: Photographs of indented FMLs (a) T-50(3) (b) T-60(3) (c) T-70(3).

4. CONCLUSION

The effect of fibre length, loading and treatment of kenaf bast fibre reinforced metal laminates on the energy absorption under quasi-static indentation loading and the damage mechanisms were investigated. Based on the results, the following conclusions were drawn. FMLs reinforced with treated kenaf fibre recorded an average of 19% increments in energy absorption and 4% increments in maximum load compared to FML reinforced with untreated kenaf fibre. This study has found that FMLs with a fibre length of 9 cm showed better energy absorbing properties compared to FMLs with a fibre length of 6cm and 3 cm regardless of fibre treatment and loading. FML reinforced with 50 wt% untreated 9cm kenaf fibre absorbed 30.59 J of energy which is 19.4 and 23.5% higher than FML reinforced with untreated 6 and 3cm kenaf fibre respectively at similar loading. Likewise, FML reinforced with 60% treated 9cm kenaf fibre recorded an increment of 7.16 and 31.6% in energy absorption compared to the ones with treated 6 and 3cm fibre respectively at similar fibre loading. The second major finding was that the energy absorption properties of FMLs increases as the fibre weight percentage increases from 50 to 70% regardless of fibre length and treatment. The energy absorbed by FML reinforced with 60 wt% treated 3 cm kenaf fibre was 16.1% higher than FML reinforced with 50 wt% treated 3 cm kenaf fibre. Similarly, there was an increment of 15.5% in energy absorption when the treated fibre loading is further increased to 70 wt% at similar fibre length.

ACKNOWLEDGEMENT

Authors would like to thank Universiti Teknikal Malaysia Melaka for the continuous support on this research project. Authors would also wish to express their gratitude towards grant FRGS/1/2015/SG06/FKM/03/F00276 from Ministry of Higher Education Malaysia.

REFERENCES

Abdullah, M.R., Pang, C.L., Husain, N.A. & Abdi, B. (2014). Indentation Fracture Behaviour of Fibre Metal Laminates Based on Kenaf/Epoxy. *Int. Rev. Mech. Eng*., **8**: 265-270.

Avella, M., Bogoeva-Gaceva, G., Bužarovska, A., Errico, M.E., Gentile, G. & Grozdanov, A. (2008). Poly (lactic acid) based biocomposites reinforced with kenaf fibers. *J. Appl. Poly. Sci.,* **108**: 3542-3551.

Bakar, A., Ahmad, S. & Kuntjoro, W. (2010). The mechanical properties of treated and untreated kenaf fibre reinforced epoxy composite. *J. Biobased Mater. Bio*., **4**: 159-163.

Chai, G.B. & Manikandan, P. (2014). Low velocity impact response of fibre-metal laminates–A review. *Compos. Struct*., **107**:363-81.

Cieh, N.L., Sulaiman, S., Mokhtar, M.N. & Naim, M.N. (2017). Bleached kenaf microfiber as a support matrix for cyclodextrin glucanotransferase immobilization via covalent binding by different coupling agents. *Process Biochem.* **56**: 81-89.

Compston, P., Cantwell, W.J., Jones, C. & Jones, N. (2001). Impact perforation resistance and fracture mechanisms of a thermoplastic based fiber-metal laminate. *J. Mater. Sci. Lett.* **20**: 597–599.

Cortes, P. & Cantwell, W.J. (2006). The prediction of tensile failure in titanium-based thermoplastic fibre–metal laminates. *Compos. Sci. Technol.*, **66**: 2306-2316.

DharMalingam, S., Compston, P. & Kalyanasundaram, S. (2009). Process Variables Optimisation of Polypropylene Based Fibre-Metal Laminates Forming Using Finite Element Analysis. *Key Eng. Mater*., **410**: 263-269.

DharMalingam, S., Sivaraos, Selamat, M.Z., Said, M.R. & Kalyanasundaram, S. (2014). Effects of Process Parameters during Forming of Glass Reinforced-pp based Sandwich Structure. *Adv. Environ. Biol*., **20**: 3143-3150.

Farahani, G.N., Ahmad, I. & Mosadeghzad, Z. (2012). Effect of fiber content, fiber length and alkali treatment on properties of kenaf fiber/UPR composites based on recycled PET wastes. *Polym. Plast. Technol. Eng*., **51**: 634-639.

Langdon, G.S., Lemanski, S.L., Nurick, G.N., Simmons, M.C., Cantwell, W.J. & Schleyer, G.K. (2007). Behaviour of fibre–metal laminates subjected to localised blast loading: Part I—Experimental observations. *Int. J. Impact Eng.,* **34**: 1202-1222.

Lemanski, S.L., Nurick, G.N., Langdon, G.S., Simmons, M.C., Cantwell, W.J. & Schleyer, G.K. (2007). Behaviour of fibre metal laminates subjected to localised blast loading—Part II: Quantitative analysis. *Int. J. Impact Eng.,* **34:** 1223-1245.

Mahjoub, R., Yatim, J.M., Sam, A.R.M. & Raftari, M. (2014). Characteristics of continuous unidirectional kenaf fiber reinforced epoxy composites. *Mater. Des.*, **64:** 640-649.

Ng, L.F., Sivakumar, D., Zakaria, K.A. & Selamat M.Z. (2017). Fatigue performance of hybrid fibre metal laminate structure. *Int. Rev. Mech. Eng.* 11: 61-68.

Pang, C.L., Husain, N.A. & Abdullah, M.R. (2015). Effect of loading rate on indentation behaviour of fibre metal laminates based on kenaf/epoxy. *Appl. Mech. Mater.* **735**: 26-30.

Ramesh, M. (2016). Kenaf (Hibiscus cannabinus L.) fibre based bio-materials: A review on processing and properties. *Prog. Mater. Sci.*, **78**: 1-92.

Rodi, R. (2012). *The residual strength failure sequence in fibre metal laminates*. PhD Thesis, Department of Mechanics, Aerospace Structures & Materials, Delft University of Technology, Netherlands.

Salman, S.D., Leman, Z., Ishak, M.R., Sultan, M.T.H. & Cardona, F. (2017). Quasi-static penetration behavior of plain woven kenaf/aramid reinforced polyvinyl butyral hybrid laminates. *J. Ind. Text.,* **0:** 1-20.

Santiago, R., Cantwell, W. & Alves, M. (2017). Impact on thermoplastic fibre-metal laminates: Experimental observations. *Compos. Struct.*, **159**: 800-817.

Sinmazçelik, T., Avcu, E., Bora, M. Ö., & Çoban, O. (2011). A review: Fibre metal laminates, background, bonding types and applied test methods. *Mater. Des*, **32**: 7, 3671-3685

Sivakumar, D., Kathiravan, S., Selamat, M.Z., Said, R. & Subramonian, S. (2016). A study on impact behaviour of a novel oil palm fibre reinforced metal laminate system. *ARPN J. Eng. Appl. Sci*., **11**: 2483-2488.

Sivakumar, D., Ng, L.F., Selamat, M.Z. & Sivaraos. (2017). Investigation on fatigue life behaviour of sustainable bio-based fibre metal laminate. *J. Mech. Eng.*, **1**: 123-140.

Sivakumar, D., Ng, L.F., Lau, S.M. & Lim, K.T. (2017). Fatigue life behaviour of glass/kenaf woven-ply polymer hybrid biocomposites. *J.Polym. Environ*. Epub ahead of print 24 February 2017. DOI: 10.1007/s10924–017–0970–0.

Sulaiman, S., Cieh, N.L., Mokhtar, M.N., Naim, M.N. and Kamal, S.M.M. (2017). Covalent immobilization of cyclodextrin glucanotransferase on kenaf cellulose nanofiber and its application in ultrafiltration membrane system. *Process Biochem.* **55:** 85-95.

Tay, G.S., Azniwati, A.A., Azizah, A.B., Rozman, H.D. & Musa, L. (2012). The flexural and impact properties of kenaf-polypropylene composites filled with montmorillonite filler. *Polym. Plast. Technol. Eng.*, **51**: 208-213.

USA Standard Association. (1998). ASTM D6264-98. *Standard test method for measuring the damage resistance of a fiber reinforced polymer-matrix composite to a concentrated quasi-static indentation force*. Standards Association International, USA.

Vieira, L.M.G., Santos, J.C., Panzera, T.H., Rubio, J.C.C. & Scarpa, F. (2017). Novel fibre metal laminate sandwich composite structure with sisal woven core. *Ind. Crops Prod*., ***99***: 189-195.

Vogelesang, L.B. & Vlot, A. (2000). Development of fibre metal laminates for advanced aerospace structures. *J. Mater. Process. Technol.*, **103**: 1-5.

Yahaya, R., Sapuan, S.M., Jawaid, M., Leman, Z. & Zainudin, E.S. (2014). Quasi-static penetration and

ballistic properties of kenaf–aramid hybrid composites. *Mater. Des.*, **63**: 775-782.
Zampaloni, M., Pourboghrat, F., Yankovich, S.A., Rodgers, B.N., Moore, J., Drzal, L.T., Mohanty, A.K. & Misra, M. (2007). Kenaf natural fiber reinforced polypropylene composites: a discussion on manufacturing problems and solutions. *Compos. Part A- Appl. S.*, ***38***: 1569-1580.

VIBRATION MONITORING ON BALL BEARING OPERATED UNDER HEXAGONAL BORON NITRIDE (hBN) NANOPARTICLES MIXED WITH DIESEL ENGINE OIL

Noor Shakinah Rudzlan Apandi & Rainah Ismail*

Faculty of Mechanical Engineering, Universiti Teknikal Malaysia Melaka (UTeM), Malaysia.

*Email: rainah@utem.edu.my

ABSTRACT

The aim of this research is to determine the vibration characteristic on ball bearing operated with the hexagonal boron nitride (hBN) nanoparticles mixed with diesel engine oil types SAE 15W40. The vibration monitoring condition and finite element analysis are carried out to validate the performance of hBN nano-lubricant as an additive in the reduction of vibration amplitudes with different volume of concentrations of hBN. It is found that the significant and non-synchronous peaks of new and defected bearing in the numerical approach show excellent predictive agreement with the experimental work. Conclusively, both methods are capable to predict the vibration behaviour of the new and defected bearings, and hBN nanoparticles can be a promising additive in lubricant for vibration reduction.

Keywords: *Rolling element bearing; hexagonal boron nitride; vibration condition monitoring.*

1. INTRODUCTION

Helicopter transmissions, turbine engines, missile trucks power train and aircraft components are important area where monitoring methods are needed in order to detect performance deterioration, damage or emerging failure, and to detect the source of the problem and foresee its sequence of failure. The generated data sources from condition monitoring are include direct physical inspection, non-destructive material inspection techniques, examination of lubricating oil and oil borne wear debris are gained while the machine is in operation. Among all, the most commonly used parameter is machine vibration. Vibration analysis has been widely used for evaluating the condition of gear transmissions and bearing failure since different, distinct meshing frequencies can be identified and spectrum analysis using the Fourier Transform analyser has effectively become a standard technique for this purpose (Swansson & Favaloro, 1984).

Rolling element bearing is a bearing that is known to be capable of withstanding high loads under extreme conditions and pressure. However, this type of bearing often causes problems due to overuse, extreme vibrations or improper upkeep. Bearing type is directly correlated to vibration measurements because excessive vibrations will lead to excessive forces and will harm the bearing life and performance (Prakash *et al.,* 2013). Therefore, a suitable lubricant is needed to ensure the longevity of the rolling bearing by reducing vibration levels, temperature and pressure. Nowadays, finding a new additive has attracted a great deal of interest amongst researchers in search of a suitable lubricant that can reduce both wear and friction coefficient (Greenberg *et al.,* 2004).

Nanoparticles are nano-oil additives and are one of the most promising additives of all. A low concentration of nanoparticles is sufficient to improve the tribological properties (Ay *et al.,* 2016). Abdullah *et al.* (2013) found that a 0.5 vol% concentration of hexagonal boron nitride (hBN) nanoparticles provided the best anti-wear behaviour and friction reduction. Wan *et al.* (2015) found that the best concentration of boron nitride was 0.1 wt%, which produced the best anti-wear behaviour

and friction reduction. Friction reduction and anti-wear behaviour are dependent on the characteristics of the nanoparticles, such as size, shape and concentration. This is because the size of the nanoparticles can range from 2 to 120 nm (Qiu *et al.,* 2001; Wu *et al.,* 2007; Li *et al.,* 2011). Many studies have been conducted on the tribological performance of lubricants mixed with nanoparticles. However, there have been very limited studies on the vibration measurements of ball bearings in order to justify the performance of mixing nanoparticles into the base oil. Until now, none of this research has provided clarification of the hBN nanoparticle on reduction in vibration amplitude. Hence, the goal of this paper is to determine the effect of hexagonal boron nitride nanoparticles on reducing the vibrations of ball bearings. The originality of this research stemmed from the fact that low vibrations lead to lower costs and are more environmentally friendly. Furthermore, nanoparticles mixed with conventional diesel engine oil will enhance the performance of machines and the durability of bearings. Yadav *et al.* (2013) an early researcher in this field, studied the effect of unbalanced forces for a cylindrical rolling element bearing with eight (number of) rollers. It was concluded that route to chaos, is an intermittent mechanism due to periodic doubling behaviour. Tiwari *et al.* (2000) investigated the effects of an unbalanced rotor, supported by a deep groove ball bearing (SKF 6002) having nine (number of) balls. It was concluded, that the frequency spectra displayed multiples of 1X and VC and the linear combination of the two frequencies. Experimental analysis, finite element analysis and structural dynamics were used to analyse the dynamic properties of the bearing structure.

Many research works have been done in the field of signal analysis in rolling element bearing. Patel *et al.* (2014) in their research, conducted a study on the failure analysis of ball bearings by the creation of artificial cracks of different sizes on various elements. In addition, their study was extended to a Finite Element Analysis to study the peaks at its outer and inner ring defect frequencies. They concluded that with constant defect sizes and constant loads with various speeds, the amplitudes increased. Kadarno *et al.* (2008) investigated the effect of defect sizes and the vibration signal responses of defected bearings compared with normal bearings. The pattern from the simulation was found to have similar characteristics to experimental data. Similar to their findings, Ding *et al.* (2015) investigated the level of vibration responses of ball bearings having different sized defects on the outer races using explicit dynamic analysis in ABAQUS. Liu *et al.* (2015) also investigated the impact of shape defects, radial load and shaft speed using explicit dynamic finite element analysis.

Therefore, in this paper, the vibration suppression characteristic of ball bearing supplied with hBN nanoparticles additives in engine diesel oil will be investigated. This vibration study could validate and further improve performance of diesel engine oil when mixed with hBN nanoparticle.

2. CHARACTERISTIC BEARING DEFECT FREQUENCIES

The vibrations generated by bearing faults appear at different frequency range. Periodically occurring transient pulses are produced at frequencies determined by the bearing geometry and speed. The frequencies of transient pulses depend on the characteristic frequencies of the bearing. The vibrations of ball bearing with defect can be detected at various characteristic defect frequencies which can be calculated by using the formula as follows:

$$BPFO = \frac{N_b}{2} f_s \left(1 - \frac{B_d}{P_d} \cos \phi \right) \tag{1}$$

$$BPFI = \frac{N_b}{2} f_s \left(1 + \frac{B_d}{P_d} \cos \phi \right) \tag{2}$$

$$NB = \frac{\omega N}{60} \tag{3}$$

where N_b is the number of balls, f_s is the shaft speed in rpm, P_d is the pitch diameter in mm, B_d is the ball diameter in mm and ϕ is the contact angle. The rolling element and outer race fault experience variation in load while passing through the load zone. This has effect of modulating the impulse train

by either the ball pass outer race frequency or the cage speed. For roughness fault, it is no longer impulsive, but rather has a randomly distributed phase, since the rolling elements are on different position on the rough surface discrete multiple points for every revolution.

2.1 Calculation of Bearing Frequencies

Bearing frequencies for the new and defected bearings can be calculated as follow;

i. New bearing (Fundamental frequency)

$$f_{NB} = \frac{\omega N}{60}$$

$$f_{NB} = \frac{\omega(1440)}{60}$$

$$f_{NB} = 25Hz$$

ii. Outer defected bearing, OD

$$BPFO = \frac{N_b}{2} f_s \left(1 - \frac{B_d}{P_d}\cos\phi\right)$$

$$f_{BPFO} = \frac{0.4nX}{60}$$

$$f_{BPFO} = \frac{0.4(1440)(9)}{60}$$

$$f_{BPFO} = 86.4Hz$$

iii. Inner defected bearing, ID

$$BPFI = \frac{N_b}{2} f_s \left(1 + \frac{B_d}{P_d}\cos\phi\right)$$

$$f_{BPFI} = \frac{0.6nX}{60}$$

$$f_{BPFI} = \frac{0.6(1440)(9)}{60}$$

$$f_{BPFI} = 129.6Hz$$

3. EXPERIMENTAL WORK

3.1 Sample Preparation

In this research, hBN nanoparticles of 70 nm size is prepared by dispersing different volume concentrations of 0.2, 0.5 and 1.0 vol.% into the SAE 15W40 diesel engine oil. The samples are homogenized by using an ultrasonic homogenizer (Sartorius Labsonic P) for 30 minutes with a 50% amplitude and an active interval of 0.5 (as shown in Fig. 1). The specifications of SAE 15W40 which is used as a lubricant in heavy duty diesel and marine motor oils is shown in Table 1.

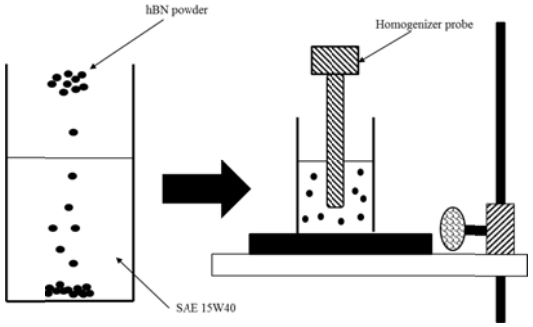

Figure 1: Ultrasonic homogeniser.

Table 1: Properties of SAE 15W40 diesel engine oil.

Properties	SAE 15W40
Kinematic viscosity @40°C, m^2s^{-1}	1.06 X 10^{-4}
Kinematic viscosity @100°C, m^2s^{-1}	1.35 X 10^{-5}
Viscosity index	127
Flash point temperature, °C	218
Total base number (TBN)	7.38
Total acid number (TAN)	4.70

The photographs shown in Figure 2 are the final product of the nano-oil for the different volume concentrations of hBN nanoparticles mixed with diesel engine oil.

0.2 vol% of hBN **0.5 vol% of hBN** **1.0 vol% of hBN**

Figure 2: Final products of nano-lubricants.

3.2 Vibration Test

The main components of the experimental setup used are a motor, flexible coupling, ball bearings and a lubricant container. The shaft is connected to the DC motor using the flexible coupling and supported the bearing. All the components are mounted on a steel channel which is welded together to avoid unwanted vibrations. The steel channel had a heavy-duty caster for easy mobility. A DC electric motor of 1 Horse Power (Volt-240V, Current-2.3 A) with an operating speed of 1,440 rpm is used. An accelerometer mounted on top of the bearing housing vertically was used to measure the radial vibration. The accelerometer is equipped with the portable and rugged data acquisition device, SignalCalc Ace, powered by the Quattro hardware platform. Quattro is connected to a host personal computer or laptop through USB 2.0 connectivity as illustrated in Figure 3.

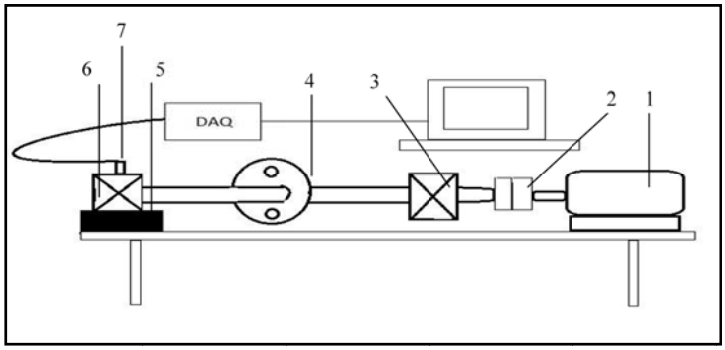

1-Single phase motor; 2-Flexible coupling;3-Healthy bearing;4-Rotating mass; 5-Lubricant storage;6-Tested bearing;7-Accelerometer

Figure 3: The schematic layout of the vibration test.

Time domain signals acquired from the SignalCalc is interpreted by using the Fast Fourier Transform (FFT) within MATLAB software to obtain the frequency domain graph.

3.3 Bearing Geometry

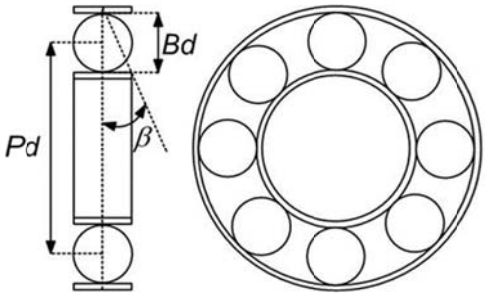

Figure 4: Schematic diagram of single deep groove ball bearing. (http://www.skf.com/in/products/bearings-units-housings/ball-bearings/deep-groove-ball-bearings/single-row/index.html)

Single row deep groove ball bearings SKF 6206 as shown in Figure 4 is used in this research because of its versatility, overall performance and the fact that it is widely used. It is also characterized by having deep raceway grooves in which the inner and outer rings have circular arcs of a slightly larger radius than that of the balls. The parameter detail of the bearing used is given in Table 2.

Table 2: The ball bearing parameters details.

Bearing specification SKF 6206	
Outer diameter, D	62 mm
Inner diameter, d	30 mm
Pitch diameter, P_d	35 mm
Ball diameter, B_d	10 mm
Outer ring width, B	16 mm
Number of ball, N_b	9
Contact angle, α	0^0

In this research, three bearings of different conditions are taken into consideration, which are a new bearing, a 0.5 mm outer defected bearing and a 0.5 mm inner defected bearing. The artificial defect is done by using the milling process with a computer numerical control (CNC) machine (as shown in Figure 5)

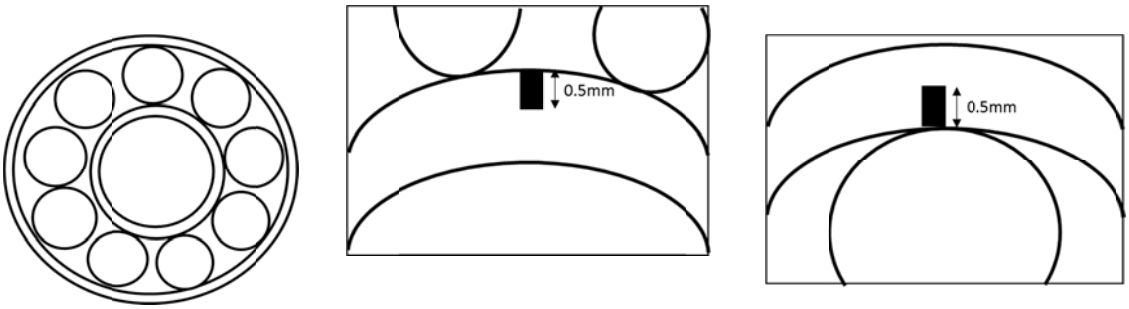

(a) New bearing (b) 0.5 mm outer defected bearing(c) 0.5 mm inner defected bearing

Figure 5: Schematic diagrams of new and defected bearing.

3.4 Experimental Results

Experimental results on vibration measurement of the ball bearings are obtained and discussed in this section. The vibration amplitudes are measured at the various concentrations of hBN used, conditions of the bearings and the unbalanced mass applied to the rotor. The desired significant and non-synchronous peaks for new and defected bearings are determined experimentally. These amplitudes are measured at the bearing characteristic fault frequencies. These bearing frequencies can be estimated from the theoretical formula mentioned in the previous section. Figure 6 shows the schematic diagram of unbalanced loads on the rotor applied at the centre of the shaft.

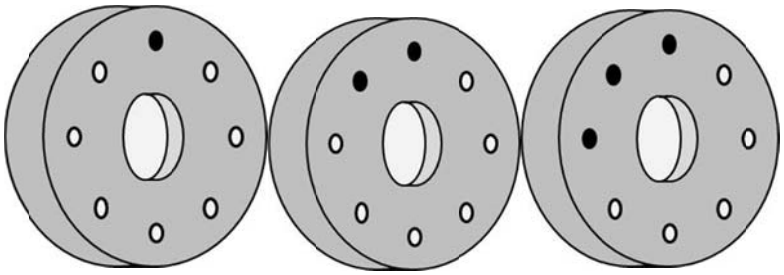

Figure 6: Schematic diagram of the position of unbalanced mass applied on the rotor.

3.4.1 Significant and Non-Synchronous Peak for Bearing System

Significant peak is the peak appeared to show the actual speed of the induction motor and theoretically appeared on the 1X significant peak. The ball passing frequency at which to expect the rolling element problems will depend on the number of the ball. The specific frequencies on the outer defected bearing appeared on the 3X non-synchronous peak while for the inner defected bearing, the non-synchronous peak came up on 5X non- synchronous peaks and the results are tabulated in Table 3.

Table 3 : Significant and non-synchronous peaks.

Theoretical value	Experimental results
New bearing f_{nb}=25 Hz	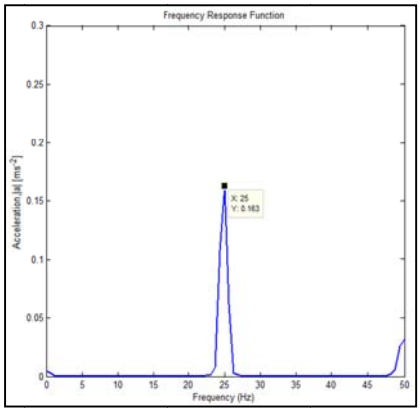
Outer defected bearing f_{bpfo}=86.4 Hz	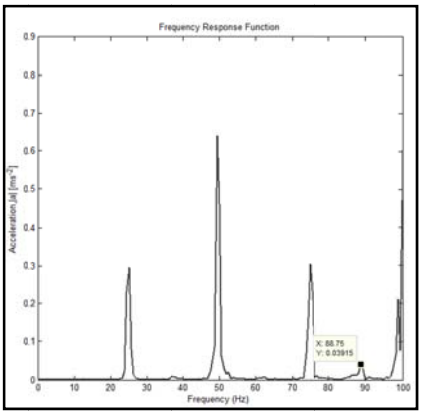
Inner defected bearing f_{bpfi}=129.6 Hz	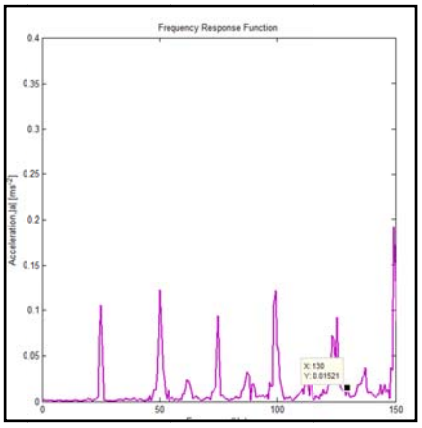

3.4.2 Frequency Domain Graph

Frequency domain graph for the 0.0 vol%, 0.2 vol%, 0.5 vol% and 1.0 vol.% of concentration of hBN for the new bearing condition is illustrated in Figure 7. From the graph, it can be seen that the new bearing shows significant peak at 1X which is known as fundamental frequency. The amplitude obtained was 0.163 ms^{-2}, 0.141 ms^{-2}, 0.276 ms^{-2} and 0.278 ms^{-2} at 25 Hz for the new bearing

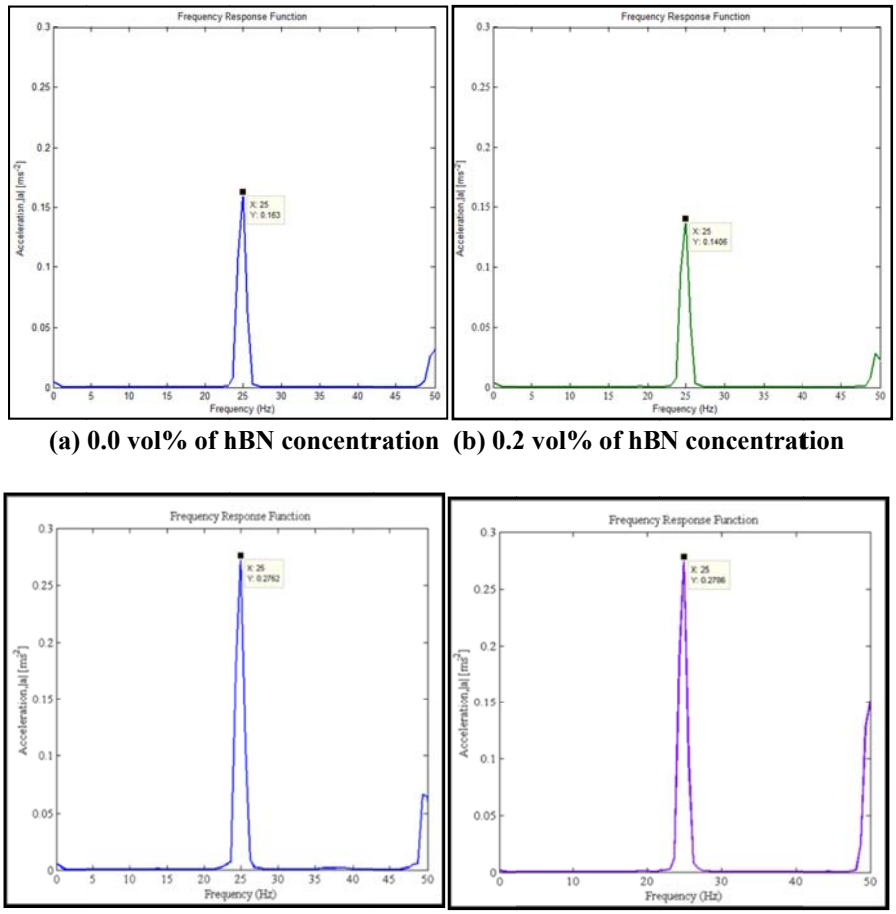

(a) 0.0 vol% of hBN concentration (b) 0.2 vol% of hBN concentration

(c) 0.5 vol% of hBN concentration(d) 1.0 vol% of hBN concentration

Figure 7: Frequency domain graph for new bearing.

There was an increase in the peak amplitude of vibrations when the outer defected bearing was used as shown in Figure 8. The bearing characteristic fault frequency for the outer defected bearing is 86.4 Hz theoretically. Meanwhile, the vibration amplitudes obtained for 0.0 vol%,0.2 vol%, 0.5 vol% and 1.0 vol% are 0.039 ms^{-2}, 0.022 ms^{-2}, 0.033 ms^{-2} and 0.038 ms^{-2} respectively. These values are taken from the 3 x BPFO frequency.

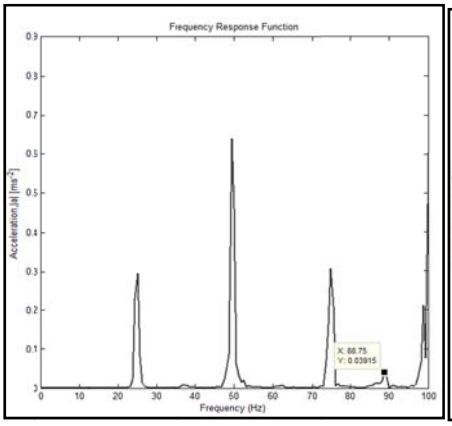

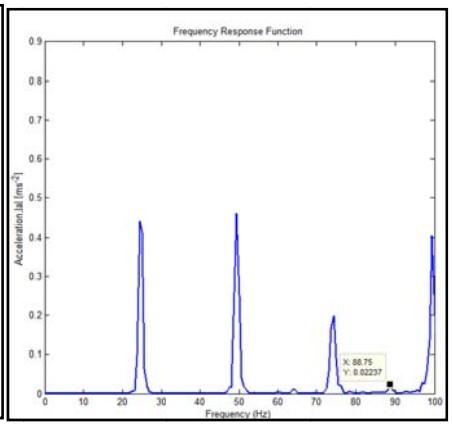

(a) 0.0 vol% of hBN concentration (b) 0.2 vol% of hBN concentration

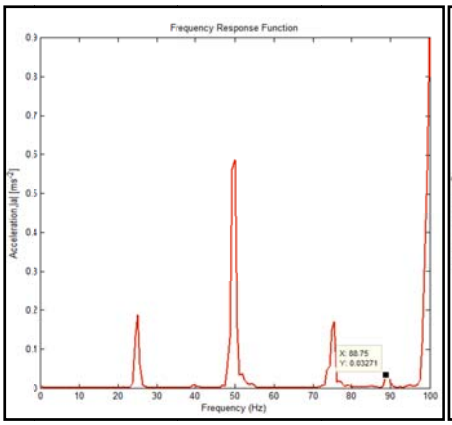

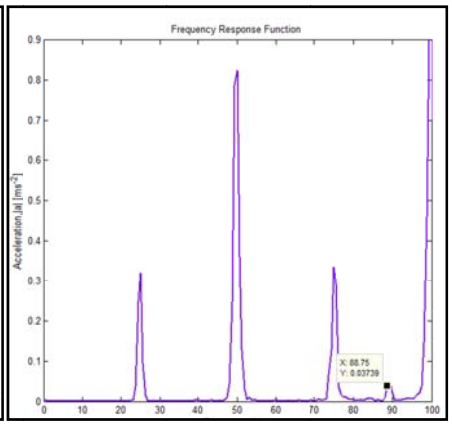

(c) 0.5 vol% of hBN concentration(d) 1.0 vol % of hBN concentration

Figure 8: Frequency domain graph for outer defected bearing.

With the inner defected bearing, the non-synchronous peak obtained was 5 x BPFI at a 130 Hz shaft rotation frequency. Thus, the value of BPFI for 0.0 vol%, 0.2 vol%, 0.5 vol% and 1.0 vol% of hBN is 0.015 ms^{-2}, 0.010 ms^{-2}, 0.017 ms^{-2} and 0.019 ms^{-2} respectively as shown in Figure 9. The different vibration amplitudes are measured with the various bearing conditions as tabulated in Table 4.

From Table 4, it is found that a 0.2 vol% concentration of hBN produced the lowest vibration amplitude values for the new and defected bearing. The reduction in vibration amplitudes is due to the spherical shape of the hBN nanoparticles. A rolling motion effect created from this spherical shape can reduce the wear and the vibration of the bearing system. The absorbed nanoparticles may result in the rolling effect between rubbing surfaces, causing the surfaces to roll rather than slide against one another. Therefore, the vibrations are reduced. For the 0.5 vol% and 1.0 vol% concentration of hBN, the agglomeration happened as the volume of concentration of the hBN nanoparticles increased. Therefore, the friction happened between the rubbing surface will increase causing the addition of vibration amplitude value. The significant peaks on new bearing and the non-synchronous peaks which appeared on the inner and outer defected bearings show good predictive agreement with the bearing characteristic fault frequencies. It is also clearly seen that the vibration amplitude for the outer defected bearing is higher compared to the inner defected bearing.

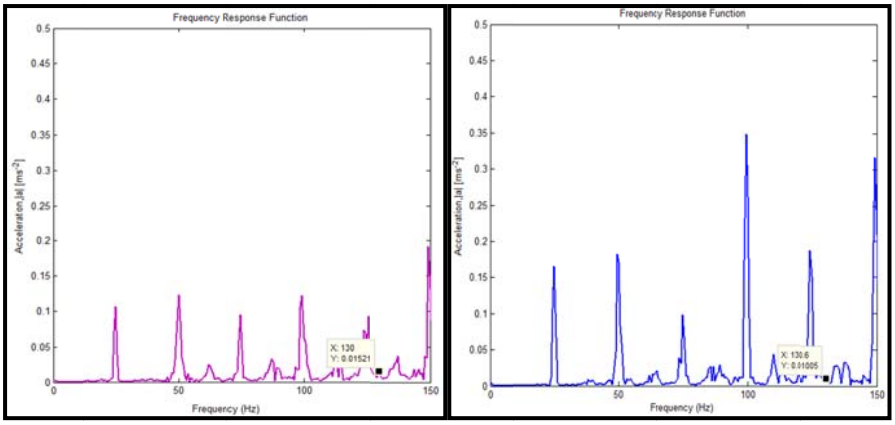

(a) 0.0 vol% of hBN concentration(b) 0.2 vol% of hBN concentration

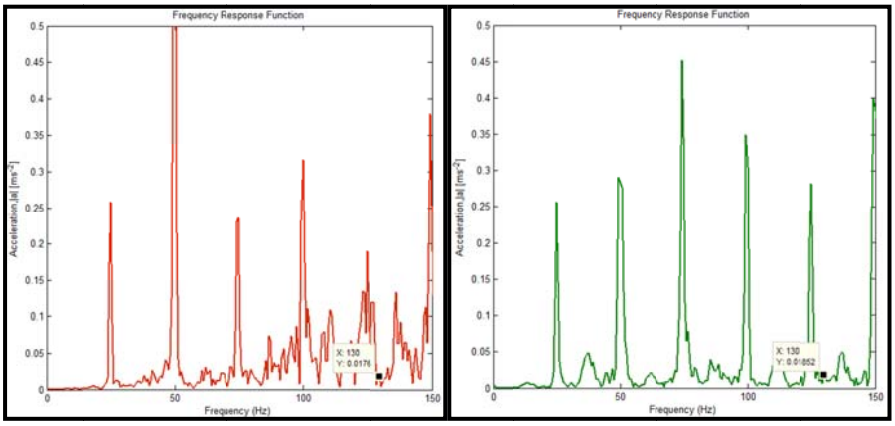

(c) 0.5 vol% of hBN concentration (d) 1.0 vol% of hBN concentration

Figure 9: Frequency response for inner defected bearing.

Table 4: Amplitudes of vibration measurement.

Types of bearing	% volume of hBN concentration			
	0.0%	**0.2%**	**0.5%**	**1.0%**
New bearing	0.163	0.141	0.276	0.279
Outer defected bearing	0.039	0.022	0.033	0.038
Inner defected bearing	0.015	0.010	0.017	0.019

4. NUMERICAL SIMULATION TECHNIQUES: FE METHOD

For reasons of validation and comparison of the experimental work, a finite element model within ANSYS WORKBENCH 16.0 is used for a further bearing analysis in order to corroborate the effect of hBN volume concentrations on the vibration amplitudes as obtained from experimental results. Finite element analysis (FEA) is a numerical technique which can be applied to obtain approximate solutions for a variety of situations in engineering such as a steady state, vibrational, transient, linear and non-linear, fluid flow and others. To perform the finite element analysis, the lubricant of hBN nanoparticles mixed with diesel engine oil is assumed as a frictional force, F_f that is applied at the outer surface of the bearing. This frictional force applied can be calculated from the COF value obtained from the tribological test that has been done.

4.1 Tribological Test

The vibration characteristics of ball bearings depend on various parameters such as bearing conditions, types of concentration, loads and coefficient of friction (COF). Therefore, tribological testing is performed to determine the COF by using a four-ball tester as shown in Figure 10. The procedure followed the ASTM D4172 standard test method. The speed, load, time and temperature used are 1200 rpm, 392.4 N, 3600 seconds and 75^0C respectively. The four-ball tester required three chromium carbon steel ball bearings of 12.7 mm diameter clamped together and covered with the nano-lubricants. The fourth steel ball is held in a collet inside the spindle and rotated together with the AC motor. The top ball is rotated whilst in contact with the other fixed ball which was immersed in the oil sample.

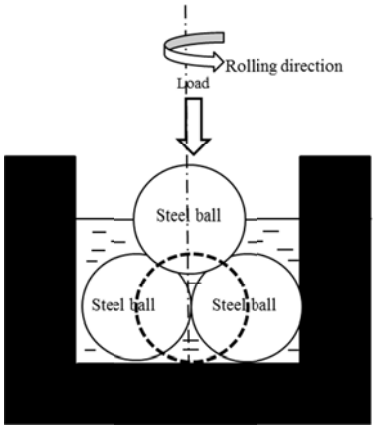

Figure 10: A schematic diagram of four ball testers.

The COF was recorded using a data terminal processing system. Detailed mechanical properties of the balls are shown in Table 5.

Table 5: Mechanical properties of ball bearing.

Properties	**Ball bearing (Carbon-chromium steel)**
Hardness (*H*), HRC	61
Density (*p*), g/cm^3	7.79
Surface roughness R_a, µm	0.022

The COF value acquired for the hBN mixed lubricant with a 0.0 vol%, 0.2 vol%, 0.5 vol% and 1.0 vol% of concentrations was tabulated in Table 6.

Table 6: COF values of the nano-lubricant.

vol% of concentration of hBN	**COF values**
0.0	1.00
0.2	0.09
0.5	0.07
1.0	1.20

4.2 Numerical Approach Using ANSYS

In this research, FEA was specifically carried out using the ANSYS WORKBENCH 16.0 package. For the analysis, 6206 deep groove ball bearing and a shaft were drawn in the CATIA software and the complete model is imported to the ANSYS software as shown in Figure 11.

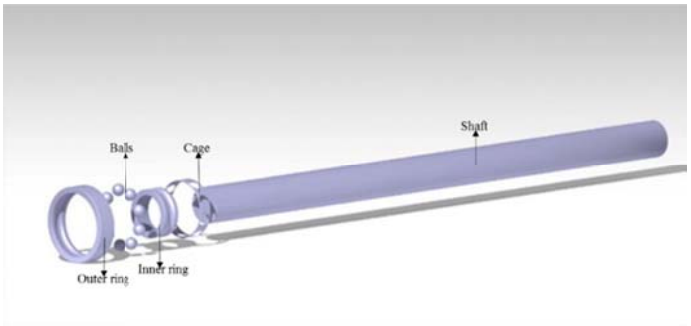

Figure 11: CATIA modeling.

Modal and Harmonic Response analyses are performed to obtain a better response from the bearings. The results are obtained using the frequency response function. The Initial Graphics Exchange Specification (IGES) file is the model bearing system imported from the CATIA V5 software into the ANSYS WORKBENCH 16.0 program. The material and element properties of the model are shown in Table 7. The material used in this study is chrome steel; which is commonly used to manufacture bearings.

Table 7: Properties of bearing system.

Property name	
Name	Chrome steel
Density, ρ	7 800 kg/m^3
Young's Modulus, E	206 GPa
Poisson's ratio, υ	0.33

Figure 12 shows the meshed model for the new and defected bearings. A finite element mesh is generated using both local and global meshing features. Various types of meshing are used in different bearing elements. Tetrahedron (Solid 168) free meshing is used for outer and ball elements and free mapped meshing, Hexahedron (Solid 164), is used for the rest. The meshing is of the hard type, the total number of nodes is 87,378 with the number of elements is 31,947. A fixed boundary condition is applied to the surface of the outer ring.

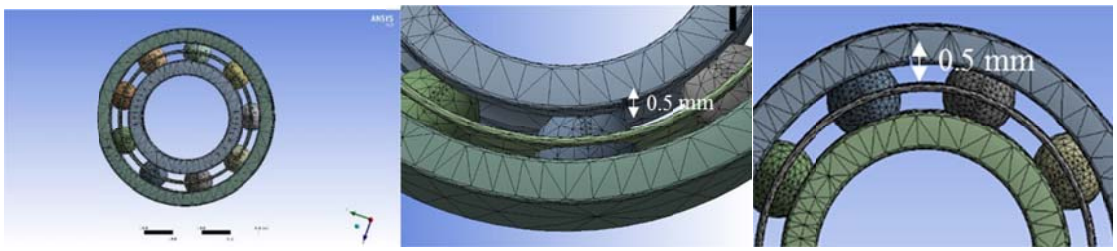

(a) New bearing **(b) 0.5 mm outer defected bearing** **(c) 0.5 mm inner defected bearing**

Figure 12: Meshed model for the bearing system.

The actual speed of the motor is 1440 rpm which is equivalent to 25 Hz, therefore the moment of 5 Nm represent the input torque from the motor. The moment is applied on the shaft as the motor rotates the shaft. In addition, to exhibit the existences of hBN nanoparticles mixed lubricant, the frictional force, $F_f$is applied by calculating the frictional force by using the following equations:

$$F_f = \mu N \quad (4)$$

where μ is the coefficient of friction (COF) and N represents the normal load. The values of F_f are shown in Table 8 and are applied to the surface of the inner ring to represent the movement of the nanoparticles rotating inside the bearing.

Table 8: Frictional force values.

Vol% of concentration of hBN	COF values	F_f values (N)
0.0	1.00	2.00
0.2	0.09	1.80
0.5	0.07	1.40
1.0	1.20	2.40

4.3 Simulation Analysis

Modal analysis is performed to obtain the mode shapes and natural frequencies for the analysis. Then, the frequency responses are obtained from the Harmonic Responses. Table 9 shows a summary for the first three mode shapes for all three types of bearings.

Table 9: Summary of mode shapes for all conditions of bearings.

Types of bearing	Mode shape		
New bearing	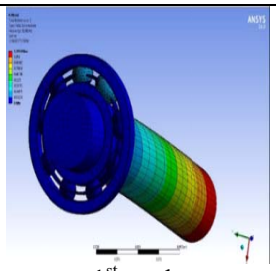 1st mode	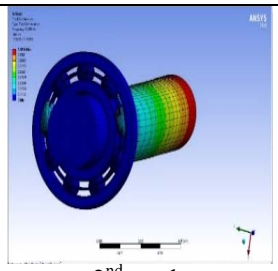 2nd mode	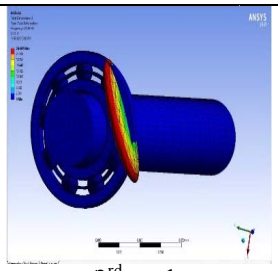 3rd mode
Outer defected bearing	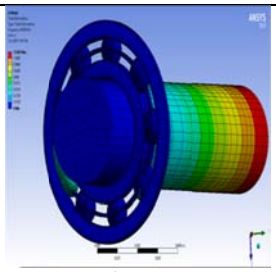 1st mode	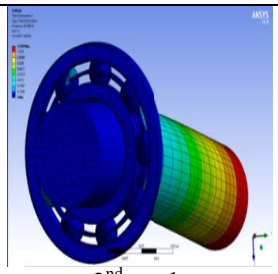 2nd mode	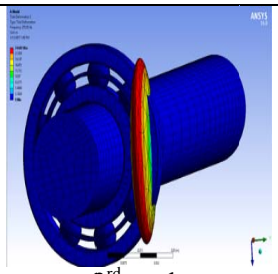 3rd mode

Inner defected bearing	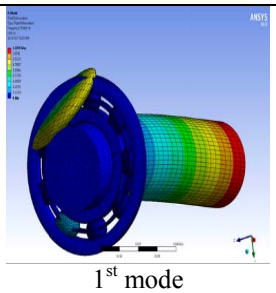 1st mode	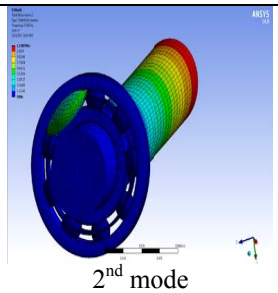 2nd mode	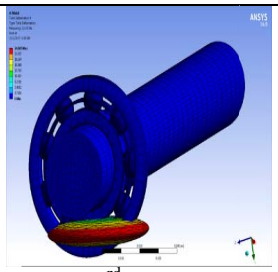 3rd mode

From Table 9, the 1st mode shape for the new bearing shows that a deflection occurred at the end of the shaft. This was due to the rotational speed from the motor applied to the shaft. For the outer defected bearing, the mode shapes showed that deflection occurred on the 2nd mode whereas for the inner defected bearing, the deformation only occurred at the balls, as the defect occurred in the inner surface of the bearing. For new and outer defected bearing, the ball will expand at the 3rd mode to show the rotation of the ball in and out of the zone. The frequency domain graphs from the ANSYS WORKBENCH 16.0 for all bearing conditions are shown in Figure 13.

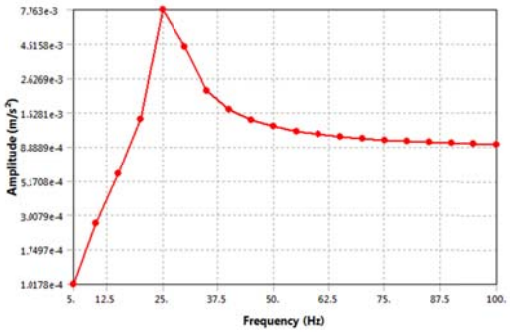

(a) New bearing

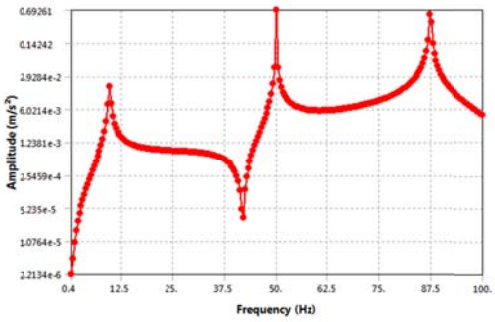

(b) Outer defected bearing

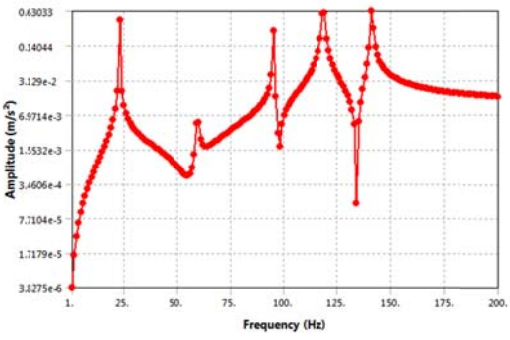

(c) Inner defected bearing

Figure 13: Frequency domain graphs.

Figure 13 shows the vibration responses for the new bearing, outer defected bearing and inner defected bearing. Based on the previous theoretical formula, the defect frequencies can be detected by the significant peak and non-synchronous peaks that appeared on the frequency graph. Fig.13 (a) shows the significant peaks of the fundamental frequency of the bearing system at 1X. Particularly for ball pass frequency outer (BPFO), the non-synchronous peak was detected at 3X as shown in Figure 13(b) as the bearing defects resulted in harmonic, multiples of frequency, of the defected frequencies in the vibration spectrum. The repetitive of the vibration signal of defects can be observed as peaks in the frequency spectrum. Figure 13(c) shows that the non-synchronous peak for ball pass frequency inner (BPFI) was detected at 5X. Table 10 shows the bearing frequencies obtain from the theoretical, experimental and finite element analysis at the running speed of 25 Hz.It can be seen that agreement between the theoretical, experimental and finite element result is found to be remarkably good (Saruhan *et al.,* 2014).

Table 10: Bearing frequencies at 25 Hz.

	Bearing frequencies, Hz		
SKF 6206	**Theoretical**	**Experimental**	**Simulation**
NB	25	25	25
BPFO	86.4	88.7	87.5
BPFI	129.6	130	130

The result also shows the existence of required significant peaks and non-synchronous peaks for the new and defected bearings, respectively. In addition, the outer and inner defected bearing results showed a stronger impact wave with the more non-synchronous peaks compared to the new bearing. The vibration amplitude also changed because of the defect size where it showed the stronger amplitude. The vibration amplitude for the new and defected bearings was also taken to see the performance of hBN nanoparticles in reducing vibration. The data from the simulation is tabulated in Table 11.

Table 11: Vibration amplitude responses.

Types of bearing	**Amplitude (ms^{-2})**			
	0.0 vol% of hBN	**0.2 vol% of hBN**	**0.5 vol% of hBN**	**1.0 vol% of hBN**
New bearing	0.0097	0.0078	0.0105	0.0112
Outer defected bearing	0.4191	0.3878	0.4056	0.4105
Inner defected bearing	0.0145	0.0124	0.0135	0.0152

From Table 10, it is found that a 0.2 vol% concentration of hBN produces the lowest vibration amplitude for the new and the defected bearings. Another reason for the lower amplitude was the nanometre size of nanoparticles which allowed it to enter the defected area easily and form the hydrodynamic boundary for the bearing. It was also found that the vibration amplitude for the outer defected bearing was higher than the inner defected bearing. This is because the outer race defect remained at the load zone at the maximum position whilst the inner race defect moved in and out of the load zone. The strong vibration amplitude occurs in the load zone while weaker vibration amplitude is produced when the defect is outside the load zone.

5. COMPARATIVE ASSESSMENT

The FEA analysis and experimental results at different volumes of concentration of hBN and bearing defect sizes are plotted in Figure 14 and the comparison is made respectively as tabulated in Table 12.From Figure 14, the vibration amplitude reduces more at 0.2 vol% of concentration of hBN for both experiment and simulation in all types of bearing condition. However, comparison data between experiment and simulation shows no correlation to each other due to the insufficient data in the simulation. The parameters during the simulation such as noise, isolator bed, stiffness of the system and the number of elements and nodes were beyond control. These factors were also not considered during the experimental test. The assumption is made to ensure the model is simple and easy to be read by the software. Meanwhile, in the experimental test, the unwanted noise can be reduced and it has a complete system to record the vibration amplitude compared to the simulation. The manipulated variables also can be controlled by the user.

Table 12: Comparison data from FEA and experiment results.

Types of bearing	% volume of concentration of hBN							
	Experiment				FEA			
	0.0%	0.2%	0.5%	1.0%	0.0%	0.2%	0.5%	1.0%
New bearing	0.163	0.141	0.276	0.279	0.010	0.008	0.011	0.013
Outer defected bearing	0.039	0.022	0.033	0.038	0.419	0.388	0.406	0.411
Inner defected bearing	0.015	0.010	0.017	0.019	0.015	0.012	0.017	0.019

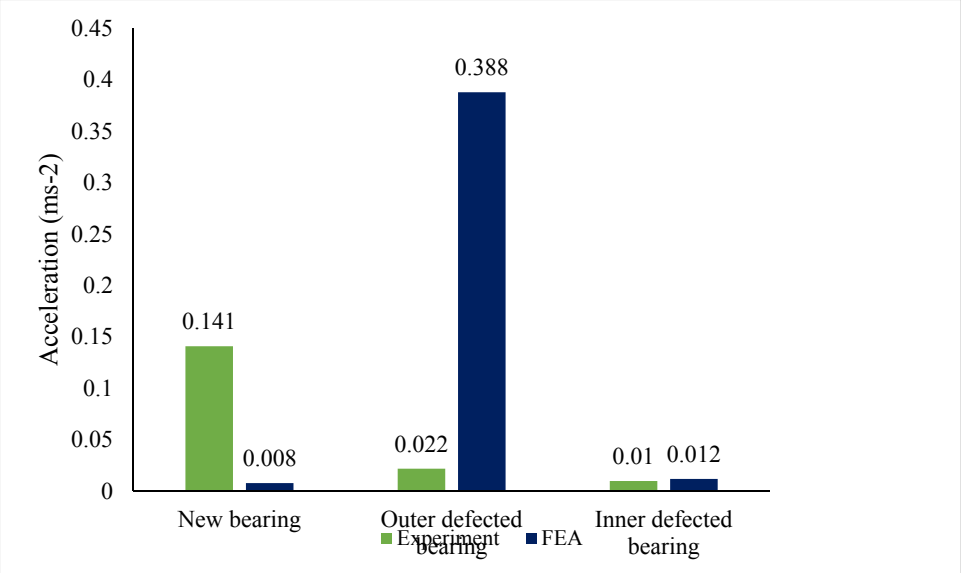

Figure 14: Comparison data between experiment and FEA results.

6. CONCLUSION

The experimental test was proposed to determine the performance of hexagonal boron nitride nanoparticles mixed lubricant in reducing the vibration amplitude for new and defected bearings, compared to the numerical approach using ANSYS WORKBENCH 16.0. The desired significant peaks and non-synchronous peaks from both experiment and simulation work show a good agreement with the theoretical bearing frequency. As for the new bearing, 1X significant peak appeared clearly at 25 Hz, outer defected bearing shows 3X non-synchronous peak at 89 Hz and lastly, inner defected bearing shows 5X non-synchronous peak at 130 Hz.

It is found that 0.2 vol% concentration of hBN is effective in reducing the vibration amplitudes on new and defected bearings compared to the other volume concentrations. The results give good agreement between the experimental testing and numerical simulation. The reasons for the high reduction of vibration were the formation of a full film lubrication regime and the increase in the viscosity of the lubricant as the nanoparticles increased. The nanoparticles suspended in lubricating oil functioned like ball bearings between friction surfaces. It also formed a protective film to some extent by coating the rough friction surfaces. The roughness of the lubricating surface was reduced by nanoparticle-assisted abrasion, which has a polishing effect. Besides, the nanometre size of nanoparticles which enabled it to easily enter the surface of the defected area. Finally, from both methods it is found that the outer defect bearings gave off a higher vibration amplitude because the defect present on the outer element remained in the load zone at maximum position whereas the inner element moved in and out of the load zone during each revolution of the shaft.

The experimental test conducted by using vibration test can be simulated in numerical approach. It also can be used as one of the method in vibration condition monitoring to detect the early deterioration on bearing due to the characteristic frequency obtained from the frequency spectrum. In conclusion, the performance of the hBN nanoparticles mixed diesel engine oil can be determined through the vibration analysis method by identifying the bearing frequencies as well as in the finite element method analysis. In future, the 3D finite element bearing model presented in this paper will be used to investigate the vibration response of the bearings on different sizes of defects and the performance of the different nano-lubricants in reducing vibrations.

ACKNOWLEDGEMENT

The authors gratefully acknowledged the Centre for Advanced Research on Energy (CARe), the financial support from Universiti Teknikal Malaysia Melaka and The Ministry of Education, Malaysia under Short Term Research Grant, Grant no. RAGS/1/2014/TK01/FKM/B00066.

REFERENCES

Ay, N., Ay, G. M., & Göncü, Y. (2016). Environmentally friendly material: Hexagonal boron nitride. *J.Boron*, **2**: 66–73.

Abdullah, M. I. H. C., Abdollah, M. F. B., Amiruddin, H., Tamaldin, N., & Nuri, N. R. M. (2013). Optimization of Tribological Performance of hBN/Al_2O_3Nanoparticles as Engine Oil Additives. *Procedia Eng.*, **68**:313-319.

Ding, W., Zhang, Z. & Zhao, F. (2015). Vibration response of ball bearings with different defect sizes in the outer raceway: Simulation with a 3-D finite element model.*14th IFToMM World Congress,* Taipei, Taiwan.

Greenberg, R., Halperin, G., Etsion, I. & Tenne, R. (2004). The effect of WS_2nanoparticles on friction reduction in various lubrication regimes. *Tribol.Lett.*,**2**:179-186

Kadarno, P., Taha, Z., Dirgantara, T. & Kimiyuki M. (2008). Vibration analysis of defected ball bearing using finite element model simulation. *9thAsia Pacific Ind. Eng. Manag. Syst. Conf.*, Bali, Indonesia.

Liu, J., Shao, Y., & Zhu, W. D. (2015). A new model for the relationship between vibration characteristics caused by the time-varying contact stiffness of a deep groove ball bearing and

defect sizes. *J. Tribol.,***3**:031101.
Patel, V.N., Tandon, N. & Pandey, R.K. (2014). Vibrations generated by rolling element bearings having multiple local defects on races. *Procedia Technol.*, **14***:*312-319.
Prakash, E., Kumar, S. & Muthu Kumar, K. (2013). Experimental studies on vibration characteristics on ball bearing operated with copper oxide nanoparticle mixed lubricant. *Int. J. Eng. Technol.*, **5***:*4127-4130.
Qiu, S., Zhou, Z., Dong, J. & Chen, G. (2001). Preparation of Ni nanoparticles and evaluation of their tribological performance as potential additives in oils. *J. Tribol.*,**3**:441-443.
Saruhan, H., Sandemir, S., Çiçek, A. & Uygur, I. (2014). Vibration analysis of rolling element bearings defects. *J. Appl. Res. Technol.*, **12**:384-395.
Swansson, N.S.& Favaloro, S.C. (1984). *Applications of Vibration Analysis To The Condition Monitoring Of Rolling Element Bearings.* Aero Propulsion Report, Department of Defence, Defence Science and Technology Organization Aeronautical Research Laboratories, Melbourne.
Tiwari, M., Gupta, K. & Prakash, O. (2000). Dynamic response of an unbalanced rotor supported on ball bearings. *J. Sound Vib.*,**5**: 757-779.
Wu, Y.Y., Tsui, W.C. & Liu, T.C. (2007). Experimental analysis of tribological properties of lubricating oils with nanoparticle additives. *Wear*, **7**:819-825.
Wan, Q., Jin, Y., Sun, P. & Ding, Y. (2015). Tribological behaviour of a lubricant oil containing boron nitride nanoparticles. *Procedia Eng.*, **102**:1038-1045.
Yadav, H.K., Upadhyay, S.H. & Harsha, S. P. (2013). Study of effect of unbalanced forces for high speed rotor. *Procedia Eng.*, **64**:593-602.

NOISE EXPOSURE INSIDE A PASSENGER CAR CABIN IN TROPICAL ENVIRONMENTAL CONDITION

Shamsul Akmar Ab Aziz[1,*], Adam Gani[1], Aizul Fazli Suhaimi[1], Shamsiah Kalil[1], Aznida Yusuf@Md Yusuf[1] & Mohd Zaki Nuawi[2]

[1]Science and Technology Research Institute for Defence (STRIDE), Ministry of Defence, Malaysia
[2]Department of Mechanical and Material Engineering, Faculty of Engineering and Built Environment, Universiti Kebangsaan Malaysia (UKM), Malaysia

[*]E-mail: shamsulakmar.abaziz@stride.gov.my

ABSTRACT

The present study provides an evaluation of cabin noise inside a passenger car cabin for two types of roads in tropical environmental conditions in Malaysia. Tropical weather conditions are hot and humid, with rain also giving effect to the road surface condition. Noise exposure was measured using a DuO sound level meter, which is capable to record sound pressure in unit of Pa, and comparisons were made between the two types of roads; tarmac and dirt. The data was analysed using Integrated Kurtosis-based Algorithm for Z-notch Filter (I-kaz^{TM}*) in relation to varying speeds of the car, in order to determine the degree of data scattering for the noise signals. Based on the results obtained, noise exposure levels can be presented using sound pressure, sound pressure level (SPL), I-kaz*^{TM} *coefficient (*Z^{∞}*) and I-kaz*^{TM} *display. Test comparisons were made between the two types of roads in the same test speed, which showed that the values of* Z^{∞} *and SPL were higher, and the size for I-kaz*^{TM} *display was larger for the dirt road as compared to the tarmac road. It was found that rough roads exhibit higher noise exposure variation as the vehicle speed changes in the tropical environmental condition.*

Keywords: *Noise exposure; tropical environmental conditions; passenger car cabin; data scattering.*

1. INTRODUCTION

Prolonged and excessive exposure to noise inside passenger car cabins can cause long-term harm and adverse effects to drivers. Aziz *et al*. (2014a) developed a new method for determination of noise exposure in the driver's compartment based on changing vehicle speed using regression models. Nopiah *et al*. (2012) developed a vehicle acoustical comfort index (VACI) to evaluate the noise annoyance level and sound quality of noise. In order to fulfil the study's requirements, the test was conducted in two categories, stationary and highway, as the interaction between tyres and road surfaces gives major effect to the generated noise in the passenger compartment. The study by Nopiah *et al.* (2012) shows that an increase of engine speed can increase the annoyance level by decreasing the value of VACI; in other words it will contribute to more noise. However, the study was not conducted for different road surfaces with constant speed. Nor *et al*. (2008) and Daruis *et al*. (2008) evaluated VACI according to the most frequently used sound quality metrics, namely, Zwicker loudness, sharpness, roughness and fluctuation of strength. As a result, the researchers could use this index for several types of roads and different road roughness characteristics. These models represent the road as point or line sources, whose sound emission levels are differently expressed as the function of vehicle type, flow, speed, road surface and so forth (Cho *et al*., 2004).

The objective of this study is to explain the changes of noise readings between two different types of roads in the tropical environment condition. The tropical environment is often hot, humid and dense. The 'tropics,' defined as the area around the equator, lie between the Tropic of Cancer (23.5° north) and the Tropic of Capricorn (23.5° south). Rain forests, predominated by trees and lianas (woody vines), are the principal biome in the tropics, and they contain a diversity of plants and animals that is

greater than in any other habitat on Earth (Schnitzer & Carson, 1999). The study by King *et al*. (1998) examined army tropical test missions to define the conditions that best provide the environmental challenges needed for tropical testing. The study identified the climatic, physical and biological characteristics defining the ideal tropical test environment and identified regions of the world that best fit the composite specifications of an ideal tropical test environment. Worldwide, 16 areas were identified, including Malaysia, as suitable localities for army tropical testing (King *et al*., 2006).

Tropical testing of vehicles requires extensive lengths of roads of all surface types, including natural soils, all situated within the hot tropical climate domain (King *et al*., 2006). Therefore, the choice of two kinds of road surfaces will be able to describe the state of different road conditions in a tropical environment. Figure 1 shows the two kinds of road surfaces used for this study, which were tarmac and dirt roads. The selection of different road surfaces was because the interaction between the tyres and road surface gives major effect to the generated noise exposure on the driver and passenger. The tarmac road has a flat, smooth surface and occasional unevenness, which resulted in minimum disturbances. The dirt road is an unpaved road made from subgrade materials and has frequent random irregularities that produced excessive noise (Aziz *et al*., 2014a).

Figure 1: Tropical environment in Malaysia with the two types of roads used for this study: (a) tarmac and (b) dirt roads.

2. METHODOLOGY

2.1 Statistical Method

In this study, statistical analysis for noise exposure in tropical environmental condition is performed using the Integrated Kurtosis-based Algorithm for Z-notch Filter (I-kaz^{TM}) method. This method is an alternative and effective tool that serves in two capacities: to summarise the data and to assist in interpretation. The I-kaz^{TM} method provides a 3D dimensional graphical representation of the measured noise signal and I-kaz^{TM} coefficient (Z^{∞}) to measure the degree of data scattering and signal frequency distribution. The time domain signal is decomposed into three frequency ranges, which are *x*-axis, low frequency (LF) ranges between 0 - 0.25f_{max}; *y*-axis, high frequency (HF) ranges between 0.25f_{max} - 0.5f_{max} and z-axis, very high frequency (VHF) ranges between 0.5f_{max} - f_{max} (Nuawi *et al*., 2008). The selection of 0.25f_{max} and 0.5f_{max} implies the concept of a 2nd order in the signal decomposition process (Daubechies, 1992). The space scattering of I-kaz^{TM} representation was measured by the Z^{∞} value obtained from Equation 1. The Z^{∞} coefficient can be written in terms of the means μ as follows:

$$Z^{\infty} = \sqrt{\frac{\sum_{i=1}^{N}(x_i^L-\mu_L)^4}{N^2} + \frac{\sum_{i=1}^{N}(x_i^H-\mu_H)^4}{N^2} + \frac{\sum_{i=1}^{N}(x_i^V-\mu_V)^4}{N^2}} \quad (1)$$

where x_i^L, $x_{i,}^H$ and x_i^V are the values of discrete data in the LF, HF and VF ranges respectively at the i^{th} sample of time, while μ_L, μ_H and μ_V are the means of each frequency band, and N is the number of data.

2.2 Test Method

This study was conducted on a highway with tarmac and dirt roads in Malaysian tropical environmental condition. It was conducted on a sunny day with temperature of about 28-30 °C. The condition of both roads was dry. The wind speed was less than 5 ms^{-1} during the test. According to ISO 5128:1980 (Acoustics - Measurement of Noise Inside Motor Vehicles), the wind speed must be less than 5 ms^{-1} to ensure that the wind velocity does not give impact to the results.

A DuO smart noise monitor that utilises an *A*-weighted scale was used to measure sound pressure in the truck driver's compartment, with its calibration performed using a Brüel & Kjær Type 4231 calibrator. The tests were conducted for two conditions, which were stationary, and moving at constant speed of 30 kmh^{-1} on the tarmac and dirt roads. Previous studies on several vehicles showed that the noise level inside the driver's cabin increases with increasing vehicle speed (Aziz *et al*., 2012, 2014a, b). By using a Proton Inspira 2.0 as the vehicle under test, the speed selection was made based on the road surface condition. Rough road surface for dirt roads could give impact to safety during driving, resulting in the maximum speed for the test on the dirt road fixed at just 30 kmh^{-1}. The same speed on every road type was chosen so that any comparison between two types of road can be observed and analysed. The microphone position was set up according to ISO 5128: 1980 as shown in Figure 2.

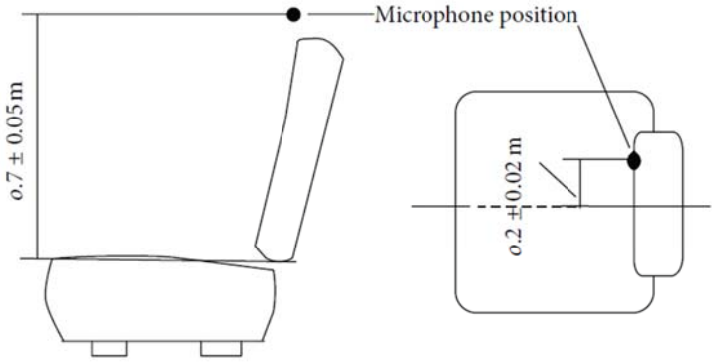

Figure 2: Microphone position.
(Source: ISO 5128: 1980)

3. RESULTS AND DISCUSSION

Noise in the passenger car's driving compartment was measured using a DuO smart noise monitor, connected to a computer for analysis using the dBTrait software. This sound level meter is capable of recording raw instantaneous sound pressure in Pa for up to 50Hz. The recording for duration of 180 s intervals contained 9,000 samples of instantaneous sound pressure raw data. The sampling period, which is the time difference between two consecutive samples, is 1/50 Hz = 0.02 s (Aziz *et al*., 2014a). The dBTrait analysis allows us to calculate the time domain difference between the measurement point and the dBTrait coding point. The difference between the time domain is then analysed and checked automatically to detect an event occurring from the total of all other sources of noise (01dB, 2012).

When the car is moving at increasing speed, the noise from the engine, exhaust, road-tyre interaction, rear cabin and others increase. Figure 3 shows the noise time domain signal in the cabin while the vehicle is stationary. The noise level is low and in the range of 44-49 dB(A). At this time, the noise recorded from the vehicle engine is switched on together with the noise from air conditioner mounted

from the vehicle without any interference from external noise. According to Harrison (2004), vehicle interior noise inside the driver's cabin is a combination of engine, road, intake and exhaust, aerodynamics, components and ancillaries, and brakes. Noise and vibration also originate from outside the vehicle, interacting with the vehicle structure and then producing radiated sound inside the driver's cabin. In the stationary condition, there is no interaction effect between the vehicle's tyres with the different road surfaces and hence, noise exposure to the driver on the tarmac road is the same as on the dirt road (Aziz *et al*., 2014a).

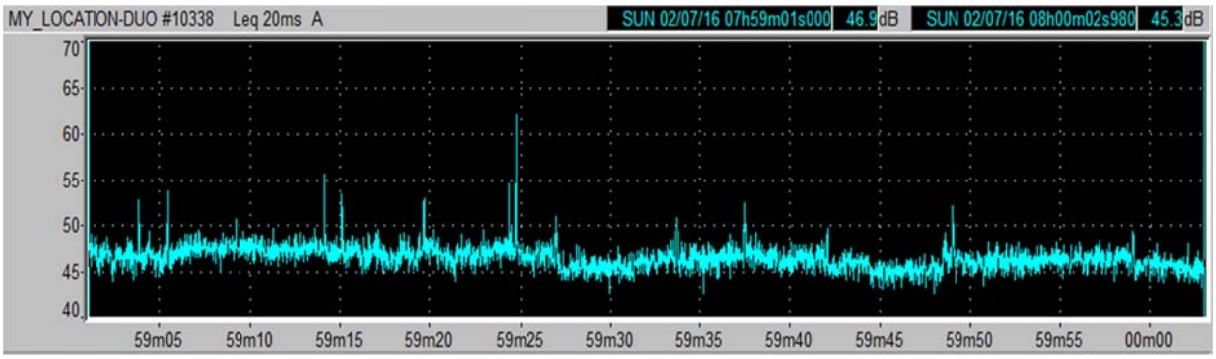

Figure 3: Noise time domain signal measured in stationary condition.

Figures 4 and 5 show the noise time domain signal while the car is moving at the speed of 30 kmh^{-1} on the tarmac and dirt roads respectively. The noise levels recorded while driving on the tarmac road were rather stable in the range of 55-68 dB(A). However, the noise level while driving on the dirt road that had a rough surface had spikes within a larger range of 55-75 dB(A). The larger range and uneven surface graphs were caused by the rough dirt road, which consists of pebbles and sometimes medium-size rocks that impact vibration to the vehicle. With reference to the dispersion and movement graphs for both these diagrams, it was found that the dispersion of the variance for Figure 5 is larger than for Figure 4.

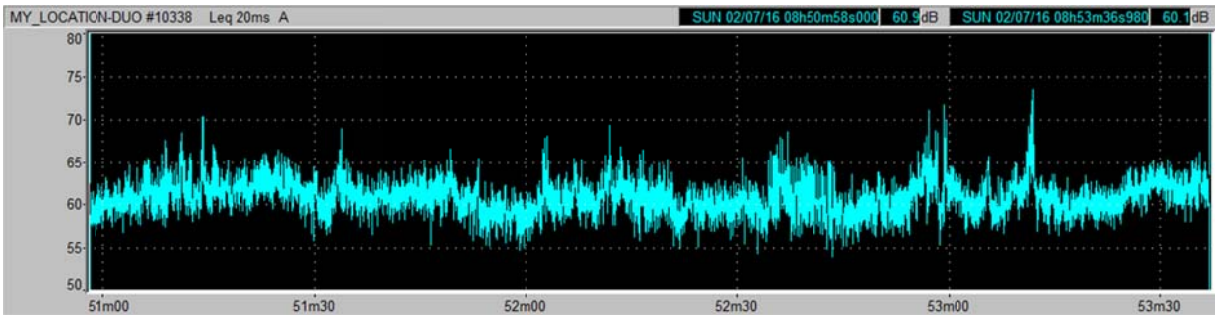

Figure 4: Noise time domain signal measured when driving at the speed of 30 kmh^{-1} on the tarmac road.

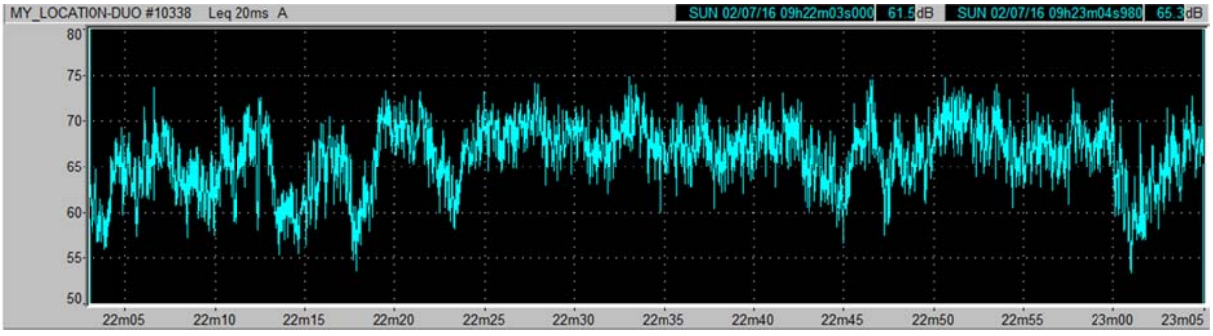

Figure 5: Noise time domain signal measured when driving at the speed of 30 kmh^{-1} on the dirt road.

Table 1 shows the comparison of results of sound pressure, sound pressure level (SPL) and $\not{Z}^{\infty}$ between the stationary condition, and moving at 30 kmh^{-1} on tarmac and dirt roads. All the readings for the dirt road were higher than for the tarmac road. Differences in noise exposure across the two types of roads were also found. In general, driving on the dirt road resulted in higher noise exposure, while driving on the tarmac road resulted in lower exposure.

Table 1: Summary of SPL_{avg} and $\not{Z}^{\infty}$ values for the various speeds of the passenger car while driving on the tarmac and dirt roads.

	Stationary condition	**Tarmac road (30 kmh^{-1})**	**Dirt road (30 kmh^{-1})**
Sound pressure, Pa	4.22 x 10^{-3}	2.26 x 10^{-2}	4.41 x 10^{-2}
Sound pressure level, SPL_{avg} dB(A)	46.5	61.1	66.9
$\not{Z}^{\infty}$	9.10 x 10^{-10}	1.10 x 10^{-8}	1.18 x 10^{-7}

Using the I-kaz^{TM} method, the signals obtained can be used to generate graphical representations that show the values of $\not{Z}^{\infty}$ (Figure 6). The figures show that for both types of roads, when the vehicle speed was increased, the range values of $\not{Z}^{\infty}$ became larger, which is consistent with the findings observed in Aziz *et al*. (2015, 2016, 2017). Driving on the dirt road produced higher value of $\not{Z}^{\infty}$ (1.18 × 10^{-7}) than for the tarmac road (1.10 x 10^{-8}). This finding is strongly supported by the greater space between the scattered $\not{Z}^{\infty}$ values in the I-kaz^{TM} displays. These graphical representations show larger spaces between the scattered $\not{Z}^{\infty}$ values due to higher noise exposure. The car moving on the dirt road had a large scattering of data due to their larger noise exposure value, 66.9 dB(A), as compared with that for the tarmac road, 61.1 dB(A).

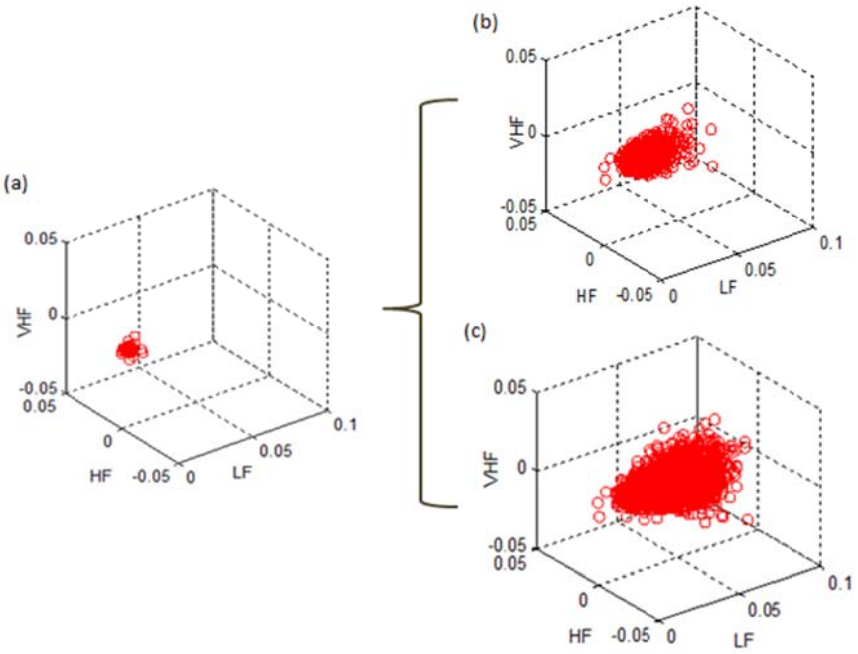

Figure 6: 3D graphical representations that show the changes in $\not{Z}^{\infty}$ values from (a) idle to driving at speed of 30 kmh^{-1} on the (b) tarmac and (c) dirt roads.

4. CONCLUSION

In this paper, noise exposure for passenger car drivers was analysed using the I-kaz^{TM} statistical analysis method. From the I-kaz^{TM} display, for the tests conducted at constant speed of 30 kmh^{-1}, there was increasing size of data scattering for the unpaved dirt road than the smooth surfaced tarmac road in tropical environmental condition. It was found that rough roads exhibit higher noise exposure variation as the vehicle speed changes. In other words, differentiation of noise with respect to speed is higher on harsh road conditions. The interaction between road surfaces and car tyres has a major effect on the noise generated inside the car cabin. It was also found that SPL on the dirt road is higher than the tarmac road even at the same speed 30 kmh^{-1}. In addition, these results were supported by the scattering of Z^{∞} values in the I-kaz^{TM} displays, which showed larger spaces between scattered Z^{∞} values as the vehicle speeds increased.

REFERENCES

01dB (2012). *DuO Smart Noise Monitor Technical Datasheet*. 01dB, Limonest, France.

Aziz, S.A.A., Nuawi, M.Z., Nor, M.J.M. & Daruis, D.D.I. (2014a). New regression models for predicting noise exposure in the driver's compartment of Malaysian Army three-tonne trucks. *Adv. Mech. Eng.*, **616093.**

Aziz, S.A.A., Nuawi,M.Z., Nor, M.J.M. & Daruis, D.D.I. (2014b). Study of noise, vibration and harshness (NVH) for Malaysian Army (MA) 3-tonne trucks. *Appl. Mech. Mater.*, **471**: 74–80.

Aziz, S.A.A., Nuawi, M.Z. & Nor, M.J.M. (2015). New regression model for predicting hand-arm vibration (HAV) of Malaysian Army (MA) three-tonne truck steering wheels. *J. Occup. Health*,**57**: 513–20.

Aziz, S.A.A., Nuawi, M.Z. & Nor, M.J.M. (2016). Predicting whole-body vibration (WBV) exposure of Malaysian Army three-tonne truck drivers using integrated kurtosis-based algorithm for Z-notch filter technique 3D (I-Kaz 3D). *Int. J. Ind. Ergon.***52**: 59–68.

Aziz, S.A.A., Nuawi, M.Z. & Nor, M.J.M. (2017). Monitoring of hand-arm vibration. *Int. J.Acoust. Vib,***22**: 34-43.

Aziz, S.A.A., Sohaimi, R.M., Pu'ad, M.H. & Yaman, M.A.M. (2012). Noise, vibration and harshness (NVH) study on Malaysian Armed Forces (MAF) tactical vehicle. *Appl. Mech. Mater.*, **165:** 165–169.

Cho, D.S., Kim, J.H., Choi, T.M., Kim, B.H .& Manvell, D. (2004). Highway traffic noise prediction using method fully compliant with ISO 9613: comparison with measurements. *Appl. Acoust.*, **65**: 883–892.

Daruis, D.D.I., Nor, M.J.M., Deros, B.M. & Fouladi, M.H., (2008). Whole-body vibration and sound quality of Malaysian cars. *Proc. 9thAsia Pacific Ind. Eng.Manage. Syst. Conf.*, pp. 110-117.

Daubechies, I. (1992). *Ten Lectures on Wavelets*.Society for Industrial and Applied Mathematics (SIAM), Philadelphia.

Harrison, M. (2004). *Vehicle Refinement - Controlling Noise and Vibration in Road vehicles*. Elsevier Butterworth-Heinemann.

ISO 5128 (1980). *Acoustics: Measurement of Inside Motor Vehicles*. International Organization for Standardization (ISO), Geneva.

King,W.C., Harmon, R., Bullard,T., Dement,W., Doe, W., Evans, J., Larsen, M.C., Lawrence, W., McDonald, K. & Morrill, V. (1998). *A Technical Analysis to Identify Ideal Geographic Locations for Tropical Testing of Army Materiel and Systems*. United States Army Research Office, North Carolina.

King, W.C., Harmon, R., Juvik, J., Hendrickx, J.M.H. & Palka, E.J. (2006). *A Technical Analysis of Suriname for Tropical Testing of Army Materiel and Systems*. United States Army Research Office, North Carolina.

Nor, M.J.M., Fouladi, M.H., Nahvi, H. & Ariffin, A.K. (2008). Index for vehicle acoustical comfort inside a passenger car. *Appl.Acoust.*, **69**: 343–353.

Nopiah, Z.M., Junoh, A.K., Muhamad, W.Z.A.W., Nor, M.J.M., Ihsan, A.K.A.M. & Fouladi, M.H. (2012). Linear programming: Optimization of noise and vibration model in passenger car

cabin. *Int. J. Soft Comput. Softw. Eng.*, **2**: 1-13.
Nuawi, M.Z., Nor, M.J.M., Jamaludin, N., Abdullah, S., Lamin, F. & Nizwan, C.K.E. (2008). Development of integrated kurtosis-based algorithm for Z-filter technique. *J. Appl. Sci.*, **8**: 1541–1547.
Schnitzer, S.A. & Carson, W.P. (1999). *Environmental Geology*. Springer, Netherlands.

RECOGNITION OF MOST COMMON DIESEL ENGINE CONDITION MONITORING METHODS

Yogeswaran Sinnasamy*, Mohd Razali Mat Yassin, Noor Aishah Sa'at, Hasril Nain, Faiz Azmi Sutarji, Azmahani Sulaiman, Ibrahim Tahir, Rosdi Yaakob, Ahmad Subardi Mohd Wazir, Kamil Azwan Salehuddin, Mohd Ridzuan Mohd Rashid, Abbas Zubir, Hanizah Kasmoni, Elizabeth Louisnaden & Khairul Anuar Ahmad

Science and Technology Research Institute for Defence (STRIDE), Ministry of Defence, Malaysia

*Email: yoges.sinnasamy@stride.gov.my

ABSTRACT

Condition monitoring or CM is one of the approaches which have been widely applied in industry nowadays, particularly to identify the presence of symptoms of incipient faults and eventually prevents catastrophic failures on critical machineries. One of these critical machineries is diesel engine which is mainly used for ship's main propulsion and auxiliary propulsion in Royal Malaysian Navy (RMN). A lot of research has been performed and still undergoing to come up with more reliable and accurate condition monitoring system on diesel engine. The main factors which influence the researches are engine speed and loading condition, fuel injection pressure and valve clearance, types of defects, various forms of sensors and signal processing techniques. Based on these factors and in accordance with their respective CM techniques, a simple segregation procedure has been introduced to group all the shortlisted publications. We found out that vibration analysis (VA) and acoustic emission (AE) were popular among researchers and one of the defects which are abnormal valve clearance has been main focus among researchers as well. Also, we found out that CM is playing a very important part to monitor the performance of diesel engine and other related components. This procedure of identifying the most popular CM methods on diesel engine and most common types of defect studied shall be expanded on other types of ship propulsion machineries such as gear box, bearing, stern tube, oil distribution box and propeller.

Keywords: *Condition monitoring (CM); diesel engine; incipient faults, catastrophic; defects.*

1. INTRODUCTION

Condition Monitoring or Condition-based Monitoring is defined as the continuous evaluation of the health of the plant and equipment throughout its service life. It is important to be able to detect faults while they are still developing. This is called incipient failure detection (Elamin, 2014). Meanwhile, failure is the termination of the ability to perform the required function and, fault is defined as a situation, which exists after a failure (Elamin *et al*., 2010). The incipient detection of diesel engine failures also provides a safe operating environment and becoming increasingly important to use comprehensive CM schemes for continuous assessment of the combustion and mechanical conditions of reciprocating machineries (Gu *et al*., 2006).

By using CM, it is possible to provide adequate warning of imminent failure. In addition, it is also possible to schedule future preventive maintenance and repair work. This can result in minimum down time and optimum maintenance schedules (Lamaris *et al*., 2010). CM and fault diagnosis scheme allow

the machine operator to have the necessary spare parts before the machine is stripped down, thereby reducing outage time. Therefore, effective CM of diesel engine is critical in improving the reliability, safety and productivity.

Abnormal running conditions for a diesel engine can vary widely in severity and consequences from slightly affecting an engine's performance to catastrophic equipment failure. These events can be expensive, sometimes dangerous and occasionally cause environmental, and health and safety issues. Good CM can ensure the engine provides the required power under safe conditions with less fuel consumption, lower emissions and lower maintenance cost. Detecting faults and diagnosing the underlying problem as quickly as possible and providing assistance to correct the problem are the goals of engine abnormal situation prevention.

CM of diesel engines can be assessed on a continuous or periodic basis from observation or measurement of selected parameters. The application of CM and fault diagnosis strategies to a diesel engine is a well-recognised method of increasing its operational efficiency and reducing consequential damage, spare parts inventories and breakdown maintenance. Use of a particular method depends upon case to case. Sometimes, a single technique does not help. Most of the times, a combination of techniques is employed in problem-solving (Rajul *et al*., 2014).

The main job of most monitoring systems is to obtain information about the engine in the form of primary data and, through the use of modern signal processing techniques, to provide vital information to the engine operator and the engine control system, before any failure occurs with the engine in service. Good monitoring systems for diesel engines can achieve at least the following benefits:

a. Improved decision making capability for selection of optimum engine operation conditions.
b. Only defective equipment or assemblies are replaced, reducing time and cost of maintenance.
c. Effective prediction and planning of maintenance operations. Time scheduled for maintenance can be used effectively since the nature of the fault is known in advance and both spare parts and labour can be organised accordingly.
d. Reduction of engine emissions and fuel consumption.

Diesel engines are widely used in naval application to empower the ship main and auxiliary propulsion systems. These are among the most critical systems onboard. Any malfunction or failure on these systems could severely jeopardize the military operation of the navy. In our Royal Malaysian Navy (RMN), diesel engines from various brands and models have been used widely due to the capability working in harsh and extreme weather conditions. These engines can be divided into three different speed categories which are high, medium and low based on the class of the ship. In this paper, we are going to review publications between 2010 and 2016 to identify the most common type of diesel engine CM methods based on various types of defect simulation on diesel engine components.

2. LITERATURE REVIEW

Conventionally, diesel engine is monitored based on pressure and temperature indications. Nevertheless, both of these parameters were not sufficient enough to detect incipient fault which could lead to catastrophic failure on diesel engine (Porteiro *et al*., 2011). Nowadays, other CM methods such as vibration analysis (VA), acoustic emission (AE) and instantaneous angular speed (IAS) were improved and adapted as part of diesel engine monitoring system in most of machineries. Nevertheless, some of

these methods were not able to detect and diagnosis such type of defect. Therefore, further studies have been in progress for the past few decades to synchronize different types of data to form more reliable and accurate diesel engine CM system. Most of the studies influenced by the following factors:

a. Engine speed and loading conditions and their influence on combustion performance.
b. Fuel injection pressure and valve clearance.
c. Certain types of defects on diesel engine components such as crack on valve head.
d. The application of various forms of sensors for capturing different set of data.
e. Various forms of signal processing techniques.

2.1 Engine Speed and Loading Conditions

The engine load is the torque output of the engine and normally measured by using torque sensor. The measurement of engine torques playing an important part on monitoring engine performance. Based on studies performed by Elamin *et al*., 2010, the raw AE signals were collected under constant engine speed at 1000 RPM and four different loading conditions; 0, 50, 100 and 150 NM. Meanwhile, Alhouli *et al*. (2015) has performed studies under four different loadings and engine speed; 0, 20, 40 and 60 NM at 1,000 and 1,500 RPM. Nevertheless, it was found that both of these studies focused on different types of defects. For instance, Elamin *et al*. (2010) studies focused on variation of fuel injection pressure influence on combustion performance. Meanwhile, Alhouli *et al*., 2015 studies mainly focused on valve leakage which was seeded by adjusting the exhaust valve clearance.

2.2 Fuel Injection Pressure and Valve Clearance

Fuel injection system is one of the most critical systems on diesel engine and has been main focus of study among researchers. One of the most common types of fault related on fuel injection system is misfiring. Examples of studies were related on adjusting the nominal fuel injection pressure. By doing the adjustment, the severity of the misfiring has been detected at higher and lower level of nominal fuel injection pressure. Another focus of studies among researchers is fuel supply and simulated by completely unscrewed and cut off in the fuel supply of the cylinder the nut connecting the high-pressure fuel line to the corresponding element of the injection pump as shown in Figure 1. By varying the tightness of the high pressure fuel line, it was possible to reduce gradually the amount of fuel injected into the cylinder from the rated value to zero, to simulate a wide range of malfunctions up to a complete misfire (Gawande *et al*., 2010). Only exhaust valve clearance faults were investigated by Alhouli *et al*. (2015). As shown in Figure 3, cylinder no.1 exhaust valve clearance was altered from 0.4mm (healthy clearance) to 0 mm, 0.25mm, and 0.6mm. This simulates leakage to some extent, exhaust valve timing and in-cylinder pressure. Valve clearance typically refers to the clearance between the rocker and valve cap. Each internal combustion engine (ICE) has a normal valve clearance value designed to allow for thermal expansion. An abnormal valve clearance will result in improper valve closing and timing, degrading engine performance (Flett and Bone, 2016). Figure 3 gives an illustration of valve clearance.

2.3 Certain Types of Defects on Diesel Engine Components

There are publications which dealt with damages on diesel engine components such as crack on valve head shown in Figure 4 (Jafari *et al*., 2014), wear on cylinder wall (Gowtham *et al*., 2016) and deformed spring (Flett & Bone, 2016). Meanwhile, there are few publications which studied more than one type of defect such as abnormal fuel injector and misfiring (Elamin *et al*., 2010), misfiring, shaft imbalance,

clogged intake filter and leaking start plug (Porteiro *et al*., 2011), abnormal valve clearance and piston ring fault (Arroyo *et al*., 2013) and valve spring fault and abnormal valve clearance (Flett & Bone, 2016). Exhaust and intake valves which have been the study focus on abnormal valve clearance, also has been utilized in other studies such as crack propagation on valve head as shown in Figure 5.

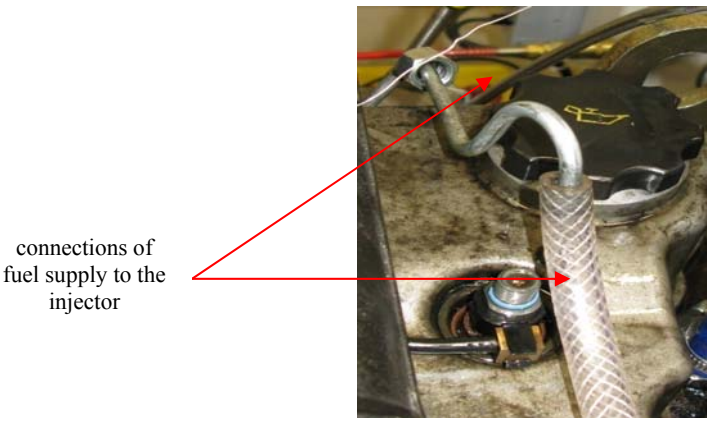

Figure 1: Arrangement for total misfire (Elamin *et al*., 2010).

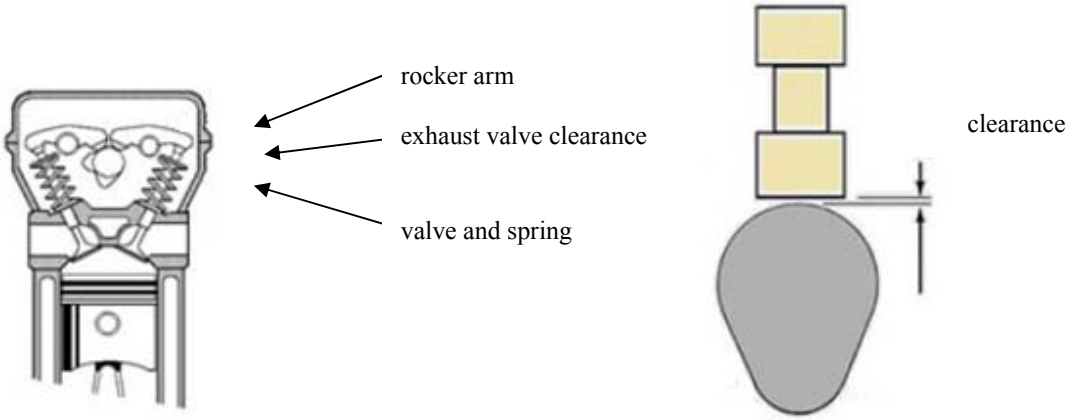

Figure 2: Exhaust valve clearance alteration (Alhouli *et al*., 2015).

Figure 3: Valve clearance (Flett and Bone, 2016).

Some of the studies were conducted on subsystems that supporting the performance of the diesel engine and not connected inside the engine itself. As shown in Figure 6, erosion and microcracks occur on the surface of the rubber component of an elastic coupling, which will cause the coupling torsional stiffness to change inevitably (Wanyou *et al*., 2016). Elastic coupling is a connection between diesel engine and gear box. The main function of elastic coupling is to absorb excessive torsional vibration and prevents damages on shafting line. Hence, it is crucial to calculate the shafting torsional characteristics correctly and evaluate the stability of the shafting rationally by determining the torsional stiffness of the elastic coupling when it is operating (Wanyou *et al*., 2016).

Meanwhile, Yan *et al*. (2013) conducted study on wear debris analysis by introducing a slight crack on a gear pump of the tested diesel engine. In the experiment tests, the diesel engine has run for 100 hours. The on-line ferrographic sensor and oil moisture and viscosity detection device sampled the lubricant oil every 2 hours, and the lubricant oil was collected every 12 hours for the purpose of off-line oil analysis. In order to improve the reliability of condition monitoring system on diesel engine, some other monitoring methods such as vibration, acoustic emission or others could be combined with wear debris data.

(a) (b)

Figure 4: Semi-cracked valve (a) Cylinder No. 1 and (b) Cylinder No. 2 (Alhouli *et al*., 2015).

(a) (b)

Figure 5: (a) Notched exhaust valve of cylinder No. 3 and (b) Healthy valves of cylinder No. 4. Clearance fault was simulated by lift on valves (Alhouli *et al*., 2015).

Figure 6: Elastic coupling (Wanyou *et al*., 2016).

2.4 The Application of Various Forms of Sensors

The number and type of sensors utilized by researchers in their study were not same and varied depending mostly on the severity or types defects under their study. As shown in Figure 7, four (4) sensors have been applied on diesel engine, one (1) on coupling between engine and dynamotor and one (1) on the dynamotor itself. Both vibration and pressure sensors mounted on diesel engine surface were connected to the amplifier before data acquisition unit. Charge type of accelerometer used because the temperature on diesel engine could exceed 100°C. This could give more disturbances on the captured data and the usage of external amplifier will minimize this errors obtained during the measurement process (Mobius Institute, 1999-2011). Torque sensor is used for measuring the loading condition on diesel engine. We found that this type of sensor has been used in most of studies as shown in Figure 7, 8, 9 and 10. Meanwhile, Arroyo *et al*. (2013) used four sensors, vibration, AE, pressure and optical encoder. In study performed by Alhouli *et al*. (2015), three different sensors have been used; TDC, cylinder vibration and cylinder pressure. Both these cylinder sensors have the same functions as vibration and pressure sensors used by Arroyo *et al*. (2013) and Albarbar (2013).

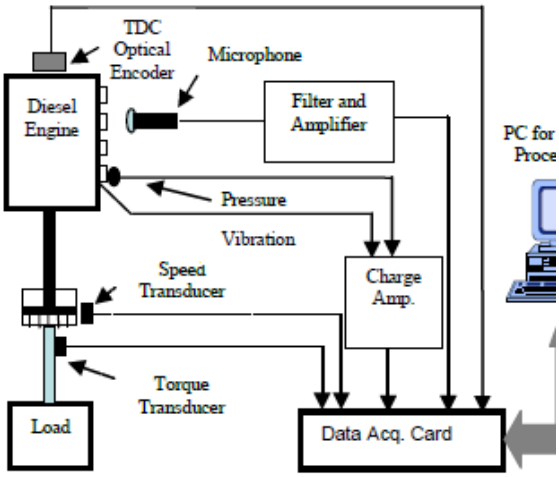

Figure 7: Schematic diagram of engine test system (Albarbar, 2013).

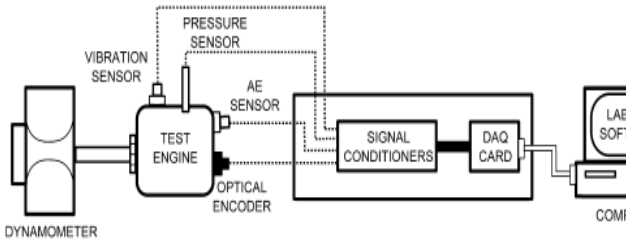

Figure 8: Experimental system (Arroyo *et al*., 2013).

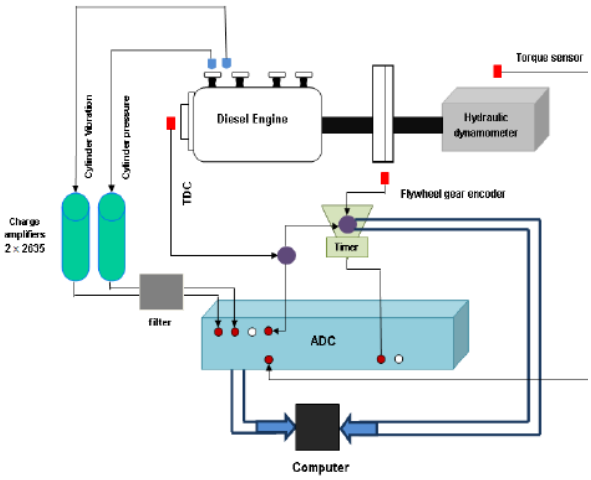

Figure 9: Monitoring system wiring diagram (Alhouli *et al*., 2015).

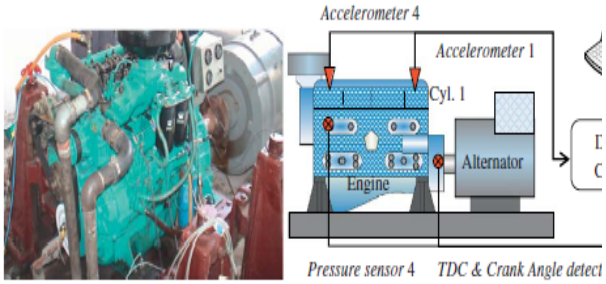

Figure 10: Image of the tested generator and its experimental setup (Li *et al*., 2010).

In contrast with the above studies, Li *et al*., 2010 used two types of accelerometers, which is vibration sensors and same sensor to capture TDC position and crank shaft angle. Most of researchers used two different sensors for these signals in their study.

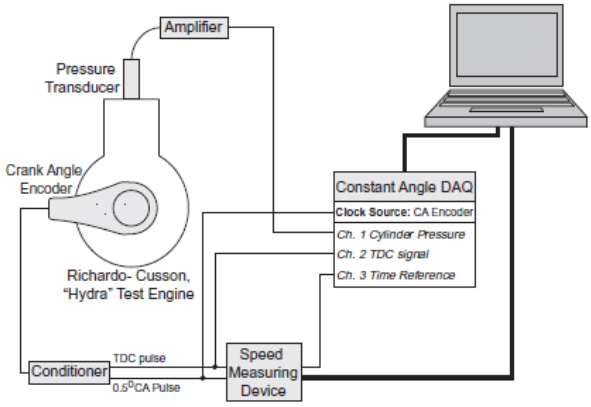

Figure 11: Schematic representation of the experimental setup. Pressure transducer is mounted on cylinder's head; crank angle encoder is mounted on crankshaft free end (Antonopoulos & Hountalas, 2012).

Figure 11 shows the measurement setup conducted by Antonopoulos & Hountalas (2012). Instead of using vibration sensor, a cylinder pressure sensor has been used in this study to measure the pressure signal on cylinder head surface at different loadings and engine speeds. Basically, these show that most of researchers using different measurement setup in their studies. Nevertheless, both vibration and pressure sensors have been the most important sensor in their study, especially to study the combustion characteristics and monitor engine performance.

2.5 Various Forms of Signal Processing Techniques

Elamin *et al*. (2010) compared three different signal processing techniques; angular domain, frequency domain and angular-frequency domain. The analysis discussed in the previous show that AE signals in the angular domain can produce diagnosis results for no load condition but not for higher load conditions whereas spectrum presentation allows fault deletion for all cases but not diagnosis. To combine the capabilities in both the angular and frequency domains, joint angular-frequency analysis is applied to the AE signals. The joint angular-frequency analysis can provide both detection and diagnosis for both the small and large injection faults and their original cylinder and has the potential of separating several AE sources occurring at the same time but having different frequency content.

Albarbar (2013) used continuous wavelet transform (CWT) as a linear time-frequency technique to analysis diesel engine airborne acoustics signals. The results from CWT analysis of the air-borne acoustic signals, for an engine running under faulty conditions, reveal its advantages in fault detection, as abnormal combustion related faults of different severity were identified by the time-frequency representation of the acoustic signals in the high frequency bands. Figure 12 shows the acoustic waveform of the diesel engine in the time domain and the continuous wavelet transform (CWT). From the CWT representation, we can see clearly four peaks representing the combustion events of the engine cylinders in the firing order from left to right (3, 1, 2, and 4).

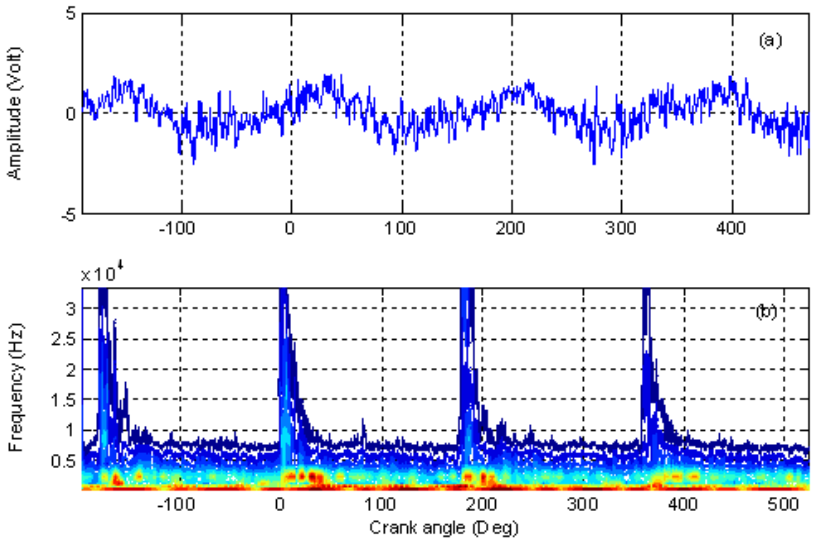

Figure 12: The acoustic waveform of the diesel engine in the time domain and the continuous wavelet transform (CWT).

Alhouli *et al*. (2015) compared two different signal processing techniques; time domain and frequency domain. The time domain technique has been used to extract the information from the vibration signal of the diesel engine at different speeds and loads by plotting the amplitude to relate it to the engine events (crank angle). After analyzing the data in the time domain and frequency domain there were some differences in the vibration signals changing rate around the (TDC), due to exhaust valve clearance variations. In frequency domain there was a clear difference between the signals of the healthy case and the faulty case, a frequency of 50 Hz, a side band of high amplitude was appeared.

3. METHODOLOGY

In this paper, around 100 publications on CM have been screened and it was found that only 23 publications between 2010 and 2016 could be reviewed for further process based on their suitability in terms of research and development on diesel engine CM system. Basically, all these selected publications can be divided into three categories; those studies or researches based on engine revolution and loading conditions (Antonopoulos & Hountalas, 2012), fuel supply (Wargante *et al*., 2013), injection pressure variation (Albarbar *et al*., 2013) and combustion performance (Chiatti *et al*., 2014); those studies based on inducing certain fault by disconnecting fuel supply to simulate misfiring (Elamin *et al*., 2010) and those studies based on inducing critical defect such as crack on valve (Jafari *et al*., 2014) and wear on piston rings and cylinder wall (Gowtham *et al*., 2016). Figure 13 shows the process flow which has been utilized in this study for each publication.

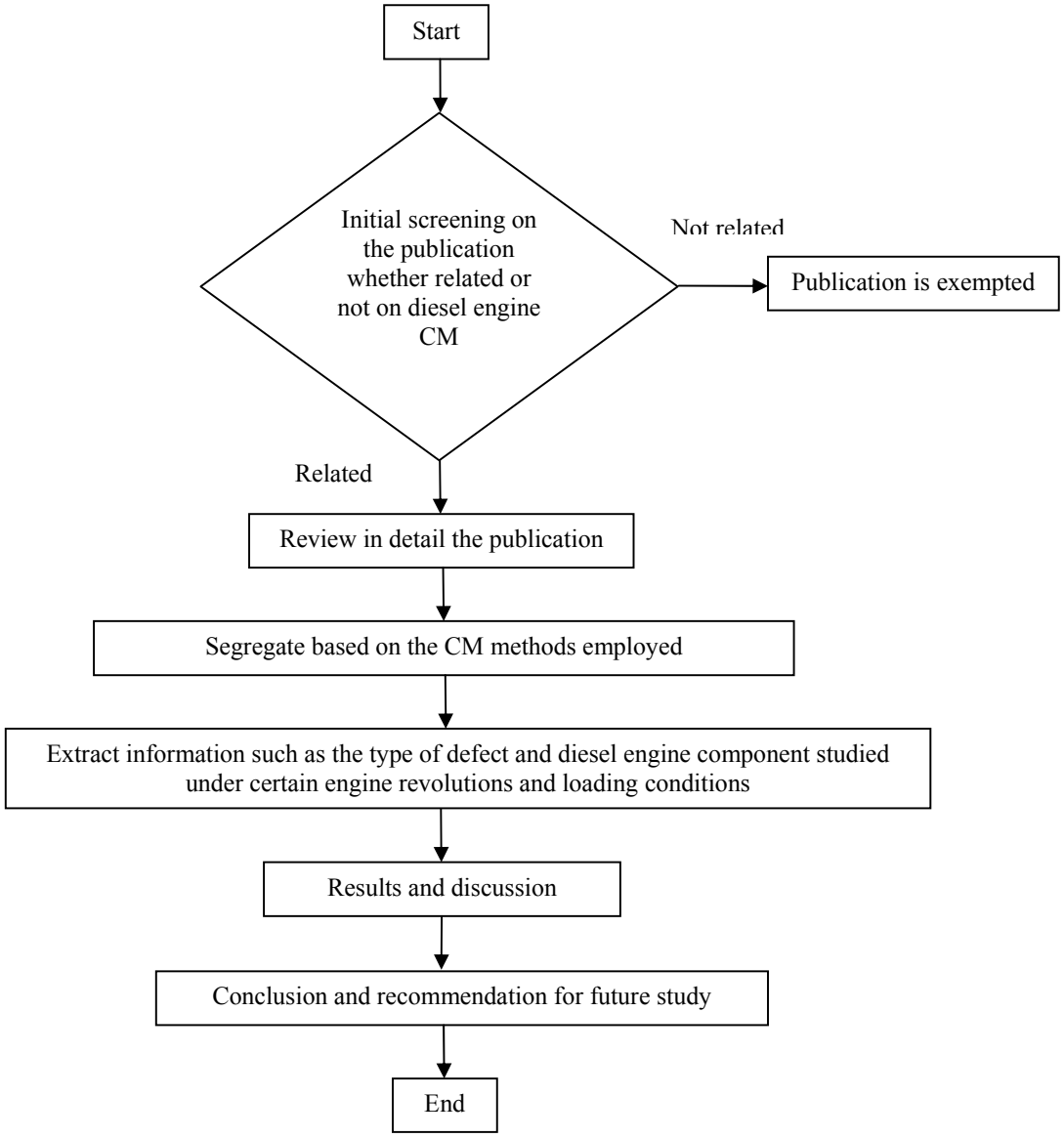

Figure 13: Process flow indicates the screening, reviewing and extraction information from various publications.

4. RESULTS & DISCUSSION

Table 1 shows the summary of publications between year 2010 and 2016 on research and development diesel engine CM. Based on Table 1, we found that abnormal valve clearance (Elamin *et al.,* 2010, Li *et al.,* 2010, Wu *et al.,* 2012, Jafari *et al.,* 2014, Alhouli *et al.,* 2015; Flett & Bone, 2016) and faulty fuel injector (Elamin *et al.,* 2010, Gawande *et al.,* 2010, Porteiro *et al.,* 2011; Lin 2013) are the most common types of study among researchers. The vibration analysis (VA) and in-cylinder were the most common CM methods and employed by most of the researchers and followed by acoustic emission (AE). Other methods such as in-cylinder pressure, temperature, instantaneous angular speed (IAS) and others also been employed as shown in Table 1. Meanwhile, wear debris analysis is one of CM methods which mostly used to study the condition of lubrication oil of diesel engine after certain running hours. A

microscopic image processing technique based on-line ferrographic monitor is adopted to analyze the wear debris characteristics of the engine oil, and an on-line moisture and viscosity detection sensor is used to monitor the lubricant condition (Yan *et al*., 2013).

From this study, it is obvious that vibration and in-cylinder methods have the capability to detect some of the most common types of defects such as misfiring and valve leakage which normally happened due to abnormal injection pressure and abnormal valve clearance respectively. AE also has ability to detect misfiring and valve leakage (Elamin *et al*., 2010). Besides that, AE sensor which is one of CM technologies has the fundamental capability to detect certain types of critical defects such as crack on valve head and leakage and piston ring fault (Arroyo *et al*., 2013).

Table 1: Summary of publications on diesel engine CM.

Authors	Subsystem(s) or component(s) studied	Types of defect(s) studied	CM method(s) employed
Elamin *et al*., 2010	fuel injector	abnormal fuel injection; misfiring	AE
Li *et al*., 2010	intake and exhaust valves; piston ring	abnormal valve clearance	VA, crank shaft encoder, tachometer (TDC), pressure sensor
Gawande *et al*., 2010	fuel injection pump (fuel supply)	wide range of malfunctions up to a complete misfire	combustion pressure (piezoelectric pressure transducers)
Porteiro *et al*., 2011	selected locations on diesel engine surface	misfiring of each of the three cylinders; shaft imbalance; clogged intake filter and a leaking start/glow plug	vibration (VA) and exhaust temperature sensors
Lowe *et al*., 2011	engine block and head	excessive diesel knock level	AE, cylinder pressure, TDC, crank angle encoder
Satyanarayana Murthy, 2011	cylinder head	detect the "knock" level	VA
Wu *et al*., 2012	cylinder exhaust valve	valve gap abnormal	VA
Li *et al*., 2012	valve rocker arm	broken rocker arm	VB & speed encoder
Antonopoulos and Hountalas, 2012	cylinder head, crankshaft free end	cylinder pressure depends on engine load and speed	engine speed, torque, injection timing, cooling water and lubricating oil temperature, fuel and exhaust temperatures
Heidary *et al*., 2013	fuel injection system	the effect of the fuel blends on the engine vibration	VA and optical-contact tachometer
Yan *et al*., 2013	gear pump	slight crack	on-line ferrographic monitor & an on-line moisture and viscosity detection sensor
Lin *et al*., 2013	fuel injector	pintle head partly grounded off	IAS (using crank shaft encoder)
Arroyo *et al*., 2013	intake and exhaust	engine motored; ignition angle	AE & VA

	valves, piston ring	variations; intake valve clearances; exhaust valve clearances; piston ring fault	
Wargante *et al*., 2013	crankcase; cylinder block	vibration level of single cylinder diesel engine	VA
Albarbar, 2013	various locations on cylinder block	the impact on combustion performance based on injection pressure variation	air-borne acoustic -condenser microphone, in-cylinder (combustion) pressure, vibration, speed, TDC position, temperature
Narayan, 2013	engine block	DFT of in cylinder of motored and un-motored	in-cylinder pressure and optical crank encoder
Jafari *et al*., 2014	intake and exhaust valves	semi-cracked valve; notched valve and excessive clearance	AE
Chiatti *et al*., 2014	in a selected location of the engine block	to characterize the combustion process	VA, intake & exhaust pressures, temperature, engine speed and the crank angle position
Espadafor *et al*., 2014	various locations on cylinder block	different system loads	VA, optical encoder, strain gauge
Alhouli *et al*., 2015	exhaust valve	abnormal valve clearance	cylinder vibration (VA), cylinder pressure, TDC, flywheel gear encoder, torque sensor
Gowtham and Kumar, 2016	piston rings and cylinder walls	possible of wear in the engine components	spectrophotometer oil analysis (wear metal analysis)
Wanyou *et al*., 2016	flexible coupling	torsional stiffness of the elastic coupling	VA (torsional vibration)-magnetic-electric sensor or encoder
Justin *et al*., 2016	valve trains system	deformed valve spring faults and abnormal valve clearance faults	VA & rotary encoder

5. CONCLUSION AND RECOMMENDATION FOR FUTURE STUDY

This paper presented the summary on publications which dealing the research and development of CM system on diesel engine. The types of defects have been among the important factors for researchers to decide the types of sensors. Besides that, the results and analysis has been highly influenced by experimental requirements that could induce certain type of defects or symptoms such as loading conditions and engine speeds. Various forms of signal processing tools such as angular-frequency, time-frequency, CWT, etc have been used to enhance and improve the quality of captured signal to detect and diagnosis the defects. There are certain areas such as engine mounting and flexible coupling which could be studied in future due to lack of publications on these areas. Besides that, a new sensor and data acquisition unit shall be designed that capable to measure all different signals rather than using different sensor for each different signal. This will helps researchers to minimize the time and space needed to conduct their experimental studies.

REFERENCES

Albarbar, A. (2013). Diesel engine air-borne acoustic signals analysis using continuous wavelet transform. *Adv. Appl. Acoust.,* **2**: 2599–2604

Alhouli, Y., Alkhaledi, A.., Alzayedi, A., Alardhi, M., & A, A.I. (2015). *Study of diesel engine vibration condition monitoring. Global J. Res. Eng.*, **15**: 38-44.

Antonopoulos, A.K. & Hountalas, D.T. (2012). Effect of instantaneous rotational speed on the analysis of measured diesel engine cylinder pressure data. *Energy Convers. Manage.,* **60**: 87-95.

Arroyo, J., Muñoz, M., Moreno, F., Bernal, N. & Monné, C. (2013). Diagnostic method based on the analysis of the vibration and acoustic emission energy for emergency diesel generators in nuclear plants. *Appl. Acoust.,* **74**: 502-508.

Chiatti, G., Chiavola, O. & Recco, E. (2014). Combustion diagnosis via block vibration signal in common rail diesel engine. *Int. J. Engine Res.,* **15**: 654-663.

Elamin, F., Gu, F. & Ball, A. (2010). Diesel engine injector faults detection using acoustic emissions technique. *Modern Appl. Sci.,* **4***:* 3-13.

Elamin, F. (2014). *Fault Detection and Diagnosis in Heavy Duty Diesel Engines Using Acoustic Emission.* Doctoral thesis, University of Huddersfield, Huddersfield, UK.

Espadafor, F.J., Villanueva, J.A.B., Guerrero, D.P., Garcia, M.T., Trujillo, E.C. & Vacas, F.F. (2014). *Mech. Syst. Signal Proc.,* **49***:* 135–153.

Flett, J. & Bone, G.M. (2016). Fault detection and diagnosis of diesel engine valve trains. *Mech. Syst. Signal Proc.,* **72-73**: 316–327.

Gawande, S.H., Navale, L.G., Nandgaonkar, M.R., Butala, D.S. & Kunamalla, S. (2010). Cylinder imbalance detection of six cylinder direct injection diesel engine using pressure variation. *Int. J. Eng. Sci. Tech.,* **2**: 433 - 441.

Gowtham, S. & Rajesh Kumar, P. (2016). CM of I.C. engines by using oil analysis. *Int. J. Innovative Res. Sci. Tech.*, **12**: 370-385.

Gu, F., Yesilyurt, I., Li, Y., Harris, G. & Ball, A. (2006). An investigation of the effects of measurement noise in the use of instantaneous angular speed for machine diagnosis. *Mech. Syst. Signal Proc.,* **20***:* 1444-1460.

Heidary, B., Hassan-beygi, S.R., Ghobadian, B. & Taghizadeh, A. (2013). Vibration analysis of a small diesel engine using biodiesel fuel blends. *Agric. Eng. Int.*, **15**: 117-126

Jafari, S.M., Mehdigholi, H. & Behzad, M. (2014). Valve fault diagnosis in internal combustion engines using acoustic emission and artificial neural network. *Shock Vib.*, **Vol. 2014**: Article ID 823514.

Lamaris, V.T., & Hountalas, D.T. (2010). A general purpose diagnostic technique for marine diesel engines – Application on the main propulsion and auxiliary diesel units of a marine vessel. *Energy Convers. Manage.,* **51**: 740-753.

Lin, T.R., Tan, A. C. C., Ma, L. & Mathew, J. (2013). Estimating the loading condition of a diesel engine using instantaneous angular speed analysis. *Proceedings of the Sixth Annual World Congress on Engineering Asset Management [Lecture Notes in Mechanical Engineering], Springer, Duke Energy Center, Cincinatti, Ohio*, pp. 259-272.

Li, Y., Tse, P.W., Yang, X. & Yang, J. (2010). EMD-based fault diagnosis for abnormal clearance between contacting components in a diesel engine. *Mech. Syst. Signal Proc.*, **24**: 193–210.

Li, Z., Yan, X., Guo, Z., Zhang, Y., Yuan, C. & Peng, Z. (2012). CM and fault diagnosis for marine diesel engines using information fusion techniques. *Electr. Electrical Eng.,* **123***:*.109-112

Lowe, D.P., Lin, T.R., Wu, W. & Tan, A.C.C. (2011). Diesel knock combustion and its detection using acoustic emission. *J. Acous. Emiss.,* **29**: 78-88.

Narayan, S. (2013). Wavelet analysis of diesel engine noise. *J.Eng. Appl. Sci.,* **8***:* 255-259.

Mobius Institute, Vibration Training Course Book Category II, (1999-2011). *Chapter 4 (pp.15-20). Rev. 31-03-10.*

Porteiro, J., Collazo, J., Patiño, D. & Míguez, J.L. (2011). Diesel engine CM using a multi-net neural network system with nonintrusive sensors. *Appl. Therm. Eng.,* **31**: 4097-4105.

Rajul, M. & Pahuja, G. L. (2014). Multiple techniques used for CM of induction motor: Experimental study. *Int. J. Electr. Electrical Comput. Syst.,* **3**: 17-26

Satyanarayana Murthy, Y.V.V. (2011). Combustion analysis and knock detection in single cylinder DI-diesel engine using vibratin signature analysis. *Int. J. Eng. Sci. Tech.,* **3**: 10-16.

Wargante, A.R. & Gawade, S.S. (2013). Experimental analysis of single cylinder diesel engine. *Int. J. Eng. Res. Tech.,* **2**: 1035-1038.

Wu, A. & Zhao, X. (2012). Fault diagnosis of diesel based on wavelet transform and support vector machine. *J. Commun. Comput.,* **9**: 1130-1134.

Yan, X., Li, Z., Yuan, C., Guo, Z., Tian, Z. & Sheng, C. (2013). Online CM and remote fault diagnosis for marine diesel engines using tribological information. *Chem. Eng. T.,* **33**: 805-810.